UNIVERSITY OF CALIFORNIA

Los Angeles

Seismic Modeling, Quantifying and Protection of Highway Bridges Considering Shaking

and Lateral Spreading

A dissertation submitted in partial satisfaction of the

requirements for the degree Doctor of Philosophy

in Civil Engineering

by

Yazhou Xie

2017

ABSTRACT OF THE DISSERTATION


Seismic Modeling, Quantifying and Protection of Highway Bridges Considering Shaking

and Lateral Spreading


by


Yazhou Xie

Doctor of Philosophy in Civil Engineering

University of California, Los Angeles, 2017

Professor Jian Zhang, Chair


This dissertation systematically addresses the modeling, quantifying, and protection of

highway bridges against earthquake hazards. Firstly, the research substantially improves the

*p-y* spring based simulation method to predict the seismic responses of highway bridges that

accounts for various soil-structure interaction effects. Closed-form formulae are provided for

the *p-y* spring input parameters to capture the bridge-embankment interaction effects, based

on which an integrated step-by-step modeling procedure is developed. The procedure is

applied to simulate the seismic responses of a well instrumented highway overcrossing and

validated against the recorded responses during the 1992 Petrolia earthquake.

Secondly, the study derives a response modification factor to quantify the relative impact

of liquefaction induced lateral spreading with respect to seismic shaking on column drifts for highway bridges. The column drift response under lateral spreading is correlated to the crust layer energy imposed on the pile foundation at bridge piers. Under seismic shaking, the column drift ratio is directly related to the peak ground acceleration. By normalizing the column drift under the lateral spreading to that of under the seismic shaking, the proposed modification factor captures key features of how columns respond under both lateral spreading and seismic shaking, and offers reliable column drift demand predictions.

Thirdly, this study investigates the effectiveness and optimal design of seismic protective devices for highway bridges. Component-level fragility functions are developed by using the probabilistic seismic demand analysis. To transparently quantify the bridge performance at the system level, seismic repair cost ratios are derived to combine damage probabilities, damage ratios and replacement costs of critical bridge components. Thereafter, a multi-objective genetic optimization method with the Pareto optimal concept is employed to identify the optimal design parameters of protective devices.

Subsequently, the research derives a consistent performance index to facilitate the performance-based design and optimization of seismic protective devices. By converting the system-level repair cost ratio to be a function of median-level engineering demand parameters, a uniform design surface is generated for various protection designs. The derived surface can be easily implemented in the performance-based seismic protection design and optimization without iteratively updating the design goal when a new group of design parameters are considered. The robustness of the proposed method is examined in a case study to identify the

optimal protection designs by using a genetic optimization scheme.

Lastly, the study derives the seismic demand models for bridge rocking columns with foundation on rigid supports when subject to horizontal near-fault strong motions. The system equations of motion are derived and solved to incorporate the column flexibility and the rocking impact mechanism. By representing the near-fault ground motions with corresponding pulses, dimensional analyses are carried out to regress the closed-form expressions of system's drift and uplift demands. A rigorous validation process is implemented to demonstrate that the proposed models can be used with confidence to predict the seismic demands of the rocking system directly from structural and ground motion characteristics.

The dissertation of Yazhou Xie is approved.

Scott Joseph Brandenberg

Ertugrul Taciroglu

Christopher S. Lynch

Jian Zhang, Committee Chair

University of California, Los Angeles

2017

To my parents, Guoliang Xie and Aidi Xie

my sister, Yafeng Xie

my wife Yanyun Zhu and son Ryan Xie

for their love, support and patience.

# TABLE OF CONTENTS

# LIST OF FIGURES

## LIST OF TABLES

# ACKNOWLEDGES

# VITA

**EDUCATION**

| | | | |
|---|---|---|---|
| M.S. in Bridge Engineering, | Tongji University, | Shanghai,China, | May 2011 |
| B.E. in Civil Engineering, | Tongji University, | Shanghai,China, | July 2008 |

**ACADEMIC EXPERIENCE**

| | | |
|---|---|---|
| Graduate Student Researcher, | University of California, Los Angeles, | 2012-2017 |
| Teaching Assistant/Fellow, | University of California, Los Angeles, | 2012-2016 |
| Research Assistant, | Tongji University, | 2008-2011 |

**HONORS AND AWARDS**

| | |
|---|---|
| Dissertation Year Fellowship,  UCLA Graduate Division, | 2016-2017 |
| Conference Travel Award for Graduate Students,  UCLA, | 2016 |
| Graduate Student Researcher Assistantship and Department Grant, UCLA, | 2013-2016 |
| Martin Rubin Scholarship,  UCLA, | 2013-2014 |
| Outstanding Student Scholarships and Excellent Graduate Award, Tongji University, | 2008-2011 |
| Outstanding Student Scholarships, Tongji University, | 2005-2008 |

**PROFESSIONAL MEMBERSHIPS AND SERVICES**

| | |
|---|---|
| President,  UCLA EERI Student Chapter, | 2015-2016 |
| Vice President,    UCLA EERI Student Chapter, | 2014-2015 |
| Student Member, American Society of Civil Engineers (ASCE), | 2013-present |
| Student Member, Earthquake Engineering Research Institute (EERI), | 2013-present |
| Engineer-in-Training (EIT), State of California, | 2016-present |

**PUBLICATIONS**

**Refereed Journal Publications**

1. Xie, Y., Huo, Y., Zhang, J. (2016). "Development and validation of p-y modeling approach for seismic response predictions of highway bridges" Earthquake Engineering and Structural Dynamics DOI: 10.1002/eqe/2804.

2. Xie, Y., Zhang, J. (2016). "Optimal Design of Seismic Protective Devices for Highway Bridges Using Performance Based Methodology and Multi-objective Genetic Optimization" ASCE Journal of Bridge Engineering, 10.1061/(ASCE)BE.1943-5592.0001009, 04016129.

3. Xie, Y., Zhang, J., Huo, Y. (2016). "Simplified drift demand prediction of bridges under liquefaction induced lateral spreading" Earthquake Engineering and Structural Dynamics (submitted).

4. Xie, Y., Zhang, J. "Performance-based seismic design and optimization of protective devices for highway bridges" Engineering Structures (in preparation).

5. Xie, Y., Zhang, J., Wu, G. "Simplified seismic response predictions of controlled rocking columns for bridges" Earthquake Engineering and Structural Dynamics (in preparation).

6. Xie, Y., Xi, W., Zhang, J. "Active control of the benchmark highway bridge using hybrid simulation" ASCE Journal of Bridge Engineering (in preparation).

7. Chai, S., Xiao, R., Zhang, X., Xie, Y. (2012) "Study of Longitudinal Stiffness of Middle Pylon in Multi-span Suspension Bridge" China Journal of Highway and Transport 25(2): 67-71(in Chinese).

**Book Chapter**

Xie, Y., Wu, X., Li, Y. (2013) "Arch Bridge Systems", Bridge Structural Systems S.K. KATARIA & SONS.

**Conference Papers**

1. Xie, Y., Zhang, J. (2016) "Evaluating the Effectiveness and Optimal Design of Isolation Bearings and Fluid Dampers for a Highway Bridge Using a Fragility Function Method and Genetic Optimization" Geotechnical and Structural Engineering Congress pp. 1317-1330.

2. Xie, Y. (2012) "Structural Study of Arch Bridge with a Span of 600m. Part I: Trial Design; Part II: Measures to Improve Mechanical Performance" 2nd International Conference on Applied Mechanics and Mechanical Engineering, Applied Mechanics and Materials, Vols. 138-139, 289-293; 294-298.

3. Xie, Y., Xiao, R., Li, Y. (2011) "Structural Comparison of Three Arch Systems" Highway Engineering 5, 80-85 (in Chinese).

4. Xie, Y., Zhuang, D., Sun, Bin, Xiao, R. (2010) "Construction Control of Replacing Bearings of Continuous Curved Girder Bridge" Shanghai Highway 3, 43-46 (in Chinese).


**PRESENTATION**

Xie, Y. (2016) "Evaluating Effectiveness and Optimal Design of Isolation Bearings and Fluid Dampers for a Highway Bridge Using Fragility Function Method and Genetic Optimization" Oral presentation, Performance Based Design Session, *Geotechnical and Structural Engineering Congress* Feb. 2016, Phoenix, Arizona.


**PROFESSIONAL EXPERIENCE**

Technical Intern in *Simpson Gumpertz & Heger*,                     Jun. 2016-Dec.2016

Technical Intern in *Simpson Gumpertz & Heger*,                     Jun. 2015-Sep.2015

# 1. INTRODUCTION

## 1.1 BACKGROUND

As one of the most critical links in the transportation networks, highway overcrossings commonly consist of reinforced concrete box-girder bridges with end-abutments supported on approaching embankments and center bents supported by pile foundations. Such layout together with short-to-medium span length render that the natural frequencies of highway bridges are usually close to the dominant frequencies of earthquake loadings, which makes them vulnerable to earthquake hazards.

Over the past forty years highway bridges have experienced severe damages under major earthquake events causing significant direct and indirect economic loss (Figure 1.1). During the 1971 San Fernando earthquake, 42 bridge structures experienced significant damage while 5 elevated overcrossings collapsed due to the loss of support at end spans (Jennings and Wood 1971). After the 1989 Loma Prieta earthquake, 144 highway bridges from 9 counties were observed damaged (Gordon, 2002). A major disaster of this earthquake was the collapse of the two-level Cypress Street Viaduct of Interstate 880 in West Oakland, which killed 42 people and injured many more (Tarakji 1992). Several years later, the 1994 Northridge earthquake damaged 286 highway bridges and 7 of them lost their functionality due to severe damage (Caltrans 1994). A rough estimation of the cost for repairing about 230 bridges damaged in the 1994 Northridge earthquake was 150 million dollars, while around 120 million dollars were spent on the 6 collapsed bridges (Kiremidjian and Basöz, 1997). Later the 1995 Kobe earthquake resulted in collapses of 9 highway bridges and destructive damages of 16 bridges

(Ministry of Construction of Japan, 1995). The most extensive damage occurred at an 18-span viaduct of Hanshin Expressway, which collapsed due to the failure of RC columns resulted from the premature shear failure. In 1999, the Chi-Chi earthquake of Taiwan, more than 10 bridges, including a cable-stayed bridge, were severely damaged (Chang et al. 2000). Most recently, during the 2008 Wenchuan earthquake in Sichuan Province, China, among the 320 major bridges and other transportation facilities investigated, 46 bridges were severely damaged, 128 bridges were moderately damaged. The total losses of the transportation system due to the Wenchuan earthquake were over 10 billion dollars, most of which consisted of damage to bridges (Han et al. 2009).

In view of these extensive bridge damages, many research programs have been launched since the 1971 San Fernando earthquake event. Improvements have been achieved in following areas: (1) analysis tools and approaches have been developed for better understanding the seismic responses of highway bridges; (2) modern codes have been formulated with detailed seismic designs for critical bridge components; (3) seismic retrofit programs have been implemented in practice to improve the safety of aged bridges; (4) performance-based earthquake engineering (PBEE) has been developed to link bridges' performance to the associated socio-economic impacts; (5) innovative materials, devices, systems and technologies have been investigated to protect highway bridges against earthquake hazards.

(a) Expansion Joint Damage during the 2008 Wenchuan earthquake


(b) Unseating failure during the 1999 Chi-Chi earthquake


(c) Retaining block damage during the 2008 Wenchuan earthquake


(d) Column shear failure in Hanshin Expressway during the 1995 Kobe earthquake.


(e) Column flexural failure during the 1995 Kobe earthquake.


(f) Bearing failure during the 1995 Kobe earthquake.


(g) Span collapse of the Nishinomiya Bridge following the 1995 Kobe earthquake


(h) Span collapse and pier failure of the Showa Bridge in the 1964 Niigata earthquake

Figure 1.1. Highway bridge failures observed in case histories

Although considerable progresses have been made towards seismically resilient and sustainable highway bridges, some inherent challenges still remain unsolved in research community, among which three important subjects are: (1) to assess the seismic performance of the soil-foundation-bridge system under complex loading scenarios; (2) to evaluate, design, and optimize seismic protective devices in a performance-based manner; and (3) to quantify the effectiveness of innovative designs, systems, and technologies for highway bridges. Detailed discussions for each subject are presented in following sections.

## 1.2 SEISMIC ASSESSMENT OF BRIDGE-FOUNDATION-SOIL SYSTEMS

The above-mentioned case histories have shown a variety of damage mechanisms such as brittle shear failure of short columns, pullout of column reinforcing bars, rotation of skewed superstructures, overturning of piers, abutments and wingwalls, failure at expansion joints, etc. However, the observed various damage cases can be mainly attributed to two damage scenarios, namely seismic shaking and geotechnical failure. Seismic shaking causes bridge damage by imposing excessive inertial loads and displacements onto the structure, while geotechnical failure will accumulate a large amount of soil that push on bridge foundations. A typical damaging scenario of geotechnical failure is the soil liquefaction induced lateral spreading.

### 1.2.1 Soil-structure Interaction (SSI) Effects under Seismic Shaking

The field observations after major earthquakes and plenty numerical studies have shown that seismic responses of bridges are influenced by structural characterization, nonlinear

behavior, ground motion characteristics and SSI effects (Crouse et al. 1987; Werner et al. 1987; MaCallen and Romstad 1994; Kappos et al. 2002; Zhang et al. 2008). The SSI effects are more prominent in highway bridges due to several factors: (1) the flexibility and nonlinearity introduced at end embankments and pile foundations that support the superstructure; (2) the energy dissipation due to large volume of soil involved through approach embankment; (3) the significant kinematic responses at end embankments that result in amplified foundation input motion.

Despite the significance of SSI effects on bridges, there exists large gap between greatly simplified design approaches and realistic yet computationally efficient modeling procedures to capture their potential detrimental role. Existing methods to incorporate SSI effects in bridges include system identification, the substructure method, full 3D bridge-foundation-soil finite element method and the *p-y* models.

The system identification method relies on the available response data from instrumented bridges to back configure the stiffness and energy dissipation of bridge foundations (Werner et al. 1987; Goel and Chopra 1997; Chaudhary et al. 2001; Rahimi et al. 2012; Kampas and Makris 2013). The identification results confirmed the significance of SSI effects, especially the dynamic characteristics of the embankment, which would dominate the output of the bridge-embankment system. However, the applicability of identification results is limited on the vast majority of non-instrumented bridges due to variability of earthquake motions and structural characterization of bridges.

One commonly adopted approach to address SSI problems is the substructure method,

5

where dynamic characteristics of a soil-pile-foundation system or an approach embankment are usually solved separately by simplified soil-substructure models with lumped parameters. Frequency dependent or independent springs and dashpots are usually derived based on frequency domain analysis (Makris et al. 1994; Dobry and Gazetas 1988; Zhang and Makris 2002a, 2002b; Price and Eberhard 2005; Dezi et al. 2009; Carbonari et al. 2011; Lesgidis et al. 2015). Zhang and Makris (2002a) developed kinematic response functions and dynamic stiffness of the approach embankment based on a 2-D shear wedge model. Along with the closed-form expression of the critical length, $L_c$, the dynamic stiffness of the 3D embankment can be derived. They further demonstrated the substructure method in predicting the seismic responses of two instrumented bridges and noted the importance of capturing the amplified embankment crest motions in the analysis (Zhang and Makris 2002b). In general, substructure method offers an attractive manner to investigate SSI effects of bridge structures since it clearly reveals the interaction behaviors between soil foundations and bridge superstructures in a very efficient way; however, assumption of viscous elastic soil material is usually required to solve the dynamic stiffness of the foundation. Hence pursuing a solution of the SSI problem based on substructure method can lead to an incorrect response of the bridge structure as foundation components may display nonlinear behavior, especially when subjected to strong motions.

One direct yet 'expensive' approach on the SSI problem is the numerical solution of the coupled semi-infinite soil-structure system with the use of the finite element method (FEM) (Elgamal et al. 2008; Kwon and Elnashai 2008; Jeremic et al. 2009; Lu et al. 2011; Rahmani et al. 2014). Although the entire coupled bridge-soil system can be analyzed simultaneously by

using the FEM method, the huge size of the semi-infinite soil domain approximation sharply

increased the modeling burden so that extensive computational efforts have to be made to

perform such analysis. By using advanced computing techniques, such as parallel computing

(Lu et al. 2011) and hybrid simulation (Kwon and Elnashai 2008), the execution time of the 3D

FEM analysis can be reduced, nevertheless, this approach still remains unattractive to the

common design process of bridge structures.

An attractive method is the dynamic beam on nonlinear Winkler foundation (*p-y*) method,

which balances between the acceptable accuracy and computational efficiency. The *p-y* model

originates from the study on pile foundation under earthquake loadings (Matlock et al. 1978;

Novak and Sheta 1980). It utilizes distributed springs along the length of the pile to simulate

the pile-soil interaction force as nonlinear function of the pile displacement at given depth.

Various forms of *p-y* elements have been proposed with the help of the laboratory and

centrifuge tests (Nogami et al. 1992; Badoni and Makris 1996; Wang et al. 1998; Allotey and

Naggar 2008; Choi et al. 2015). The *p-y* model typically includes an interface (gap) element

between the pile and soil, a near field nonlinear spring element to account for the strong

nonlinear interaction behavior and the associated hysteretic damping; and a far field element to

simulate the elastic soil medium as well as the radiation damping. Boulanger et al. (1999)

developed a dynamic *p-y* element and implemented it into the finite element program of

OpenSees (Mazzoni et al. 2006). This element is later modified by Brandenberg et al. (2012) to

simulate dynamic SSI behavior of piles in liquefiable soil. The *p-y* model is effective in

accounting for the realistic soil profile, nonlinear interaction and the depth varying foundation

input motions. It has been applied in a few cases to simulate the whole soil-foundation-bridge systems (Aygun et al. 2011; Wang et al. 2013). However, the important bridge-embankment interaction is normally not simulated with the standard *p-y* model.

## 1.2.2 Bridge Response under Liquefaction Induced Lateral Spreading

Besides SSI effects under shaking, seismic responses of highway bridges are strongly influenced by the supporting soil-foundation system in a different way, i.e. local soils impose permanent lateral displacements onto bridge foundations when soil liquefaction is triggered. Soil liquefaction is a phenomenon whereby a saturated or partially saturated soil substantially loses strength and stiffness because of the pore pressure build-up in response to an applied stress, usually earthquake shaking or other sudden change in stress condition, causing it to behave like a liquid. The liquefaction of a shallow underlying deposit during earthquake can then cause considerable lateral displacement for a gently sloping ground. Although fundamental aspects of the liquefaction induced lateral spreading mechanism have been studied by case histories, physical models and numerical simulations in recent years, an efficient yet reliable analysis approach to evaluate the soil liquefaction hazard on highway bridges is still lacking. As a consequence, there exist both difficulty and inconsistency to interpret bridge damages observed using the existing studies. For example, many bridge damage cases under soil liquefaction induced lateral spreading cannot be fully interpreted (Chu et al. 2008); inconsistency occurs between observed damages and analytical conclusions that are based on existing guidelines (Kiremidjian et al. 2006).

When bridges are susceptible to liquefaction induced lateral spreading, an appropriate

numerical framework to accurately predict their seismic responses requires following issues

being addressed: (1) a nonlinear site response analysis to capture the mechanical features of

liquefaction and predict ground lateral spreading, (2) an advanced approach to simulate the SSI

effects for liquefiable soils, (3) a performance-based procedure to cover the inherent

variabilities and uncertainties in association with the large bridge-soil inventory. These issues

have not been fully resolved by current design recommendations (Caltrans 2013), which rely

on component-based static analysis methods, but can be tackled by using global dynamic

analysis procedure under the PBEE framework.

Benefited from the advanced soil models that can effectively simulate the liquefaction

process (Yang et al. 2003; Boulanger and Ziotopoulou 2012) and the development of dynamic

$p$-$y$ spring approach that can capture the liquefiable SSI effects (Brandenberg et al. 2012),

global dynamic analyses of highway bridges under soil liquefaction have been conducted in a

handful of recent studies. Kramer et al. (2008) used a detailed nonlinear finite element analysis

to predict the physical damage and economic loss of highway bridges on liquefiable soil.

Aygun et al. (2011) developed a coupled bridge-soil-foundation model that consists of a

three-dimensional bridge system with two-dimensional soil column models and

one-dimensional $p$-$y$ springs to investigate the influence of soil liquefaction on the seismic

fragility of a multi-span continuous steel bridge. Subsequently, Wang et al. (2014) employed

the same modeling approach to explore the influence of liquefaction on the effectiveness of

base isolation for the similar bridge. Although these studies have provided a deep insight of

how bridge-soil system would perform under soil liquefaction and demonstrated the feasibility

of global dynamic analysis procedure as a robust simulation tool to address the effects of liquefaction on highway bridges, the global dynamic analysis cannot be easily embraced or incorporated with bridge design practice, due to its still significant computational and modeling efforts involved.

### 1.2.3 Motivation of This Study

For bridge responses under seismic shaking, existing analysis tools fail to correctly and efficiently capture the bridge-embankment interaction effects, despite ample field evidences. Moreover, there lacks an integral modeling approach that can simultaneously account for various SSI effects associated with the bridge-foundation-soil system such as bridge-embankment interaction, soil-pile interaction, soil-pile-cap interaction, and amplified motion inputs at end abutments. Partial work of this dissertation is motivated by the need of a complete and accurate assessment of the multiple SSI effects on bridges. An integral *p-y* spring modeling approach is developed and validated for this purpose.

On the other hand, to deal with bridges that are susceptible to liquefaction induced lateral spreading, current practices often rely on component-based static analysis methods. It is because that the dynamic three-dimensional simulation method using advanced soil constitutive models that can capture liquefaction and lateral spreading features is too computationally demanding to be considered in routine practices. The failure mechanisms of bridges exhibited by seismic shaking or liquefaction induced lateral spreading inevitably show different patterns due to distinct load transferring mechanisms, resulting in differences in damaging potential under these two situations. Zhang et al. (2008) have studied the failure

potential of bridges with different structural configurations. Their study concludes that bridge fragility functions due to either ground shaking or lateral spreading show significant correlation with the structural characterizations despite the differences in responses. This study casts light on the derivation of a simple yet dependable tool to quantify the relative influence of soil liquefaction in this dissertation.

## 1.3 PROTECTION SCHEMES OF HIGHWAY BRIDGES

Considerable efforts have been made to better protect highway bridges against earthquake hazards, where traditional methods focus on designing well-confined pier columns with sufficient capacity and ductility, or using steel jackets or composite materials to retrofit existing bridges (FHWA 2006). In recent years, seismic protective devices have demonstrated great promise for seismic hazard mitigation of highway bridges. In the prospective of structural control theories, protective devices can be classified into passive devices, semi-active devices and active control systems (Housner et al. 1997; Spencer and Nagarajaiah 2003). A literature review is provided in the following two sections for the passive devices and the active control techniques, respectively.

### 1.3.1 Passive Devices for Seismic Protection of Highway Bridges

Passive protection devices in the forms of isolation bearings and energy dissipation devices are attractive techniques for seismic hazard mitigation of highway bridges (Buckle and Mayes 1990; Skinner et al. 1993; Priestley et al. 1996; Wang et al. 1998; Kunde and Jangid 2003; Makris and Zhang 2004; among others). As shown in Figure 1.2, several bridges worldwide are equipped

with such devices. The rapid success of seismic protection in buildings has accelerated the implementation of large-capacity damping devices in bridges (Delis et al. 1996). The newly constructed 91/5 bridge in Orange County, California, appears to be the first overcrossing equipped with fluid dampers in United States (Figure 1.2 (c)). At each end abutment of this bridge, four fluid dampers have been installed in together with the elastomeric bearing pads.



(a) Lead rubber bearings used on Fukae Viaduct after 1995 Kobe earthquake
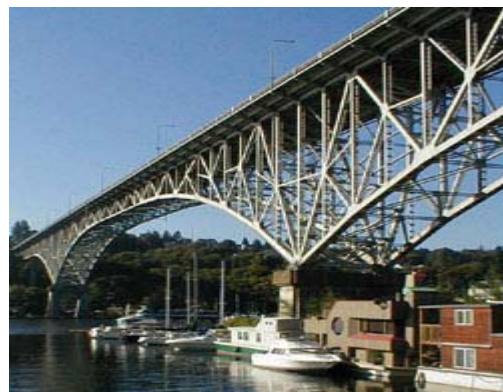


(b) Friction pendulum system used in George Washington Memorial Bridge



(c) Viscous fluid damper used on 91/5 Overcrossing

Figure 1.2. Seismic protective devices used for highway bridges

By lengthening the natural periods of bridges as well as limiting the forces that being transferred to substructures, isolation devices can significantly reduce the damaging potential of pier columns. Also the high initial elastic stiffness of isolators can provide the required rigidity under frequently occurring loads, such as wind and braking (Mayes et al. 1992).

Moreover, supplemental energy dissipation devices such as fluid dampers can provide a distinct form of energy dissipation to effectively control the displacement demand of isolation devices. The incorporation of passive protection devices increases the complexity of seismic evaluation and design for highway bridges, where two major challenges are: (1) a comprehensive evaluation is required to assess the seismic performance of highway bridges that are equipped with passive protection devices, including the incorporation of the uncertainties inherent with ground motions and the damage states of multiple critical components (e.g. columns and isolation bearings); (2) an effective design procedure, which is able to consider nonlinearities in structures and protective devices, a wide choice of mechanical parameters for isolation devices, as well as conflicting responses of isolation bearings and piers, is required to achieve the optimal design parameters of protective devices.

This dissertation is motivated by addressing the origin of these two major challenges, namely evaluation and optimal design of isolation bearings and fluid dampers for seismic protections of highway bridges. Although some studies have been conducted in this area, there remains a potential need to fully solve the problem.

The effectiveness of protective devices for bridges has been extensively studied during the past three decades by using deterministic methods (Wang et.al 1998; Makris and Zhang 2004; Jangid 2005, 2007; Soneji and Jangid 2007; Ozbulut and Hurlebaus 2011; among others). In these studies, seismic responses of bridges that are equipped with protective devices were investigated by conducting nonlinear time history analyses under seismic spectra or a small number of strong ground motions. The results from deterministic methods may not be applied

to other cases due to the variation of ground motions. To account for the uncertainties of earthquake motions, recent studies utilized performance-based evaluation methods to investigate the influences of isolation devices and other retrofit measures on seismic performance of bridges (Karim and Yamazaki 2007; Padgett and DesRoches 2008; Agrawal et al. 2012; Siqueira et al. 2014). Karim and Yamazaki (2007) utilized a simplified model to investigate the isolation efficiency by comparing seismic fragilities of isolated bridges with non-isolated cases for a total of 30 bridge models under 250 motion records. However, their study did not consider the damage stages of isolation devices. By assessing seismic fragilities of multiple key components in a bridge system with various retrofit measures, Padgett and DesRoches (2008) necessitated the derivation of bridge system fragilities since "a given retrofit measure may have a positive impact on some components, yet no impact or a negative impact on other critical components". The effectiveness and optimal design of isolation devices for highway bridges were studied in detail by Zhang and Huo (2009), where a composite damage index was developed to derive the bridge system fragility, also the optimal isolation parameters have been identified as a function of column properties through an extensive parametric study. The studies that consider the bridge performance at the system level have offered an appealing way to evaluate the effectiveness of protective devices for seismic protection of highway bridges.

In addition, recent studies have employed structural control technologies to design smart devices (Housner et al. 1997; Spencer and Nagarajaiah 2003; Narasimhan et al. 2006; Agrawal et al. 2009), such as active or semi-active control devices, and equivalent passive systems

(Gluck et al. 1996; Reinhorn et al. 2009). The essential idea embedded in these studies is originated by a general optimization problem - that is, the best protective devices should provide minimized bridge responses. In this dissertation, an innovative genetic optimization algorithm is utilized to find the optimal design parameters of protective devices. By forming a stochastic evolutionary process where an initial randomly selected population evolves to a superior final solution, applications of genetic algorithm in structure engineering were pioneered in the early 1990s (Adeli and Cheng 1994) and followed by more recent studies for seismic protections of bridges and structures (Jiang and Adeli 2008; Kim and Roschke 2006; Cha et al. 2012; among others). The genetic optimization algorithm is directly used in this study to identify optimal design parameters for passive protective devices.

### 1.3.2 Active Control for Seismic Protection of Highway Bridges

Passive devices have been widely implemented in buildings since they are relatively easy to install and are reliable during natural hazards. However, restricted by their mechanical characteristics, passive devices are not sufficiently adaptive to structure changes and varying loading conditions (Spencer and Nagarajaiah 2003). On the other hand, semi-active and active control systems are designed to capture structural responses in real time and generate appropriate external forces accordingly, which will allow these devices to be adapted to a wide range of loading conditions and structures (Soong 1990; Housner et al. 1997; Spencer and Nagarajaiah 2003; among others).

Recently, a highway benchmark structural control problem was defined for the above-mentioned 91/5 highway overcrossing (Agrawal et al. 2009). The dynamics of the

bridge was represented by a reduced-order model that was exclusively built in the program of

Matlab/Simulink. Various control strategies and devices have been implemented and compared

under this benchmark framework (Agrawal and Nagarajaiah, 2009), which provided

pioneering means for the seismic protection of highway bridges (e.g. the one as shown in

Figure 1.3). However, the dependability of these proposed control methods is restricted by the

fact that the adopted simplified model cannot fully capture the bridge's actual dynamic

behavior, which is indeed influenced by multiple effects such as nonlinear behaviors of

protective devices, SSI effects, structure nonlinearities and complex geometry, etc. In light of

that finite element models can realistically simulate the seismic responses of highway bridges,

a convincing way to investigate the control efficiency on highway bridges lies in developing a

platform that can combine structural control methods with finite element models.
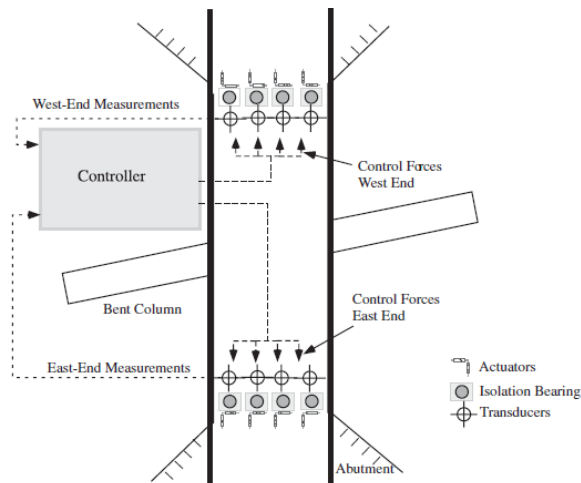


Figure 1.3.  Scheme of active control for the 91/5 Overcrossing (after Narasimhan 2009)

Originally developed as an economic tool to combine physical testing and numerical

modeling, hybrid simulation can be used as an innovative approach to couple structural control

algorithm and finite element models. By maintaining the compatibility and equilibrium at the interface between experimental and numerical substructures, large coupled structure systems can be analyzed separately on different platforms through hybrid simulation. The hybrid simulation scheme for an actively controlled highway bridge is proposed in Figure 1.4, where the bridge structure and SSI effects are modeled using the finite element program of OpenSees (Mazzoni et al. 2006), while supplemental protective devices and control algorithms are implemented in Matlab. The bridge model and the structural control are coupled by sharing forces and displacements at common nodes through a platform designed for hybrid simulation: UI-SIMCOR (Kwon et al. 2007, 2008), which enables various substructures being analyzed in separate modules. The main body of UI-SIMCOR utilizes $\alpha$-OS integration scheme to control each module and perform integration (Kwon et al. 2007). As a good candidate for pseudo-dynamic testing, the $\alpha$-OS integration scheme provides the unconditional stability while preserving the implementation simplicity of explicit schemes (Combescure and Pegon 1997). To improve computational efficiency, UI-SIMCOR adopts static condensation to remove the degree-of-freedoms (DOFs) that do not correspond to applied loadings or points of interest. Reyleigh damping is assumed to generate the system damping matrix.
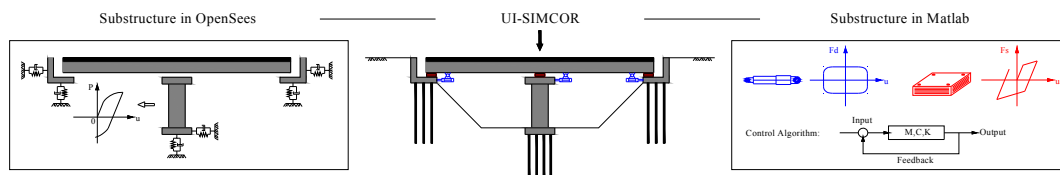


Figure 1.4. Hybrid simulation scheme for actively controlled highway bridges

## 1.4 ROCKING COLUMNS FOR HIGHWAY BRIDGES

Other than the seismic protective devices, this dissertation also investigates the effectiveness of using rocking column-foundation systems to protect highway bridges against earthquake hazards. The conventionally designed bridges expect columns to exhibit inelastic responses under strong earthquakes, which will inevitably cause considerable damages and permanent deformations. During the past several decades, column damages under seismic shaking have occurred in numerous case histories that require expensive and time-consuming retrofit efforts (Jennings and Wood 1971; Gordon, 2002; Chang et al. 2000; among others). To improve column's seismic performance, recent studies have investigated the effectiveness of an innovative design that involves the use of rocking foundations (Ugalde et al. 2010; Deng et al. 2012, 2014; Liu et al. 2013; Espinoza and Mahin 2012; Antoellis and Panagiotou 2014; Antonellis et al. 2015; Kutter et al. 2016; Hakhamaneshi and Kutter 2016). The rocking foundation considered in these studies features a narrower shallow footing directly sitting atop the supporting soils, in which way the bridge-foundation system will uplift and impact the soil when subject to earthquake excitations. As such, the seismic energy can be absorbed by the soils, and the ductility demand of the column can be reduced. However, a dominant concern to challenge the merit of the rocking foundation concept lies in the competence of the supporting soils. Because of the strong momentum induced by the rocking impact, excessive permanent deformations may occur at the pivot locations of the supporting soil, which will significantly increase the vertical and lateral displacement of the bridge. Therefore, this study examines the seismic performance of an alternative rocking foundation system by

replacing the supporting soils with a rigid support, which can be easily realized with the pier foundation or an embedded concrete block designed underneath.

The pioneering study of the rocking behavior under seismic excitation can be traced back several decades ago by Housner (1963). Following Housner's study, a large number of studies have been conducted to further elucidate the complex dynamics of the free-standing rigid blocks (Psycharis and Jennings 1983; Hogan 1990; Zhang and Makris 2001; Makris and Konstantinidis 2003; Makris and Vassiliou 2013; among others). Zhang and Makris (2001) investigated in depth the overturning potential of free-standing rigid blocks under cycloidal pulses, where they discovered two modes of overturning: (1) by exhibiting one or more impacts; and (2) without exhibiting any impact. Subsequently, several studies are conducted to investigate the practical applications of rigid structures designed for rocking, such as the development of the rocking spectrum (Makris and Konstantinidis 2003), and rocking responses of vertically restrained blocks (Makris and Zhang 2001; Dimitrakopoulos and Dejong 2012; Vassiliou and Makris 2015), rigid blocks with isolated bases (Vassiliou and Makris 2012), and multiple aligned free-standing rigid columns (Makris and Vassiliou 2013), etc.

However, compared with free-standing rigid blocks, additional research efforts have to be made to address the complexity associated with rocking columns on rigid supports, such as the influences of column flexibility. Relative studies have been conducted to investigate the transient drift and rocking responses of rocking columns on rigid supports by deriving and solving the system EOMs (Chopra and Yim 1985; Oliveto et al. 2003; Acikgoz and DeJong

2012, 2016; Vassiliou et al. 2015). It has been found through these studies that in contrast to the fixed-base condition, fundamental discrepancies exist if the foundation is designed for rocking. Particularly, geometric nonlinearity and the rocking impact have to be taken into account to accurately predict the dynamic performance of the system. Because it remains difficult to simulate both the large deformation effect and the non-continuous energy loss during instantaneous rocking impacts, relatively few studies have been conducted to develop finite element models for the deformable rocking column systems (Barthes 2012; Vassiliou et al. 2014; 2016).

In light of the facts that (1) previous studies mainly focused on the seismic behavior of the rocking foundation supported by soils; (2) the associated complex dynamics cannot be easily simulated by using the finite element methods; (3) the analytical methods developed are vigorous yet too complicated to be used in practice, this research aims to develop simplified demand models to efficiently quantify the seismic performance of the rocking column system with rigid supports.

## 1.5 PBEE OF HIGHWAY BRIDGES

Rather than conventionally investigate the seismic performance of highway bridges using force-based or displacement-based methods, the Performance Based Earthquake Engineering (PBEE) attempts to investigate highway bridge performance through linking component actions and deformations (e.g. drifts, curvatures) first to damage states and then to the likely post-earthquake functionality. Along with the probabilistic form, PBEE can be broken into four steps: (1) seismic hazard analysis that quantifies the seismic input at the site in terms of

intensity measures (IM); (2) structural analysis that relates the seismic input to structural responses that is revealed by engineering demand parameters (EDPs); (3) damage analysis that relates the structural response to damage measures (DMs); (4) loss analysis that relates damage to decision variables (DV). By using this four-step procedure, the PBEE is able to assist decision makers with transparent information to allocate resources for new construction and retrofitting targeting the desired performance of highway bridges when facing earthquakes.

Devoted studies have been conducted to analyze and design highway bridges using PBEE in recent years. New documents have been published, such as the HAZUS manual (FEMA 2003) for post-earthquake loss estimation of highway bridges, and the NCHRP SYNTHESIS 440 - Performance-Based Seismic Bridge Design (2013) for performance-based seismic design of highway bridges.

In research community, the PBEE methodology has been utilized as a powerful tool to evaluate the seismic performance of different highway bridge systems, including skewed bridges (Huo and Zhang 2013; Deepu et al. 2014; Yang et al. 2015), isolated bridges (Karim and Yamazaki 2007; Zhang and Huo 2009; Siqueira et al. 2014), retrofitted bridges with various measures (Padgett and DesRoches 2008; Agrawal et al. 2012), bridges installed with smart materials and devices (Choi et al. 2010; Bhuiyan and Alam 2012; Billah et al. 2013), bridge-foundation-soil systems (Bradley et al. 2010; Aygun et al. 2011), deteriorating bridges (Alipour et al. 2011; Dong et al. 2013; Zanini et al. 2013), etc. All these studies have demonstrated the attractive promise of implementing the PBEE method; namely it provides a probabilistic framework to account for the uncertainties from the ground motion hazard, the

corresponding structural responses, and the damage and economic losses sustained.

An important step for PBEE is developing the seismic fragility functions, which define the conditional probability of attaining or exceeding a specified damage state for a given set of input intensity measures. Depending on the data resources, fragility functions can be generated as empirical ones that are based on bridge damage data from major earthquakes (Basoz et al. 1999; Shinozuka et al. 2000), or analytical ones derived from numerical analysis results (Karim and Yamazaki 2007; Padgett and DesRoche 2008; Agrawal et al. 2012; Siqueira et al. 2014; Zhang and Huo 2009; among others). Due to the absence of adequate empirical data, analytical fragility functions have been increasingly used in both research and practical communities, where seismic response are obtained from nonlinear time history analysis, elastic spectra analysis or nonlinear static analysis (Choi et al. 2004). In this dissertation the analytical fragility function method and the PBEE framework are utilized as effective tools to investigate the bridge performance probabilistically.

## 1.6 ORGANIZATION

Chapter 2 develops a systematic, step-by-step *p-y*-spring-based simulation procedure for predicting the seismic response of highway bridges that accounts for various SSI effects. The modeling-based simulation procedure is applied to assess the seismic responses of a well instrumented highway overcrossing and validated through comparisons with the recorded responses during the 1992 Petrolia earthquake.

Chapter 3 derives a response modification factor for column drift ratio under seismic shaking to quantify the comparative influence of liquefaction induced lateral spreading on

highway bridges. The proposed method captures key features of how bridges perform under liquefaction induced lateral spreading, and offers reliable column drift predictions.

The effectiveness and optimal design of seismic protective device are investigated in Chapter 4. Component-level fragility functions are first derived by probabilistic seismic demand analysis using nonlinear time history analyses that include SSI effects and ground motion uncertainties. The bridge repair cost ratios (RCRs) are then derived using a performance-based methodology and the associated component failure probability. The multi-objective genetic optimization method that utilizes Pareto optimal concept is employed to identify the optimum design parameters of protective devices.

Chapter 5 develops an integral performance-based design and optimization framework for seismic protections of highway bridges. By converting the seismic RCR to be a function of the median EDPs, a uniform design surface is derived for a variety of protected bridge systems. The soundness of using the derived RCR surface is examined in a case study where the optimal protection designs are identified without iteratively updating the fragility functions at every time when a new design is considered. It therefore validates that the proposed framework can significantly facilitate the design and optimization of protective devices in a probabilistic manner.

Chapter 6 quantifies the seismic responses of the rocking column-foundation systems on rigid supports. The system equations of motion are derived analytically and solved numerically to simultaneously account for the superstructure mass inertia, the column flexibility, the uplift condition, and the rocking impact mechanism. Dimensional analyses are

developed to derive the closed-form expressions of peak column drifts and uplift angles as functions of ground motion characteristics and geometric and dynamic parameters of the column. The proposed models are validated against the numerical simulations for five as-built bridge column cases under twelve recorded near-fault motions.

Finally, a summary and discussion of future work are presented in Chapter 7.

# 2. SEISMIC RESPONSE PREDICTIONS OF HIGHWAY BRIDGES UNDER SEISMIC SHAKING

Figure 2.1 shows a schematic sketch of a typical highway bridge. Pile foundations are often used to support bridge columns at center bent and end abutments. They transfer the axial load, shear force and bending moments of the superstructure to the surrounding soil through the combinations of axial soil-pile friction, lateral soil resistance, and end bearing forces, in addition to the resistance provided by the pile cap. Furthermore, typical highway bridges are supported at ends by abutment and embankment soils, whose dynamic characteristics affect appreciably the earthquake responses of highway bridges. This chapter aims to develop an integral modeling approach that can efficiently capture the soil-pile interaction, the bridge-embankment interaction, the soil-pile-cap interaction, and the embankment motion amplification effect. In view of its robustness, the *p-y* modeling approaches are considered herein.
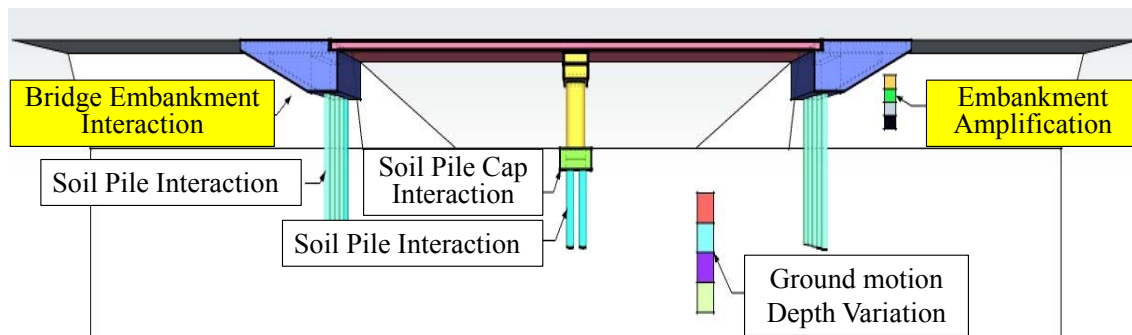


Figure 2.1.  Schematic sketch and SSI effects of typical California highway bridges

## 2.1 THE *p-y* MODELING FOR PILE FOUNDATIONS

As shown in Figure 2.2, pile foundation consists of a pile cap supported by multiple pile columns, where the former is modeled by rigid beam elements and the latter can be modeled by linear or nonlinear beam elements that possess appropriate tributary masses and pile stiffness. The *p-y* method is an efficient way to model the interactions between soil and pile (such as axial soil-pile friction, lateral soil resistance, and end bearing forces) and pile cap resistance using empirically derived nonlinear soil springs (Wang et al. 1998; Boulanger et al. 1999; Curras et al. 2001). The fundamental assumption is that the pile-soil interaction force at a given depth only depends on the relative soil displacement at that location. At each depth below ground, foundation nodes are connected with horizontal *p-y* springs. In addition, *t-z* and *q-z* springs are incorporated to account for soil resistances in the vertical direction, where the former simulates pile skin frictions and the latter considers bearing capacity of the soil at pile tips. Horizontal foundation input motions are applied to the free ends of all *p-y* elements, while for *t-z* and *q-z* elements, their free ends are fixed to exclude vertical motion inputs, whose magnitudes are typically smaller compared with horizontal motions. In addition, the energy dissipation and group effects due to interaction between the piles need to be considered in *p-y* method.
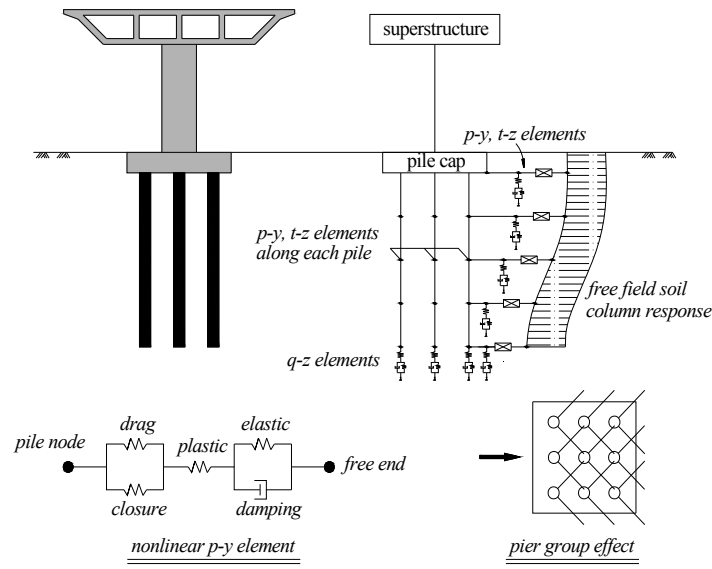
Figure 2.2. Schematic of dynamic *p-y* spring modeling at pile foundation

### 2.1.1 Nonlinear *p-y* Elements

Consistent with previous studies (Nogami et al. 1992; Boulanger et al. 1999), the nonlinear *p-y* elements chosen in this study consists of a gap closure element, a plastic element and an elastic element in series (Figure 2.2), representing the gap formation at the pile-soil interface, the nonlinear interaction behavior in the near field and the elastic soil medium (radiation damping) in the far field, respectively. The constitutive behavior of the *p-y* springs for soft clay is based on Matlock's recommendations (1978), while the American Petroleum Institute (API) sand model is used for sand (API 1993). Two key input parameters in association with each *p-y* spring are $p_{ult}$, the ultimate resistance force that the soil can exert under lateral loading, and $y_{50}$, the displacement when 50% of the ultimate resistance is mobilized, both of which can be calculated by the *PySimple*1 command in *OpenSees* based on soil properties (Mazzoni et al. 2006). The *p-y* springs are also used to model the

soil-pile-cap interaction effects with additional adjustments that are considered by Curras et al. (2001), i.e. soil lateral resistance is summed by passive pressure on the front and skin frictions on two sides (bottom frictions are ignored). In this study pile cap is considered as a retaining structure backed with infinite long soil layers, such that the passive pressure can be calculated by a static pushover analysis of a two-dimensional finite element model that consists of pile cap and back-soils. The modeling procedure is very similar as that considered for the abutment SSI effects in the longitudinal direction, which will be explained in detail later.

### 2.1.2 Pile Group Effects and Input Motions

Pile group effect is considered using the *p-y* element of a single pile in conjunction with the concept of superposition criterion; i.e. the ultimate capacity of each pile is adjusted with a proper reduction factor due to the dynamic interactions of one pile with other piles in a group (Figure 2.2). The superposition method was originally developed for static loads by Poulos (1968) and later justified for dynamic loads by other researchers (Curras et al. 2001; Kaynia and Kausel 1982; Sanchez-Salinero 1983; Roesset 1984). An average reduction factor $m_p$ (also named as the '*p*-multiplier') is usually derived for dynamic loads since the 'front' and 'rear' rows alternate between being the leading and following row during cyclic loading (Curras et al. 2001). In this study, the method used by Zhang and Makris (2001) is adopted to calculate the value of the $m_p$ factor.

Furthermore, depth varying horizontal motions that are applied to the free ends of all *p-y* spring can be generated by one-dimensional site response analysis using either equivalent

linear program or nonlinear program. In this study the equivalent linear program SHAKE91 (Idriss and Sun 1992) is adopted, which calculates the seismic site response based on the vertical propagation of shear waves and approximates nonlinear soil behavior with strain dependent shear modulus and damping curves.

### 2.1.3 Equivalent Pile Foundation with Reduced Piles

Given that a typical pile foundation consists of large number of single piles, the modeling of each individual pile with associated $p$-$y$, $t$-$z$ and $q$-$z$ springs increase significantly the computational effort required. In the interest of a practice-oriented modeling approach, this study develops an approximation method to simplify the pile group that has M rows and N columns of piles with an equivalent 2×2 pile group (Huo 2011), such that both translational and rotational behaviors of the pile group can be captured. Based on matching the static force displacement relations of the original pile group, the equivalent 2×2 pile group is developed by the following assumptions: (1) The size of the pile cap is unchanged; (2) The center-to-center spacing between the piles in the equivalent 2×2 pile group is approximately two thirds of the center-to-center distance between the corner piles in the original pile group; (3) The axial and bending stiffness (as well as the capacities if using nonlinear elements) of the equivalent 2×2 pile group is amplified by a factor of 1/4 of the total pile number M×N; and (4) The ultimate capacities of $p$-$y$, $t$-$z$ and $q$-$z$ springs are modified by a factor of 1/4 of the total pile number M×N.

Following the approach described above, a 4×5 pile group is converted into the equivalent 2×2 pile group and the accuracy of the proposed procedure is evaluated. Figure 2.3

plots the force-displacement relations of the original case (4×5 piles) together with the simplified case (2×2 piles) under three translational and three rotational loadings, respectively. As shown in the figure, consistent results between these two models can be identified in *Z*, *RX* and *RY* directions, while about 30% difference exists in two translational directions regarding values of both stiffness and ultimate capacity. Discrepancies can also be observed in terms of the initial stiffness in *RZ* direction. Nevertheless, given the significant saving in computational effort (roughly 20% of the original problem size), the simplified model is adopted despite the slight loss in accuracy. More importantly, later case study indicates that such simplification will result in almost negligible errors for bridge level responses.
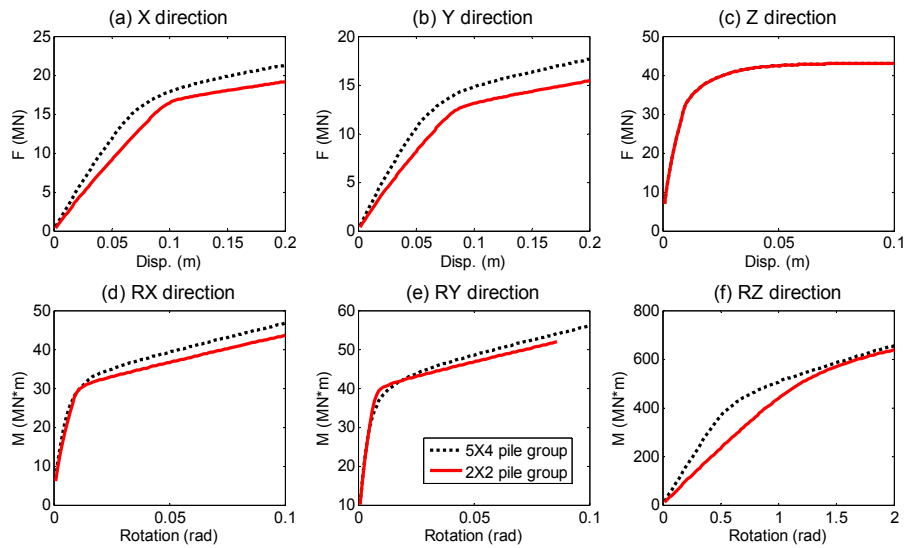


Figure 2.3. Static response comparison of the 4 × 5 pile group and 2 × 2 equivalent pile group.

## 2.2 DEVELOPMENT OF *p-y* MODELS FOR EMBANKMENTS

### 2.2.1 Bridge-embankment Interaction in Longitudinal Direction

Typical highway bridges are supported at ends by abutments and embankment soils. Along the longitudinal direction, the behavior of abutment-embankment system can be assumed as abutment wall backed with embankment fill in plane strain condition (Richards and Elms 1979; Al-Homoud and Whitman 1999; Shamsabadi et al. 2010). A 2D finite element model of abutment-backfill system is built in the commercial finite element software ABAQUS to derive the input parameters of *p-y* springs for embankment along the longitudinal direction.

As shown in Figure 2.4, the abutment wall is modeled as a rigid beam element with a height of *H*; embankment fill is modeled as the Drucker-Prager (D-P) material, which offers a smooth approximation of the Mohr-Coulomb (M-C) hexagonal shape yield surface so that convergence issues can be avoided. Vertical boundaries of the backfill are placed at a distance of 5*H* to the right and 1*H* to the left. The total height of the embankment is 2*H*. The computation domain needs to be big enough to cover the finite deformation zone behind the abutment. Horizontal constraints are applied at vertical boundaries, whereas both horizontal and vertical degrees are fixed at the bottom. Contact Coulomb friction elements are used between abutment wall and backfill to simulate the frictional behavior, where the wall-soil friction angle, $\delta$, is considered to change from 0 to soil friction angle, $\varphi$, depending on the wall roughness and drainage condition. With the 2D FEM model, the *p-y* spring inputs are obtained using a two-step analysis procedure: (1) embankment response under passive

loading condition is derived by a static pushover analysis, i.e. the backfill is pushed by the

abutment wall with prescribed horizontal displacements until passive failure occurs; (2) $p$-$y$

spring inputs of $p_{ult}$ and $y_{50}$ are obtained by regressing the force-displacement curve of the

embankment with multiple vertically distributed $p$-$y$ springs.
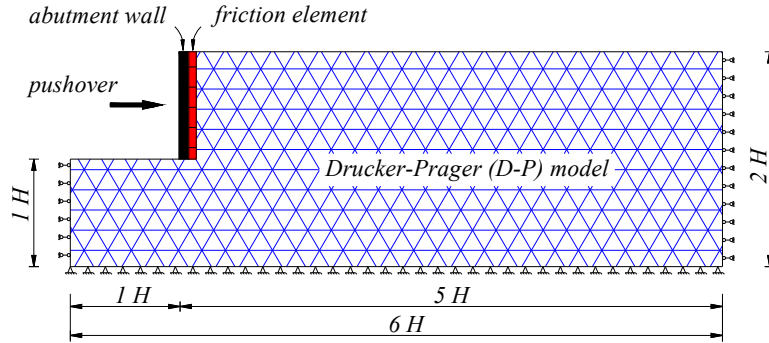


Figure 2.4. 2D finite element model of the abutment-backfill system in the longitudinal
direction

The soundness of the numerical model is firstly examined against the full-scale test

results of a seat-type abutment backed with granular backfill (Lemnitzer et al. 2009), which

consists a wall height of $H$ = 1.67m, effective wall width of $W$ = 4.87m, silty sand with

friction angle of $\varphi$ = 40° and cohesion of $c$ = 14.0kPa, soil unit weight of $\gamma$ = 20.0kN/m³, and

mobilized wall-soil friction angle of $\delta$ = 14°. Figure 2.5 shows the deformation contour of the

numerical model as well as the comparison of force-displacement curves between numerical

model and the full-scale test. As shown in Figure 2.5(a), the deformed shape of the backfill at

failure stage is consistent with a logarithmic spiral curve that has been observed in the test

(Lemnitzer et al. 2009). Also as can be seen from Figure 2.5(b), the pushover curve of the

finite element model agrees well with the test results, especially in capturing small strain

32

stiffness and ultimate capacity. It is noted that the numerical curve cannot capture peak resistance and strength degradation, which can be expected since the adopted D-P soil model does not possess strain-softening features.
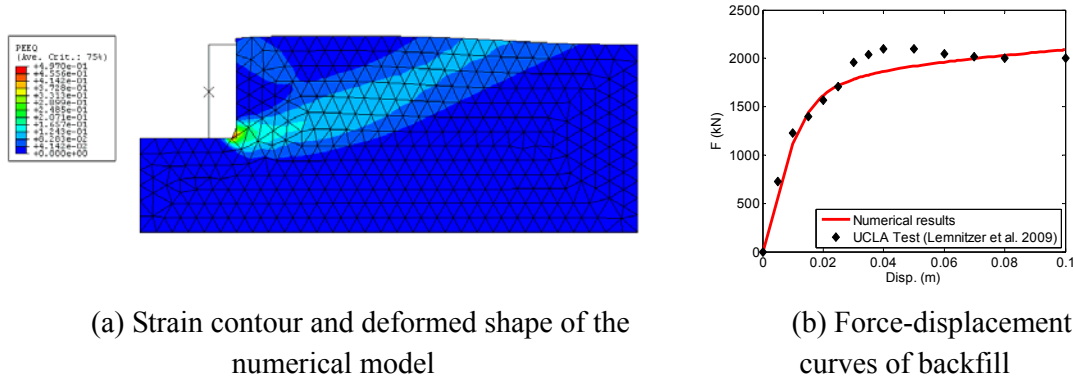


(a) Strain contour and deformed shape of the numerical model

(b) Force-displacement curves of backfill

Figure 2.5. 2D FEM calibration of the longitudinal abutment wall - backfill system

The force-displacement curve of the embankment is regressed by a group of vertically distributed $p$-$y$ springs through the least square method. Given that passive pressure of the backfill linearly increases along wall depth, all regressed $p$-$y$ springs are designed to have linearly increasing ultimate capacities while maintaining a constant $y_{50}$. As shown in Figure 2.6, the regression process is conducted for two cases, i.e. the one using 10 $p$-$y$ springs and the other using 3 $p$-$y$ springs vertically distributed. It is found that for the 10-spring case, the total capacity is 2030kN, while for the 3-spring case, the best result yields a total capacity of 1990kN. The $y_{50}$ value is 0.0093m for both cases. Figure 2.6 also plots the backbone curve of each spring for the 3-spring case. As can be seen in the Figure 2.6, regressed $p$-$y$ curves for these two cases are on top of each other and can both capture the small strain stiffness, large strain stiffness and ultimate capacity of the backfill.

33
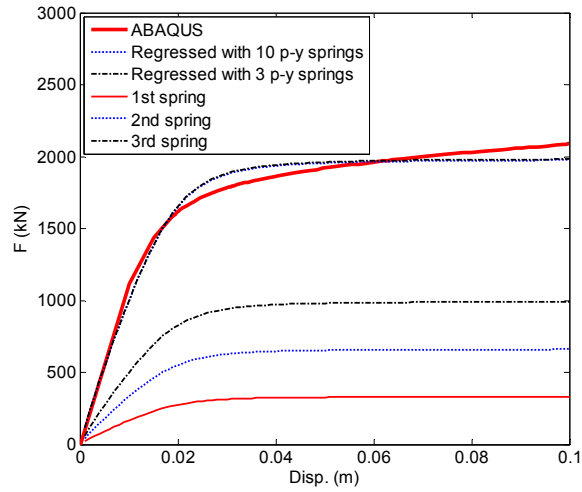
Figure 2.6. Force-displacement curves using *p-y* spring regression

It's worth mentioning that ideally backfill will exert static pressure $K_0$ and active pressure $K_a$ when the abutment starts moving away from the embankment fill. These two kinds of pressures are much smaller and for simplicity they are ignored. Instead a serially connected gap element is modeled along each *p-y* element to capture gap openings. The original gap-closing effect in association of the *p-y* elements for pile foundations is excluded, which can be easily achieved by setting the closing coefficient equals to 0 (or a very small value to avoid convergence issues).

Extensive theoretical studies have been conducted to derive earthquake-induced earth pressures on retaining walls that are backed with cohesionless soils (Caquot and Kerisel 1948; Sokolovski 1965; Mylonakis et al. 2007; among others). In this study, the regressed *p-y* input values of $p_{ult}$ are verified through comparing numerical passive pressure coefficients $K_p$, which can be calculated by $\Sigma p_{ult}$ divided by $1/2\gamma H^2$, with theoretical solutions. Table 2.1 lists

34

$K_p$ values from numerical modeling in this study as well as those obtained from leading analytical studies. It can be seen that numerical $K_p$ values are very close to the solutions from log-spiral theory, Sokolovski's method and Mylonakis's model. Also it is expected that Rankine theory underestimates the passive pressure since it neglects soil frictions at soil-wall interface and soil base, while Coulomb theory overesitmates the passive pressure, resulting from the fact that the actual sliding surface is curved, rather than being a plane as assumed in the Coulomb theory.

Table 2.1.   Comparison of $K_p$ values between FEA results and theoretical solutions

| $\varphi$ | $\delta$ | Finite element analysis results $H$ (m) | | | | Theoretical solutions | | | | |
|---|---|---|---|---|---|---|---|---|---|---|
| | | 1.5 | 2.5 | 3.5 | 4.5 | $K_P^{*1}$ | $K_P^{*2}$ | $K_P^{*3}$ | $K_P^{*4}$ | $K_P^{*5}$ |
| 20° | 0° | 2.02 | 2.01 | 2.01 | 1.98 | 2.04 | 2.04 | 2.03 | 2.04 | 2.04 |
| | 10° | 2.53 | 2.42 | 2.38 | 2.33 | 2.04 | 2.64 | 2.59 | 2.55 | 2.52 |
| | 20° | 2.75 | 2.61 | 2.52 | 2.44 | 2.04 | 3.53 | 3.00 | 3.04 | 2.87 |
| 30° | 0° | 3.51 | 3.22 | 3.15 | 3.07 | 3.00 | 3.00 | 3.04 | 3.00 | 3.00 |
| | 15° | 5.12 | 4.74 | 4.63 | 4.61 | 3.00 | 4.98 | 4.85 | 4.62 | 4.44 |
| | 30° | 6.67 | 6.27 | 6.11 | 5.89 | 3.00 | 10.10 | 6.50 | 6.55 | 5.80 |
| 40° | 0° | 5.86 | 5.36 | 5.16 | 4.98 | 4.60 | 4.60 | 4.72 | 4.60 | 4.60 |
| | 20° | 10.83 | 9.99 | 9.89 | 9.61 | 4.60 | 11.80 | 10.66 | 9.69 | 8.92 |
| | 40° | 16.81 | 15.65 | 14.71 | 14.23 | 4.60 | 92.60 | 18.00 | 18.20 | 14.40 |

Note: *1 Rankine theory; *2 Coulomb theory; *3 Log-spiral theory (Caquot and Kerisel 1948); *4 Sokolovski 1965; *5 Mylonakis et.al 2007.

## 2.2.2 Bridge-embankment Interaction in Transverse Direction

In the transverse direction, 3D finite element model is built to capture the wedge-shaped cross section of the embankment fill as well as the interaction zone between abutment and embankment fill. As shown in Figure 2.7(a), the abutment wall is modeled as rigid elements with a width of $B_c$ and a height of $H$, the embankment fill is modeled by the D-P soil model

with a top width of $B_c$, a base width of $B_b$, a length of $L_E$, and a height of $H_E$. The embankment slope is $S$. The bottom surface of the embankment is constrained with all three translational degrees. A static pushover analysis is conducted to derive the force-displacement relation of the embankment in transverse direction, from which input parameters of transversely distributed $p$-$y$ springs are calculated by regressing $p$-$y$ curves to the pushover curve. It is noted that other than the pushover analysis assuming abutment wall and backfill are strictly connected, the friction effect at the interface of abutment wall and backfill may induce a sliding mechanism in between. To capture this sliding mechanism, a gap-friction element that is used to model the gap opening in longitudinal direction is also connected in serial with the $p$-$y$ spring in transverse direction. In other words, the gap-friction element is assigned with zero tension capacity along longitudinal direction to model the gap opening and a normal pressure dependent friction capacity in transverse direction to model the sliding mechanism. Therefore, as shown in Figure 2.7(b), abutment-embankment interaction effects are simulated by the gap-friction element and the $p$-$y$ spring elements connected in series for both longitudinal and transverse directions.
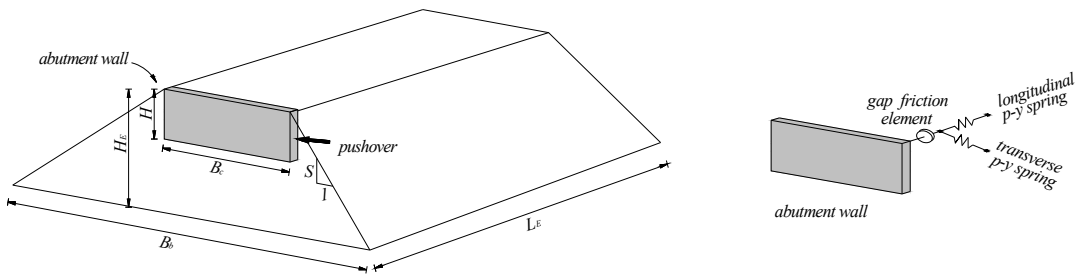


(a) 3D finite element model          (b) $p$-$y$ modeling scheme
Figure 2.7.  The $p$-$y$ modeling scheme of embankment in transverse direction

A case study is carried out to illustrate the numerical modeling procedure. The 3D numerical model consists of a top width of $B_c$ = 20.0m, a bottom width of $B_b$ = 70.0m, an embankment height of $H_E$ = 9.6m, a wall height to embankment height ratio of $H/H_E$ = 0.3, and a slope inclination of $S$ = 1:2.6. Soil properties are chosen to be the same as those in the longitudinal case study. Figure 2.8(a) shows the plastic strain contour at one displacement step for the pushover analysis, where it can be seen that embankment fill deforms within a limited range. Only a small part that is very close to the abutment wall is mobilized at large strains. The force-displacement curve and the *p-y* regression curve are shown in Figure 2.8(b), where identical force-displacement relationships can be observed between numerical data and *p-y* regression curve. In addition, Figure 2.8(b) presents the friction limits at wall-soil interface with three different cases: the one with static pressure and a friction angle of $0.5\varphi$, the one with passive pressure and a friction angle of $0.5\varphi$, and the last one with passive pressure and a friction angle of $\varphi$. It can be seen that friction limits vary in a big range with different combinations of normal pressures and friction angles. For the case of passive pressure with a friction angle of $0.5\varphi$, which is very likely to happen during earthquakes, abutment transverse mobilization will be determined by both passive loading mechanism and sliding mechanism, while the ultimate capacity of the backfill will be dominated by the sliding friction limit. Therefore, the coupled modeling procedure that is composed of a gap-friction element connected in serial with the *p-y* springs can accurately capture the interaction behavior of abutment-embankment system in the transverse direction.

37
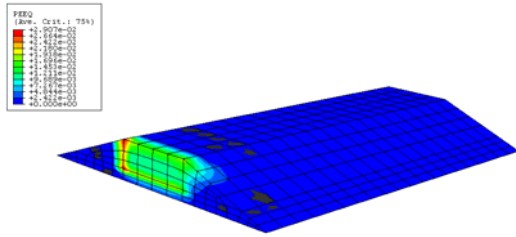
(a) Strain contour and deformed shape of the numerical model
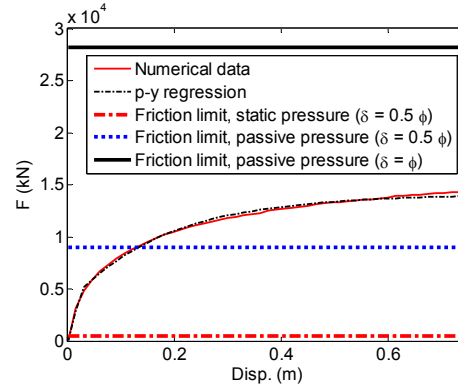


(b) Force-displacement curves of jointed mechanism and sliding mechanism together with *p-y* spring regression

Figure 2.8. Force-displacement of jointed mechanism and estimated sliding mechanism

### 2.2.3 Closed-form *p-y* Model Parameters

Given that the proposed *p-y* modeling scheme requires considerable efforts to set up both 2D and 3D finite element models for each bridge-embankment case, this study seeks to provide closed-form expressions of *p-y* spring model parameters by building an extensive group of numerical models that can cover most highway bridge cases. The total ultimate capacity of $\Sigma p_{ult}$ and $y_{50}$ values are developed as functions of backfill properties and geometric parameters of abutment wall and embankment fill.

In the longitudinal direction, four modeling parameters are varied to cover a comprehensive range of abutment-embankment systems. The abutment wall height $H$ is varied from 1.0m to 4.5m with an increment of 0.5m. The soil friction angle $\varphi$ is varied from 20° to 40° with an increment of 5°. The soil cohesion $c$ starts from 0kPa and is varied from 5kPa to 125kPa with an increment of 20kPa. The wall-soil friction angle $\delta$ is varied from 0 to $\varphi$ with an increment of 5°. Hence, a total of 2520 models are built by changing these four input parameters. Based on the passive pressure coefficient developed by Mylonakis et.al

38

(2007) for the cohesionless case, least square numerical regressions are carried out to develop

the formulae of p-y model parameters $\Sigma p_{ult}$ and $y_{50}$, as follows:

$$\Sigma p_{ult,L} = \frac{[1+\sin\varphi\cos(\theta+\delta)]e^{(\theta+\delta)\tan\varphi}}{(1-\sin\varphi)\cos\delta} \cdot \left[0.5\gamma H^2 + \cos\varphi\cdot cH\right] + \cos\varphi\cos(\theta+\delta)\cdot cH \qquad \text{(kN/m)} \quad (2.1)$$

$$y_{50,L} = \frac{0.5\Sigma p_{ult,L}}{K_{s,L}} \qquad\qquad\qquad \text{(m)} \qquad (2.2)$$

where $\Sigma p_{ult,L}$ and $y_{50,L}$ are the total ultimate capacity and $y_{50}$ value of the 2D embankment fill

in longitudinal direction respectively, the former has a unit of kN/m and the latter is in meters,

$\gamma$ is the soil unit weight of 20 kN/m³, soil friction angel $\varphi$ and wall-soil friction angle $\delta$ are in

radians, $\theta$ is an internal variable defined as $\sin^{-1}(\sin\delta/\sin\varphi)$. $K_{s,L}$ is the longitudinal secant

stiffness that corresponds to 50% total ultimate capacity, which has a unit of kN/m² and can

be calculated as:

$$K_{s,L} = 5\gamma W_0 e^{3\varphi}\left[43-12\delta\right] \qquad\qquad \text{(kN/m}^2\text{)} \quad (2.3)$$

where $W_0$ is the unit length in meter. It is noted that Eq. (2.1) will yield the same results as the

Rankine and Coulomb theories if wall-soil friction and soil cohesion are neglected.

Essentially, Eq. (2.1) provides the identical horizontal force as the one theoretically derived

by Mylonakis et.al (2007) for the cohesionless soil case.

The soundness of derived closed-form expressions of $\Sigma p_{ult,L}$ and $y_{50,L}$ are examined by

comparing them with numerical data. As shown in Figure 2.9(a), comparisons between

39

numerical data and closed-form solutions are firstly provided with respect to soil friction

angle and cohesion by keeping abutment wall height as 3m and wall-soil friction angle as 10º.

It is evident that the closed-form expressions provide good agreement with the numerical data

when soil friction angle and cohesion are the chosen variables. Similarly, Figure 2.9(b)

checks the consistency between numerical data and closed-form results with respect to wall

height and wall-soil friction angle by keeping soil friction angle as 40º and soil cohesion as

5kPa. It also can be seen that closed-form expressions are capable of providing almost

identical *p-y* spring inputs as numerical data when the other two parameters, i.e. wall height

and wall-soil friction angle, are changing.
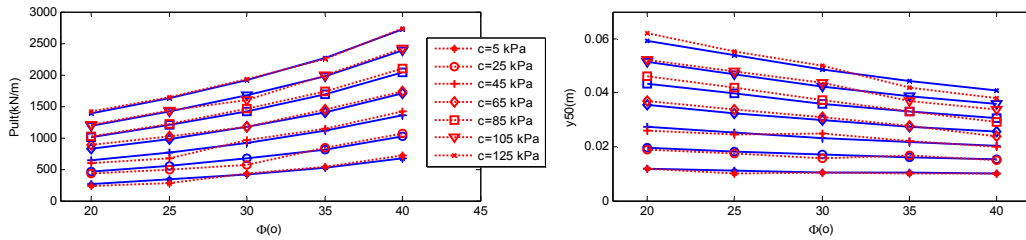


(a) $\Sigma p_{ult,L}$ and $y_{50,L}$ comparisons when $H$=3.0m and $\delta$=10°
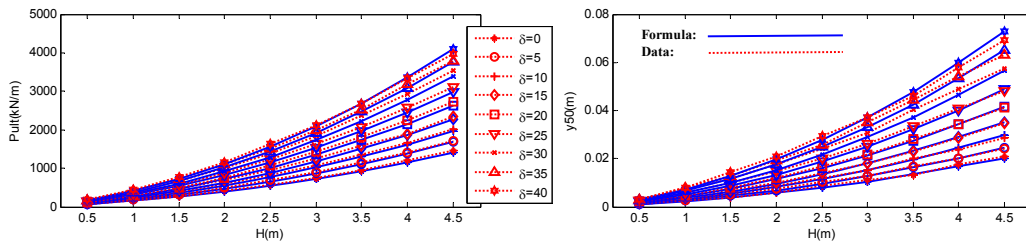


(b) $\Sigma p_{ult,L}$ and $y_{50,L}$ comparisons when $\varphi$=40° and $c$=5kPa

Figure 2.9. Comparisons of $\Sigma p_{ult,L}$ and $y_{50,L}$ between numerical data and closed-form
solutions in the longitudinal direction

The pushover analysis in the transverse direction assumes a strict connection at wall-soil

interface, i.e. no friction angle is considered in this step. Therefore, five modeling parameters in total are varied to cover typical 3D bridge-embankment systems. The embankment height $H_E$ is varied from 4.0m to 12.0m with an increment of 2.0m. The wall height to embankment height ratio $H/H_E$ is varied from 0.3 to 0.9 with an increment of 0.2. The wall width $B_c$ is varied from 8.0m to 24.0m with an increment of 4.0m. The soil friction angle $\varphi$ is varied from 20° to 40° with an increment of 5°. Soil cohesion $c$ is varied from 0kPa and then from 5kPa to 125kPa with an increment of 30kPa. The embankment length $L_E$ is set to be large enough such that the mobilized region can be fully included in each model. Meanwhile, as concluded by Zhang and Makris (2001), the cross section shape of the embankment fill has insignificant influence to abutment transverse response, the slope inclination $S$ is kept as 1:2.0 for all numerical models. Note that although the modeling scale is reduced by making this simplification, a total of 2500 models have been built by changing above five parameters. The same numerical regression process is taken to derive closed-form expressions of the two input parameters, $\Sigma p_{ult}$ and $y_{50}$, for transverse p-y curves:

$$\Sigma p_{ult,T} = 0.06 e^{\left(6.3\varphi + \frac{2.5H}{H_E}\right)} \cdot \left\{ \frac{1.1H_E}{B_c} + \frac{1}{3\left[\ln\left(\frac{H}{H_E}\right) + 2\right]} \right\} \cdot \left(0.612c + \gamma \cdot L_{eff}\right)H_E \quad \text{(kN/m)} \quad (2.4)$$

$$y_{50,T} = \frac{0.5\Sigma p_{ult,T}}{K_{s,T}} \quad \text{(m)} \quad (2.5)$$

where $\Sigma p_{ult,T}$ and $y_{50,T}$ are total ultimate capacity per unit width at top and $y_{50}$ value of the 3D embankment fill in transverse direction respectively, the former has a unit of kN/m and the

latter is in meters, $L_{eff}$ is a constant length value, which is given as 1.143m, all other parameters are consistent with those used in Eqs. (2.1) to (2.3). $K_{s,T}$ is the transverse secant stiffness that corresponds to 50% total ultimate capacity, which has a unit of kN/m² and can be calculated as:

$$K_{s,T} = \left[\left(\frac{400c}{\gamma \cdot W_0} + 1874\right) \cdot \sin\varphi + 364\left(\frac{c}{\gamma \cdot W_0}\right)^{0.2}\right] \cdot e^{\left(\frac{1.2H}{H_E} + \frac{0.045B_c}{W_0}\right)} \cdot \frac{\gamma \cdot W_0^2}{B_c} \quad \text{(kN/m}^2\text{)} \quad (2.6)$$

where $W_0$ and $\gamma$ are the same constants used in Eq. (2.3).

Figure 2.10 shows the comparisons between closed-form solutions and the numerical data. The consistency between numerical data and closed-form solutions is investigated with respect to two parameters at a time by fixing the rest three as constants. As shown in Figure 2.10(a), although small discrepancies can be observed, closed-form equations of $\Sigma p_{ult,T}$ and $y_{50,T}$ are capable of providing appropriate values and identical trends when abutment wall height ratio and embankment height are the changing parameters. Similar conclusions can be obtained from Figure 2.10(b) and Figure 2.10(c), i.e. general trends and close values can be captured by the closed-form expressions when soil friction angle, soil cohesion, and abutment wall width are the changing variables.
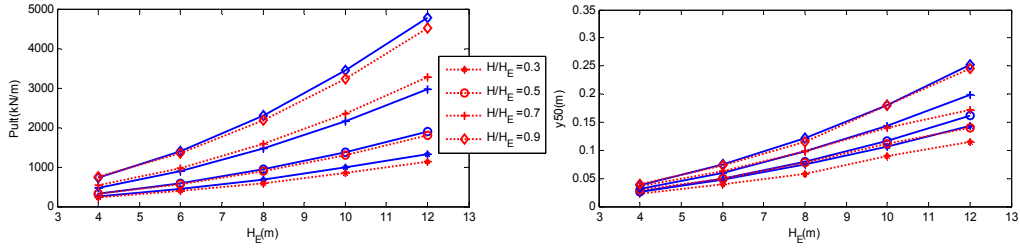
(a) $\Sigma p_{ult,T}$ and $y_{50,T}$ comparisons when $\varphi=30°$, $c=5$kPa and $B_c=16$m
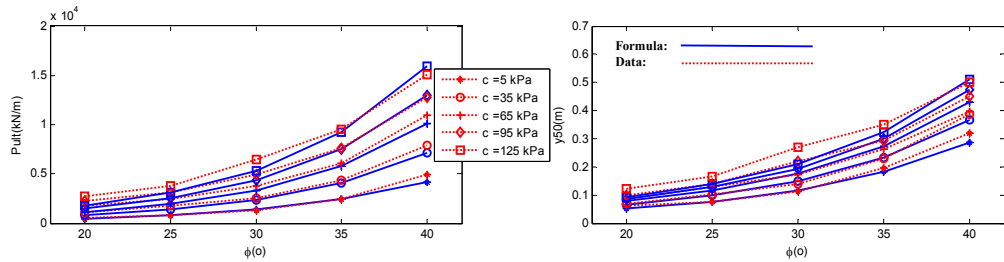


(b) $\Sigma p_{ult,T}$ and $y_{50,T}$ comparisons when $H_E=10$m, $H/H_E=0.5$ and $B_c=16$m
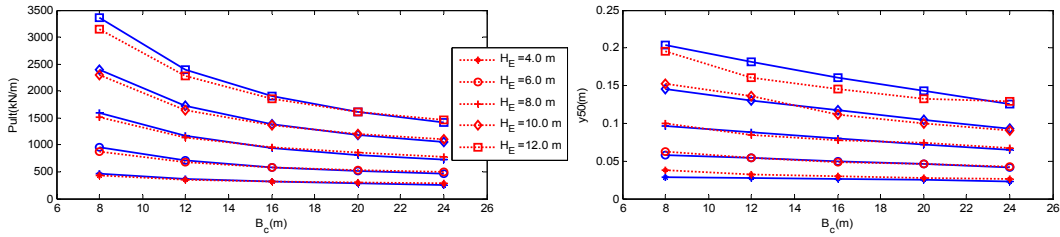


(c) $\Sigma p_{ult,T}$ and $y_{50,T}$ comparisons when $\varphi=30°$, $c=5$kPa and $H/H_E=0.5$

Figure 2.10.    Comparisons of $\Sigma p_{ult,T}$ and $y_{50,T}$ between numerical data and closed-form solutions in the transverse direction

## 2.2.4 Kinematic Response of Embankment

The last part to finalize the *p-y* spring approach for seismic assessment of highway bridges is determining input motions at abutment ends. Due to topographic effects on seismic waves, the amplitude of ground motion varies significantly when it passes through the embankment fill. As a result, the crest motion of the approach embankment has much larger intensities comparing to the free field ground level motion, e.g. as reported by Maroney et al.

(1990), the embank crest motion is more than two times the motion recorded near the pile cap

of center bent. In this study, the method developed by Zhang and Makris (2002a) is used to

estimate motion amplification of embankment fill, where they utilized a frequency domain

approach to solve a 2D shear wage model based on equivalent linear soil properties. For a

harmonic ground level (embankment base) input motion with frequency $\omega$, the transfer

function of the shear wage $I(\omega)$ is solved as:

$$\left| I\left(\omega\right) \right| = \left| \frac{u_{g0} + u\left(z\right)}{u_{g0}} \right| = \left| \frac{c_1 J_0\left(kz\right) + c_2 Y_0\left(kz\right)}{u_{g0}} \right| \tag{2.7}$$

where $u_{g0}$ and $u(z)$ are the displacement magnitude at embankment bottom and height $z$ that is

measured from the top vertex of the triangle extended from embankment slope to the

embankment depth of interest; $k=\omega/V_s$ and $V_s$ is the shear velocity; $J_0$ and $Y_0$ are the

zero-order first and second kind Bessel functions respectively; two parameters $c_1$ and $c_2$ are:

$$c_1 = \frac{u_{g0}}{J_0\left(kz_0 + kH\right) - \frac{J_1\left(kz_0\right)}{Y_1\left(kz_0\right)} Y_0\left(kz_0 + kH\right)} \quad c_2 = \frac{J_1\left(kz_0\right)}{Y_1\left(kz_0\right)} c_1 \tag{2.8}$$

where $z_0$ is the height from top vertex to embankment top; $J_1$ and $Y_1$ are the first-order first

and second kind Bessel functions, respectively. It should be noted that the kinematic transfer

function $I(\omega)$ requires the values of shear modulus and damping to calculate the shear

velocity $V_s$ in the complex domain (Zhang and Makris 2002a), while since these two

parameters are strain dependent and the strain level is unknown beforehand, iterations are

needed to find the converged shear strain and its correspondent soil properties, i.e. shear

modulus $G$ and damping coefficient $\eta$. In their study, the strain dependent shear modulus and

damping curves of the embankment fill are selected by taking the average of the ones that

developed by Seed and Idriss (1970), Iwasaki et al. (1978), Tatsuoka et al. (1978), Vucetic

and Dobry (1991), among others.

## 2.3 NUMERICAL VALIDATION

### 2.3.1 Painter Street Overcrossing (PSO) and Its Finite Element Model

The Painter Street Overcrossing (PSO) located in Rio Dell, California, is selected to

validate the *p-y* modeling approach developed here. It is a two-span prestressed concrete

box-girder bridge that is supported on monolithic end abutments and a two-column central

bent, both with a skew angle of 39°. Each pier column is supported by a pile group consisting

of 4×5 concrete driven friction piles. At west end, the abutment foundation consists of a 1×16

pile group underneath the abutment wall, while east end abutment wall has the same size but

supported by a 1×14 pile group instead.

Figure 2.11 shows the side view (top) and plan view (bottom) along with the locations of

recording channels. Based on standard penetration test (SPT) measurements, the soil profile

was identified with some simplifications and shown in Figure 2.11(a). The 8m thick

embankment fill consists of a compacted sand with a friction angle of 38°. Beneath it, there

are three different soil layers, a 3m thick silty clay layer, a deep 10.9m medium dense sand

layer and a dense gravel sand layer. In 1992, the PSO was severely shaken by the Petrolia

earthquake, and the motions were recorded at all channels, including the ones at the free field (C12-C14), atop one pile cap (C1-C3), atop west embankment (C18-C20) and east embankment (C15-C17), along the bridge deck for transverse responses (C4, C7, C9), vertical responses (C5, C6, C8, C10) and longitudinal response (C11).
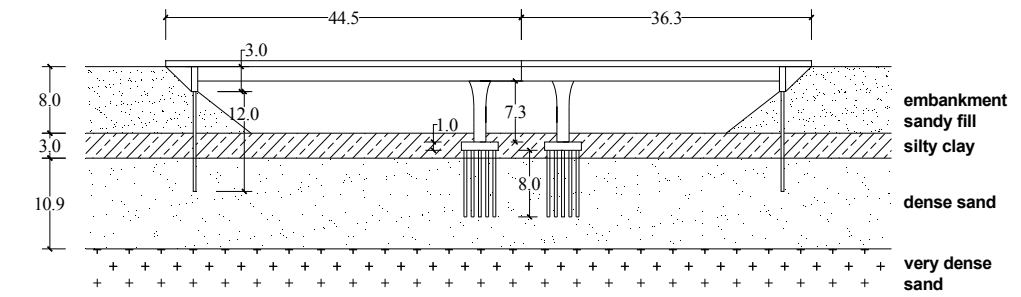


(a) Elevation and soil profile (unit: m)
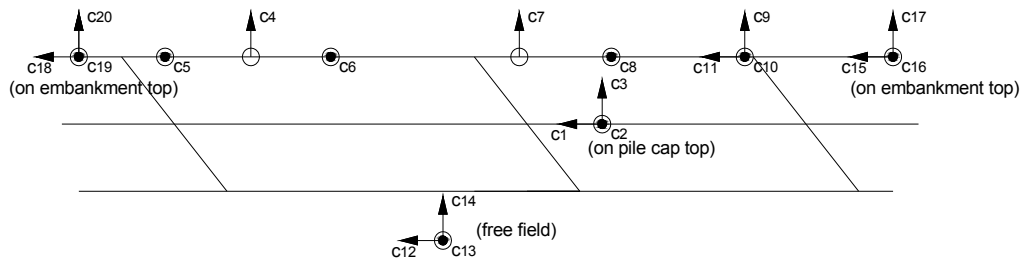


(b) Plan view and recording channels

Figure 2.11.    PSO bridge sketch plots and recording channels

Following the aforementioned SSI modeling scheme, finite element model of the PSO is built in OpenSees as shown in Figure 2.12 for both the full scale pile group case (Figure 2.12 (a)) and the equivalent pile group case (Figure 2.12(b)). The bridge superstructure consists of beam elements with rigid components at each end and center bent, the former preserve the skewed geometry and serve as the connecting elements between the deck and the end

46

abutments while the latter connect the deck with two center pier columns. The bridge deck is modeled with equivalent elastic beam elements while nonlinear beam column elements with bilinear sectional moment-curvature relations are used for the pier columns. Linear elastic beam elements are adopted for modeling pile columns under the pile caps and abutment walls, both of which are modeled with rigid frames. As previously discussed, the equivalent 2×2 pile group is used to represent the 4×5 pile group under each column, and the equivalent 1×2 pile group is modeled to substitute the original 1×16 and 1×14 pile groups at west abutment and east abutment, respectively. Distributed $p$-$y$, $t$-$z$ and $q$-$z$ springs are used to simulate soil lateral resistance, axial friction, and pile tip ending bearing resistance for each pile. Bridge embankment interaction effects are modeled with longitudinal and transverse $p$-$y$ springs connected with the 3D contact-friction elements, which are used to capture the tension gap effects in the longitudinal direction and transfer the friction forces in both transverse and longitudinal directions as long as the contact between backfill and abutment wall is established. Equivalent $p$-$y$ and $q$-$z$ springs are also attached to model the SSI effects at pile caps.
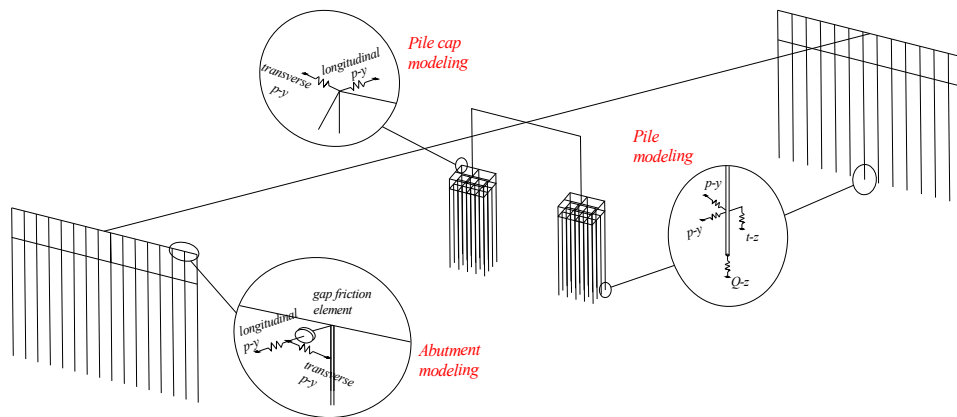


(a) Full scale model
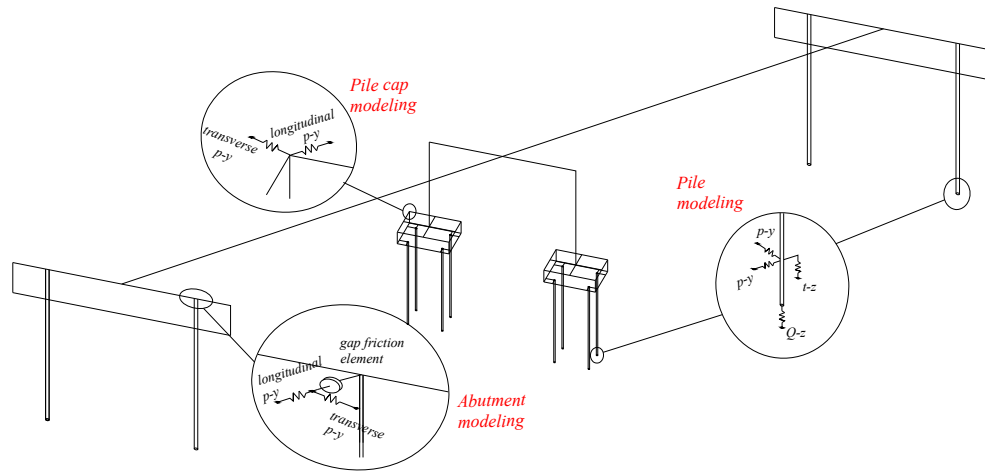
(b) Model with equivalent pile groups

Figure 2.12.    3D finite element model of the PSO

## 2.3.2 Foundation Input Ground Motions

As previously mentioned, the underground motion inputs at center bents are obtained using the equivalent linear site response analysis program of SHAKE91 in this study. Strain dependent shear modulus and damping curves are specified for each soil layer. Since the ground motion of the 1992 Petrolia earthquake is well recorded at ground level, a de-convolution analysis is conducted to find the depth varying ground motions under the ground level. Figure 2.13 presents the input ground motions along the transverse direction at the center bent. As shown in the Figure 2.13, the transverse motions under the ground generally increase from the pile bottom to the top of the pile cap. The longitudinal ground motions are not plotted herein while similar results can be achieved as from the transverse motions.
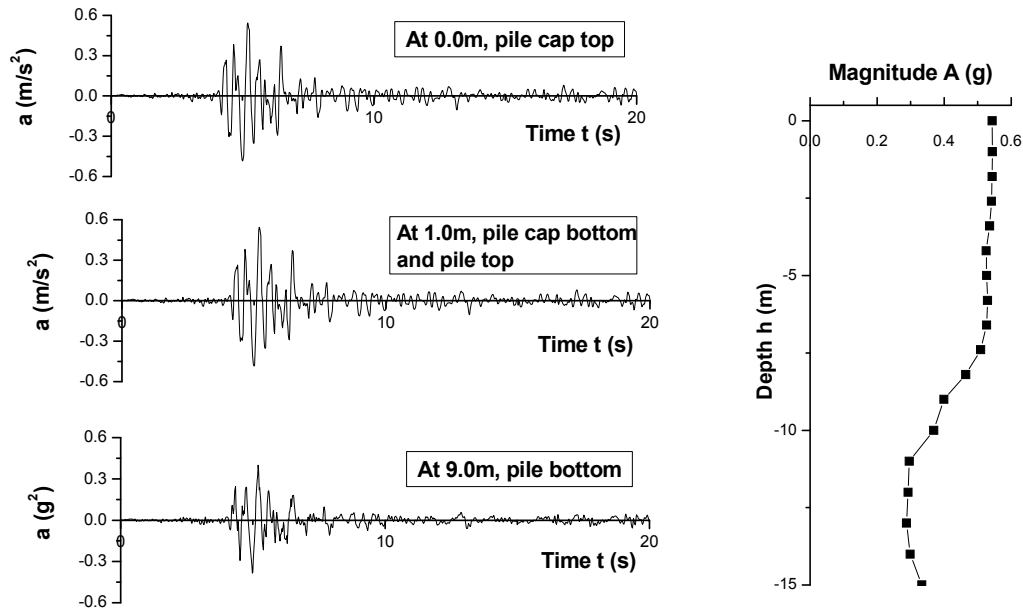
(a) Computed motions        (b) Magnitude

Figure 2.13.    Site response de-convolution results under pier foundation in transverse direction

The input ground motions at end abutments can be separated into two groups: (1) underground motions that can be determined by using site response analyses, and (2) embankment-fill motions resulted from the embankment amplification effect. The underground motions are calculated by using SHAKE91 in this study, while the transfer function method developed by Zhang and Makris (2002a) is used to obtain the embankment-fill motions. Since the PSO has well recorded motions at both embankment tops and free-field ground levels, this study firstly computed the embankment-fill motions using the crest motion as the input and compared the calculated motions at the embankment bottom with the ground level motion records. Good agreements between the calculated and the recorded motions validate the transfer function method. Subsequently, the underground motions are calculated using the ground level motion records as the input. In this way, both

49

the motion records at embankment top and free field have been utilized. Figure 2.14 shows the computed transverse motions in the west embankment fill (Channel 17) at different depths. It is seen that the motion magnitude also varies along the embankment height with crest motion much larger than the motion at base of embankment. Such depth varying motions are required to yield accurate bridge response.



(a) Computed motions  (b) Magnitude
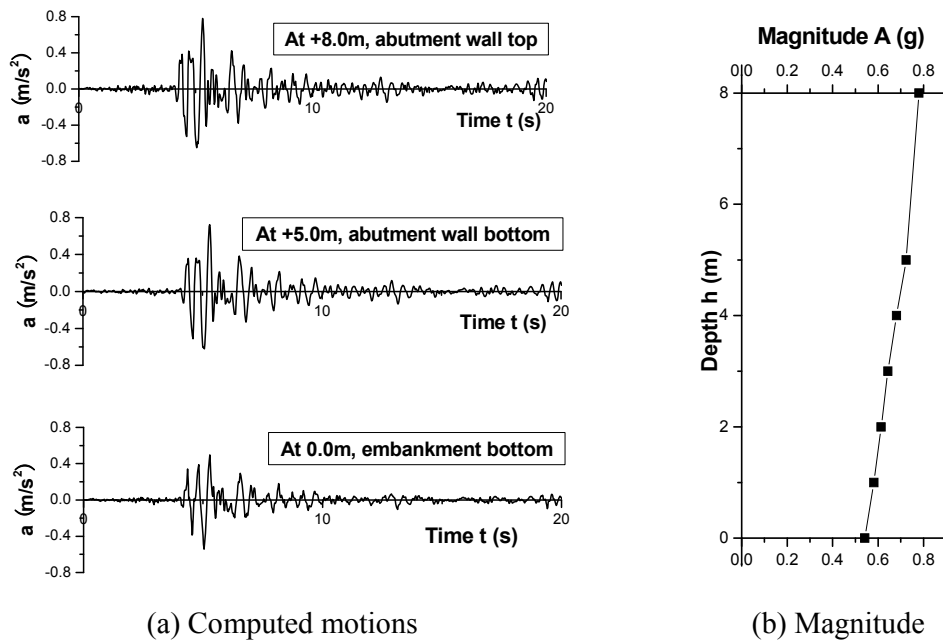
Figure 2.14.    Embankment motion amplification of Channel 17

### 2.3.3  Numerical Simulation Results

This section compares the numerical responses of the proposed modeling scheme with their recorded counterparts. For comparison purposes, three other modeling schemes that are widely used in academic and engineering practices are also presented in this study. Table 2.2 summarizes the modeling details of each scheme. Case 1 is the proposed method which combines detailed *p-y* springs for SSI effects with depth varying input motions at both pile

foundations and end abutments. Case 2 keeps the *p-y* springs but ignores ground motion

depth variations. A uniform free field motions at the ground level is used as foundation input

motions at all depth. In other words, neither the depth varying mechanism along the piles nor

the motion amplification effects of embankments is included in this case. Case 3 keeps the

detailed *p-y* modeling scheme at pile foundations while uses equivalent macro springs and

dashpots to model the SSI effects at abutment foundations. Recorded embankment crest

motions are applied to the free end of macro springs and dashpots. Case 4 is a full

substructure modeling scheme, which uses equivalent macro springs and dashpots at all

foundations with recorded free field motion input at pier foundations and recorded

embankment crest motions at abutment foundations. The macro spring and dashpot values

used in Case 3 and Case 4 are from the substructure approach developed by Zhang and

Makris (2002b).

Table 2.2.   Numerical comparisons of different modeling schemes

| Modeling schemes | SSI modeling | | Input ground motions | |
|---|---|---|---|---|
| | Pile foundation | Abutment foundations | Pile foundations | Abutment foundations |
| Case 1 (Proposed) | *p-y* springs | *p-y* springs | Depth varying motions | Depth varying motions |
| Case 2 | *p-y* springs | *p-y* springs | Free field motions | Free field motions |
| Case 3 | *p-y* springs | Macro springs and dashpots | Depth varying motions | Embankment crest motions |
| Case 4 | Macro springs and dashpots | Macro springs and dashpots | Free field motions | Embankment crest motions |

Figures 2.15 to 2.18 compare numerical results and recorded responses for the transverse

response at west, middle, and east of the bridge (C4, C7, C9) and the bridge longitudinal response (C11), respectively. As can be seen from the first column of these four figures, numerical results by the proposed modeling scheme are in very good agreement with their recorded counterparts in terms of absolute accelerations, relative velocities and relative displacements. The errors between the peak values are also provided in the plots, where except the relative velocity at C9, all other computed responses from the proposed modeling scheme have errors smaller than 10%.

When uniform ground level input motion is imposed ($2^{nd}$ column in Figures 2.15 to 2.18), large discrepancies can be observed and the errors between peak values of numerical results and actual records can be easily larger than 60%, which demonstrates the particular importance of incorporating depth varying motions along the piles and amplified motions up through the embankment fill depth when the $p$-$y$ spring method is utilized. More importantly, most response components are dramatically underestimated in this case. To further explore the main source of the large error in bridge responses, a slightly different Case 2b is constructed by modifying Case 2 with the embankment crest motion imposed uniformly at abutment foundations. Case 2b, therefore, includes the effect of embankment amplified motion but neglect the depth varying motion at pile foundation. Comparing to the recorded data, the results of Case 2b have errors about 20%, which is reduced from that of Case 2. This comparison indicates that neglecting the significant embankment motion amplification is essentially the main attribute for the poor performance of Case 2.

The importance of using $p$-$y$ springs to model the SSI effects at abutment foundations is

examined by the third column of the figures, where the abutment SSI modeling is replaced with macro springs and dashpots and embankment crest motion is used as the input at bridge ends. It can be seen that errors of the peak values are universally larger than the proposed model (Case 1). Nevertheless, it captures the general trend of the actual records and the errors are much smaller comparing to Case 2. Therefore, if the abutment responses are not of interest, this method can be adopted to save some modeling efforts.

The fourth column of these figures check the numerical responses of the fully substructure modeling method (Case 4), in which case substructures are no longer modeled and the SSI effects are substituted with equivalent linear springs and dashpots at both pile foundations and abutment foundations. Comparable results can be seen between computed responses and actual records for this case, while the computational effort is less. However, the proposed method (Case 1) in this study becomes more appealing than the macro spring method when following factors are considered. It incorporates both superstructure and substructure into the modeling of the bridge-foundation-soil system, where advanced analysis can be further carried out, such as sensitivity study of various SSI effects, soil liquefaction effect, pile foundation response, etc. The proposed method is relatively easy to apply to different highway bridges as long as structure and soil information are available. On the other hand the macro spring method requires the knowledge of input ground motions beforehand, since spring stiffnesses and dashpot constants are strain dependent and will change under different ground motions (Zhang and Makris 2002b).
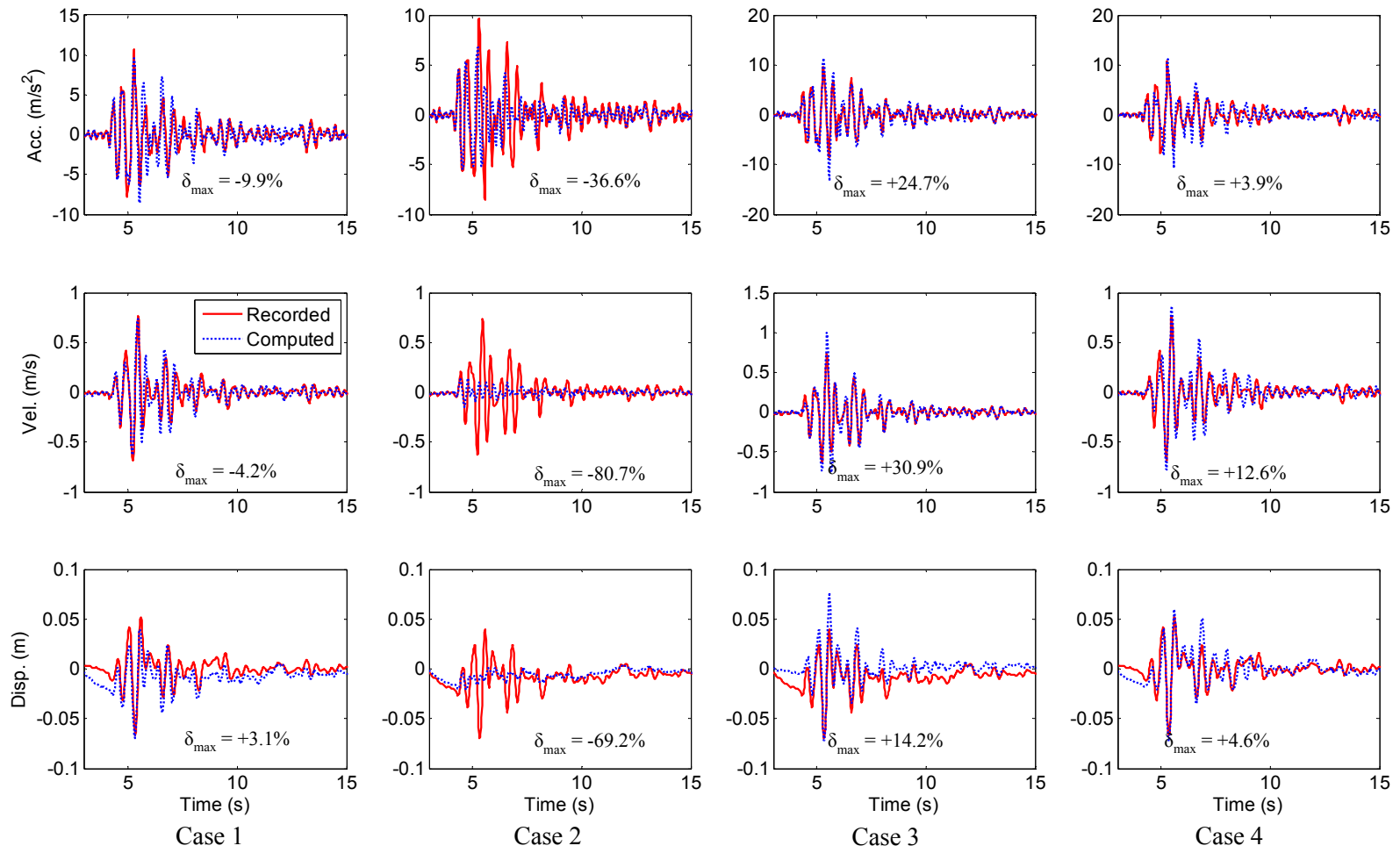
Figure 2.15. Comparison of recorded and computed motions at Channel 4 for different modeling cases

54
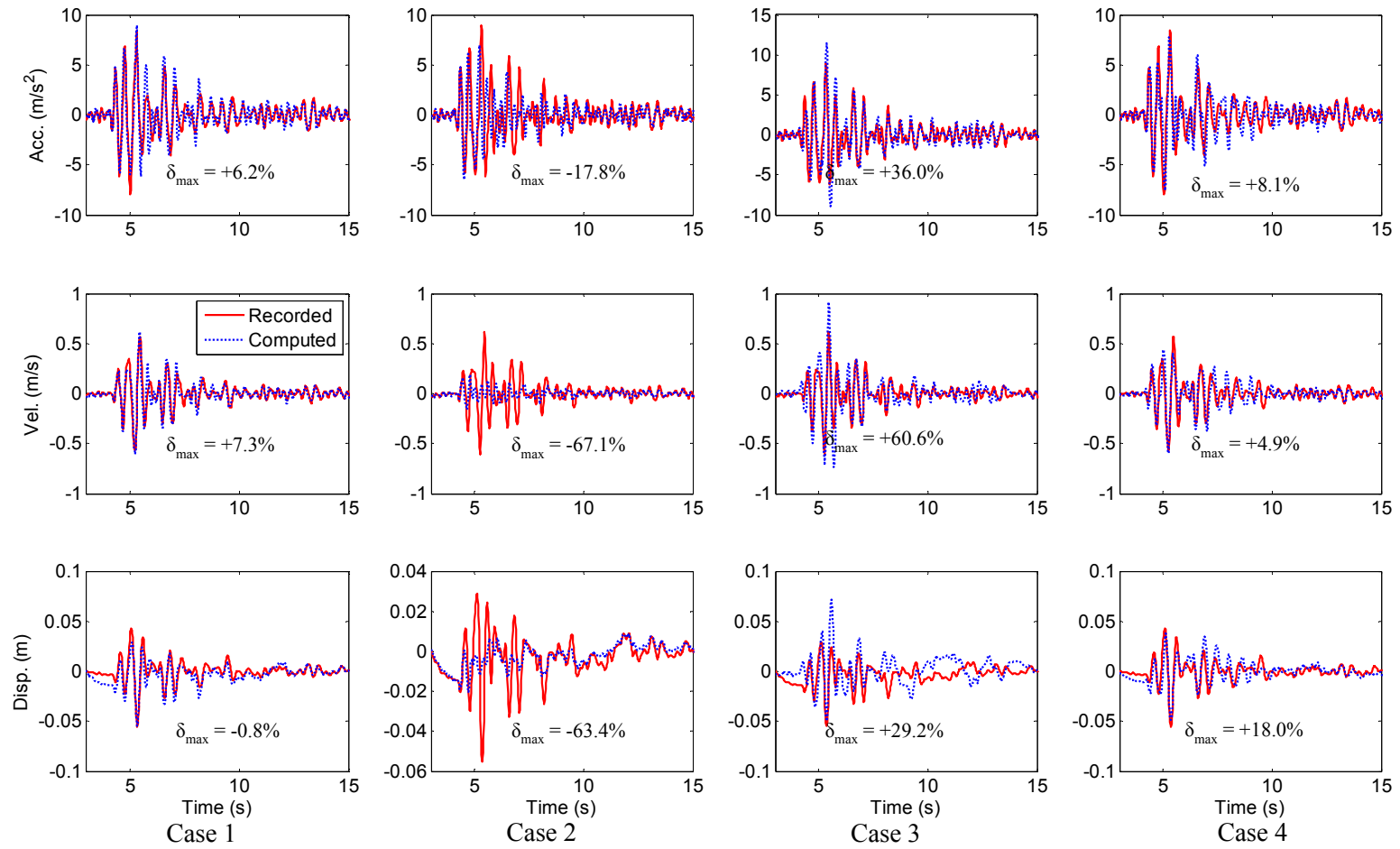
Figure 2.16.    Comparison of recorded and computed motions at Channel 7 for different modeling cases

55
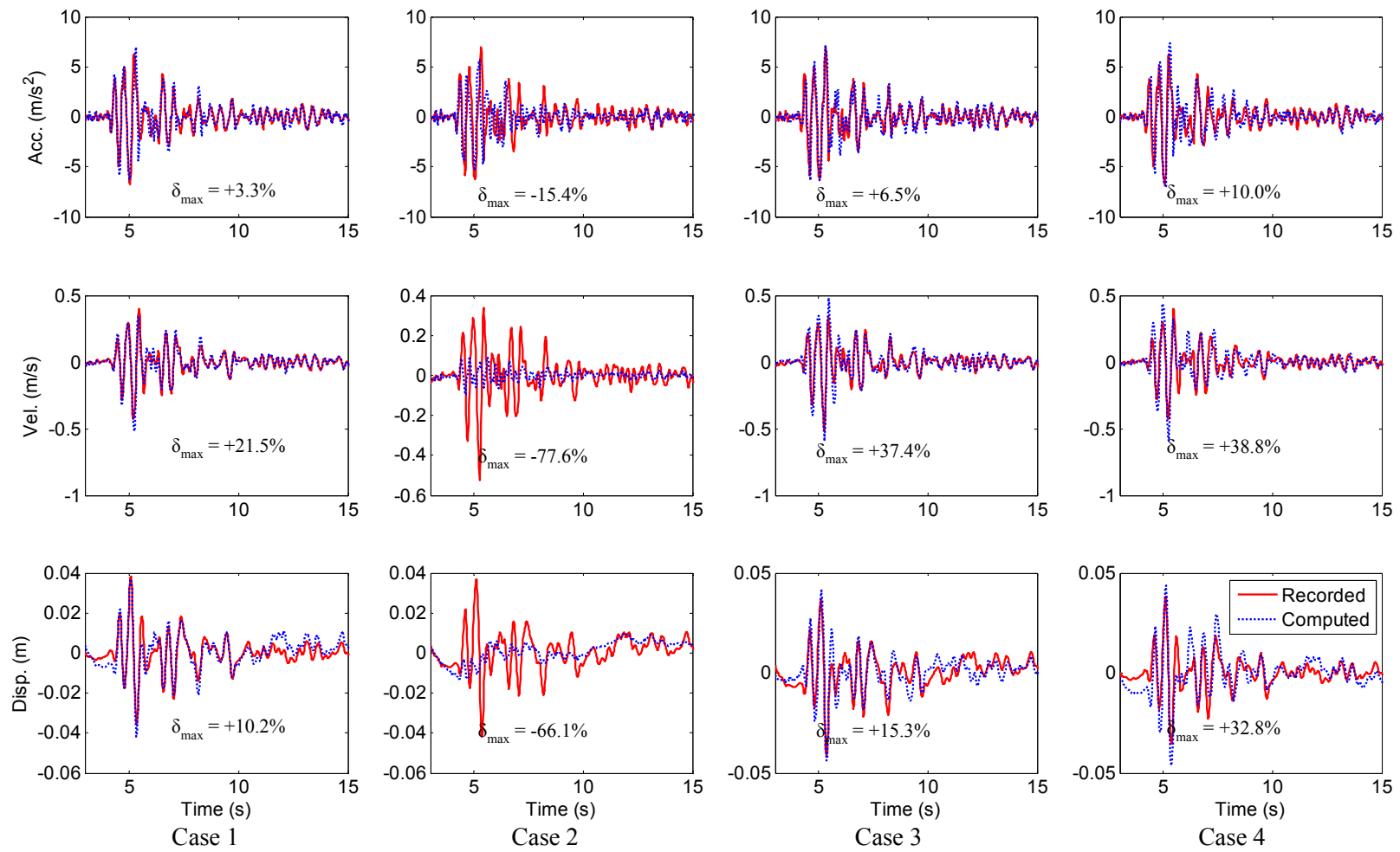
Figure 2.17.    Comparison of recorded and computed motions at Channel 9 for different modeling cases
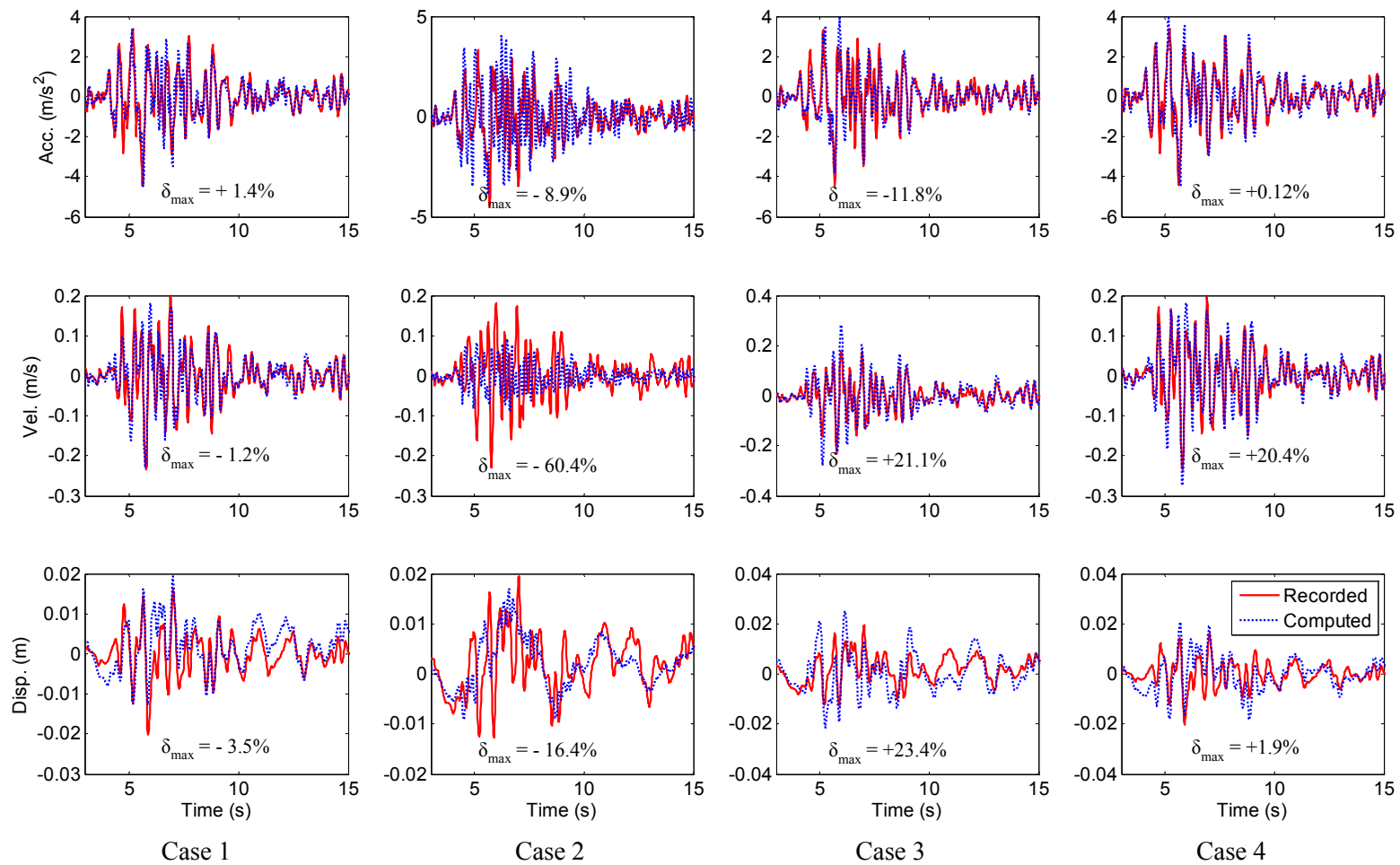
Figure 2.18. Comparison of recorded and computed motions at Channel 11 for different modeling cases

57

Figure 2.19 also compares the Fourier spectrums of the absolute acceleration responses at four different channels (C4, C7, C9, and C11). The thick line stands for the spectrum for recorded motions and the thin lines are spectrum of the computed results from the proposed method. Consistent with the time domain comparison, computed spectrums are very close to recorded ones at most frequencies and the peaks happen at same frequencies with similar peak magnitudes observed for all the channels. This further confirms that the proposed modeling method captures the SSI effects very well and can provide accurate seismic response predictions of highway bridges.
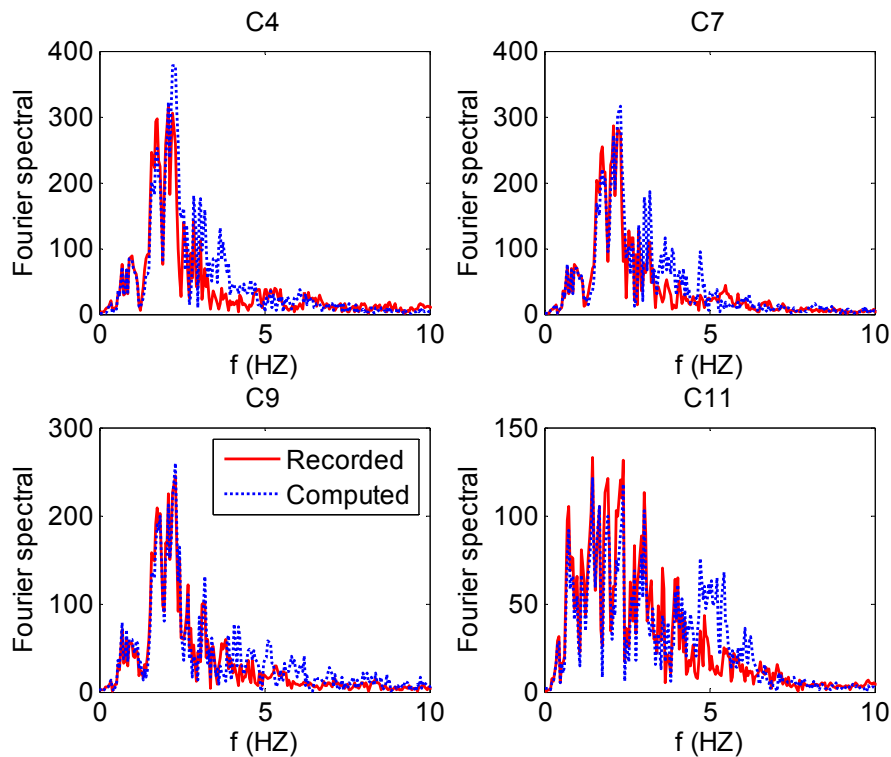


Figure 2.19.    Comparison of the recorded and computed absolute acceleration response Fourier spectrums

## 2.4 SUMMARY OF PROPOSED PROCEDURE

The numerical study of the PSO presented in this paper develops and validates a step-by-step procedure to estimate the seismic response of highway bridges using *p-y* modeling approach. The detailed steps are summarized below:

(1) Construct a three-dimensional stick model of the bridge that consists of both superstructures and substructures. To save modeling efforts, large pile groups can be substituted with the equivalent 2×2 pile groups (or 1×2 pile groups if only one row of piles are designed) using the proposed method in Section 2.1.2.

(2) Use standard *p-y* spring elements (e.g. the one developed by Boulanger et al. 1999) in conjunction with the *p*-multiplier to simulate the SSI effects along piles. Scale the spring input parameter of ultimate capacity if the equivalent 2×2 pile group is used in Step 1. Simulate the SSI effects at pile caps by adding side friction resistances to the *p-y* spring elements developed in Step 3 and 4.

(3) Use regressed *p-y* spring elements and a serially connected compression gap element to simulate the SSI effects of the embankment fill in longitudinal direction. The input *p-y* model parameters can be calculated by Eqs. (2.1) to (2.3).

(4) Use regressed *p-y* spring elements and a serially connected contact-friction elements to simulate the SSI effects of the embankment fill in transverse direction. The input parameters can be calculated by Eqs. (2.4) to (2.6).

(5) Compute depth varying ground motions for pile foundations using either equivalent linear or nonlinear site response programs. Compute the ground motions along the

embankment fill depth by amplifying the free-field motion with the kinematic

transfer function developed by Zhang and Makris (2002b).

(6) Conduct the nonlinear time history response of the highway bridge by combining the

model constructed in Step 1 with $p$-$y$ spring elements developed in Step 2 to Step 4 as

well as the input motions calculated from Step 5.

## 2.5 CONCLUDING REMARKS

This chapter aims to realistically simulate the seismic responses of typical highway

bridges in California with considerations of SSI effects. The $p$-$y$ modeling approaches are

developed and validated for embankments and pile foundations of bridges. The $p$-$y$ approach

models the lateral and vertical foundation flexibility with distributed $p$-$y$ springs and

associated $t$-$z$ and $q$-$z$ springs. Building upon the existing $p$-$y$ models for pile foundations, the

study develops the nonlinear $p$-$y$ springs for embankments based on nonlinear 2D and 3D

continuum finite element analysis under passive loading condition along both longitudinal

and transverse directions. Closed-form expressions are developed for two key parameters, $p_{ult}$

and $y_{50}$, of embankment $p$-$y$ models as functions of abutment geometry (wall width and

height, embankment fill height, etc.), and soil material properties (wall-soil friction angle,

soil friction angle and cohesion). In order to account for the kinematic and site responses,

depth varying ground motions are derived and applied at the free-end of $p$-$y$ springs, which

reflects the amplified embank crest motion. The modeling approach is applied to simulate the

seismic responses of the PSO and validated through comparisons with the recorded responses

during the 1992 Petrolia earthquake. By comparing actual recorded responses of the PSO

60

with numerical results from the proposed modeling method and three other commonly adopted modeling schemes, the dependability of the proposed approach is validated. This chapter concludes:

(1) The developed and validated closed-form expressions for $p$-$y$ modeling parameters of embankment, namely $p_{ult}$ and $y_{50}$ along both transverse and longitudinal directions, can effectively take into account of abutment geometry and soil properties.

(2) The proposed modeling approach yields comparable response quantities in both time domain and frequency domain to the actual recorded responses of the PSO. It is capable to accurately predict the seismic responses of typical highway bridges considering SSI effects.

(3) The modeling efforts of the proposed model are modest, yet the proposed modeling approach possesses its own advantages of not only revealing the response of both superstructures and superstructures but also being convenient to be implemented into different highway bridges as long as structural and soil information are provided.

(4) It is demonstrated that SSI effects at end embankments and depth varying ground motions are very important modeling aspects for accurately predicting the bridge responses. The significance of the abutment contribution is particularly true for typical highway bridges with short periods. The proposed $p$-$y$ modeling approach, including the closed-form $p$-$y$ parameters, can realistically incorporate these two important aspects easily.

It should be noted that the $p$-$y$ modeling approach has its own limitations. For example,

the $p$-$y$ springs in two orthogonal directions are not coupled. Furthermore, the depth varying

motions have to be generated separately. Nevertheless, the proposed $p$-$y$ spring based integral

modeling approach can serve as a robust tool in predicting the seismic response of typical

highway bridges in California. The important effects of SSI and depth varying ground

motions can be captured reliably by the $p$-$y$ modeling approach proposed here.

# 3. SIMPLIFIED DRIFT DEMAND PREDICTION OF BRIDGES UNDER LIQUEFACTION INDUCED LATERAL SPREADING

As discussed in Chapter 1, compared with seismic shaking, relative few reliable approaches are available to efficiently quantify the seismic responses of highway bridges when subjected to liquefaction induced lateral spreading. This chapter develops an innovative way to predict the column drift of typical highway bridges on liquefiable soil on the basis of the column responses under seismic shaking. The *p-y*-spring-based global dynamic analysis procedure developed in Chapter 2 is implemented and modified to analyze the responses of a benchmark bridge-foundation-soil system under seismic shaking and liquefaction induced lateral spreading, respectively.

## 3.1 GLOBAL DYNAMIC ANALYSIS OF THE BENCHMARK HIGHWAY BRIDGE

### 3.1.1 Benchmark Highway Bridge

A benchmark highway bridge is constructed in this chapter to represent typical highway bridges in California that are seismically designed after 1971. It is a three-span continuous concrete bridge supported by two single-column bents and monolithic abutments. Figure 3.1 shows the geometry of the bridge, the designs of pier columns and pile foundations, as well as the soil profile. The 1.83m-diameter RC pier consists of 26 #11 longitudinal bars with #4 transverse reinforcement at 0.30m spacing. The pile foundation consists of a 4.0m×5.5m pile cap and a 3×4 pile group of 0.61m-diameter cast-in-drilled-hole (CIDH) piles. The abutment wall is 3.0m deep, 12.0m wide and 0.8m thick, with a row of 6 CIDH piles supporting it. The

soil profile used in this chapter is representative of sites with a non-liquefiable clay crust over liquefiable loose sand with non-liquefied dense sand below. Such configuration is a major cause of bridge damages during past earthquakes under soil liquefaction (Brandenberg et al. 2005; Hamada and O'Rourke 1992). Variations in the soil parameters were based on the USGS database of cone penetration test (CPT) soundings in the San Francisco bay area, where the median values of the parameters are used in this chapter. The embankment fill consists of cohesionless sand with a friction angle of 38° sitting on top of the crust layer of clay, which has an undrained shear strength of 70kpa. The liquefiable loose sand layer underneath has a friction angel of 32°, whereas the dense sand layer below has a friction angel of 38°. The inclination angle of the ground is selected as 4° towards bridge center.
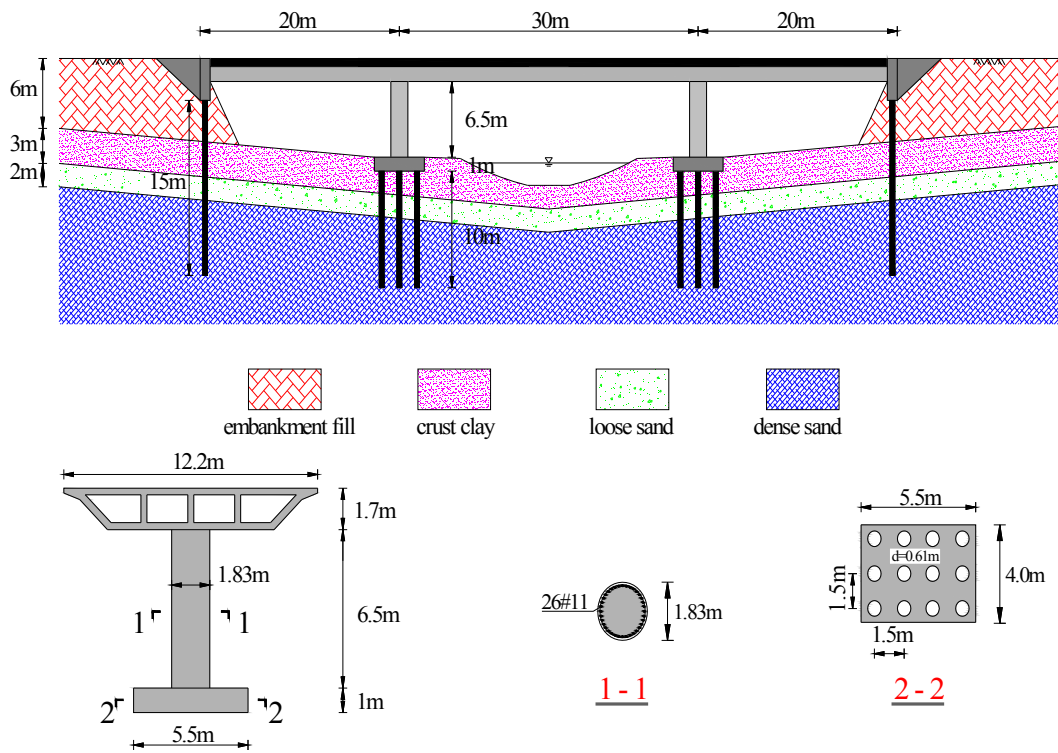


Figure 3.1.  Bridge structure and foundation sketch

64

### 3.1.2 Numerical Modeling of Bridge Structure

Three-dimensional numerical models were built in software platform *OpenSees* (Mazzoni et al. 2006). Elastic beam elements are used for the bridge deck, and nonlinear beam elements are used to model pier columns and pile groups. Abutment walls and pile caps are modeled as real size rigid beam elements to capture their rotational resistances. As shown in Figure 3.2, to save considerable modeling efforts, the 3×4 pile groups at pier foundations and the 1×6 pile groups at abutment foundations are simplified with equivalent 2×2 pile groups and 1×2 pile groups respectively using the approach discussed in Chapter 2. Two parallel massless rigid beams are built at each intersection (deck ends, pier column tops, and bridge center) to reflect the deck width and to incorporate different bridge characteristics later in this chapter.
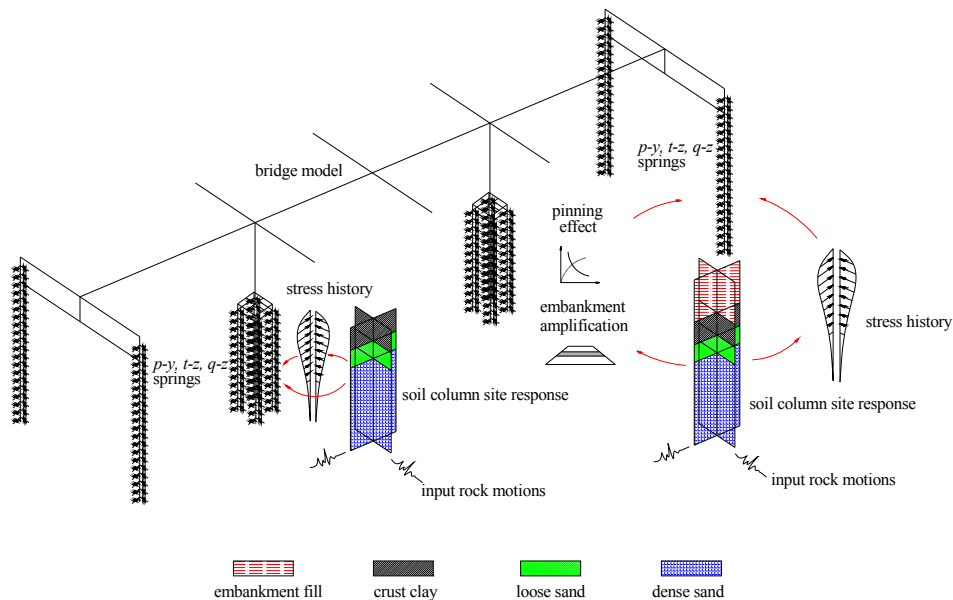


Figure 3.2. 3D numerical model of the bridge benchmark

### 3.1.3 Numerical Modeling of Soil Liquefaction Effects

Different modeling schemes have to be considered to capture distinct loading mechanisms associated with soil liquefaction and seismic shaking. In particular, liquefaction affects load resistance of soil layers, the SSI effects, and depth varying ground motion inputs. The first two aspects are modeled by using the dynamic *p-y* spring approach, which is effective in accounting for the layered soil profile, nonlinear interaction and the depth varying ground motions. The last aspect is considered through nonlinear site response analyses incorporating liquefiable soil.

In this chapter a new class of *p-y* elements, the '*PyLiq*1' element, which was developed by Brandenberg et al. (2012), is used to model the SSI effects with and without soil liquefaction. Consistent with previous studies (Nogami et al. 1992; Boulanger et al. 1999), the '*PyLiq*1' element consists of a gap closure element, a plastic element and an elastic element in series, representing the gap formation at the pile-soil interface, the nonlinear interaction behavior in the near field and the elastic soil medium (radiation damping) in the far field, respectively. Two key input parameters of the '*PyLiq*1' spring are $p_{ult\_liq}$, the ultimate capacity that liquefiable soil can exert under lateral loading, and $y_{50}$, the displacement when 50% of ultimate resistance is mobilized. A fundamental feature of the '*PyLiq*1' element lies in that the ultimate capacity of the liquefiable soil is defined as a function of the mean effective stress rather than a material constant, such that the pore pressure fluctuation associated with the liquefaction process can be effectively incorporated. The closed-form expression of the ultimate capacity $p_{ult\_liq}$ is given as:

$$p_{ult\_liq} = p_{res} + (p_{ult} - p_{res})\frac{\sigma'}{\sigma_0'}$$ (3.1)

where $p_{ult}$ is the ultimate capacity without soil liquefaction, $p_{res}$ is the residual capacity when the mean effective stress reaches 0, $\sigma'$ is the mean effective stress, and $\sigma_0'$ is the initial free-field effective stress. The '$PyLiq1$' element can also be used for non-liquefied soil layers if the effective stress $\sigma'$ is kept the same as the initial stress $\sigma_0'$ so that the ultimate capacity $p_{ult\_liq}$ equals $p_{ult}$.

The '$PyLiq1$' element can be directly utilized to model the soil resistances and the SSI effects for the liquefied sand layer and the bottom dense sand layer if the input parameters in Eq. (3.1) are known. However, due to the soil liquefaction underneath, the ultimate capacity of the crust layer needs to be calculated separately by considering two possible failure mechanisms: (1) the individual mechanism, i.e. the crust layer laterally spreads and flows around each pile; (2) the block mechanism, i.e. the crust layers are trapped between the piles and the whole group acts as an equivalent block (Brandenberg et al. 2007). The total ultimate capacity associated with each failure mechanism is calculated and compared, and the smaller value is the dominant one. It is worth mentioning that since the *p-y* springs are attached to pile caps and piles individually (as shown in Figure 3.2), which is consistent with the individual mechanism, a multiplier $m_p$ is implemented to consider the influences of these two possible failure mechanisms:

$$m_p = \begin{cases} 1.0 & \text{if individual mechanism controls} \\ \dfrac{F_{bl}}{F_{in}} & \text{if block mechanism controls} \end{cases} \tag{3.2}$$

where $F_{bl}$ is the total ultimate capacity calculated by the blocking mechanism, and $F_{in}$ is the total ultimate capacity calculated by adding the capacities of all the piles and the pile cap. Besides the ultimate capacity, the clay displacement at the ultimate capacity is computed based on the empirical formula developed by Caltrans (2013) in this chapter, and $y_{50}$ value for the crust layer is adjusted to match this 'ultimate' displacement value.

### 3.1.4 Nonlinear Site Response Analysis under Soil Liquefaction

As shown in Figure 3.2, nonlinear site response analysis is conducted to generate depth varying ground motions and mean stress histories (used as '$PyLiq1$' springs inputs) under soil liquefaction. First, a free field soil column response analysis is carried out by using the pressure sensitive and insensitive soil materials that were developed by Yang et al. (2003) to model sand and clay, respectively. The inclined angle of 4° is modeled in the longitudinal direction (towards bridge center), such that a horizontal force component of soil self-weight can generate lateral spreading towards bridge center. A dashpot is attached at the bottom to model the interaction effect between the dense sand layer and the rock layer (Zhao 2011). A group of 40 unscaled ground motions that were selected by Baker et al. (2011) are used as the input rock motions, where fault normal components are applied along the longitudinal direction and fault parallel components are exerted along the transverse direction. Table 3.1 lists the selected motions used in this chapter. A preliminary computational attempt shows

that more than a half of site cases have limited ground shaking and almost no noticeable lateral spreading occurs if these 40 motions are used directly. A scale factor of 2.0 is therefore applied to the selected motions, such that different levels of lateral spreading can be expected.

Free field motions can be directly used as pile foundation inputs. However, the site responses at end abutments need to be further modified by considering two additional effects, i.e. the embankment amplification and the pinning due to restricted abutment movement when lateral spreading push toward bridge center on both ends (as shown in Figure 3.2). The kinematic responses of the approach embankment amplify ground motion input at end abutments. This motion amplification effect is estimated based on the method developed by Zhang and Makris (2002a). On the other hand, the pinning effect on abutments over liquefied ground considers the restraining force provided by the bridge structure, which in turn significantly reduces the magnitude of soil lateral spreading. The procedure proposed by Boulanger et al. (2006) is adopted to address the pinning effect.

Figure 3.3 plots the longitudinal displacement profile at several time instants when subject to the TCU138 station record of the 1999 Chi-Chi earthquake (i.e. the motion No. 10 in Table 3.1). It can be seen that ground lateral spreading reaches up to about 1.5m at pier foundations, while the pinning effect sharply reduces the amplitudes of ground motions at end abutments, where the maximum lateral displacements are smaller than 0.25m.

Table 3.1. Selected 40 rock motion inputs (Baker et al. 2011)

| No. | Earthquake, Year | Station | Mag-nitude | No. | Earthquake, Year | Station | Mag-nitude |
|-----|------------------|---------|------------|-----|------------------|---------|------------|
| 1 | San Fernado,1971 | Lake Hughes #4 | 6.6 | 21 | Helena Montana-01,1935 | Carroll College | 6 |
| 2 | Loma Prieta,1989 | Gilroy Array #6 | 6.9 | 22 | Northridge-01,1994 | Vasquez Rocks Park | 6.7 |
| 3 | Kocaeli Turkey,1999 | Izmit | 7.5 | 23 | Chi-Chi Taiwan,1999 | WNT | 7.6 |
| 4 | Northridge-01 ,1994 | LA Wonderland Ave | 6.7 | 24 | Loma Prieta,1989 | Golden Gate Bridge | 6.9 |
| 5 | Imperial Valley-06,1979 | Cerro Prieto | 6.5 | 25 | Loma Prieta,1989 | UCSC | 6.9 |
| 6 | Hector Mine,1999 | Hector | 7.1 | 26 | Victoria Mexico,1980 | Cerro Prieto | 6.3 |
| 7 | San Fernando,1971 | Pasadena Seismo Lab | 6.6 | 27 | Northridge-01,1994 | Santa Susana | 6.7 |
| 8 | Duzce Turkey,1999 | Lamont 531 | 7.1 | 28 | Loma Prieta,1989 | Gilroy - Gavilan | 6.9 |
| 9 | Hector Mine,1999 | Heart Bar State Park | 7.1 | 29 | Duzce Turkey,1999 | Mudurnu | 7.1 |
| 10 | Chi-Chi Taiwan,1999 | TCU138 | 7.6 | 30 | Northridge-01,1994 | Burbank Howard | 6.7 |
| 11 | Chi-Chi Taiwan-06,1999 | TCU129 | 6.3 | 31 | Chi-Chi Taiwan-03,1999 | TCU138 | 6.2 |
| 12 | Coyote Lake,1979 | Gilroy Array #6 | 5.7 | 32 | Chi-Chi Taiwan-06,1999 | TCU138 | 6.3 |
| 13 | Taiwan SMART1(45),1986 | SMART1 E02 | 7.3 | 33 | Loma Prieta,1989 | UCSC Lick Observatory | 6.9 |
| 14 | Irpinia, Italy-01,1980 | Bagnoli Irpinio | 6.9 | 34 | Loma Prieta,1989 | Gilroy Array #1 | 6.9 |
| 15 | Loma Prieta,1989 | Santa Teresa Hills | 6.9 | 35 | Northridge-01,1994 | LA Dam | 6.7 |
| 16 | Irpinia, Italy-01,1980 | Bisaccia | 6.9 | 36 | Northridge-01,1994 | LA 00 | 6.7 |
| 17 | Chi-Chi Taiwan,1999 | TCU045 | 7.6 | 37 | Sitka Alaska,1972 | Sitka Observatory | 7.7 |
| 18 | Kocaeli Turkey,1999 | Gebze | 7.5 | 38 | Northridge-01,1994 | LA Chalon Rd | 6.7 |
| 19 | Northridge-01,1994 | Pacoima Dam | 6.7 | 39 | Loma Prieta,1989 | Belmont | 6.9 |
| 20 | Denali Alaska,2002 | Carlo (temp) | 7.9 | 40 | Chi-Chi Taiwan,1999 | TCU129 | 7.6 |
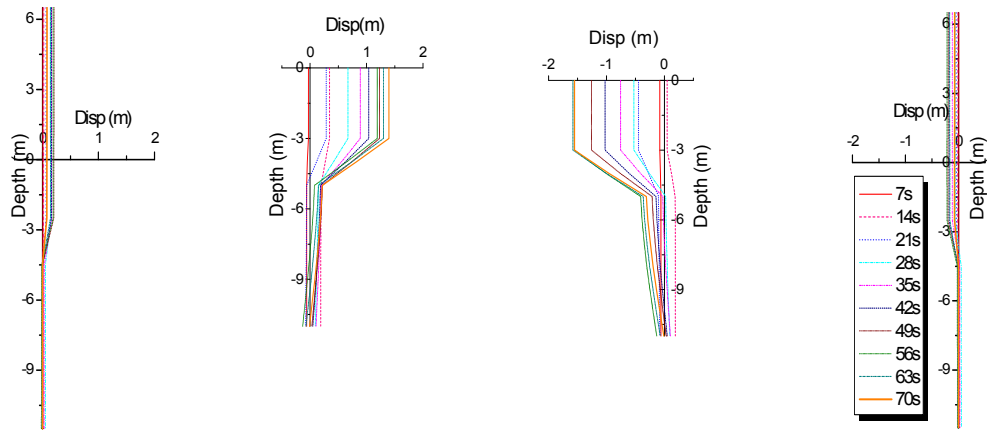
(a) Left abut        (b) Left pier        (c) Right pier        (d) Right abut

Figure 3.3. Longitudinal displacement profiles under soil liquefaction (motion No. 10)

### 3.1.5 Numerical Modeling under Seismic Shaking

Likewise, the dynamic *p-y* modeling approach developed in Chapter 2 has been utilized to assess the seismic responses of the benchmark bridge under seismic shaking. Nonlinear site response analysis is also conducted to obtain the 40 groups of depth varying motions for the non-liquefaction case. Since soil liquefaction process is excluded under seismic shaking only case, no pinning effect needs to be considered for the input motions at end abutments.

### 3.2 NONLINEAR TIME HISTORY ANALYSES

Nonlinear time history analysis offers an efficient way to distinguish the damaging mechanisms of highway bridges under seismic shaking and liquefaction induced lateral spreading. In this section, the damage mechanism of the benchmark bridge under soil liquefaction is first examined by checking its permanent deformations. Figure 3.4 illustrates the permanent displacements of the bridge when subject to the motion No. 10. As shown in Figure 3.4(a), liquefaction induced lateral spreading strongly push pier columns and pile

71

foundations toward the center of the bridge, which results in significant permanent deformations. Due to the pinning effect, abutment foundations only experience limited residual displacements in the longitudinal direction. Nevertheless, as can be observed from Figure 3.4(b), noticeable residual displacements exist in the transverse direction at end abutments, which comes from the torsional responses of the bridge. It is clear that the responses of pier columns and pile foundations are the dominant EDPs when liquefaction induced lateral spreading is the damaging mechanism.
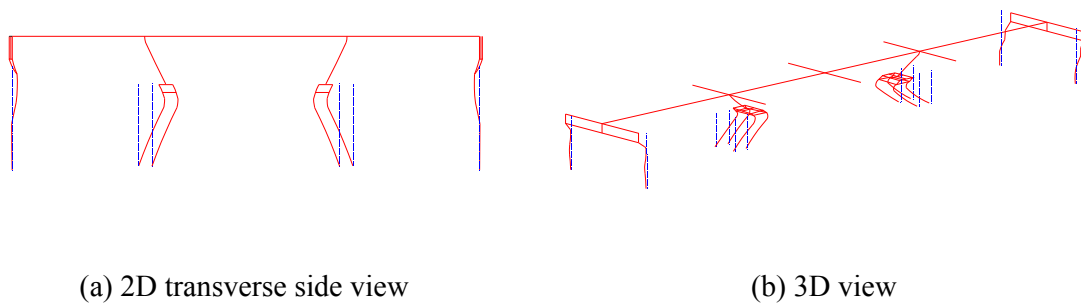


(a) 2D transverse side view                     (b) 3D view
Figure 3.4.  Bridge residual deformation under soil liquefaction when subject to motion No. 10 (deformation scaling magnitude: 10)

Considering the response characteristics of the bridge under soil liquefaction and seismic shaking, three EDPs of the bridge, namely the pile cap displacement, the abutment displacement and the column drift ratio, are selected to compare their respective responses. Figure 3.5 compares the time history responses of these three EDPs, when the motion No. 10 is used as the input motion. In addition, the response modification factor $C_{EDP}$ is proposed to quantify the effects of liquefaction induced lateral spreading on bridge responses and is defined as:

$$C_{EDP} = \frac{EDP_{Liq}}{EDP_{NonLiq}} \qquad\qquad (3.3)$$

where $EDP_{Liq}$ and $EDP_{NonLiq}$ are the peak response values of each EDP for the lateral spreading and the seismic shaking cases, respectively. As shown in Figure 3.5(a), peak displacements of the pile cap under seismic shaking and soil liquefaction agree well with each other in both transverse and longitudinal directions, where $C_{EDP}$ values are close to 1. However, liquefaction induced lateral spreading results in much larger residual displacement for the pile cap in the longitudinal direction, which is consistent with the findings shown in Figure 3.4. The response comparisons of the left abutment are shown in Figure 3.5(b). It can be seen that noticeable transverse residual displacement occurs under the liquefaction case. Meanwhile, due to the pinning effect, the longitudinal displacements of the end abutment are reduced significantly under the liquefaction case in comparison to the seismic shaking case. Figure 3.5(c) compares the column drift ratio under seismic shaking and soil liquefaction cases. In order to reflect the true damaging potential of the pier, the column drift ratio $DR_{column}$ adopted herein excludes rigid rotations at column top and bottom and is defined as:

$$DR_{column} = \frac{(\Delta_1 - \Delta_2)}{h} - \frac{(\theta_1 + \theta_2)}{2} \qquad\qquad (3.4)$$

where $\Delta_1$ and $\Delta_2$ are the translational displacements and $\theta_1$ and $\theta_2$ are the rotational displacements at top and bottom ends of column, respectively, and $h$ is the column height.

Figure 3.5(c) indicates that the column response under the liquefaction induced lateral spreading case demonstrate near static loading characteristic as observed by the relatively small vibration and dominant low frequency content in the response. More importantly, the lateral spreading case results in much larger column responses in both transverse and longitudinal directions. The square root of sum of squares (SRSS) value is therefore calculated to combine the longitudinal and transverse responses. Figure 3.5(d) also presents the combined column drift histories of the right and left piers under the motion No.10. The peak SRSS column drift ratios at the left pier are 3.7% and 0.21% for lateral spreading and seismic shaking cases, respectively. Similarly, the right column exhibits the peak column drift ratios of 4.9% (liquefaction) and 0.15% (non-liquefaction) respectively. The associated $C_{EDP}$ values are 17.57 for the left pier and 33.03 for the right pier respectively. Given the distinctive differences that have been observed for the column responses under the liquefaction and seismic shaking scenarios, the column drift ratio $DR_{column}$ is therefore selected as the target EDP to quantify the effects of liquefaction induced lateral spreading on bridge responses.
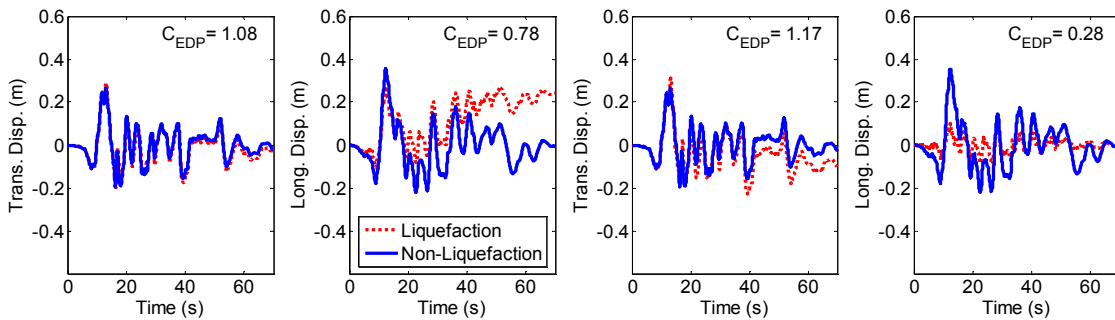


(a) Pile cap displacement          (b) Abutment displacement
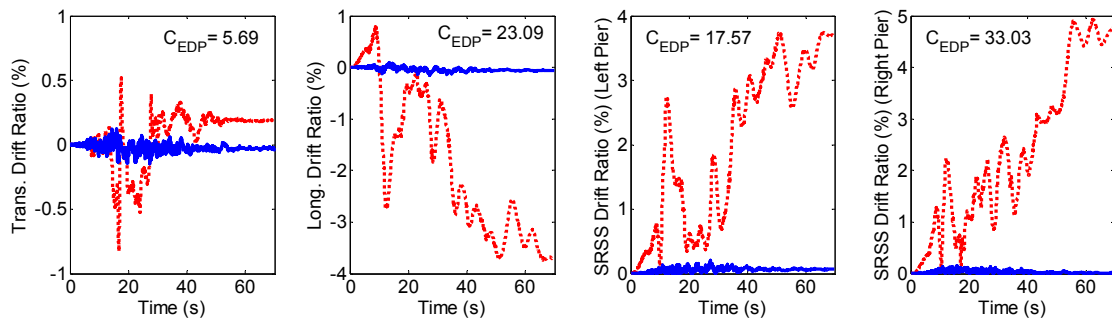
(c) Pier column drift ratio          (d) SRSS value of column drift ratio

Figure 3.5. Bridge response comparisons with various *EDPs* under the motion No. 10

## 3.3 QUANTIFYING THE EFFECTS OF LIQUEFACTION THROUGH $C_{EDP}$

Nonlinear time history results indicate that the bridge responses and their characteristics can differ significantly between the lateral spreading and seismic shaking cases. A general parameter screening procedure has been carried out to identify the parameters that will substantially influence the column drift ratio, the dominant EDP for quantifying the effects of liquefaction induced lateral spreading. For lateral spreading case, parameters such as soil profiles, SSI effects and ground motions all have significant influences on column drift ratio responses. For seismic shaking case, the column responses correlate well with the intensity of the earthquake hazard, in addition to the structural configurations. To derive the response modification factor $C_{EDP}$, the column drift ratio under lateral spreading case, $EDP_{Liq}$, is regressed with soil profiles, load resistances of soils, and ground motion IMs first while the response under seismic shaking, $EDP_{NonLiq}$, is regressed with IMs of ground motions.

### 3.3.1 Crust Layer Energy $E_{crust}$

The static loading nature under liquefaction induced lateral spreading motivates the use

of soil layer energy content to quantify column responses. As shown in Figure 3.3, due to the pinning effect at end abutments, soil energy imposed on the bridge is likely concentrated at pier foundations. To derive the energy content associated with liquefaction induced lateral spreading, Figure 3.6 presents the simplified sketch of the lateral force displacement profile at pier foundations with the following assumptions: (1) Soil displacements are very small in the bottom dense sand layer hence neglected; (2) The maximum lateral displacement $u_{max}$ increases linearly from the bottom to the top of the loose sand layer, and remains as a constant in the crust clay layer; (3) The deformations of the pile cap and piles are neglected; (4) Lateral forces are separated into two parts: a resultant force at the pile cap and a distributed force along each pile.

With above assumptions, soil energy of the crust layer and the liquefied loose sand layer can be expressed as:

$$E_{crust} = P_{cap} \cdot u_{max} + \int_{h_{cap}}^{h_{crust}} N \cdot p_{clay}(x) \cdot u_{max} dx \tag{3.5}$$

$$E_{liq} = \int_{h_{crust}}^{h_{crust} + h_{liq}} N \cdot p_{sand}(x) \cdot u(x) \, dx \tag{3.6}$$

where $E_{crust}$ is the crust layer energy, $E_{liq}$ is the loose sand layer energy, $u_{max}$ is the maximum lateral displacement of the crust clay layer, $N$ is the total number of piles, $P_{cap}$ is the resultant force at the pile cap, $p_{clay}(x)$ is the lateral force along a single pile in the crust clay layer; $p_{sand}(x)$ is the lateral force along a single pile in the loose sand layer, $h_{cap}$ is the thickness of pile cap, $h_{crust}$ is the thickness of the crust clay layer, $h_{liq}$ is the thickness of the loose sand

layer and $u(x)$ is the lateral displacement of the loose sand layer as calculated by:

$$u(x) = u_{\max} - \frac{u_{\max}}{h_{liq}}(x - h_{crust}) \quad h_{crust} < x \le h_{crust} + h_{liq} \tag{3.7}$$

Eqs. (3.5) and (3.6) provide the static equivalent energy contents of the crust clay layer and loose sand layer that is imposed on the pier foundations when liquefaction induced lateral spreading is triggered.
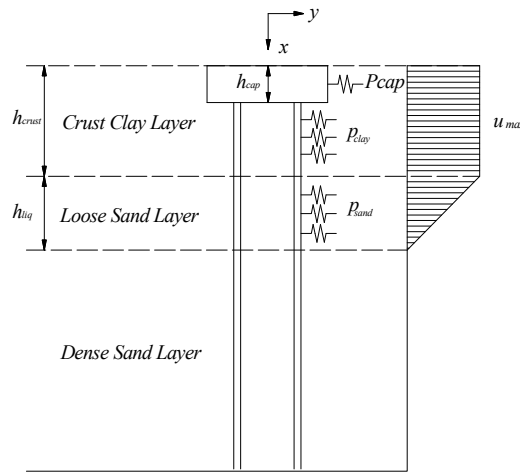


Figure 3.6. Lateral force and displacement sketch at the pier foundation

Preferably, the accurate calculation of energy contents of $E_{crust}$ and $E_{liq}$ requires compete dynamic analyses with liquefaction induced lateral spreading to obtain $u_{max}$ and the lateral forces used in Eqs. (3.5) and (3.6). However, this is too computationally demanding for routine practices. Instead, the energy contents are estimated by regressing the lateral displacement $u_{max}$ and the lateral forces with non-liquefied ground motions and empirical formulas. Furthermore, it is noted that the lateral forces provided by the liquefied loose sand

layer are considerably reduced (to roughly 5% of the force provided by the non-liquefied

sand layer), which in turn substantially decrease the energy content of $E_{liq}$, to less than 4% of

the crust clay layer energy $E_{crust}$ for the benchmark bridge with different soil profiles.

Therefore, only energy content $E_{crust}$ in the crust layer is considered herein.

### 3.3.2 $u_{max}$ - IM Search

Maximum lateral displacement $u_{max}$ of lateral spreading is strongly influenced by both

IMs of the input motion and soil parameters. Rather than theoretically explore the physical

relations between the input motion, soil parameters and the response $u_{max}$, this section

correlates $u_{max}$ to non-liquefied motion at ground surface numerically. The logarithmic linear

assumption used for the probabilistic seismic demand analysis (PSDA) is adopted herein:

$$u_{\max} = a\left(IM\right)^{b} \quad \text{i.e.} \quad \ln\left(u_{\max}\right) = \ln(a) + b\ln(IM) \tag{3.8}$$

where $IM$ is the intensity measure of the non-liquefied motion at ground surface, $a$ and $b$ are

the regression parameters that need to be determined. Table 3.2 lists the broad searching

results for the best $IM$ of the 40 non-liquefied ground motions to correlate $u_{max}$. The surface

motions at the left pier foundation are selected and the $u_{max}$ is the bigger value of peak lateral

displacements at two pier foundations under each motion. The errors shown in Table 3.2 are

defined as:

$$\delta = \frac{1}{n}\sum_{i=1}^{n}\left|\frac{u_{\max,i}^{p} - u_{\max,i}}{u_{\max,i}}\right| \tag{3.9}$$

where $u_{\max,i}^{p}$ is the value predicted by Eq. (3.8) and $u_{max,i}$ is the maximum lateral displacement that obtained from global dynamic analyses; $n$ is total number of input motions (i.e. n = 40 here). As shown in Table 3.2, the optimal $IM$ to regress the $u_{max}$ is the SRSS value of the cumulative absolute velocity ($CAV$ in the unit of m/s), where the error is only 13.4%. Figure 3.7 shows the $\ln(u_{max})$ - $\ln(CAV)$ data and the regression line for the 40 numerical cases. It can be seen that the regression line fits neatly with the data, which indicates that by adopting SRSS $CAV$ as the $IM$, it is able to obtain a sound correlation between the maximum lateral displacement of $u_{max}$ and the non-liquefied ground motions.

Table 3.2.  Linear regression and errors between $u_{max}$ and $IMs$

| IMs | Direction | Error | IMs | Direction | Error |
|---|---|---|---|---|---|
| Peak acceleration | Transverse | 0.529 | $CAV = \int_{0}^{T_d}\|a(t)\|dt$ * | Longitudinal | 0.145 |
| | Longitudinal | 0.477 | | SRSS | 0.134 |
| Peak velocity | Transverse | 0.524 | $CAD = \int_{0}^{T_d}\|v(t)\|dt$ * | Longitudinal | 0.364 |
| | Longitudinal | 0.522 | | SRSS | 0.355 |
| Peak displacement | Transverse | 0.499 | | | |
| | Longitudinal | 0.458 | | | |

* $T_d$ is the duration of each earthquake motion, $a(t)$ is the acceleration time history, and $v(t)$ is the
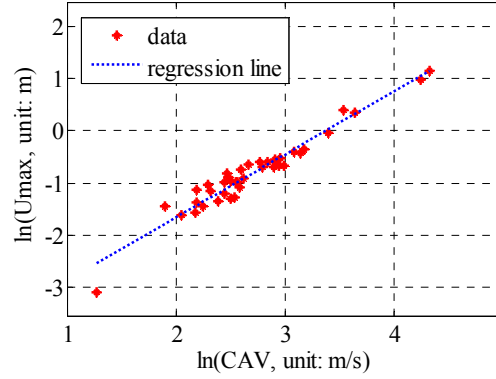
Figure 3.7. The correlation of maximum ground lateral displacement $u_{max}$ (m) and cumulative absolute velocity ($CAV$, m/s): numerical data versus regression line

### 3.3.3 $u_{max}$ - $h_{liq}$ Correlation

Because the maximum lateral displacement increases dramatically from 0 to $u_{max}$ within the liquefied loose sand layer and almost remains as a constant in the crust clay layer (as shown in Figures 3.3 and 3.6), the liquefied loose sand layer thickness $h_{liq}$ could also affect $u_{max}$, in addition to the $CAV$ of the non-liquefied motion at ground surface. In this chapter, the influence of $CAV$ and $h_{liq}$ is assumed to be uncoupled with each other. Therefore, $u_{max}$ can be calculated as:

$$u_{\max} = f(CAV) \times g(h_{liq})$$

(3.10)

As can be seen from Figure 3.7 and Table 3.2, $\ln(u_{max})$ can be closely regressed as a linear function of $\ln(CAV)$ if $h_{liq}$ is a constant, e.g. $h_{liq}$ is 2.0m for the benchmark bridge. To incorporate the impact of $h_{liq}$, the general formula of $u_{max}$ can be rewritten as:

$$u_{\max} = g(h_{liq}) \times CAV^{b'} \tag{3.11}$$

$$\ln(u_{\max}) = \ln[g(h_{liq})] + b' \cdot \ln(CAV) \tag{3.12}$$

The unknown function $g(h_{liq})$ and parameter $b'$ in Eq. (3.12) can be determined by building additional numerical models, each with a different liquefied loose sand layer thickness. Two extra simulation cases have been considered with $h_{liq}$ adjusting to 1.0m and 3.0m, respectively. Figure 3.8(a) plots out the $\ln(u_{max})$ - $\ln(CAV)$ data and the regression lines for all three cases. It can be seen that almost identical slopes can be achieved for the regressed lines when the liquefied layer thickness $h_{liq}$ is changing. Hence, the parameter $b'$ in Eq. (3.12) can be assumed as a constant. Meanwhile, the $\ln(u_{max})$ axis intercepts of the regressed lines are positively related to $h_{liq}$, which means $\ln[g(h_{liq})]$ can be considered as a function of $h_{liq}$. In this study, $g(h_{liq})$ and $b'$ are suggested as following:

$$g(h_{liq}) = 0.005 + 0.005 h_{liq} ; \quad b' = 1.25 \tag{3.13}$$

By substituting $g(h_{liq})$ and $b'$ into Eq. (3.12), the closed-form formula of $u_{max}$ can be expressed as shown in Eq. (3.14). Figure 3.8(b) also shows the $\ln(u_{max})$ - $\ln(CAV)$ data and the values from Eq. (3.14) for the above-mentioned three cases. It can be seen that the proposed formula of $u_{max}$ correlates very well with the numerical data.

$$u_{\max} = (0.005 + 0.005 h_{liq}) \times CAV^{1.25} \quad (m) \tag{3.14}$$

81

(a) Data and regression lines

(b) Data and regression lines with same slopes
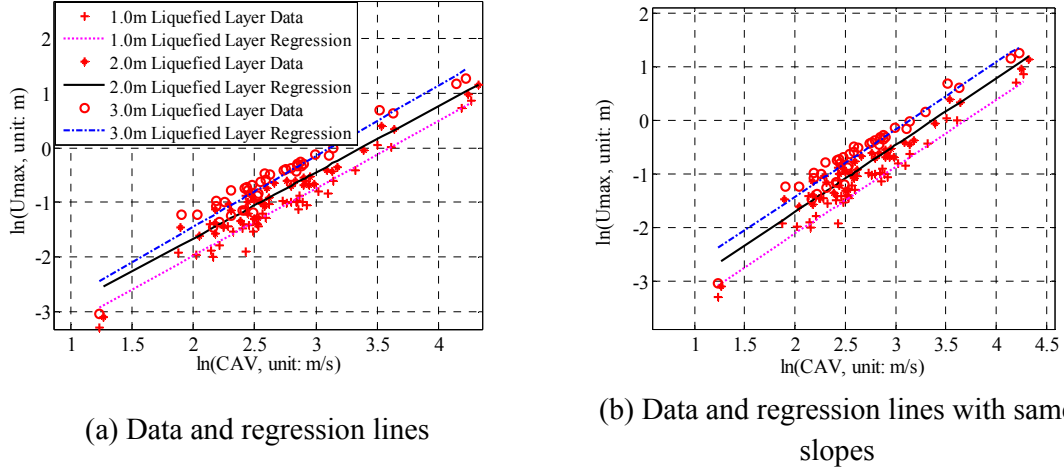
Figure 3.8. The $u_{max}$ (m)- $CAV$ (m/s) relation for different liquefied layer thickness $h_{liq}$ (m) cases

### 3.3.4 *p-y* Forces under Soil Liquefaction

The closed-form expression of the crust layer energy $E_{crust}$ in Eq. (3.5) consists of both displacement parameter of $u_{max}$ and force parameters of $P_{cap}$ and $p_{clay}$. In this section, the lateral force parameters are assumed to be consistent with the *p-y* forces that are used to model the soil lateral resistances under liquefaction. The derivation of the force parameters is based on Matlock's (1970) backbone curve for soft clay. In the crust clay layer, the *p-y* force is given as:

$$p_{clay} = 0.5(\frac{y}{y_{50}})^{0.333} \cdot p_{clay,ult} \tag{3.15}$$

where $y$ is the lateral displacement, i.e. the $u_{max}$ in this study, $p_{clay,ult}$ is the ultimate capacity of the *p-y* material for clay, $y_{50}$ is the displacement at which 50% of $p_{clay,ult}$ is mobilized. According to Matlock (1970), the ultimate capacity of clay $p_{clay,ult}$ can be determined as:

$$p_{clay,ult} = \begin{cases} (3s_u + \gamma \cdot x + \dfrac{0.5s_u \cdot x}{d}) \cdot d \cdot m_p & 0 < x < h_R \\ 9s_u \cdot x \cdot m_p & x \geq h_R \end{cases} \tag{3.16}$$

where $s_u$ is the undrained shear strength of the crust clay layer, $x$ is the soil depth, $\gamma$ is the buoyant unit weight, $d$ is the diameter of the pile, and $m_p$ is the multiplier defined in Eq. (3.2), which accounts for the two possible controlling mechanisms in association of soil liquefaction. The parameter $h_R$ is the critical depth, which can be determined by:

$$h_R = \frac{6d}{\gamma d / s_u + 0.5} \tag{3.17}$$

Furthermore, it is assumed that the resultant $p$-$y$ force at pile cap $P_{cap}$ holds the same constitutive law as is given by Eq. (3.15). However, its ultimate capacity $P_{cap,ult}$ of the soil acting on the pile cap needs to take into account of the passive loading forces and the friction forces along the two sides:

$$P_{cap,ult} = (F_p + F_s) \cdot m_p \tag{3.18}$$

where $F_p$ is the total passive force, $F_s$ is the total friction force at two sides, and $m_p$ is the same multiplier defined by Eq. (3.2). The other input parameter $y_{50}$ for the crust clay layer is adopted empirically as one eighth of the maximum displacement corresponding to the

83

ultimate capacity $p_{clay,ult}$ (Caltrans 2013). Table 3.3 provides $m_p$, $P_{cap,ult}$, $p_{clay,ult}$ and $y_{50}$ values of the pile cap and piles in the crust layer for different crust thicknesses.

Table 3.3.   Input parameters for '$p$-$y$' forces in the crust clay layer

| Crust layer thickness | $m_p$ | Pile cap $P_{cap,ult}$ (kN) | Piles $p_{clay,ult}$ (kN/m) | $y_{50}$ (m) |
|---|---|---|---|---|
| 1m | 1.000 | 1105 | -- | 0.031 |
| 2m | 0.706 | 916 | 123.7-157.0 | 0.032 |
| 3m | 0.634 | 823 | 111.1-171.0 | 0.036 |
| 4m | 0.583 | 756 | 102.2-184.7 | 0.042 |
| 5m | 0.544 | 706 | 95.3-198.0 | 0.049 |

### 3.3.5 *EDP_Liq* Derivation

The crust layer energy content $E_{crust}$ can be obtained by substituting the lateral displacement $u_{max}$ and the $p$-$y$ forces $p_{clay}$ and $P_{cap}$ into Eq. (3.5) and is given by:

$$E_{crust} = \frac{0.5u_{max}^{1.333}}{y_{50}^{0.333}}\left[P_{cap,ult} + N \cdot \int_{h_{cap}}^{h_{crust}} p_{clay,ult}(x)d_x\right] \tag{3.19}$$

As can be seen from Eq. (3.19), the derived crust layer energy $E_{crust}$ effectively incorporates lateral displacements, liquefied layer thickness, as well as the load resistances of the crust layer. Especially, it successfully reflects the static loading nature associated with the liquefaction induced lateral spreading on bridges. Therefore, it is rational to seek a possible correlation between the column drift ratio under lateral spreading $EDP_{Liq}$ and the crust layer energy $E_{crust}$. The same logarithmic linear assumption is adopted:

$$\ln\left(EDP_{Liq}\right) = \ln(c) + d\ln(E_{crust})$$  (3.20)

where $c$ and $d$ are the regression coefficients that can be obtained through a linear regression between $\ln(EDP_{Liq})$ and $\ln(E_{crust})$.

Figure 3.9 presents the numerical data and the regression results of $\ln(EDP_{Liq})$ for a total of five bridge systems, with each case considers a different soil profile. The selected 40 groups of rock motions are imposed on each of the five bridge cases, from which a total of 200 sets of bridge responses are obtained. It can be seen from Figure 3.9 that the regressed line provides a reasonable estimation of column drift ratio under liquefaction induced lateral spreading. The suggested closed-form formula is given as follows with $E_{crust}$ in the unit of kN·m:

$$\ln(EDP_{Liq}) = 0.7 \times \ln(E_{crust}) - 10.26$$  (3.21)

$$EDP_{Liq} = 3.5 \times 10^{-5} \cdot E_{crust}^{0.7}$$  (3.22)

### 3.3.6 $C_{EDP}$ Derivation

As defined in Eq. (3.3), $EDP_{NonLiq}$ is the remaining parameter to finalize the derivation of $C_{EDP}$. A broad parameter screening process indicates that the column drift ratio under non-liquefied seismic shaking scenario $EDP_{NonLiq}$ is mainly influenced by the peak acceleration ($PGA$) of non-liquefied ground motion at the ground surface. As shown in Figure 3.10, the same logarithmic linear assumption is used to derive the closed-form expression of $\ln(EDP_{NonLiq})$ for the aforementioned five bridge cases with $PGA$ in the unit of m/s$^2$:
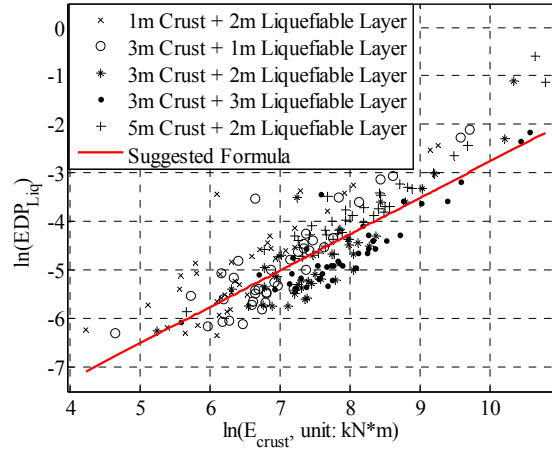
Figure 3.9. Column drift ratio $EDP_{Liq}$ – crust layer energy $E_{crust}$ (kN·m) correlation for different soil profile configurations
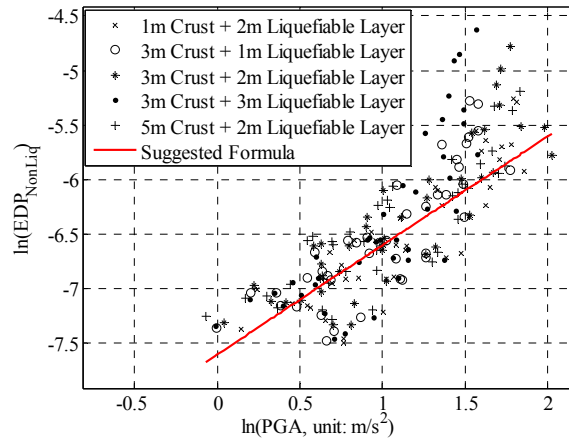


Figure 3.10. Column drift ratio under seismic shaking $EDP_{NonLiq}$- $PGA$ (m/s$^2$) correlation for different soil profile configurations

$$\ln(EDP_{NonLiq}) = \ln(PGA) - 7.6 \qquad (3.23)$$

$$EDP_{NonLiq} = 5 \times 10^{-4} \cdot PGA \qquad (3.24)$$

where *PGA* is the peak ground acceleration of the non-liquefied surface motion in longitudinal direction at the two pier foundations. Therefore, the closed-form expression of

$C_{EDP}$ can be finalized as:

$$C_{EDP} = \frac{3.5 \times 10^{-5} \cdot E_{crust}^{0.7}}{5 \times 10^{-4} \cdot PGA} = \frac{0.07 E_{crust}^{0.7}}{PGA} \tag{3.25}$$

### 3.3.7 Additional Parameters for $C_{EDP}$

The proposed formula of $C_{EDP}$ quantifies the damaging potential of liquefaction induced lateral spreading for the benchmark bridge. To derive $C_{EDP}$ for different highway bridges, the proposed formula of $C_{EDP}$ is modified by multiplying additional parameters that can incorporate other structural and foundation considerations. For typical highway bridges in California, their designs are often differed in these aspects, such as superstructure characteristics, pile designs, and pier column designs etc. In this section, four additional multipliers are incorporated in the formula of $C_{EDP}$ to capture a wide scope of highway bridge systems as follows:

$$C_{EDP} = \frac{0.07 E_{crust}^{0.7}}{PGA} \delta_t \cdot \delta_p \cdot \delta_c \cdot \delta_i \tag{3.26}$$

where $\delta_t$ is the multiplier for superstructure characteristic type, $\delta_p$ is the multiplier for pile strength, $\delta_c$ is the multiplier for pier strength, and $\delta_i$ is the multiplier for soil inclination angle.

The multiplier $\delta_t$ is used to account for highway bridges with different superstructure characteristics, i.e. bridges with seat type abutments, bridges with simply supporting piers, bridges with the combination of seat type abutments and simply supporting piers, and bridges with expansion joints built at the bridge center. Global dynamic analyses have been carried

87

out for each bridge category assuming soil profiles and input ground motions are the same as the benchmark bridge. A general searching procedure has been conducted to find the optimal $\delta_t$ value for each bridge system, where the suggested values are listed in Table 3.4. The error associated with the optimal $\delta_t$ for each bridge case is calculated as:

$$e = \frac{1}{n} \sum_n \left| \frac{C^p_{EDP,i} - C_{EDP,i}}{C_{EDP,i}} \right| \tag{3.27}$$

where $C^p_{EDP,i}$ is the value calculated by Eq. (3.26), $C_{EDP,i}$ is the value obtained from the global dynamic analysis under ith ground motion, $n$ is the total number of ground motions, i.e. n = 40 in this study. It can be seen from Table 3.4 that with the proposed multiplier $\delta_t$, the $C_{EDP}$ formula for highway bridges with different superstructure characteristics yields errors ranging from 30% to 50%.

Table 3.4.   Superstructure characteristic multiplier $\delta_t$

| Bridge Types | Monolithic Abutment & Continuous Deck | Seat Type Abutment | Simply Supporting Pier | Seat Type Abutment & Simply Supporting Pier | Expansion Joint |
|---|---|---|---|---|---|
| $\delta_t$ | 1 | 0.35 | 0.65 | 0.4 | 0.4 |
| Error (%) | 34.7 | 40.4 | 43.1 | 50.9 | 52.8 |

Other than the 0.61m diameter CIDH pile (yield moment $M_y$ = 400 kN·m) used for the benchmark bridge, two additional pile designs, i.e. the 0.38m diameter CIDH pile with a yield moment of 180 kN·m and the 0.61m diameter cast-in-steel-shell (CISS) pile with a yield moment of 1800 kN·m, are considered for typical highway bridges in California. A similar dynamic analysis and searching procedure has been conducted to identify the optimal $\delta_p$ value for these three pile designs. Table 3.5 lists the values of $\delta_p$ as well as the errors that

are calculated by Eq. (3.27), which are around 35% for all three pile cases. It is noted that the proposed $\delta_p$ value doesn't vary linearly with the yield moment of the pile, resulting from the fact once the pile strength reaches up to a certain level; i.e. when the pile foundation is much stronger than the pier column, the pile foundation will move as a rigid body, and the column drift responses will be dominated by the strength of the pier column. A simple power function that is shown in Eq. (3.28) is suggested to quantify the pile strength factor $\delta_p$ for different types of piles with $M_y$ in the unit of kN·m.

$$\delta_p = \frac{4}{M_y^{0.23}} \tag{3.28}$$

Table 3.5.  Pile strength multiplier $\delta_p$

| Pile Type | d = 0.61m CIDH | d = 0.38m CIDH | d = 0.61m CISS |
|---|---|---|---|
| Yield Strength (kN·m) | 400 | 180 | 1800 |
| $\delta_p$ | 1 | 1.2 | 0.7 |
| Error (%) | 34.7 | 34.2 | 35.3 |

The post-1971 pier that is used in the benchmark bridge owns a yield moment of 7011 kN·m. In this section two extra pier designs, one is the typical pre-1971 pier that has a yield moment of 4900 kN·m, while the other is the post-1971 strengthened pier with the yield moment up to 10510 kN·m, are considered for the pier strength multiplier $\delta_c$. Table 3.6 lists all three pier types and their corresponding $\delta_c$ values. It is worth mentioning that the suggested $\delta_c$ values equal to 1 for all three cases, which indicates that pier strength does not affect the $C_{EDP}$ too much, namely the column drift varies in the similar pace under liquefaction induced lateral spreading and seismic shaking when different pier strengths are

considered. The associated errors for the proposed $\delta_c$ values range from 30% to 40%.

Table 3.6.　Pier column strength multiplier $\delta_c$

| Pier Column Type | Post-1971 | Pre-1971 | Post-1971, strengthened |
|---|---|---|---|
| Yield Strength (kN·m) | 7011 | 4900 | 10510 |
| $\delta_c$ | 1 | 1 | 1 |
| Error (%) | 34.7 | 30.5 | 39.3 |

Instead of keeping the soil inclination angle as 4° towards bridge center for the benchmark bridge, the multiplier $\delta_i$ is identified by considering two additional soil profiles, i.e. the one with local soil inclining 2° towards bridge center and the other with no soil inclination. To be simple, lateral spreading are assumed to occur symmetrically on both sides of the bridge. Other possible cases, e.g. only left half of the bridge experiencing lateral spreading, are not considered herein. Table 3.7 lists the proposed $\delta_i$ values. The corresponding errors are from 30% to 45% for these three cases. It can be found that the suggested $\delta_i$ values vary linearly with the soil inclination angle, which can be quantified using Eq. (3.29).

$$\delta_i = 0.15\theta + 0.4 \tag{3.29}$$

where the parameter $\theta$ is the soil inclination angle in the unit of degree.

Table 3.7.　Soil incline angle multiplier $\delta_i$

| Ground Incline Angle (°) | 4 | 2 | 0 |
|---|---|---|---|
| $\delta_i$ | 1 | 0.7 | 0.4 |
| Error (%) | 34.7 | 32.7 | 45.6 |

## 3.4 NUMERICAL VALIDATION

The soundness of using the derived expression of $C_{EDP}$ to predict the column drift ratio due to liquefaction induced lateral spreading is further validated for a range of different highway bridge systems. Eight distinctive bridges, each with randomly varied structural and soil properties, are modeled and analyzed under lateral spreading and seismic shaking when subject to the selected 40 groups of ground motions. For each case, the derived $C_{EDP}$ value is compared with the numerical data with errors calculated using Eq. (3.27). Table 3.8 lists the eight bridge cases and the associated prediction errors, which ranges from 29% to 56%. Possible sources of errors in predictions include: (1) a few assumptions have been made to derive the crust layer energy under soil liquefaction; (2) inherent errors occur when using the logarithmic linear assumption to derive both $EDP_{Liq}$ and $EDP_{NonLiq}$; (3) additional structural and soil multipliers propagate the errors of the final formula. However, given that global dynamic analysis to capture the damaging potential of bridge column under liquefaction induced lateral spreading is laborious and demanding, the 29-56% of error can be deemed as acceptable for routine practices. The proposed formula is simple yet dependable in predicting the soil liquefaction effect on column drift ratios on the basis of the responses under seismic shaking.

Table 3.8.   Validation cases and computed errors of the proposed formula

| Items | | Base Model | Validation Case No. 1 | 2 | 3 | 4 | 5 | 6 | 7 | 8 |
|---|---|---|---|---|---|---|---|---|---|---|
| Abut | Monolithic | √ | √ | √ | √ | | | | √ | √ |
| | Seat type | | | | | √ | √ | √ | | |
| Deck | Continuous | √ | √ | √ | √ | | √ | | | |
| | Simply-supported | | | | | √ | | √ | √ | √ |
| Pier | $M_y$ (kN·m) | 7011 | ×1.0 | ×1.0 | ×1.5 | ×0.6 | ×0.6 | ×1.0 | ×1.5 | ×0.6 |
| Pile | $M_y$ (kN·m) | 400 | ×1.0 | ×1.5 | ×0.6 | ×1.5 | ×1.5 | ×1.5 | ×0.6 | ×1.5 |
| Soil | Incline angle (°) | 4 | 4 | 4 | 4 | 4 | 3 | 3 | 3 | 3 |
| | Crust layer thickness (m) | 3.0 | 2.0 | 4.0 | 2.0 | 4.0 | 2.0 | 4.0 | 2.0 | 4.0 |
| | Loose sand thickness (m) | 2.0 | 1.0 | 3.0 | 1.0 | 3.0 | 1.0 | 3.0 | 1.0 | 3.0 |
| Error (%) | | 34.7 | 47.7 | 29.0 | 46.7 | 47.6 | 47.1 | 40.8 | 32.9 | 56.3 |

## 3.5 Concluding Remarks

This chapter develops an effective method to quantify the effects of liquefaction induced lateral spreading on column drift responses of typical highway bridges in California. Global dynamic analyses are conducted under lateral spreading and seismic shaking scenarios respectively to predict column drift responses. Having observed the near static loading mechanism under lateral spreading, the soil energy content imposed by the non-liquefied crust layer is considered as the dominant factor for responses of bridges on liquefiable soil. The crust layer energy is derived as a function of the cumulative absolute velocity (CAV) of non-liquefied ground motion at surface, geometric parameters of the soil profile, and $p$-$y$ forces representing lateral resistance of soils. The column drift ratio under liquefaction induced lateral spreading, $EDP_{Liq}$, is subsequently derived as a function of the crust layer energy by using the linear logarithmic assumption. Under seismic shaking, the column drift ratio without liquefaction, $EDP_{NonLiq}$, is directly correlated with the peak ground acceleration of the non-liquefied motion at the ground surface. Subsequently, the effects of lateral

spreading on column drifts are quantified by using a response modification factor $C_{EDP}$ (= $EDP_{Liq}/EDP_{NonLiq}$). Four additional multipliers are identified for $C_{EDP}$ to take into account of various highway bridges with different superstructure characteristics, pile strengths, pier designs, and soil inclination angles. The proposed closed-form expression of $C_{EDP}$ has been validated through comparisons against the simulation results for eight bridge models that have varying structural and soil properties. Normalized errors of 29-56% have been found between the simplified formula and the numerical predictions. This relatively small error confirms that the proposed formula can be used with confidence in practice.

In summary, this chapter offers a simple yet dependable method to quantify the influences of liquefaction induced lateral spreading on column drift ratios with respect to the correspondent responses under the seismic shaking for typical highway bridges. The proposed method captures key response features of bridges and offers reliable column drift predictions.

# 4. OPTIMAL SEISMIC PROTECTION DESIGN OF HIGHWAY BRIDGES

Modern seismic protective devices in the forms of isolation bearings and energy dissipation devices provide attractive means to mitigate earthquake hazards for both new and retrofitted highway bridges. However, as discussed in Chapter 1, the wide choices of design parameters as well as the highly nonlinear behaviors of protective devices make the establishment of simple design rules difficult. In addition, a robust methodology is entailed to evaluate the effectiveness of seismic protective devices in the bridge-system level. This chapter bridges such gap by providing a performance-based framework to evaluate and optimize seismic protective devices for highway bridges. The Painter Street Overcrossing (PSO) that has been studied in Chapter 2 is selected as the base model in this chapter and is seismically redesigned with protective devices. Numerical modeling, component-level fragility analyses, system-level performance index, and multi-objective optimization of protective devices for the PSO are discussed in following sections.

## 4.1 NUMERICAL MODELING OF THE PSO WITH PROTECTIVE DEVICES

### 4.1.1 3D Numerical Modeling of the As-built PSO

As shown in Chapter 2, the three-dimensional stick model with macro springs and dashpots (i.e., modeling scheme 'Case 4' in Chapter 2) capturing the SSI effects and distinct motions inputs at the center bent and end abutments is capable of yielding comparable results against recorded responses. Moreover, compared with the proposed *p-y* modeling approach in Chapter 2, this modeling scheme is more computationally efficient to be implemented in the

probabilistic analysis framework. Therefore, this chapter adopts the three-dimensional stick model to analyze the seismic responses of the PSO. Recall that the PSO is a two-span prestressed concrete box-girder bridge with continuous spans of 44.5 m and 36.3 m respectively (Figure 4.1(a)). The superstructure is supported on monolithic end abutments and a two-column central bent, both with a skew angle of 39°. The 7.3 m high pier columns are designed with non-uniform cross sections, where the bottom half of each pier consists of a 1.5 m diameter circular section with 36#11 longitudinal bars (Figure 4.1(d)) and the top half is composed of variable sections with 36#11 longitudinal bars confined the inner layer and 18#5 longitudinal bars confined the outer layer (Figure 4.1(e)).



(a) E-W elevation

(b) Deck plan

(c) S-N elevation

(d) 1-1 section (1:4)

(e) 2-2 section (1:4)
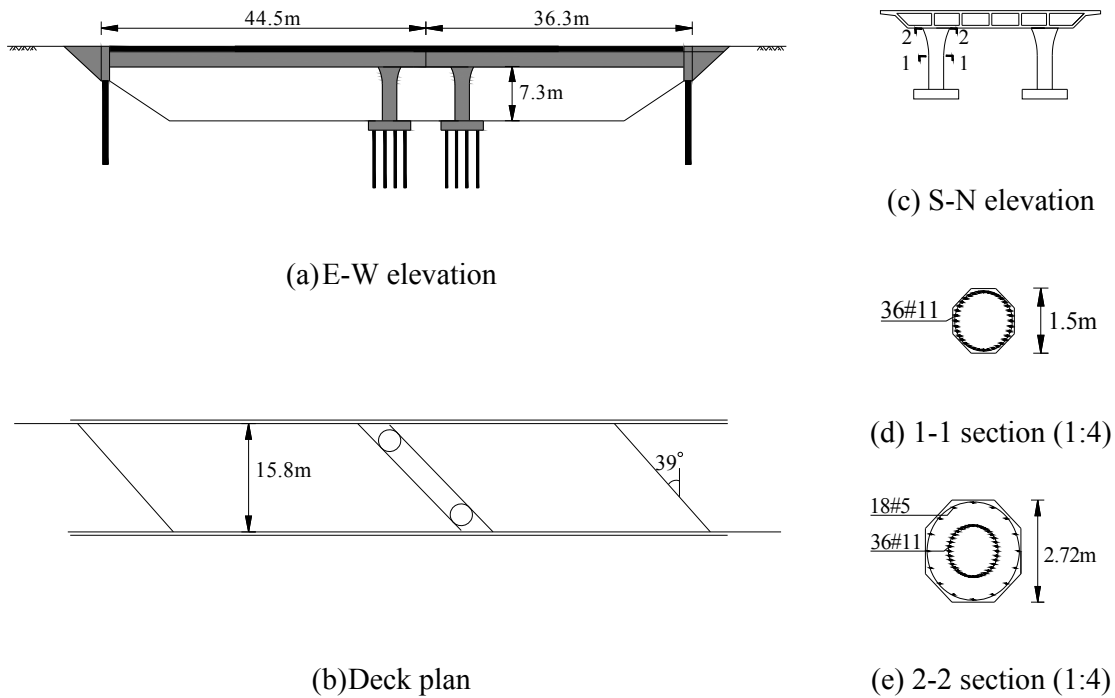
Figure 4.1. Sketch of the Painter Street Overcrossing (PSO)

The three-dimensional numerical model of the PSO is built in the software platform

OpenSees (Mazzoni et al. 2006). The bridge deck and end abutments are modelled with linear

beam elements, while the nonlinear behavior of the column is captured by using a bilinear

moment-curvature relation that is obtained from the pushover analysis of the column with fiber

section nonlinear beam elements. Figure 4.2 presents the moment-curvature relations of 1-1

and 2-2 sections that are shown in Figure 4.1 as well as the force-displacement relationship of a

single column from the pushover analysis. The sectional moment-curvature relations and the

force-displacement relationship of the column are both regressed with bilinear curves. The

former provides input parameters for the moment-curvature hardening relation in OpenSees,

and the latter offers three parameters, namely the elastic stiffness, $K_{1,C}$, characteristic strength,

$Q_C$ and post-yielding stiffness, $K_{2,C}$, all of which can be used to normalize the bearing

parameters such that its optimal design parameters can be expressed in dimensionless forms.
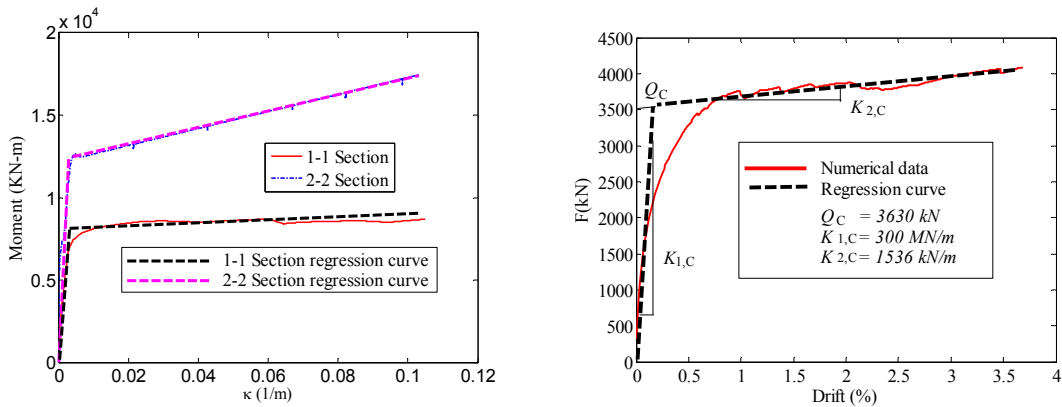


(a) Section moment curvature relation    (b) Force-displacement pushover curve
Figure 4.2.  Section properties and force-displacement curve of pier column

The SSI effects of the bridge are considered at embankments that support the end

abutments and the pile foundations at bridge center. The kinematic response function and dynamic stiffness that were derived by Zhang and Makris (2002a) are adopted to generate the amplified motion of the embankment and frequency independent springs and dashpots for SSI effects at abutment foundations, respectively. An equivalent flexural-shear beam element that is derived by Zhang et.al (2004) is used to incorporate the SSI effects at pier foundations.

### 4.1.2 Modeling of Seismic Protective Devices

The seismic protection of highway bridges can be improved with the use of various protective devices, which in general can be divided into two categories, i.e. isolation bearings and supplemental energy dissipation devices (Agrawal and Amjadian 2016). For isolation bearings, three most common types are elastomeric bearings (ERB), lead-rubber bearings (LRB), and friction pendulum systems (FPS). Although their mechanical behaviors are different from each other, a bilinear model can be used to represent their behavior (Naeim and Kelly 1999). As shown in Figure 4.3(a), the bilinear model can be characterized by three parameters: elastic stiffness $K_1$, post-yielding stiffness $K_2$, and characteristic strength $Q$. The mechanical characteristics of the three isolation devices have been summarized by Zhang and Huo (2009) and are listed in Table 4.1. Identifying these mechanical characteristics forms the basis of the seismic design of isolation devices for bridges (AASHTO 2014; Agrawal and Amjadian 2016). It can be seen that these three bearing types have different stiffness ratio $N$, which is defined as the ratio between elastic stiffness and post-yielding stiffness ($N = K_1/K_2$). The stiffness ratio $N$ typically ranges from 5 to 15 for ERB, 15 to 30 for LRB, and 50 to 100 for FPS. In this study, the stiffness ratio $N$ is varied to represent different bearing types.

Supplemental energy dissipation devices can be classified into passive, active and semi-active devices (Housner et al. 1997). Although not sufficiently adaptive to ever changing ground excitations, passive devices have been widely implemented in buildings for seismic protection since they are easy to install and stay reliable during earthquakes (Soong and Dargush 1997). As one type of passive devices, fluid viscous dampers have gained extensive attention in both research and the practice community because of their large capacity and simplicity for numerical modelling. The nonlinear damper force ($f_d$) can be analytically expressed as a fractional velocity power law as

$$f_d(t) = C_\alpha \left| v(t) \right|^\alpha \text{sgn}\left[ v(t) \right] \tag{4.1}$$

where $v(t)$ is the damper velocity, $C_\alpha$ is the experimentally determined damping coefficient with units of force per velocity raised to the $\alpha$ power; $\alpha$ is a real positive exponent with typical values in the range of 0.35-1 for seismic applications, and sgn($\cdot$) is the signum function. The linear damper force can be easily defined by Eq. (4.1) with $\alpha = 1$. Figure 4.3(b) plots out the force displacement loop of the fluid viscous damper for both nonlinear ($\alpha < 1$) and linear ($\alpha = 1$) cases.
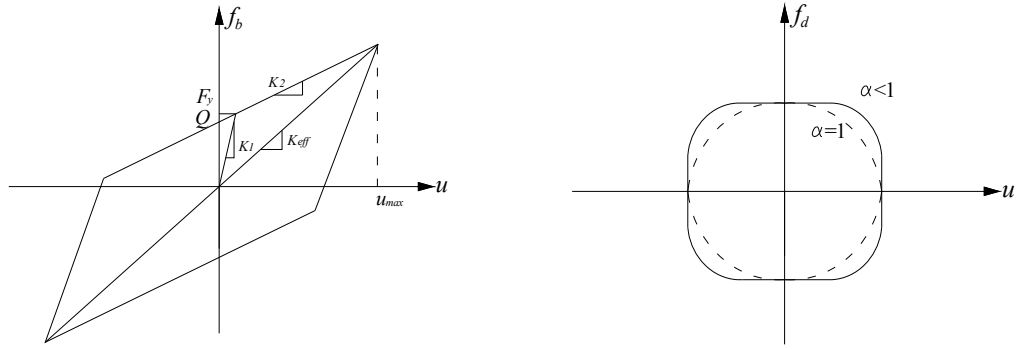
(a) Bilinear model for isolation bearings  (b) Nonlinear and linear viscous model for fluid dampers

Figure 4.3.  Numerical modeling of isolation bearing and fluid damper

Table 4.1.  Mechanical Characteristics for the Three Types of Isolation Bearings

| Bearing Type | Post-yielding ration $N$ ($N = K_1/K_2$) | Characteristic strength $Q$ | Post-yielding stiffness $K_2$ |
|---|---|---|---|
| ERB | 5-15 | From hysteresis loop | $K_2 = GA/\Sigma t_r$ |
| LRB | 15-30 | $F_y = f_y A_{Lead}$ | $K_2 = (1.15\text{-}1.20)\, GA/\Sigma t_r$ |
| FPS | 50-100 | $Q = \mu W$ | $K_2 = W/R$ |

Figure 4.4 illustrates the three-dimensional modeling scheme for the PSO with protective devices installed atop pier columns and end abutments. Note that the modeling scheme excludes the substructures by using frequency-independent springs, dashpots and equivalent linear beam elements to account for the presence of approach embankments and piles foundations, as well as the associated SSI effects. In addition, amplified motion inputs are used to account for the embankment amplification effect at end abutments.
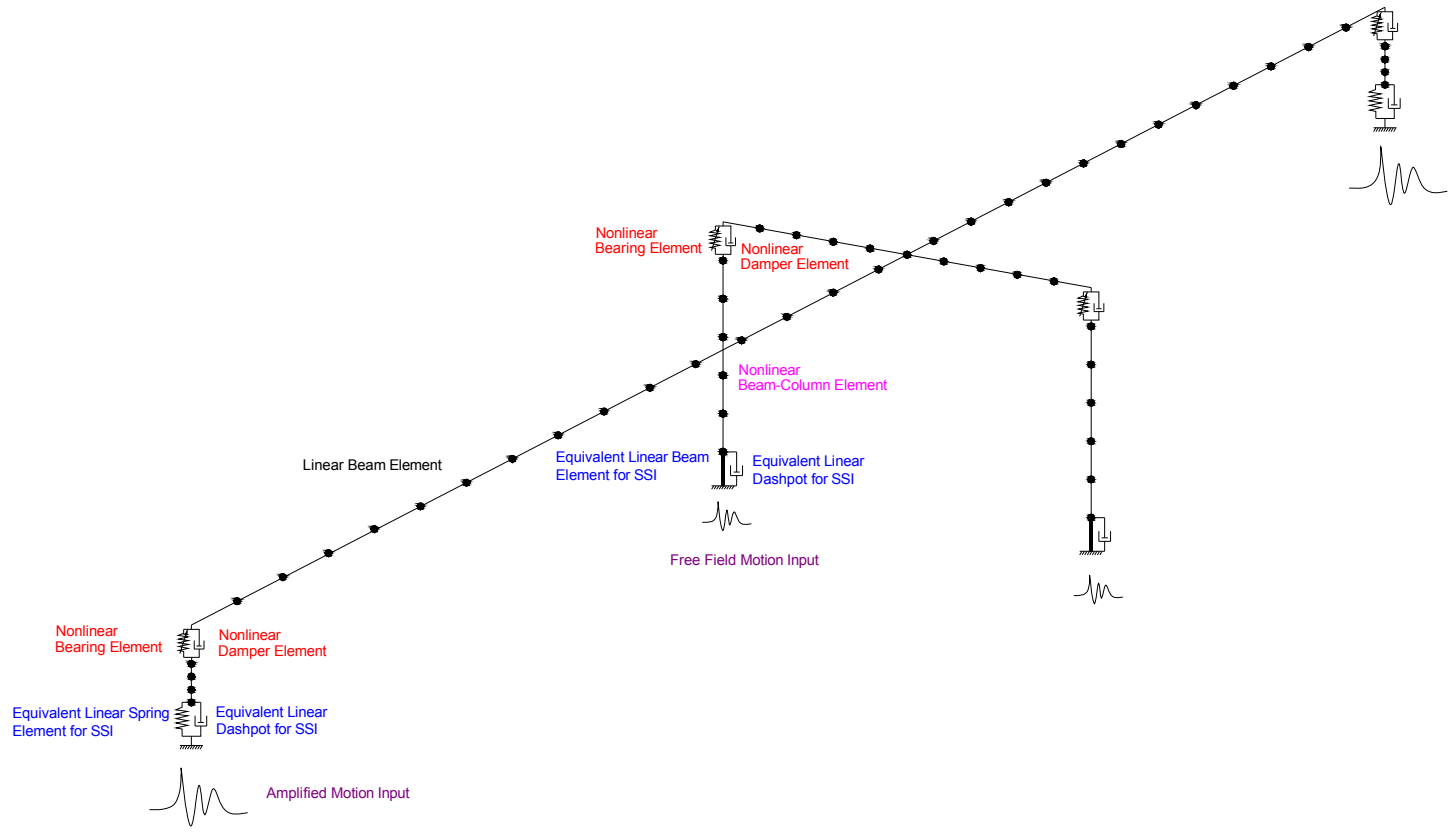
Figure 4.4. Three-dimensional numerical model of the PSO with seismic protective device

100

## 4.2 COMPONENT-LEVEL FRAGILITY ANALYSIS

By defining the conditional probability of the EPDs attaining or exceeding a specified DS for a given level of ground motion intensity, fragility curves offer useful tools to assess the vulnerability of highway bridges to earthquake hazards. Depending on the data resources, fragility functions can be generated as empirical functions that are based on bridge damage data from major earthquakes (Basöz et al. 1999; Shinozuka et al. 2000) or analytical functions with numerical analysis results (Karim and Yamazaki 2007; Padgett and DesRoches 2008; Agrawal et al. 2012; Siqueira et al. 2014; Zhang and Huo 2009). Because of the absence of adequate empirical data, analytical methods have often been used to derive bridge fragility functions. In this chapter, the component-level fragility curves of highway bridges are developed by the cloud method, which is also termed as Probabilistic Seismic Demand Analysis (PSDA). The PSDA correlates EDPs with ground motion IMs based on three assumptions: logarithmic linear assumption between median EDP and IM, constant variance assumption for all IM ranges, and log-normal distribution of EDP at a given IM level (Cornell et al. 2002). Therefore, the conditional probability for an EDP to reach a certain DS under a given IM can be written as:

$$P\left[EDP \ge LS \middle| IM\right] = 1 - \Phi\left(\frac{\ln(LS) - \ln(aIM^b)}{\xi_{EDP|IM}}\right) \tag{4.2}$$

where LS is the limit state that corresponds to each DS, parameters *a* and *b* are regression

coefficients based on the logarithmic linear assumption, $\xi_{EDP|IM}$ is the constant standard deviation of the logarithmic distribution, and $\Phi(\bullet)$ is the standard normal distribution function.

To address the uncertainties that inherent with ground motions, PSDA relies on a significant number of nonlinear time history analyses, which requires selection a large group of earthquake records. In this chapter, earthquake records selection is guided by determining the optimal IM of ground motions. Intuitively, a good choice for IM should roughly constitute a linear relation with the EDP of interest in the logarithmic domain, such that the linear assumption between median EDP and IM can be satisfied. As suggested by Padgett *et al.* (2008), PGA turns out to be the optimal choice of IM for highway bridges when a composite measure that consists of efficiency, practicality, sufficiency and hazard computability is considered. Therefore, as long as the selected ground motions are capable of covering various PGA levels, the PSDA can offer a conceptually and statistically better prediction of the damaging potential of bridge components. This study selects 140 ground motion records from the PEER Strong Motion Database ([http://ngawest2.berkeley.edu/](http://ngawest2.berkeley.edu/)) to conduct the PSDA. Figure 4.5 shows the distribution of PGA of the selected ground motion records. It can be observed that there is a smaller number of earthquake records with PGA ranges from 0.7g-0.8g and 0.9g-1.0g, while for ranges other than these two, at least 10 motion records have been selected for every PGA internal of 0.1g.
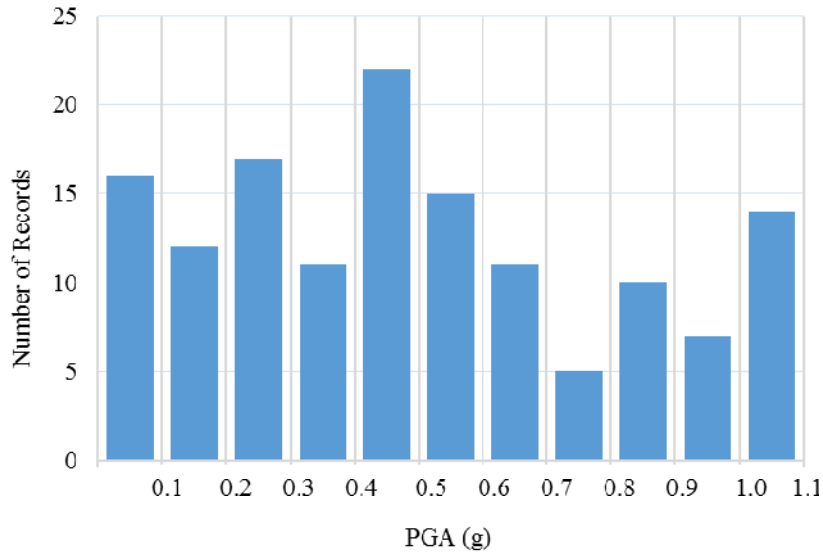
Figure 4.5. PGA distribution of selected ground motions

The last step in finalizing the derivation of component-level fragility curves for highway bridges is to pinpoint bridge components that are vulnerable to seismic damages and their corresponding LS values at various damage states. Previous studies and case histories have suggested that pier columns are the most critical component for a conventional multi-span highway bridge with continuous deck (Seible and Priestley 1999; Choi et al. 2004; Yi et al. 2007). The HAZUS (FEMA 2003) definition of four damage states (i.e. slight, moderate, extensive and collapse) is now being widely adopted as a guideline for determination of limiting values to reach various damage stages for different damage index (DI) measures, which are defined as functions of EDPs. By conducting column tests, studies have determined various DI measures for bridge piers, including curvature ductility, displacement ductility, and energy dissipation ratio etc. (Choi et al. 2004; Yi et al. 2007; FEMA 2003; Hwang et al. 2001; Karim and Yamazaki 2001). A detailed summary of the definitions for various DIs and

corresponding DI criteria was noted by Zhang and Huo (2009). This study compares the limit

states of column curvature ductility $\mu$ suggested by Choi *et al.* (2004) with those of column

drift ratio $\theta$ recommended by Yi et al. (2007) and found that corresponding limit states for these

two DI measures provide very close component fragility curves for highway bridges. The

column drift ratio $\theta$ is adopted as the DI in this study, given the simplicity of extracting its peak

demand values during fragility analysis and the optimization process. Meanwhile, for highway

bridges that are equipped with protective devices, the vulnerability of protective devices needs

to be incorporated as well. In light of the fact that supplemental energy dissipation devices (e.g.

the viscous fluid dampers considered in this study) are usually installed adjunctively on bridges,

the consequence of their damages or failures cannot be compared with that of isolation devices,

whose roles consist not only providing flexibility to the system but also supporting bridge

superstructures. Therefore, several studies investigated the damage states of isolation bearings

based on experimental observation and the consideration of resulting pounding and unseating

(Siqueira et al. 2014; Zhang and Huo 2009; Naeim and Kelly 1999; Choi et al. 2004; Mori et al.

1999; Kelly and Quiroz 1992), and general agreement was achieved that the DI of isolation

bearings can be expressed in terms of shear strains. At shear strains of about 100%, tests have

revealed a potential visible indicator of damage, which is considered as the slight damage in

this study. While at a 200% shear strain, bearings will experience uplifting and rocking under

dynamic loadings, resulting in the bending of the steel shims as well as a substantial damping

degradation (Naeim and Kelly 1999; Mori et al. 1999); therefore, extensive damage is assumed

at this level such that a high probability of bearing failure would exist. The complete damage

state is associated with ultimate failure of the bearings, severe pounding of bridge superstructures, and a potential span unseating. A shear failure test that has been conducted by Kelly and Quiroz (1992) identified that the maximum shear strain of the a elastomeric bearing could reach up to 388%, so a strain level of 350% is considered as the complete damage for bearings herein. Table 4.2 lists the EDPs, DIs, DSs and LSs for pier columns and isolation bearings.

Table 4.2.   EDPs, DIs and LSs for Concrete Column and Bearing

| Component | DI | Slight damage (DS=1) | Moderate damage (DS=2) | Extensive damage (DS=3) | Collapse damage (DS=4) |
|---|---|---|---|---|---|
| Column (Yi et al. 2007) | Drift ratio $\theta$ | $\theta > 0.7\%$ | $\theta > 1.5\%$ | $\theta > 2.5\%$ | $\theta > 5\%$ |
| Bearing | Shear strain $\gamma$ | $\gamma > 100\%$ | $\gamma > 150\%$ | $\gamma > 200\%$ | $\gamma > 350\%$ |

The effectiveness of seismic protective devices is first investigated through comparing fragility functions in the bridge component level. The PSDA is conducted on the as-built bridge and two additional cases with protective devices installed. One is designed as a fully isolated bridge, and the other is equipped with both isolation bearings and viscous fluid dampers. The 3D numerical model of the PSO is analyzed under the selected 140 motion records in the transverse direction, where dominant responses are expected. For brevity, locational variation is not considered for the protection design (i.e., all protective devices at different locations are assumed to have the same mechanical parameters). The fully isolated case is designed with ERB based on the design guideline provided by Naeim and Kelly (1999), where the mechanical

parameters of the ERB are selected as $K_{1,B}/K_{1,C} = 1.00$, $Q_B/Q_C = 0.80$, and $N = 10$. The bridge

case installed with both bearings and dampers is designed by attaching linear viscous fluid

dampers with damping coefficient $C_\alpha = 3000$ kN(s/m) in parallel with FPS, whose parameters

are chosen as $K_{1,B}/K_{1,C} = 0.5$, $Q_B/Q_C = 0.5$, and $N = 50$. A typical bearing thickness of 0.15m is

assumed for both cases. The soundness of using PSDA to compose the component level

fragility curves is first examined on the as-built case. Figure 4.6(a) plots the EDP (column drift

ratio) and IM (PGA) pairs of 140 simulations in the log-log domain, and a linear regression is

achieved to relate EDP and IM. With a constant variance ($\xi_{EDP|IM}$) of 0.41 across all IM levels,

the fragility curves of the pier columns are generated as shown in Figure 4.6(b).



(a) PSDA results                    (b) Fragility curves
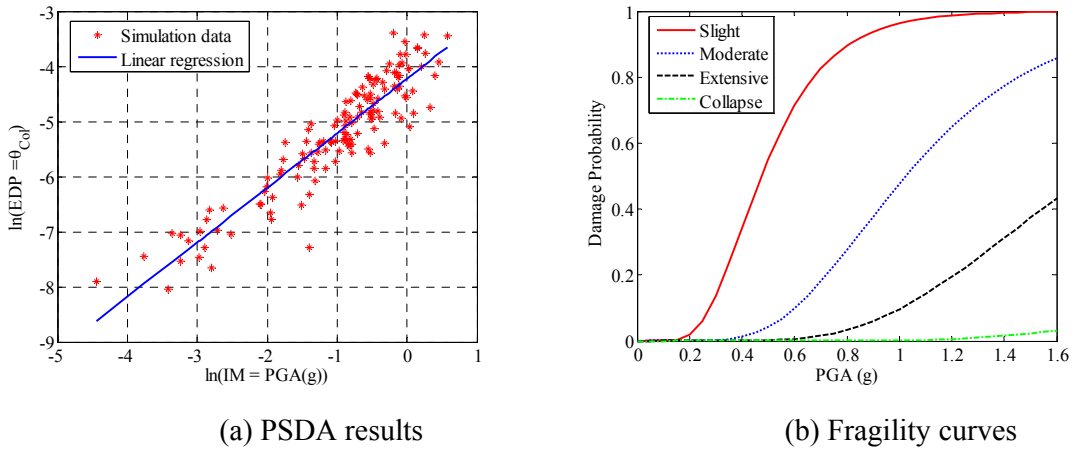
Figure 4.6.  Fragility analyses of the as-built bridge with PSDA

Figure 4.7 presents the component-level fragility curves for three cases: the as-built bridge,

the isolated bridge, and the bridge case designed with both bearings and fluid dampers. The

fragility curves of the isolated case are plotted with thick lines; and it is shown that compared

with the as-built bridge, the isolation design yields lower damage probabilities for pier columns

106

at all damage states. In other words, the damage probability of the as-built bridge can be reduced at all four damage states if the bridge is isolated. The fragility curves of the bridge case installed with both FPS and fluid dampers are shown as thin lines without markers in Figure 4.7. As can be seen from the figure, the design strategy of installing both bearings and fluid dampers can further reduce the damage probabilities of pier columns. However, this design case slightly increases the damage probabilities of isolation bearings when compared with the isolation only case. Such observations imply that: (1) the damaging potentials of isolation bearings and pier columns conflict with each other; and (2) a system-level performance index and an optimal design methodology are required to reflect and minimize the damage probabilities of the bridge in the system level, respectively.

## 4.3 BRIDGE SYSTEM LEVEL PERFORMANCE

The damage probability of pier columns and bearings can be calculated based on the aforementioned component-level fragility analysis, but the bridge's overall damaging potential will still remain unclear because piers and bearings can experience different damage states, and their contributions to bridge system performance cannot be easily quantified. Previous studies suggested that the bridge system-level fragility functions can serve as an effective tool to reflect the overall damaging potential of the bridge. These studies include: (1) estimating the load-carrying capacity of the bridge (Mackie and Stojadinovic 2005); (2) limiting bridge system fragility with two first-order bounds (i.e., a lower bound when assuming bridge components are fully correlated with each other and a upper bound representing that all components are statistically independent) (Choi et al. 2004); (3) using a joint probabilistic

seismic demand model to generate the system damage probability as a union of the component-level damage probabilities (Nielson and DesRoches 2007); and (4) developing a composite DS for the bridge system such that the components' relative importance for load carrying and the repairing cost are considered (Zhang and Huo 2009). It is important to mention that a key consideration for these methods lies in the proper way to quantify the level of correlations between critical components, because bridge components are neither totally correlated nor absolutely independent during earthquakes. Alternatively, this study derives the repair cost ratio of the bridge system and uses it as a performance index to quantify the damaging potential of a given bridge design in the system level.
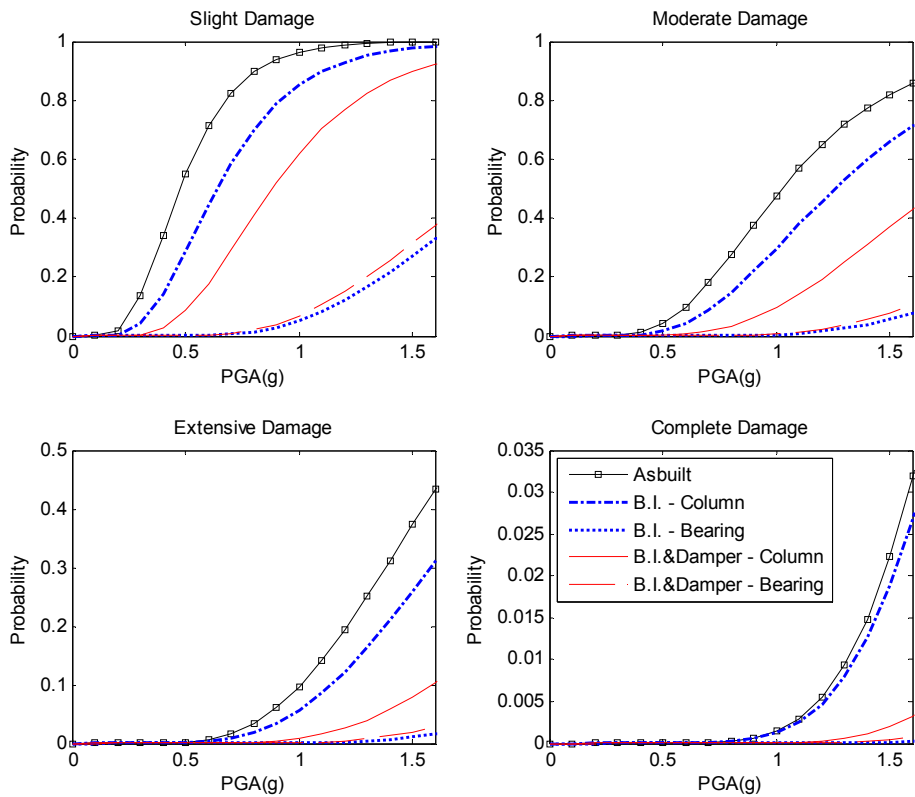


Figure 4.7. Fragility analyses of the initial isolated cases

### 4.3.1 Repair Cost Ratio of Highway Bridges

Defined by the ratio of bridge repair cost under different levels of earthquake hazards with respect to the total replacement cost of the bridge, the repair cost ratio offers an attractive quantitative measure for bridge system-level damage. Similar to the building system (FEMA 2003), at each damage state, the repair cost of a highway bridge component can be estimated using the performance-based methodology as:

$$rc_{i,j} = p_{i,j} d_{i,j} c_j \tag{4.3}$$

where subscripts $i$ and $j$ denote the $i$th damage state and the $j$th component, respectively, $rc_{i,j}$ is the repair cost, $p_{i,j}$ is the damage probability within each damage state, $d_{i,j}$ is the damage ratio that defines the percentage damaged for each damage state, and $c_j$ is the replacement cost of critical bridge component. Therefore, the closed-form expressions of the repair cost ratios for different bridge systems can be given as:

$$RCR_{con} = \sum_{i=1}^{4} p_{i,col} d_{i,col} \tag{4.4}$$

$$RCR_{iso} = \frac{c_{col} \sum_{i=1}^{4} p_{i,col} d_{i,col} + c_{iso} \sum_{i=1}^{4} p_{i,iso} d_{i,iso}}{c_{col} + c_{iso}} \tag{4.5}$$

$$RCR_{comb} = \frac{c_{col} \sum_{i=1}^{4} p_{i,col} d_{i,col} + c_{iso} \sum_{i=1}^{4} p_{i,iso} d_{i,iso}}{c_{col} + c_{iso} + c_{damp}} \tag{4.6}$$

where $RCR_{con}$ is the repair cost ratio of conventionally designed bridge cases with no protective devices installed, $RCR_{iso}$ is the repair cost ratio of the isolated bridge, $RCR_{comb}$ is the repair cost ratio of the bridge cases with both isolation devices and energy dissipation devices installed, $i = 1$ to 4 stands for the four damage states, $p_{i, col}$ and $p_{i, iso}$ are the damage probabilities of pier columns and isolation bearings within the $i$th damage state, respectively, $d_{i, col}$ and $d_{i, iso}$ are the damage ratios of pier columns and isolation bearings within the $i$th damage state, respectively, $c_{col}$ and $c_{iso}$ are the replacement costs for pier columns and isolation bearings, respectively, and $c_{damp}$ is the installation cost of the damper. As shown in Figure 4.8, damage probability $p$ can be calculated as the difference between the conditional probabilities $P$ of the bounding fragility curves. The damage ratios $d$ for the two critical components are listed in Table 4.3, where the damage ratios for columns are suggested by HAZUS (FEMA 2003) and the damage ratios for bearings are determined based on their limit states as defined in Table 4.2 and the physical damages observed from experiments. Note that Eqs. (4.5) and (4.6) can be simplified if the replacement costs of protective devices $c_{iso}$ and $c_{damp}$ are normalized by the replacement costs of pier columns $c_{col}$ as:

$$RCR_{iso} = \frac{\sum_{i=1}^{4} p_{i,col} d_{i,col} + \alpha \sum_{i=1}^{4} p_{i,iso} d_{i,iso}}{1 + \alpha} \tag{4.7}$$

$$RCR_{comb} = \frac{\sum_{i=1}^{4} p_{i,col} d_{i,col} + \alpha \sum_{i=1}^{4} p_{i,iso} d_{i,iso}}{1 + \alpha + \beta} \tag{4.8}$$

where $\alpha$ is $c_{iso}/c_{col}$, and $\beta$ is $c_{damp}/c_{col}$. In this study, the replacement costs of pier columns and

isolation bearings are considered based on the direct and indirect economical losses that are

caused by changing these two components. The complete damages of pier column is usually

associated with severe damages of bridge superstructures and foundations, and hence a

majority of cost should be considered, including redesigning and reconstructing most bridge

components, and a long duration of traffic load loss for the transportation network. For

reference, HAZUS (FEMA 2003) estimates that for a similar highway bridge as the PSO

considered in this chapter, it will cost about \$5 million and take 300–500 days to achieve full

restoration. Conversely, replacement costs of isolation bearings may come from reinstallation

of bearing devices, restoration of bridge superstructure that might be damaged through

pounding or unseating, and a short time of traffic closure. Therefore, this study recommends

that the replacement cost of the isolation bearings $c_{iso}$ is 15% of the replacement cost for pier

columns $c_{col}$ (i.e. $\alpha$ is chosen as 15%). In addition, the installation cost of fluid dampers is lower

than that of isolation bearings. Hence, 5% is assigned for the coefficient of $\beta$ herein.
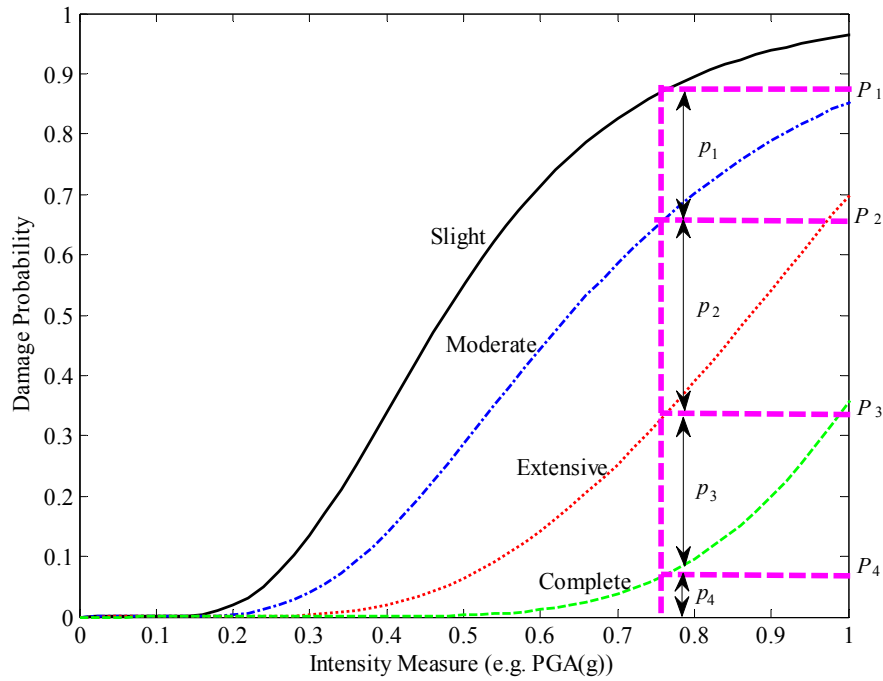
Figure 4.8. Damage probabilities of four damage states

Table 4.3. Damage Ratios for Columns and Bearings

| Item | Component | Slight damage | Moderate damage | Extensive damage | Collapse damage |
|------|-----------|--------------|-----------------|------------------|-----------------|
| Damage | Columns (FEMA 2003) | 0.03 | 0.08 | 0.25 | 1.00 |
| ratio $d$ | Bearings | 0.04 | 0.10 | 0.50 | 1.00 |

## 4.3.2 Repair Cost Ratio of the PSO with Various Protective Devices

The aforementioned three cases are utilized herein to calculate the repair cost ratios of the

PSO when different protection designs are considered. Namely, repair cost ratios are calculated

for the as-built case, the isolated case with the ERB installed ($K_{1,B}/K_{1,C} = 1.00$, $Q_B/Q_C = 0.80$,

and $N = 10$), and the bridge case with the FPS ($K_{1,B}/K_{1,C} = 0.5$, $Q_B/Q_C = 0.5$, and $N = 50$) and the

linear fluid dampers ($C_\alpha = 3000$ kN(s/m) equipped. Figure 4.9 presents the repair cost ratios of

these three bridge cases. As can be seen from the figure, although the PSO features a detailed

design of pier columns intended to resist earthquake hazards, the repair cost ratio of the as-built bridge is reduced if the bridge is fully isolated. Further reductions can be expected if the bridge is equipped with both isolation bearings and fluid dampers. It is important to mention that although the initial costs of the highway bridges are increased by implementing protective devices (e.g., 15% higher cost is considered in this study for the isolated bridges and 20% higher cost is considered for the bridges installed with both isolation bearings and fluid dampers), the expenses to repair the bridges that are designed with protective devices will be decreased. For example, under a strong earthquake that has the PGA of 1.5g, the repair cost ratio of the as-built bridge is 28.3%, whereas the repair cost ratio for the isolated bridge with initial designed ERB is reduced to 19.7%, and the initial design of combining fluid dampers with FPS yields a repair cost ratio of 9.8%. Seismic repair of highway bridges can be much more cost-effective should they are installed with optimally designed protective devices, as discussed later in this chapter.
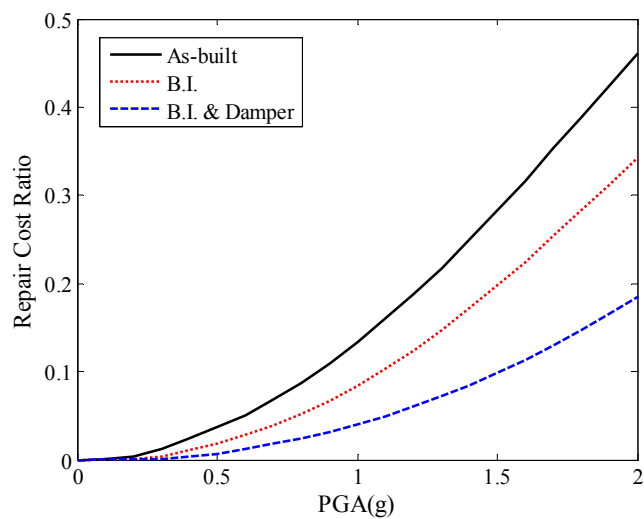


Figure 4.9. Repair cost ratios of the initial designs

**4.4 MULTI-OBJECTIVE GENETIC OPTIMIZATION OF PROTECTIVE DEVICES**

An appropriate optimization procedure is required to achieve the optimal mechanical parameters of protective devices such that the repair cost ratio of the bridge after major earthquake hazards can be substantially reduced. Because a bridge structure equipped with nonlinear bearings and dampers forms a highly nonlinear system, traditional optimization methods, such as the least-square method, cannot be easily implemented. Also, the seismic responses of the two critical components (i.e., isolation bearings and pier columns) usually conflict with each other, that is, a reduction of column drift is usually associated with an increase of bearing displacement, and vice versa. Therefore, a multi-objective optimization method that can efficiently address nonlinear systems is needed. An ideal approach to fulfill this task is the multi-objective genetic optimization procedure (Deb et al. 2002; Konak et al. 2006; Cha et al. 2013), whose methodology and capabilities are briefly explained herein.

**4.4.1 Multi-objective Genetic Optimization Methodology**

In general, two approaches can be considered for multi-objective optimization problems. The first is combining individual objective functions into a single weighted function, where proper selection of the weights is required, and a small disturbance may sometimes lead to quite distinct solutions**.** The other approach is to determine one set of solutions that is called Pareto optimal set (Deb et al. 2002; Konak et al. 2006), which gives multiple solutions that are not dominated by other solutions in the solution space. The concept of 'dominate' can be explained as follows: in a minimization problem, a possible solution dominates another solution if all its components are smaller or equal to the components in the other solution and at

114

least one of the components is absolutely smaller. The Pareto optimal concept is considered herein because it provides a front edge for all possible solutions, and the final solution can be selected based on decision-marker's choice of tradeoff. To find multiple Pareto-optimal solutions in one single simulation run, genetic algorithms that can work with a population of solutions are required. An advanced version of nondominated sorting genetic algorithm (NSGA-II) that is capable of converging a nearly Pareto optimal set and maintaining diversity at the same time is adopted in this study (Deb et al. 2002).

Figure 4.10 presents the flowchart of NSGA-II implementation to design the protective devices for highway bridges. The genetic algorithm starts by forming an initial population of design parameters for protective devices (bearings and dampers); then a parent population of optimization objectives is generated by extracting multiple EDPs from nonlinear time history analyses. A non-dominated sorting procedure is carried out for the parent population such that those solutions with lower ranks (i.e., non-dominated solutions) are selected. Meanwhile, the distances between two nearest data points are calculated and ranked to sort out solutions that are located in less crowded areas, since more crowded solutions usually have a smaller value of distance between neighbors (Deb et al. 2002). The nondomination sorting procedure guarantees convergence to Pareto optimal solutions, while the distance ranking maintains diversity among population members. Classic genetic operators of crossover and mutation are also used to generate offspring populations such that better genes of the parent population and population diversity can be kept (Konak et al. 2006). The nonlinear time history analyses are carried out in OpenSees while the genetic optimization is realized in Matlab.
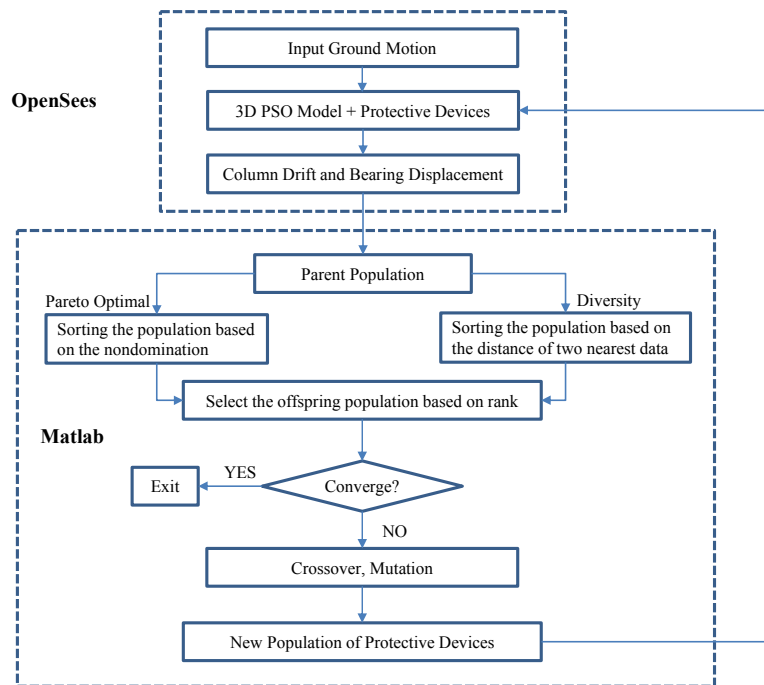
Figure 4.10.    Multi-objective genetic optimization

## 4.4.2 Optimal Design Parameters of Protective Devices

The aforementioned multi-objective genetic optimization procedure is applied to the

optimal design of protective devices for the PSO. The pushover analysis reveals that the

bilinear parameters of the pier column are $Q_c$ = 3630 kN, $K_{1,C}$ = 300 MN/m and $K_{2,C}$ = 1536

kN/m, respectively. Considering that isolation devices can be used solely or in combination

with dampers to improve seismic performance of highway bridges, two design strategies are

taken into account for the optimization procedure: one strategy of installing only isolation

bearings on bridges and the other with both isolation bearings and fluid dampers. To be simple,

protective devices at pier tops and abutment ends are assumed to possess identical mechanical

parameters for each design case. Since isolation bearings mainly differ in terms of stiffness ratios $N = K_{1,B}/K_{2,B}$, in this study $N$ is chosen to be 10, 30 and 50 to represent the ERB, LRB, and FPS, respectively. All the bearings are assumed to have a thickness of 0.15m, which is a typical value that being used in practice. Linear viscous fluid dampers are selected to avoid convergence issues given that equivalent nonlinear dampers can be transformed by linear dampers based on equaling energy dissipation per circle (Symans and Constantinou 1998). Therefore, this study considers a total of six design cases: the first three adopt three different isolation bearings, and the last three cases use a combination of isolation bearings and linear fluid dampers. For the bearing only cases, two design parameters, i.e. the post yielding stiffness $K_{2,B}$ and the characteristic strength $Q_B$, need to be optimized, while for the bearing and damper cases, damper coefficient $C_\alpha$ is the additional parameter. The bearing post yielding stiffness $K_{2,B}$ is varied from 0.01 to 0.1 times $K_{1,C}$, and the bearing characteristic strength $Q_B$ is varied from 0.1 to 1.0 times $Q_C$. The damping coefficient of the damper $C_\alpha$ is varied from 500 to 6000 kN(s/m). The EDPs of column drift ratio and bearing shear strain are chosen as two optimization objectives. The limit states at extensive damage states are used to normalize the EDPs of column drift and bearing shear strain (i.e., 2.5% for pier column drift ratio and 200% for bearing shear strain). Seven strong ground motions that were recorded in California relatively close to the fault of major earthquakes are used as the inputs. Table 4.4 lists the records of interest in historic order together with the magnitude of the earthquake and distance of the accelerograph from the causative fault. The fault normal components are selected to exert in the transverse direction.

Table 4.4.   Earthquake Records Selected for Optimization

| Record station | Earthquake | Magnitude ($M_w$) | Distance (km) | PGA (g) | PGV (m/s) |
|---|---|---|---|---|---|
| Pacoima Dam | 1971 San Fernando | 6.6 | 8.5 | 1.17 | 1.14 |
| El Centro Array No. 5 | 1979 Imperial Valley | 6.4 | 30.4 | 0.38 | 0.99 |
| El Centro Array No. 6 | 1979 Imperial Valley | 6.4 | 29.8 | 0.44 | 1.13 |
| Parachute test site | 1987 Superstition Hills | 6.6 | 7.2 | 0.45 | 1.12 |
| Los Gatos | 1989 Loma Prieta | 7.0 | 6.1 | 0.56 | 0.95 |
| Cape Mendocino | 1992 Petrolia | 7.0 | 3.8 | 1.50 | 1.25 |
| Newhall | 1994 Northridge | 6.7 | 20.2 | 0.59 | 0.96 |

Figure 4.11 to Figure 4.16 plots the optimization results as well as the selected solutions for the six design cases when subject to the above seven strong motions, respectively. As shown in each figure, multi-objective genetic optimization provides multiple Pareto optimal solutions that form a boundary line of Pareto front. The solid line of the Pareto curve is generated by connecting the Pareto optimal set and assuming a linear interpolation between two adjacent solutions. For comparison purposes, the circle points that are shown in each figure are the peak responses of column drift and bearing shear strain from the nonlinear time history analyses with randomly selected design parameters. It can be seen that all the circle points are located in the upper-right area with respect to the Pareto front, indicating that the Pareto optimal set is able to provide dominant solutions when comparing with random solutions; essentially, if a solution can be found close to the Pareto front, the design parameters correspond to this solution can be deemed as close-to-optimal parameters. On the other hand, since each point on the Pareto front comes from a distinct combination of design parameters, it is challenging to select the final design that can provide close-to-optimal responses of bearings

and piers for all seven motions. The decision maker's choice of tradeoff play a critical role in this stage, and in this study, a simple two-step procedure is carried out to seek out the final optimal design. First, one group of design parameters is selected for each ground motion such that the value of Optimization Objective 1 (i.e., the normalized bearing shear strain $\Delta U_{BI}/0.3$) is approximately 2 times the value of Optimization Objective 2 (i.e., the normalized column drift ratio $\theta_{col}/0.025$). The ratio of 2 is chosen by considering that the repair of pier columns costs much more than that of isolation bearings if both of them experience the same damage states. Second, the final design parameters are obtained by taking the average of each parameter for different motions. The square points in Figures 4.11 to 4.16 represent the peak responses of column drift and bearing shear strain from the nonlinear time history analyses with the final selected design parameters. It is clear that the square points locate very close to the Pareto front edge for all input motions, and for some cases, the square points are exactly on the Pareto front. Therefore, it can be concluded that this selection process is capable of offering close-to-optimal performances for both bearings and columns.
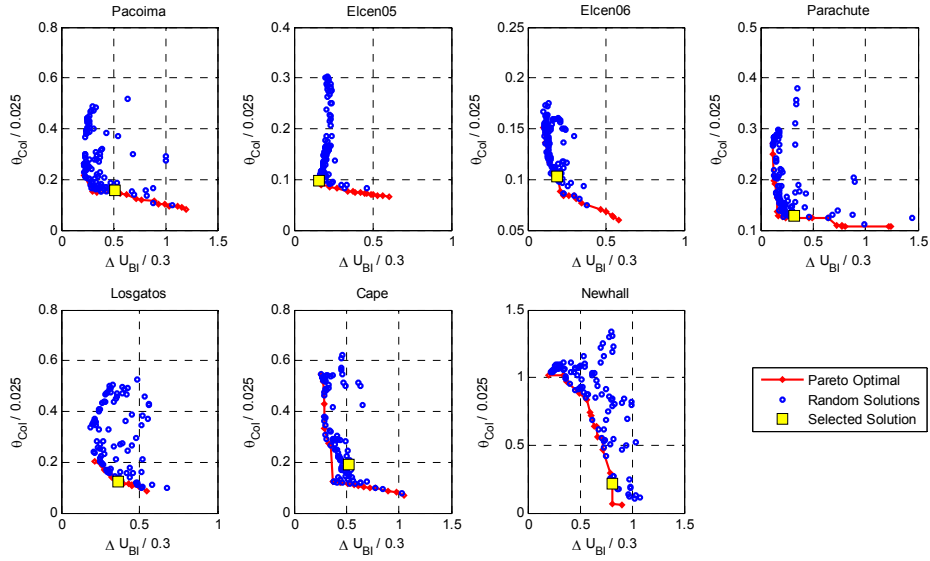
Figure 4.11.    Pareto optimal and selected solution for the PSO installed with ERB only
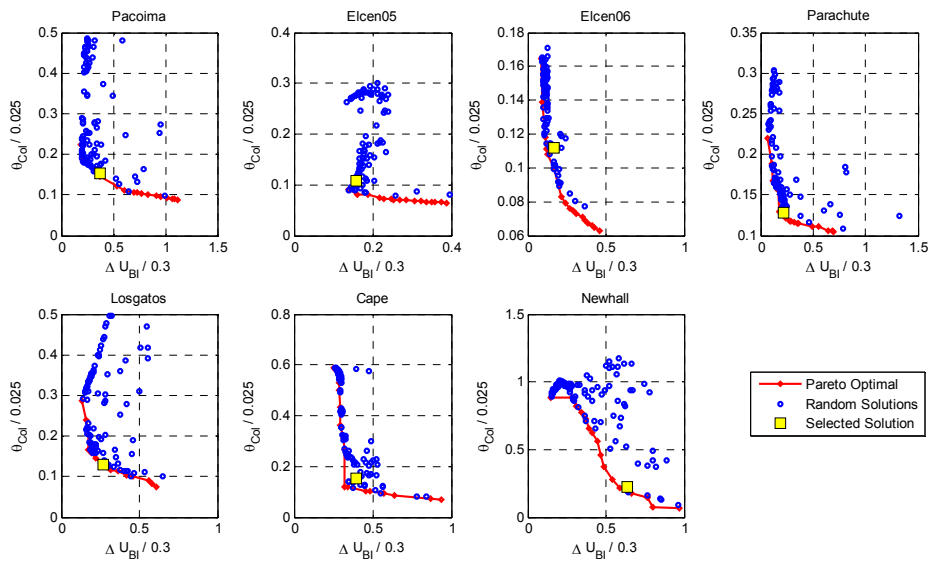


Figure 4.12.    Pareto optimal and selected solution for the PSO installed with LRB only

120
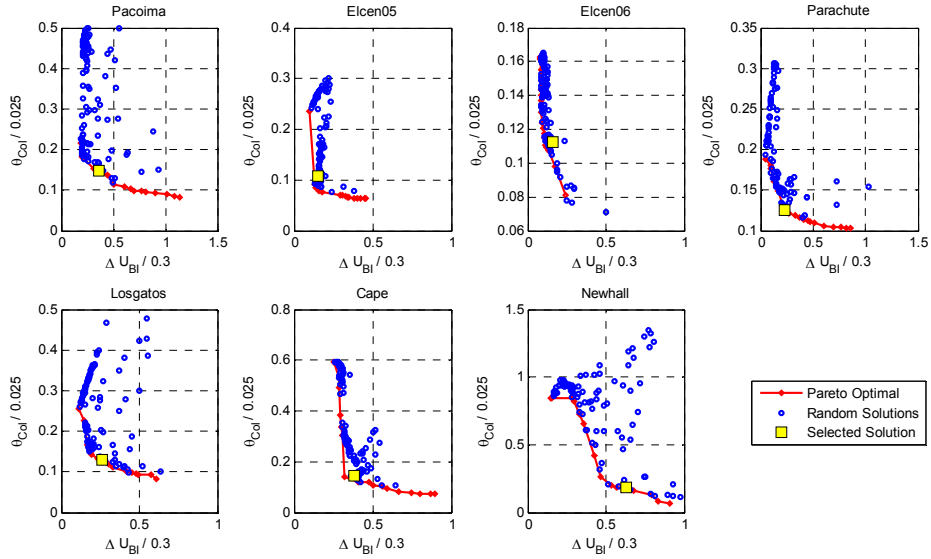
Figure 4.13.    Pareto optimal and selected solution for the PSO installed with FPS only
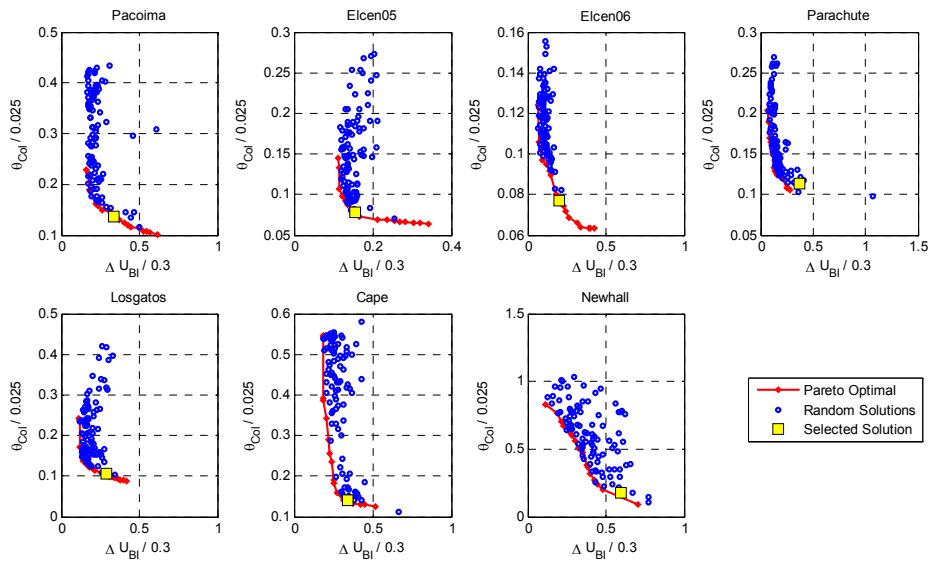


Figure 4.14.    Pareto optimal and selected solution for the PSO installed with ERB and dampers
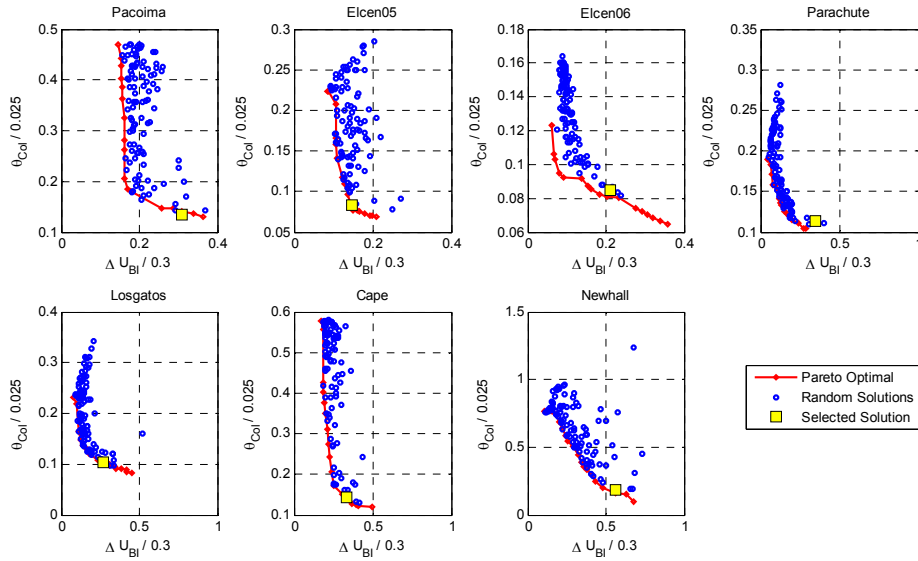
Figure 4.15. Pareto optimal and selected solution for the PSO installed with LRB and dampers
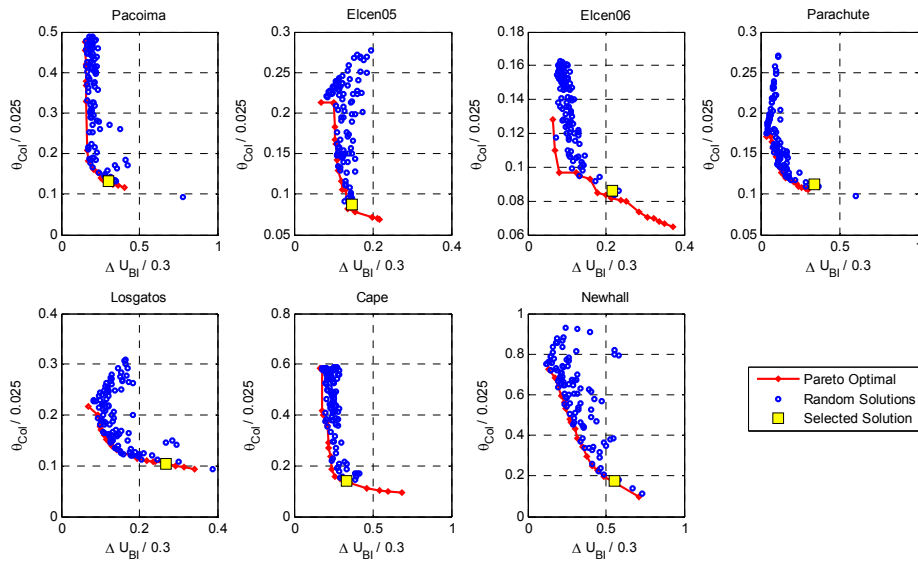


Figure 4.16. Pareto optimal and selected solution for the PSO installed with FPS and dampers

Table 4.5 lists the final optimal design parameters of protective devices for all six bridge cases. Although a slightly different combination of final design parameters is found under each case, it can be seen that for isolation only cases, the bearings with $Q_B \approx 0.35 Q_C$ would be a good

choice to isolate the PSO. If combined with fluid dampers, bearings' characteristic strength can be chosen as $Q_B \approx 0.15Q_C$. These values suggest that the optimal bearing characteristic strength $Q_B$ is not sensitive to stiffness ratio $N$. A similar conclusion can be obtained for the post-yielding stiffness $K_{2,B}$, which should be kept at approximately $0.027$-$0.032K_{1,C}$ for both isolation only cases and cases combined with fluid dampers. This essentially implies that the elastic stiffness $K_{1,B}$ plays a non-crucial role for optimal design of isolation bearings; optimized responses of bearings and columns can be achieved regardless if ERB, LRB or FPS are installed as long as they possess the same range of characteristic strength $Q$ and post-yielding stiffness $K_2$. The insignificant influences of bearing elastic stiffness on bridge's seismic performances have also been identified by previous studies (Zhang and Huo 2009; Makris and Black 2004). On the other hand, if linear fluid dampers are implemented at the same time, keeping damping coefficient $C_\alpha$ at approximately 2000 kN(s/m) is able to yield optimal performances of bearings and columns. A more meaningful interpretation of the damping coefficient value lies in calculating the additional system damping ratio provided by the fluid damper. As shown in the last column of Table 4.5, the system damping ratio can be calculated by simplifying the bridge system as a bridge deck supported by isolation bearings, such that bearing effective stiffness $K_{eff}$ (Figure 4.3) and system equivalent natural frequency $\omega_{eff}$ can be obtained when peak displacement of bearing is known. It can be seen that an additional system damping of 33%-44% can provide enough controlling mechanism for the bearing without appreciably increasing column responses.

Table 4.5.   Final Optimal Design of Protective Devices

| Bridge case | $K_{1,B}/K_{2,B}$ | $Q_B/Q_C$ | $K_{2,B}/K_{1,C}$ | $C_\alpha$ (kN s/m) | $\xi = \dfrac{C_\alpha}{2m\omega_{eff}}$ |
|---|---|---|---|---|---|
| ERB | 10 | 0.33 | 0.032 | - | - |
| LRB | 30 | 0.36 | 0.032 | - | - |
| FPS | 50 | 0.37 | 0.027 | - | - |
| ERB & fluid damper | 10 | 0.16 | 0.030 | 2020 | 33.6% - 41.5% |
| LRB & fluid damper | 30 | 0.15 | 0.031 | 2050 | 33.0% - 41.6% |
| FPS & fluid damper | 50 | 0.16 | 0.027 | 2100 | 33.2% - 43.6% |

The effectiveness of the optimally designed bearings and dampers is further evaluated

using the aforementioned performance index of repair cost ratio. Figure 4.17 presents the

comprehensive comparisons of repair cost ratios when subject to different levels of earthquake

hazards for all six optimally designed cases. The repair cost ratios of isolation only cases are

illustrated as thick lines, and thin lines are used to represent the repair cost ratios of bridge

cases that are installed with both isolation bearings and fluid dampers. For comparison purpose,

the repair cost ratios of the as-built bridge and two initial design cases are also illustrated as

thin lines with markers. As is shown from the figure, three general trends can be discovered.

First, the optimal design of protective devices can significantly reduce bridge repair cost ratios

under all levels of earthquake hazards. Second, because of the proper energy dissipation

mechanism provided by viscous fluid dampers, bridge cases that are installed with both

optimally designed isolation bearings and fluid dampers yield the best seismic performances,

which are reflected as the lowest repair cost ratios in the figure. Third, the optimal design

parameters of the isolation bearings are generally insensitive to bearing types, and thereof their

levels of effectiveness are close to one another for each design strategy. To better quantify the effectiveness of the optimal protection design, the repair cost ratios for the above-mentioned nine cases under different levels of earthquakes are given in Table 4.6, where five PGA values (i.e., 0.5g, 0.8g, 1.2g, 1.6g, and 2.0g) are selected to represent different earthquake hazard levels. As shown in the table, significant reductions of the repair cost ratios can be expected for the bridge cases that are equipped with optimally designed protective devices. For instance, when subject to extreme large earthquake events with a PGA of 2.0g, the repair cost ratio of the as-built bridge is up to 46%. While if initial designs of protective devices are used, 34% of repair cost ratio will occur for the fully isolated bridge under the same level of earthquake hazards, and 18% of the replacement cost will be needed if the bridge is installed with both isolation bearings and fluid dampers. The repair cost ratio of the fully isolated bridge with optimally designed isolation bearings can be significantly reduced to around 8%, and it will only cost approximately 5% of the total replacement cost if both the optimally designed isolation bearings and fluid dampers are installed on the bridge. The effectiveness of the optimal design procedure for protective devices is therefore verified and the proposed procedure can serve as an efficient tool to select protective devices in practice.
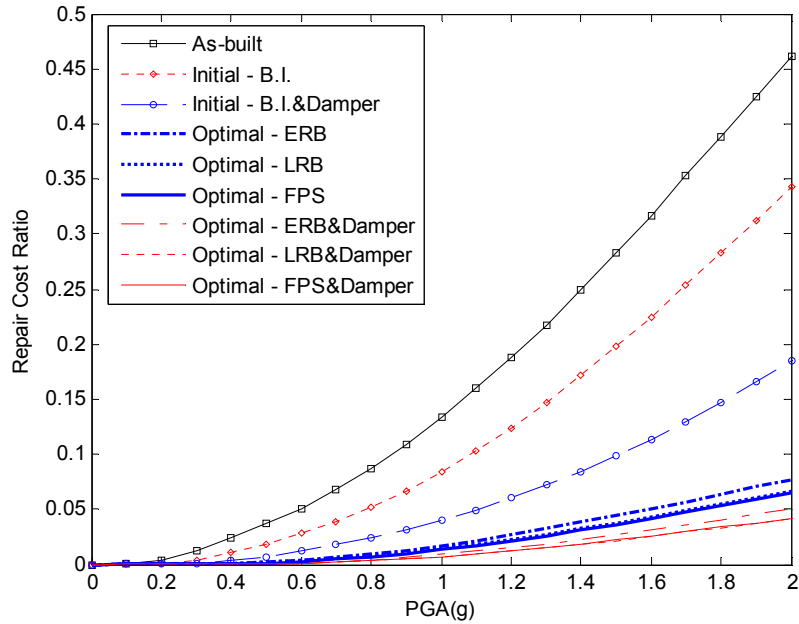
Figure 4.17.    Comparisons of repair cost ratios for various bridge cases

Table 4.6.    Repair Cost Ratios (%) of Different Bridge Cases

| Bridge case | | PGA | | | | |
|---|---|---|---|---|---|---|
| | | 0.5g | 0.8g | 1.2g | 1.6g | 2.0g |
| | As-built | 3.66 | 8.76 | 18.77 | 31.72 | 46.13 |
| Initial Designs | Base isolated | 1.86 | 5.23 | 12.40 | 22.48 | 34.32 |
| | Bearing & damper | 0.70 | 2.46 | 6.01 | 11.35 | 18.44 |
| | ERB only | 0.21 | 0.94 | 2.70 | 5.05 | 7.69 |
| | LRB only | 0.18 | 0.83 | 2.28 | 4.28 | 6.66 |
| Optimal Designs | FPS only | 0.13 | 0.72 | 2.15 | 4.13 | 6.49 |
| | ERB & fluid damper | 0.05 | 0.42 | 1.54 | 3.13 | 5.09 |
| | LRB & fluid damper | 0.03 | 0.31 | 1.22 | 2.55 | 4.16 |
| | FPS & fluid damper | 0.03 | 0.32 | 1.25 | 2.60 | 4.23 |

**4.5 CONCLUDING REMARKS**

This study investigates the effectiveness and optimal design of protective devices for the seismic protection of highway bridges. The PSO is seismically redesigned with protective devices. Component-level fragility functions are first derived by PSDA using nonlinear time history analyses that include SSI effects and ground motion uncertainties. Through derivation

126

of the repair cost ratios of highway bridges under the performance-based evaluation framework, a dependable way to evaluate the overall seismic performance of bridges is developed. Moreover, optimal design parameters of protective devices are identified through a multi-objective genetic optimization algorithm. The following conclusions can be drawn from this study:

(1) This study utilized component-level fragility functions to derive the system-level repair cost ratios of highway bridges under earthquake hazards. Based on failure probability and the importance of critical components, it effectively reflected the overall damage potential of highway bridges that are equipped with protective devices. The repair cost ratios of bridges quantify the efficiency of various protective devices. It is demonstrated that implementing protective devices can effectively reduce the repair cost ratios of highway bridges.

(2) Optimal design parameters of protective devices are identified through a multi-objective genetic optimization approach. For bridges using isolation devices only, bearings with characteristic strength $Q_B$ of approximately $0.35Q_C$ and post-yielding stiffness $K_{2,B}$ of approximately $0.027$-$0.032K_{1,C}$ are found to yield close-to-optimal responses. If fluid dampers are used in conjunction with bearings, bearings' characteristic strength $Q_B$ can be chosen as $0.15\ Q_C$, and post-yielding stiffness $K_{2,B}$ should be approximately $0.027$-$0.031K_{1,C}$. A 33-44% additional damping ratio needs to be provided by the fluid dampers to reach optimal performance.

(3) The optimal design is found to be insensitive to bearing type. With optimally designed

protective devices, significant reductions of bridge repair cost ratios can be observed. Pairing isolation bearings and fluid dampers will yield better seismic protection for highway bridges than cases using only isolation.

In summary, this chapter provides a systematic way to assess and design protective devices for the seismic protection of highway bridges. The proposed seismic performance index of repair cost ratio and the multi-objective genetic optimization algorithm can serve as efficient tools in evaluating and optimally designing the protective devices. The soundness of using the multi-objective optimization approach to determine the optimal protection design can be enhanced if it is also considered directly under the performance-based design framework. An integrated performance-based approach that starts from the hazards at the source to eventually select the design parameters using optimization is developed in Chapter 5.

# 5. PROBABILISTIC SEISMIC PROTECTION DESIGN AND OPTIMIZATION OF HIGHWAY BRIDGES

Chapter 4 addresses the evaluation and design of seismic protective devices in a separate way: the evaluation part is considered under the performance-based evaluation framework; whereas the design portion is realized by using the multi-objective generic optimization when subject to a small group of recorded motions. This chapter develops an integrated performance-based framework to readdress the design and optimization of seismic protective devices for highway bridges. The derived probabilistic methodology enables designers to avoid a highly iterative design process. In addition, it simultaneously incorporates structural nonlinearity, SSI effects, nonlinear behaviors of protective devices, and ground motion uncertainties. In this chapter, theoretical derivations to realize the proposed performance-based framework is presented in Section 5.1. A case study is carried out for the PSO in Section 5.2.

## 5.1 PERFORMANCE-BASED SEISMIC DESIGN METHODOLOGY

As expressed in Eq. (5.1), the PEER Center framework provides a mathematical formulation for performance-based seismic evaluation (PBSE) under various hazard levels by utilizing four interim variables: IM, EDP, DI and DV. Probabilistic seismic hazard analysis quantifies ground motion IMs. Structural analysis using numerical simulations or recorded responses is conducted to relate EDPs to the IMs. Damage quantifications of structural components and systems are considered to link EDPs to DIs. Finally, loss analysis is conducted to predict DVs that reflect the socio-economic impacts in terms of specific DIs:

$$\lambda(\text{DV}) = \iiint P\langle \text{DV}|\text{DI}\rangle \, dP\langle \text{DI}|\text{EDP}\rangle \, dP\langle \text{EDP}|\text{IM}\rangle \, d\lambda(\text{IM}) \qquad (5.1)$$

where $\lambda(\text{DV})$ is a desired realization of the DV, such as its mean annual frequency of exceedance, and the $P$s represent complementary cumulative distribution functions.

A flowchart to implement the PEER framework into the effectiveness evaluation of seismic protection designs is shown in the left half of Figure 5.1, where an "evaluation module" and a "common module" are utilized. As shown in the figure, for a given protection design, the evaluation framework derives component-level fragility functions to assess the damage probabilities of bridge components under various levels of earthquake hazards. It also establishes damage model or loss model to quantify the seismic vulnerability of the bridge in the system level. In this study, the performance-based seismic design (PBSD) framework is constructed by redesigning the critical steps associated with the evaluation framework: that is, as shown in the right half of Figure 5.1, the design framework is realized by substituting the "evaluation module" with the "design module". Assumptions, methods, and mathematical forms within the design framework are discussed herein.
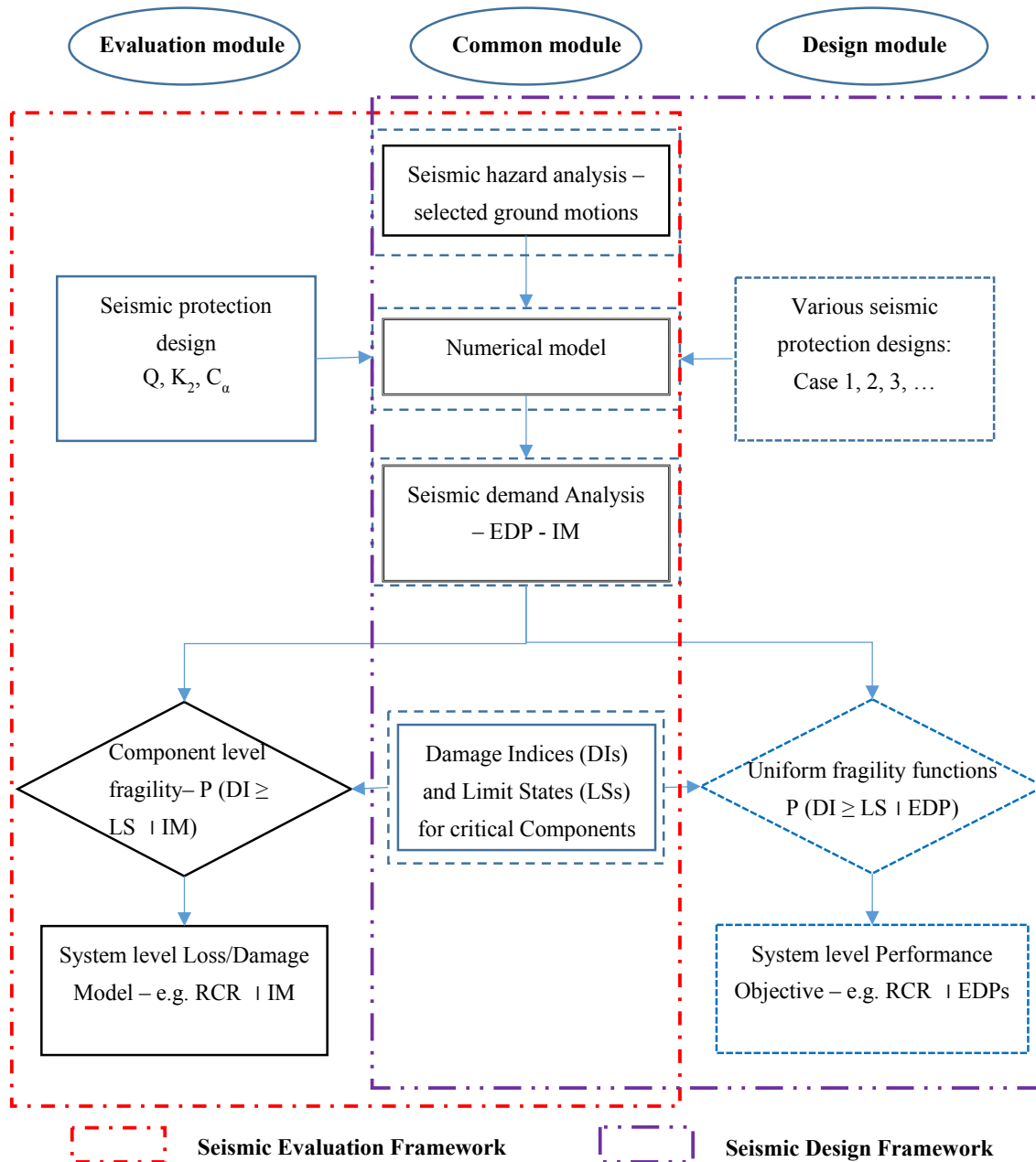
Figure 5.1. PBSE and PBSD for protective devices

## 5.1.1 Component-level Uniform Fragility Curve

As shown in the right half of Figure 5.1, the PBSD framework is constructed by substituting the "evaluation module" with the "design module", in which one distinctive step lies in that the PSDA is rather conducted for a variety of numerical systems that can cover the

general protection design scope. This can be realized by considering the design limits of protective devices for highway bridges. For instance, if bearing's two dominating parameters, $Q$, the characteristic strength and $K_2$, the post-yielding stiffness are deemed to vary in the ranges of $0.1Q_C \leq Q \leq Q_C$, and $0.01K_{1,C} \leq K_2 \leq 0.1K_{1,C}$, where $Q_C$ and $K_{1,C}$ are the characteristic strength and elastic stiffness of the pier column, respectively, at least two designs (i.e., the one with $Q$ close to $Q_C$, $K_2$ close to $0.1 K_{1,C}$, and the other with $Q$ close to $0.1Q_C$, $K_2$ close to $0.01 K_{1,C}$) need to be considered. The first design gives the weakest isolation effect while the second provides the strongest isolation.

For each protection design selected, the component-level fragility functions can be derived by using three methods, namely the incremental dynamic analysis (IDA) (Vamvatsikos and Cornell 2002), the 'cloud' approach, and the 'stripe' approach (Baker and Cornell 2006). The IDA is conducted by repeatedly scaling a suite of ground motions to find the IM level at which each ground motion reaches the given damage state. The IDA is computational expensive because it requires extensive structural analyses to be performed with increasing IM levels in order to reach each damage state, especially for the complete damage (collapse) state. The 'cloud' approach uses three rigorous assumptions to correlate the EDPs with the ground motion IMs: logarithmic linear assumption between median EDP and IM, constant variance assumption for all IM ranges, and log-normal distribution of EDP at a given IM level (Cornell et al. 2002). This method requires the least computation efforts, but may induce considerable errors since the assumptions may not hold over the entire IM range. The 'stripe' approach (also known as the multiple stripes analysis approach) requires scaling

a group of ground motions to a discrete set of IM levels, at each of which same or different

motions can be used. Because it does not require the numerical analyses to be performed up

to IM amplitudes where all ground motions reach the given damage states, the 'stripe'

approach is less computational demanding when compared with the IDA. In addition, since

no a priori assumption is made for the 'stripe' approach, it is much more persuasive to reflect

the true damaging potential of bridge components than the 'cloud' approach. Therefore, the

'stripe' approach is utilized herein to compose the component-level fragility functions for a

given protection design. At every predefined IM level, nonlinear time history analyses are

conducted, and the occurrence ratio of a specified damage state is computed as the damage

probability at the given IM level:

$$P(EDP \geq LS_i | IM) = \frac{n_i}{N} \tag{5.2}$$

where $LS_i$ is the limit state (LS) value corresponding the $i$th damage state, $n_i$ is the number of

damaged cases for $i$th damage state, and $N$ is the total number of simulation cases at each IM

level.

Figure 5.2(a) illustrates the multiple stripes analysis results for two protection designs at

IM (PGA) levels of 0.6g and 0.8g, respectively. Distributions of EDPs at each IM level can

be characterized by a median value, and a variance content. As given in Eq. (5.2), by

counting the number of EDPs that exceed each damage state and normalize it with the total

number of simulation cases, the component-level fragility functions can be easily constructed

with respect to IMs. It is noted that different protection designs will inevitably generate distinct fragility curves (as shown in Figure 5.2(b)), which will sharply impede the realization of PBSD for protective devices, because PSDA has to be carried out every time when a new protection design is proposed. However, by assuming that the variance of EDP distribution is mainly contingent on the corresponding median value for different protection designs, the component-level fragility functions can be conditioned on $\theta$ instead by substituting each IM shown in Figure 5.2(b) with its matching $\theta$ value. One notable advantage of conditioning the fragility function on the median EDP lies in that uniform curve-like data points can be generated for various protection design scenarios. The data in Figure 5.2(c) presents the uniform fragility function that conditioned on $\theta$ for the two distinct protection designs.
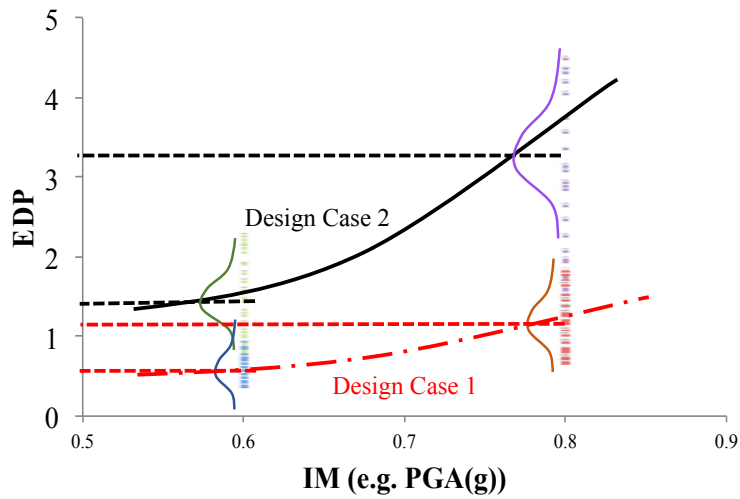


(a) Multiple stripes analysis
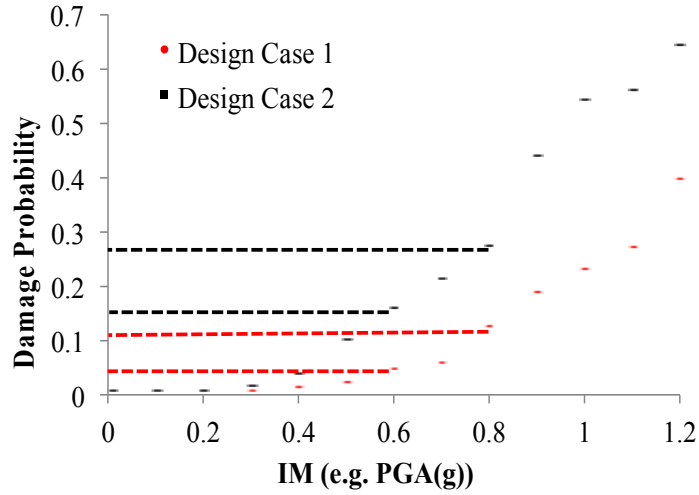
(b) Component fragility function conditioned on IM
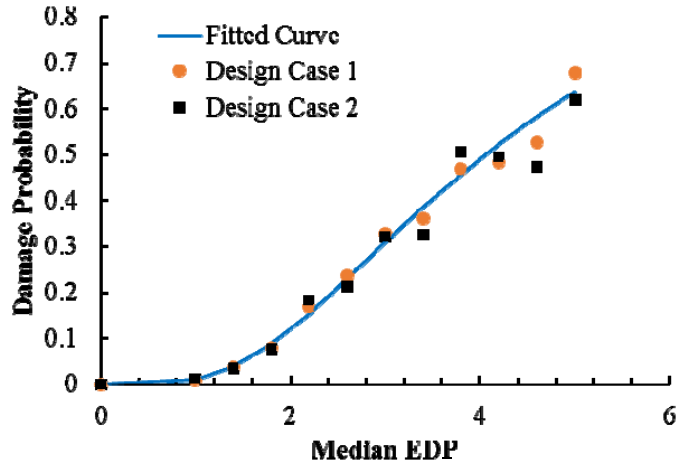


(c) Component fragility function conditioned on median EDP

Figure 5.2.  Component level fragility analysis framework

Moreover, by assuming lognormal EDP distributions and constant variance for all groups of data, the uniform fragility function can be further regressed as a continuous curve by using the maximum likelihood fitting technique (Baker 2015). For the multiple stripes analysis, the damage probability of observing $n_{j,i}$ damaged in the $i$th damage state out of $N$ ground motions with $\theta = \theta_j$ can be calculated by the binomial distribution:

$$PT_{j,i} = \binom{N}{n_{j,i}} P_{j,i}^{n_{j,i}} (1 - P_{j,i})^{N - n_{j,i}} \tag{5.3}$$

where $P_{j,i}$ is the probability that a ground motion will cause the $i$th damage state of the bridge

component. Because of the above-mentioned assumption, $P_{j,i}$ can be further written as:

$$P_{j,i} = 1 - \Phi \left[ \frac{\ln(LS_i) - \ln(\theta_j)}{\xi_i} \right] \tag{5.4}$$

Eqs. 5.3 and 5.4 form a general nonlinear optimization problem to identify the standard

deviation of $\xi_i$ for the $i$th damage state, such that the observed $n_{j,i}$ damage cases have its

highest probability, which can be measured using the concept of maximum likelihood. For

the analysis data that are obtained at multiple $\theta$ levels with different protection designs, the

likelihood of the binomial probabilities can be calculated by substituting $P_{j,i}$ into Eq. (5.3)

and taking the product for the entire data set:

$$\text{Likelihood}_i = \prod_{j=1}^{m \times l} \binom{N}{n_{j,i}} \left\{ 1 - \Phi \left[ \frac{\ln(LS_i) - \ln(\theta_j)}{\xi_i} \right] \right\}^{n_{j,i}} \Phi \left[ \frac{\ln(LS_i) - \ln(\theta_j)}{\xi_i} \right]^{N - n_{j,i}} \tag{5.5}$$

where $m$ is the number of stripes for the multiple stripes analysis, and $l$ is the number of

protection designs. Estimates of the parameter $\xi_i$ can be obtained by maximize the likelihood

function of Eq. (5.5), or equivalently maximize the logarithm of the likelihood function (Eq.

(5.6)). The solid line in Figure 5.2(c) illustrates the continuous fragility curve obtained by

using a standard nonlinear optimization procedure to identify the best estimates of $\xi_i$ in Eq. (5.6).

$$\hat{\xi}_i = \arg\max_{\xi_i} \sum_{j=1}^{m \times l} \left\langle \ln\binom{N}{n_{j,i}} + n_{j,i} \ln\left\{ 1 - \Phi\left[ \frac{\ln(LS_i) - \ln(\theta_j)}{\xi_i} \right] \right\} + (N - n_{j,i}) \ln \Phi\left[ \frac{\ln(LS_i) - \ln(\theta_j)}{\xi_i} \right] \right\rangle \quad (5.6)$$

### 5.1.2 System-level Performance Index - RCR

The derived uniform fragility curve in Figure 5.2(c) can be easily implemented into the calculation of the repair cost ratio (RCR) using the method proposed in Chapter 4, such that the seismic vulnerability of the bridge can be quantified in the system level. It is noted that the RCR turns out to be a function of multiple median EDPs, which can directly serve as the performance index for the PBSD of protective devices.

### 5.1.3 Performance-based Seismic Protection Design and Optimization

The derived system-level performance index of RCR can be easily incorporated in the PBSD framework for the design of protective devices. As shown in Figure 5.3(a), RCR can be deemed as a performance index to select protective devices when subject to specific earthquake hazards. For instance, designers can specify that under the hazard level with 10% in 50 years of return periods, the RCR of the bridge needs to be controlled within 5%. The design task becomes a trial and error process to identify the protective devices that can yield a 5% or lower RCR.
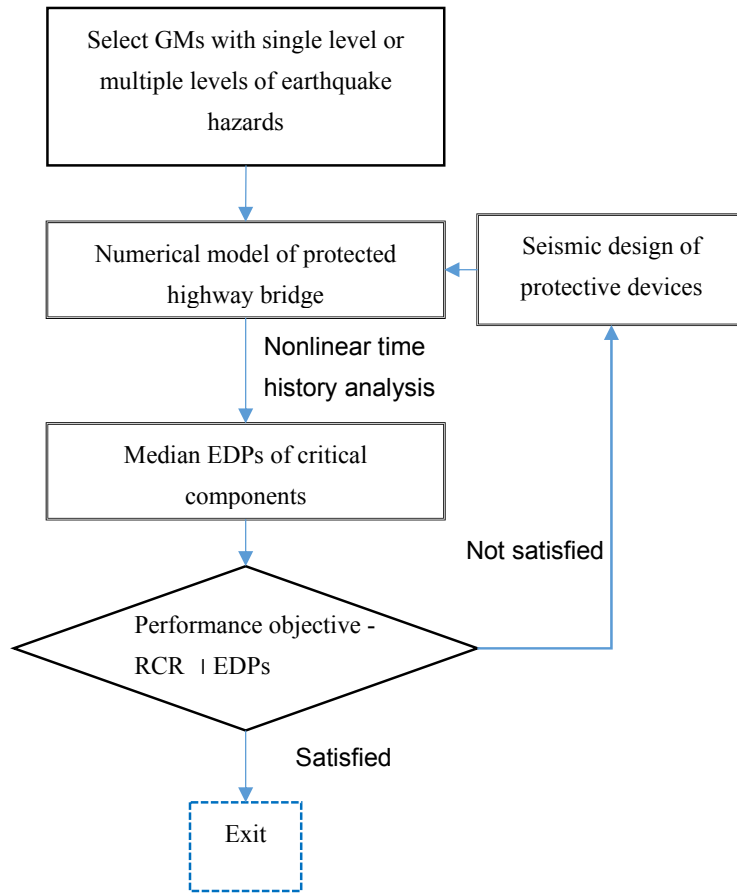
(a) Design framework
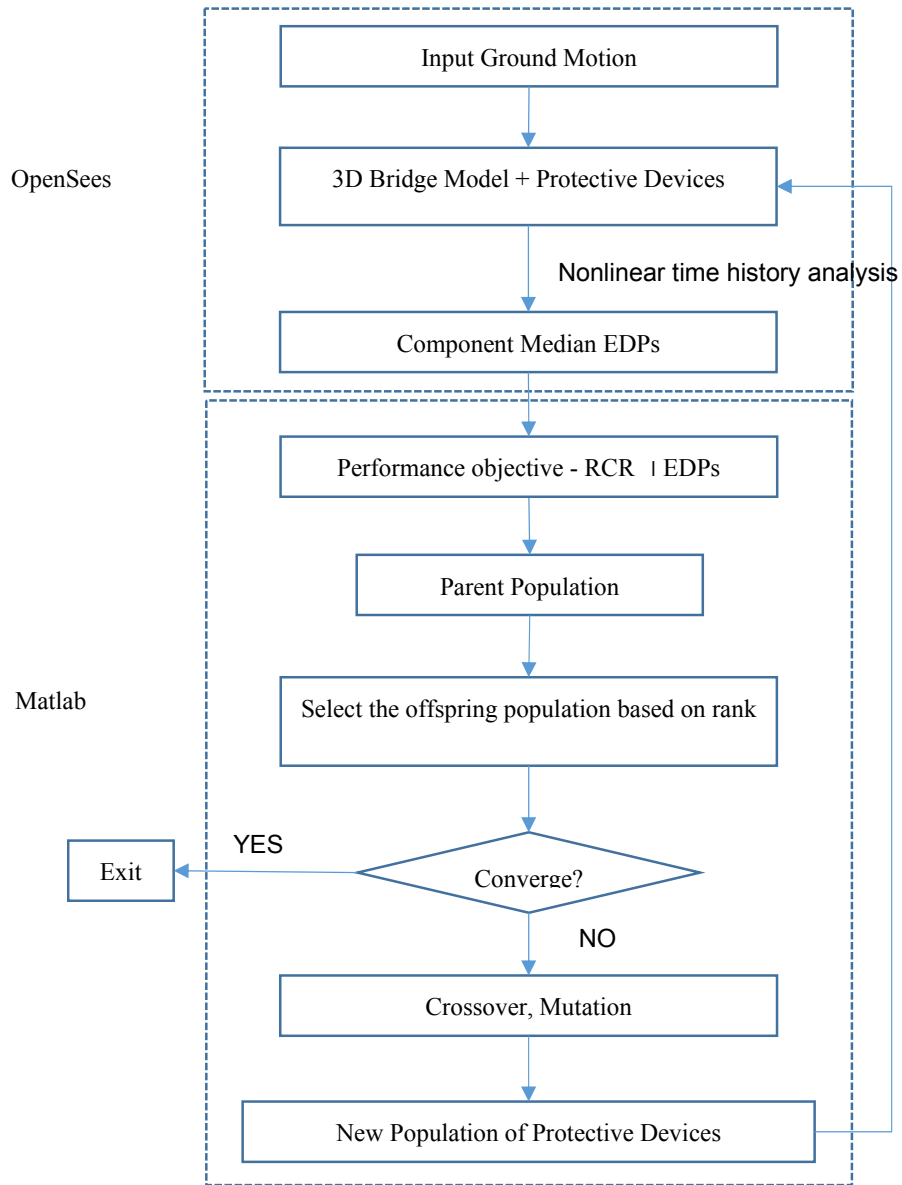
(b) Optimization framework

Figure 5.3. Performance-based seismic design and optimization framework for protective devices

A more practically attractive endeavor lies in finding the optimal design parameters of protective devices so that bridges' RCR can be minimized. A genetic optimization framework is proposed in this chapter for this purpose. The genetic algorithm is characterized by establishing a stochastic evolutionary process to yield a superior final solution. Applications of genetic algorithm in structure engineering have gained significant development since the early 1990s (Adeli and Cheng 1994; Jiang and Adeli 2008; Kim and Roschke 2006; Cha et al. 2012; among others). As shown in Figure 5.3(b), a hybrid framework is constructed where nonlinear time history analyses are conducted in the software platform of OpenSees (Mazzoni et al. 2006), and the genetic optimization is accomplished in Matlab. The former provides multiple median EDPs of interest, and the latter calculates the associated RCR and generates the offspring population with better designs until converging to the final optimal design.

## 5.2 NUMERICAL EXAMPLE – THE PSO

The soundness of utilizing the proposed PBSD methodology to identify the optimal protective devices is examined in this section. The PSO that has been considered in Chapter 4 is once again adopted herein to form a case study. Details to comprise the component-level fragility functions, such as the numerical modeling scheme, the ground motion selection, and the DI measures of pier columns and isolation bearings, are in general consistent with those defined in Chapter 4. However, following changes have been made intentionally in this chapter to distinguish the methodology considered herein: (1) the selected 140 ground motions are scaled to 14 peak ground acceleration (PGA) levels to conduct the multiple stripes analysis (i.e., 12 levels that range from 0.1g to 1.2g with 0.1g interval, and two strong

levels with PGA equals 1.6g and 2.0g, respectively); (2) the complete damage of isolation bearing happens when its shear strain is larger than 250% per the study of Zhang and Huo (2009); (3) the bearing thickness is selected as 0.1m instead of 0.15m considered in Chapter 4. The second and third changes made in this chapter expect higher levels of bearing damage should their displacements are the same as those considered in Chapter 4; hence, their displacements need to be further reduced.

### 5.2.1 Uniform Fragility Functions of PSO

In this chapter, the design range of isolation bearings is considered to be $0.1Q_C$-$0.9Q_C$ for the characteristic strength $Q$, and $0.01K_{2,C}$-$0.09K_{2,C}$ for the post-yielding stiffness $K_2$, where $Q_C$ and $K_{2,C}$ are the characteristic strength and the post-yielding stiffness of the pier columns, respectively. Therefore, the multiple stripes analysis is conducted on the PSO with three isolation designs that can cover its general range of design parameters, namely Case 1 with weak isolation effect of $Q/Q_C = 0.9$, $K_2/K_{2,C} = 0.09$, Case 2 with medium isolation effect of $Q/Q_C = 0.3$, $K_2/K_{2,C} = 0.05$, and Case 3 with strong isolation effect of $Q/Q_C = 0.1$, $K_2/K_{2,C} = 0.01$. As discussed in Chapter 4, because the elastic stiffness of bearings has minor influence on bridge's seismic performance (Makris and Black 2004, Zhang and Huo 2009, Xie and Zhang 2016), the stiffness ratio $N_K = K_1/K_2$ is kept as 20 for all these three cases.

Figure 5.4 illustrates the data results of the multiple stripes analysis for the above-mentioned three bearing design cases. As shown in the figure, a general trend of positive correlation between IM and EDPs can be observed; i.e. when the PGA increases, bearings and columns will have more cases to experience larger damage states. In addition,

different design cases will inevitably shift the damaging potential of isolation bearings and pier columns. For instance, compared with the design Case 1, Case 3 will cause more damages for isolation bearings; whereas it will reduce the damage probability of pier columns in the meantime.
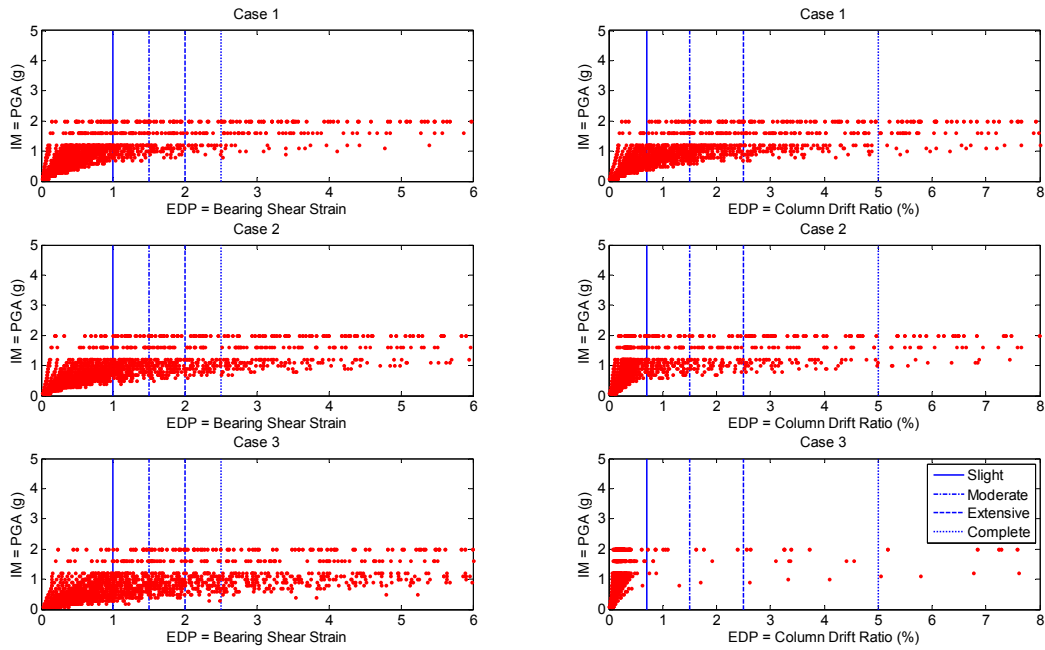


Figure 5.4. Multiple stripes analysis for three bearing design cases

Figures 5.5 and 5.6 presents the component-level fragility functions from the multiple stripes analysis results for isolation bearings and pier columns, respectively. As can be seen from both figures, the bearing designs have substantial influences on the damaging potentials of isolation bearings and pier columns under each level of earthquake hazard for all damage states. Because bearings' isolation effect will redistribute the responses of bearings and pier columns (e.g., a strong isolation may significantly reduce the response of the column, but will

substantially increase the bearing displacement), under the same level of earthquake hazard, a different protection design will yield divergent responses of isolation bearings and pier columns. The differences are captured by distinct fragility functions in both Figures 5.5 and 5.6.
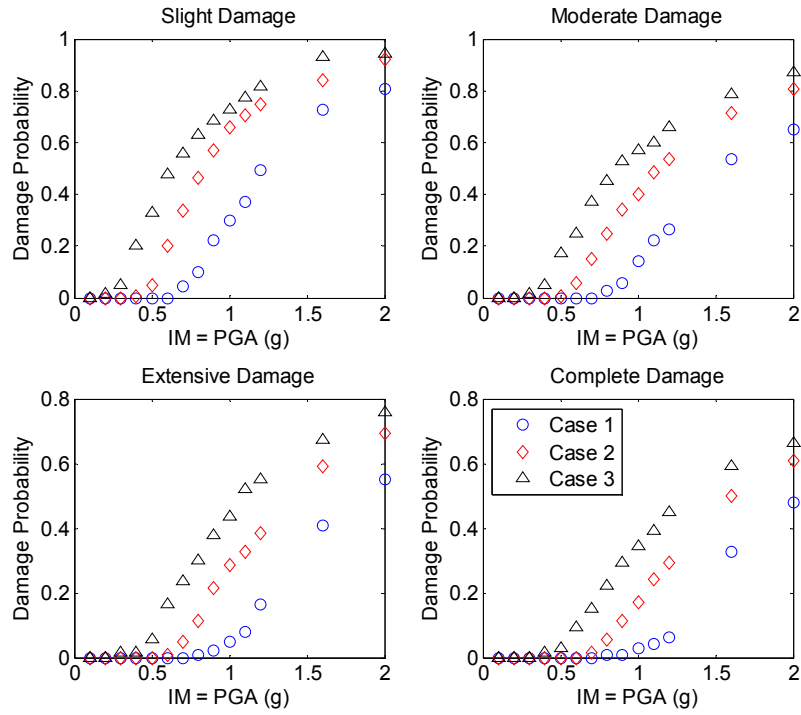


Figure 5.5.  Damage probabilities of isolation bearings conditioned on IMs
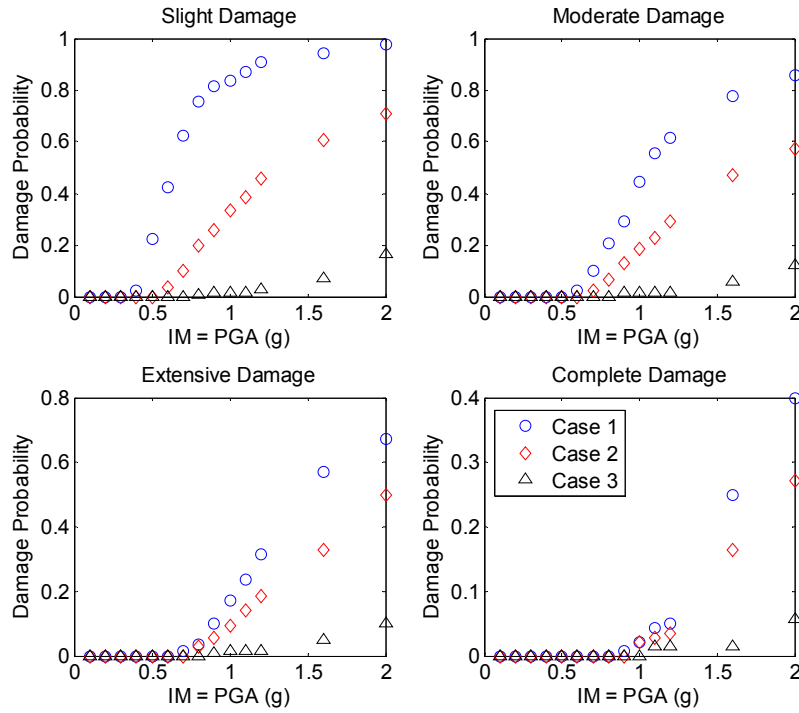
Figure 5.6. Damage probabilities of pier columns conditioned on IMs

As previously discussed, if ground motion IMs are substituted with median EDPs (i.e.,

the median bearing shear strain, and the median column drift ratio in this study), the damage

probabilities of pier columns and isolation bearings will be insensitive to protection designs.

As can be seen from the data in Figures 5.7 and 5.8, the three design cases form similar

trends in terms of fragility functions of pier columns and isolation bearings when they are

conditioned on median EDPs. The insensitivity of fragility functions essentially attributes to

the fact that when a large number of ground motions is considered to greatly reflect their

uncertainty and randomness, the respective probability distribution functions of component

EDPs will yield similar variance and skewness; and this feature will hold across different

seismic protection designs. On the other hand, the earthquake hazard intensity mainly affects

the median values of the EDPs. Furthermore, if assuming a lognormal distribution of EDPs and a constant standard deviation for all the IM range, the discrete damage probabilities can be regressed as continuous curves using Eq. (5.6), indicating by the solid curves in Figures 5.7 and 5.8.
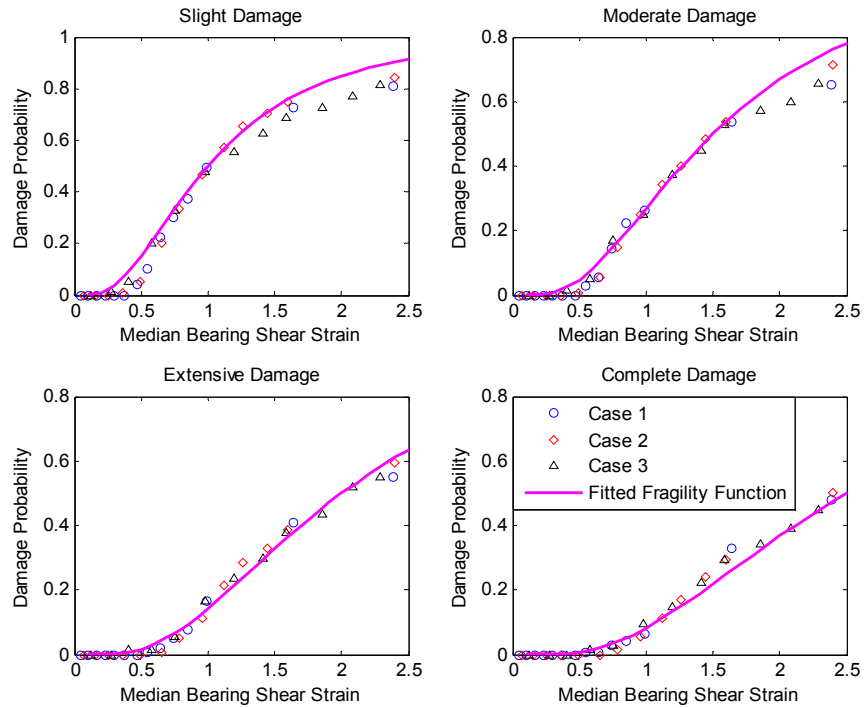


Figure 5.7. Damage probabilities of isolation bearings conditioned on median EDPs
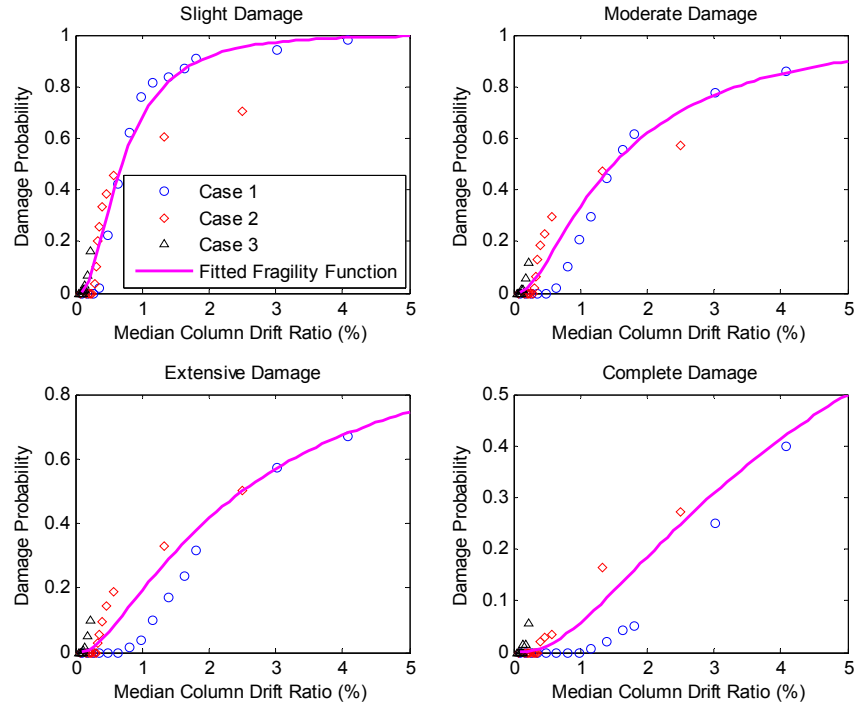
Figure 5.8. Damage probabilities of pier columns conditioned on median EDPs

## 5.2.2 RCR of PSO

The system-level RCR can be calculated using Eqs. (4.7) and (4.8) if the damage ratios and replacement costs of pier columns and isolation bearings are determined. In this chapter, the damage ratios of pier columns and isolation bearings are considered the same as those listed in Table 4.2. However, instead of being assigned as a fixed value, the replacement cost of isolation bearings is deemed to vary in the range of 15%-25% of the bridge's total cost herein. Two sets of replacement cost ratios are considered for pier columns and isolation bearings, namely Set A of $c_{stru}$: $c_{iso}$ = 0.85:0.15 and Set B of $c_{stru}$: $c_{iso}$ = 0.75:0.25, where $c_{stru}$ and $c_{iso}$ are the replacement costs that induced by the collapse of pier columns and isolation bearings, respectively. It is noted that in Eq. (4.8), the denominator has one additional term of $c_{damp}$, which is the cost of fluid dampers for the cases where both bearings and dampers are

installed. It is suggested that $c_{damp}$ is about 5% of the summation of $c_{stru}$ and $c_{iso}$ in this chapter.

Figures 5.9 and 5.10 present the calculated RCR for Set A and B cases, respectively. As can be seen from Figures 5.9(a) and 5.10(a), the performance index RCR form a monotonically increasing surface that ranges from 0 to about 60% when the median EDPs reach their corresponding complete damage values. To facilitate the design practice, Figures 5.9(b) and 5.10(b) provide the design contours of the RCR with respect to the median bearing shear strain $\gamma_{BS}$ and the median column drift ratio $\delta_{CD}$. By comparing these two figures, it can be observed that the replacement costs of bearings and columns have substantial influences on the performance index of RCR. For instance, the design contour of RCR with $c_{stru}$: $c_{iso}$ = 0.85:0.15 (Figure 5.9(b)) features smaller slopes in the horizontal direction, along which the bearing shear strain is changing, which reflects that RCR would remain less sensitive to bearing's response if its replacement costs were low.

In view that the essential components for composing the performance index of RCR lies in calculating the damage probabilities of bearings and columns, whose responses are assumed to yield lognormal distributions, this study suggests that the RCR can be regressed as a closed-form formula by using the following equation:

$$RCR_{est} = a\left\{1-\Phi\left[\frac{\ln(b)-\ln(\theta_{BS})}{c}\right]\right\}+d\left\{1-\Phi\left[\frac{\ln(e)-\ln(\theta_{CD})}{f}\right]\right\} \tag{5.11}$$

where $a, b, c, d, e, f$ are the coefficients that can be determined by minimizing the summation

147

of squared error between the regressed formula and the numerical data:

$$\{a,b,c,d,e,f\} = \arg\min \sum \left( \frac{RCR_{est} - RCR}{RCR} \right)^2 \tag{5.12}$$

A simple nonlinear optimization procedure is carried out to obtain the coefficients defined

in Eq. (5.12), which render that the closed-form expressions of RCR estimates can be written

as:

$$RCR_{est,A} = 0.16 \left\{ 1 - \Phi \left[ \frac{\ln(2.23) - \ln(\theta_{BS})}{0.72} \right] \right\} + 0.78 \left\{ 1 - \Phi \left[ \frac{\ln(3.58) - \ln(\theta_{CD})}{1.10} \right] \right\} \tag{5.13}$$

$$RCR_{est,B} = 0.26 \left\{ 1 - \Phi \left[ \frac{\ln(2.23) - \ln(\theta_{BS})}{0.72} \right] \right\} + 0.68 \left\{ 1 - \Phi \left[ \frac{\ln(3.58) - \ln(\theta_{CD})}{1.10} \right] \right\} \tag{5.14}$$

where $RCR_{est,A}$ and $RCR_{est,B}$ are the RCR estimates with Set A and B replacement cost ratios,

respectively. Figures 5.9(c) and 5.10(c) show the fitting surfaces of RCR that calculated from

Eqs. (5.13) and (5.14), respectively. It is evident that the fitting surfaces capture both the

trends and the values of the numerical data shown in Figures 5.9(a) and 5.10(a). The errors

associated with the fitting surfaces are presented in Figures 5.9(d) and 5.10(d), where it can

be found that for most EDP ranges, the RCR estimates yield errors less than 2%; and only

near the origin, the errors will reach up to about 5%. Moreover, it is concluded by comparing

Eq. (5.13) to Eq. (5.14) that for the selected two sets of replacement cost ratios, the numerically regressed RCR formulae feature the same surface shape, which are reflected by the same 'median' and 'variance' coefficients that are embedded in the lognormal distribution functions. The only differences are the multipliers in front of these two lognormal functions, denoting that RCR will be re-distributed between bearings and columns should their replacement costs are different.
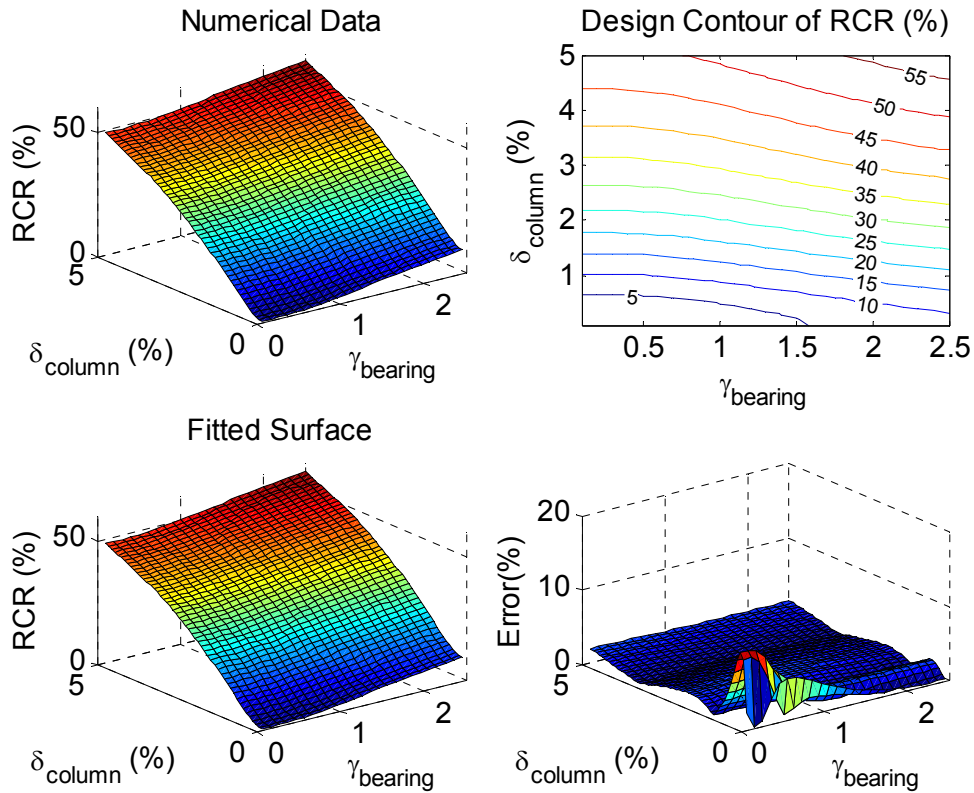


Figure 5.9. Performance index of RCR with $c_{stru}$: $c_{iso} = 0.85{:}0.15$
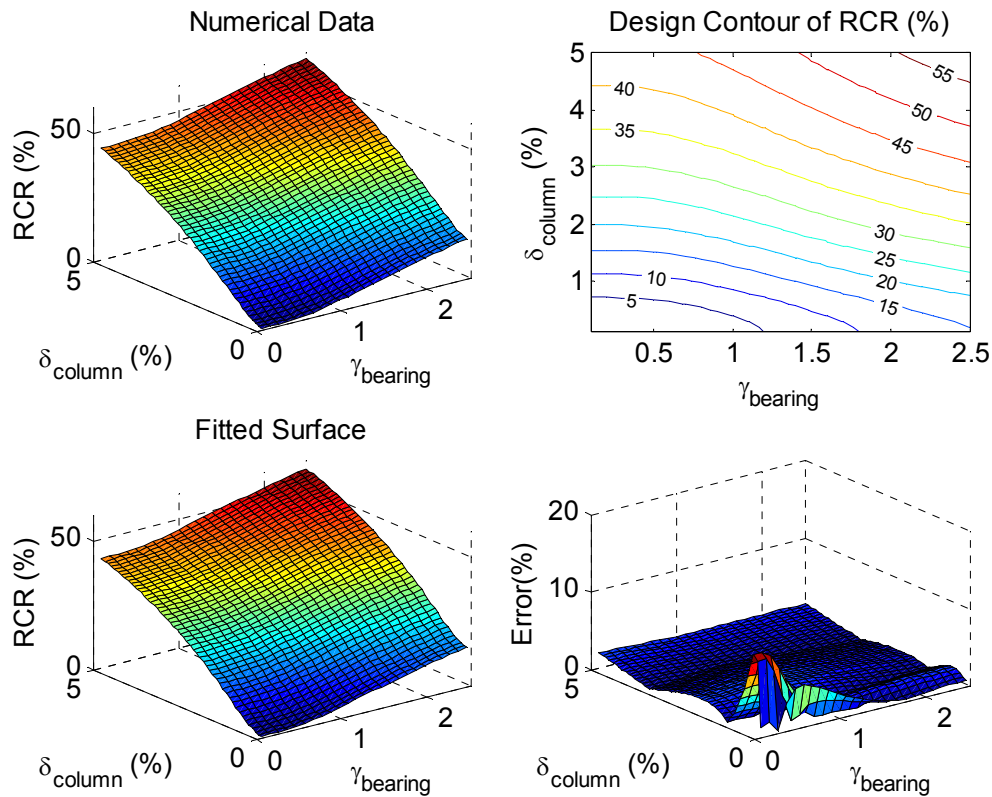
Figure 5.10.    Performance index of RCR with $c_{stru}$: $c_{iso} = 0.75{:}0.25$

## 5.2.3 Optimal Protection Designs of PSO

The derived RCR is utilized in this section to identify the optimal protection designs for the PSO using the framework illustrated in Figure 5.3(b). The Set B case of $c_{stru}$: $c_{iso} = 0.75{:}0.25$ is considered herein. The seven strong ground motions that have been listed in Table 4.4 are adopted as the ground motion inputs. Site-specific hazard levels are considered for the PSO using the ground motion interpolator developed by California Geological Survey (CGS) (http://www.quake.ca.gov/gmaps/PSHA/psha_interpolator.html). It is found that for the PSO site, the hazard levels with 10% in 50 years and 2% in 50 years of return periods have PGAs of 0.51g and 0.95g, respectively. Hence, the PGAs of the aforementioned seven

ground motions are scaled to four different hazard levels, i.e. from 0.4g to 1.0g with an interval of 0.2g. At each PGA level, the optimization process is conducted to yield one optimal protection design based on the median bearing shear strain and median column drift calculated from the seven ground motions.

Given that isolation bearings can be used solely or in combination with dampers to improve seismic performance of highway bridges, two design strategies are taken into account for the optimization procedure, i.e. the one only installs isolation bearings and the other with both isolation bearings and fluid dampers equipped. Protective devices are installed atop pier columns and end abutments, and are assumed to possess identical mechanical parameters at each location for each design strategy. For isolation bearings, stiffness ratio is assumed to be $N_K = 20$, and bearing thickness is 0.1m. As discussed in Chapter 4, linear viscous fluid dampers are selected for the case when dampers are installed. Using the bilinear model, bearings' two key design parameters are the post-yielding stiffness $K_2$ and the characteristic strength $Q$, whereas damping coefficient $C_\alpha$ is the critical design parameter for dampers. The bearing post-yielding stiffness $K_2$ is varied as $0.01\text{-}0.09K_{1,C}$, and bearing characteristic strength $Q$ is varied as $0.1\text{-}0.9Q_C$. The damping coefficient $C_\alpha$ is varied from 500 to 6000 kN(s/m).

The genetic optimization process is illustrated in Figure 5.11 for the two aforementioned design strategies under each hazard level. In each figure, both the best and mean fitness values are given at each generation. For instance, it can be seen from Figure 5.11(d) that at PGA level of 1.0g, the genetic optimization for the isolation only case starts at a RCR of 40%

and converges to the minimum RCR of 22% after 26 generations. An approximately 50% reduction can be expected by utilizing the proposed optimization framework. While for the case where fluid dampers are installed, Figure 5.11(d) shows that the genetic optimization is capable of reducing the RCR from 27% to 20%.
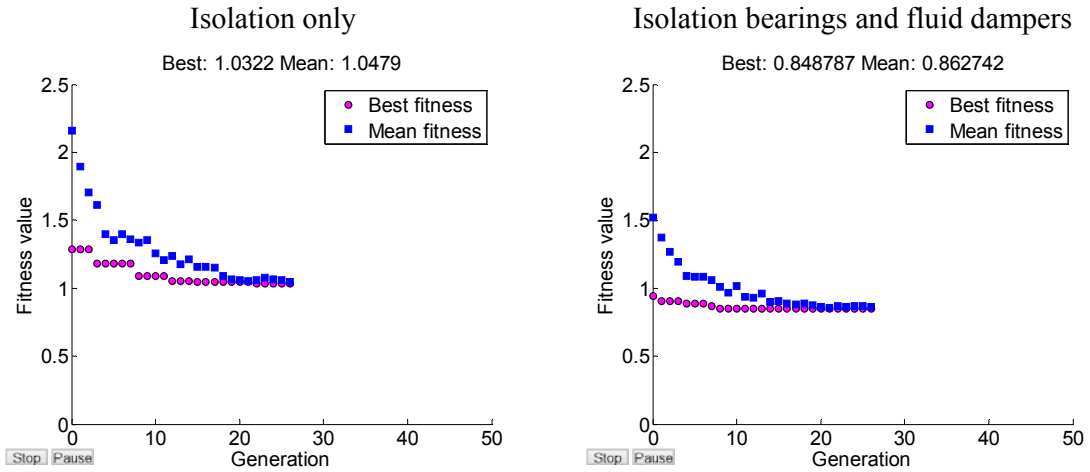


(a) PGA at 0.4g
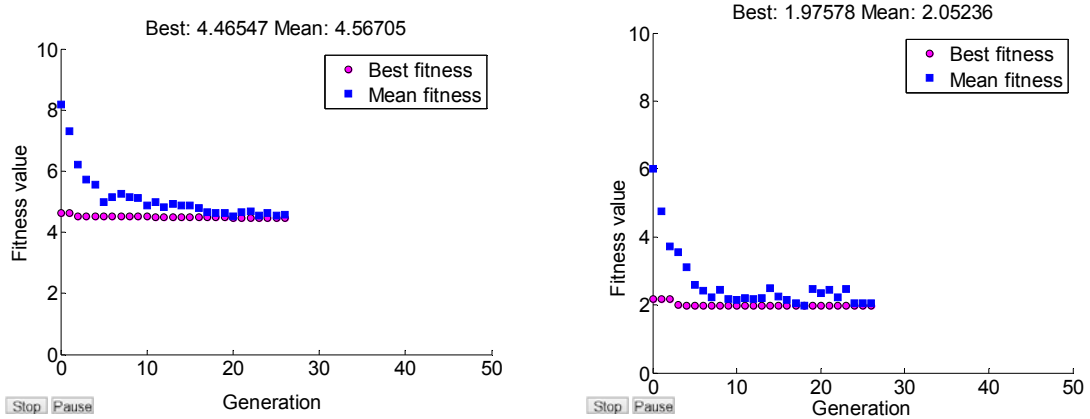


(b) PGA at 0.6g
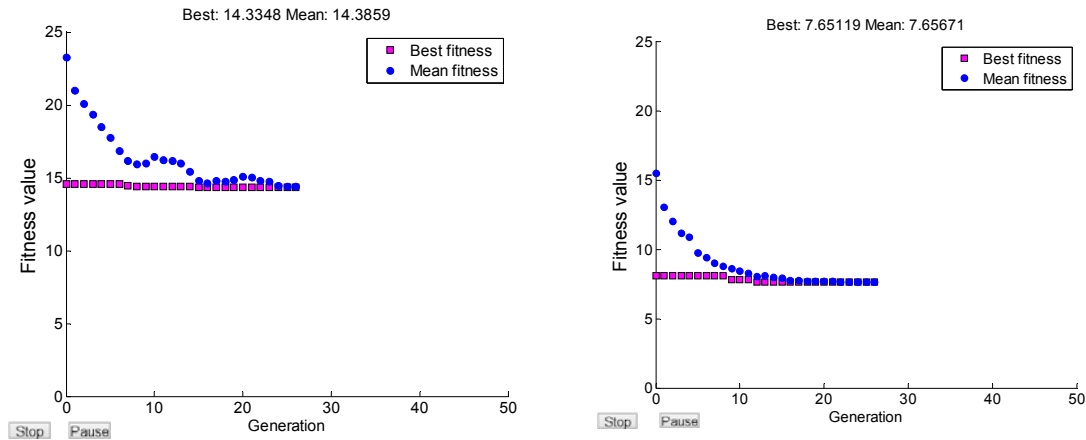
(c) PGA at 0.8g
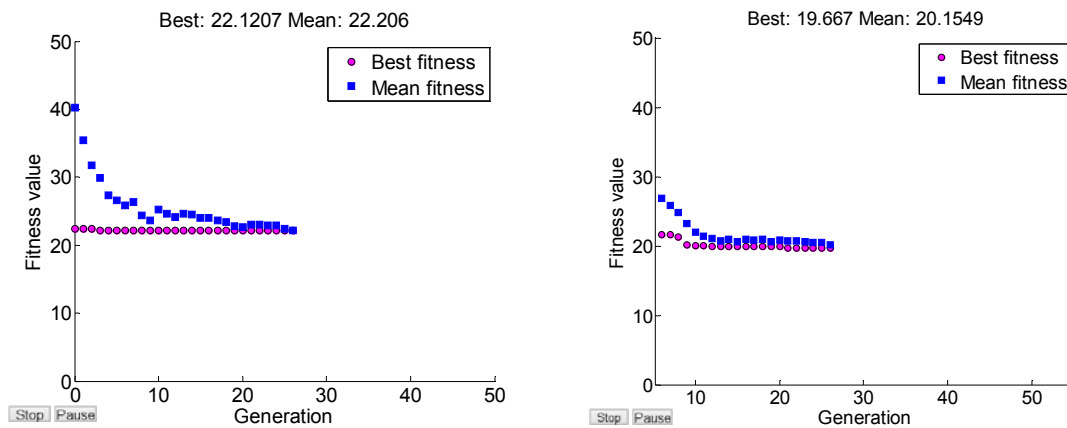


(d) PGA at 1.0g

Figure 5.11.    Genetic optimization for the PSO at PGA levels of 0.4g, 0.6g, 0.8g and 1.0g

With one optimal design obtained for each hazard level, there exist four groups of design parameters in total. To account design variance associated with different hazard levels, the mean value of each design parameter is taken to generate the suggested protection design at each hazard level. Table 5.1 lists the optimal protection designs for the PSO under hazard levels of 0.4g, 0.6g, 0.8g and 1.0g. Although different combination of final design parameters have been found under each hazard level, it can be seen that for isolation only cases, the bearings with $Q \approx 0.41Q_C$ would be a good choice to isolate the PSO. If combined with fluid dampers, bearings' characteristic strength can be chosen as $Q \approx 0.19Q_C$. A similar conclusion

can be obtained for the post-yielding stiffness $K_2$, which should be kept about $0.023K_{1,C}$ for

isolation only cases and $0.036K_{1,C}$ when combined with fluid dampers. The optimal damping

coefficient ranges from 4835 kN(s/m) to 2264 kN(s/m) for different hazard levels. This study

picks an average value of 3878 kN(s/m) as the final design.

Table 5.1.   Optimal protection designs for the PSO

| Hazard level (g) | Isolation bearings only | | Isolation bearings and fluid dampers | | |
| --- | --- | --- | --- | --- | --- |
| | $Q/Q_C$ | $K_2/K_{1,C}$ | $Q/Q_C$ | $K_2/K_{1,C}$ | $C_\alpha$ kN(s/m) |
| 0.4 | 0.32 | 0.028 | 0.20 | 0.048 | 2264 |
| 0.6 | 0.52 | 0.025 | 0.33 | 0.012 | 3932 |
| 0.8 | 0.39 | 0.027 | 0.11 | 0.049 | 4482 |
| 1.0 | 0.42 | 0.012 | 0.11 | 0.035 | 4835 |
| **Selected** | **0.41** | **0.023** | **0.19** | **0.036** | **3878** |

### 5.2.4 Effectiveness Evaluation of the Selected Optimal Designs

To further investigate the effectiveness of the selected protection designs, the PBSE

methodology shown in Figure 5.1 is utilized herein to compare the RCRs with different

design scenarios; namely rather than being converted as functions of median EDPs, the RCRs

are conditioned on IMs instead. The multiple stripes analysis is also adopted to derive the

component-level fragility functions for the two selected optimal designs. Subsequently, the

same maximum likelihood concept is utilized to regress the continuous fragility curves for

each case. Figures 5.12 and 5.13 illustrates both the multiple stripes analysis results and the

regressed fragility curves of isolation bearings and pier columns for the two selected optimal

designs, respectively, where 'Optimal 1' stands for the case where only isolation bearings are

equipped, and 'Optimal 2' is the case when both isolation bearings and fluid dampers are

installed. It can be seen from the figures that the regressed curves fit very well with the data

at each IM level.
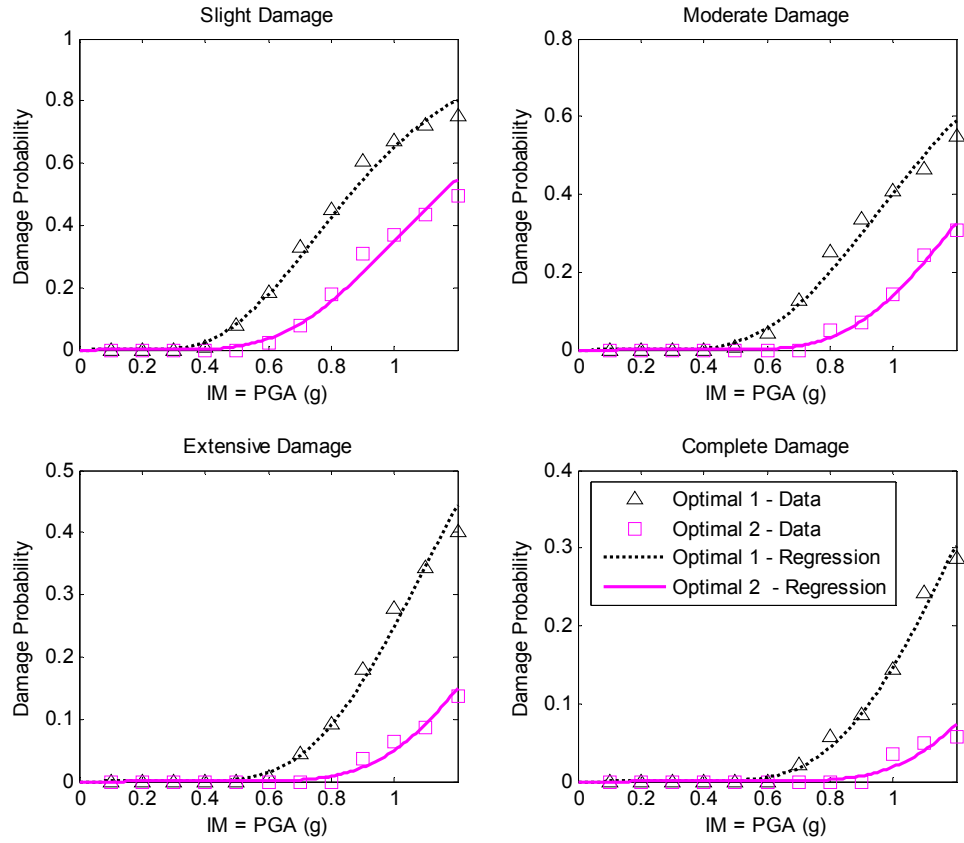


Figure 5.12.   Component-level fragility functions of isolation bearings for the two selected optimal designs
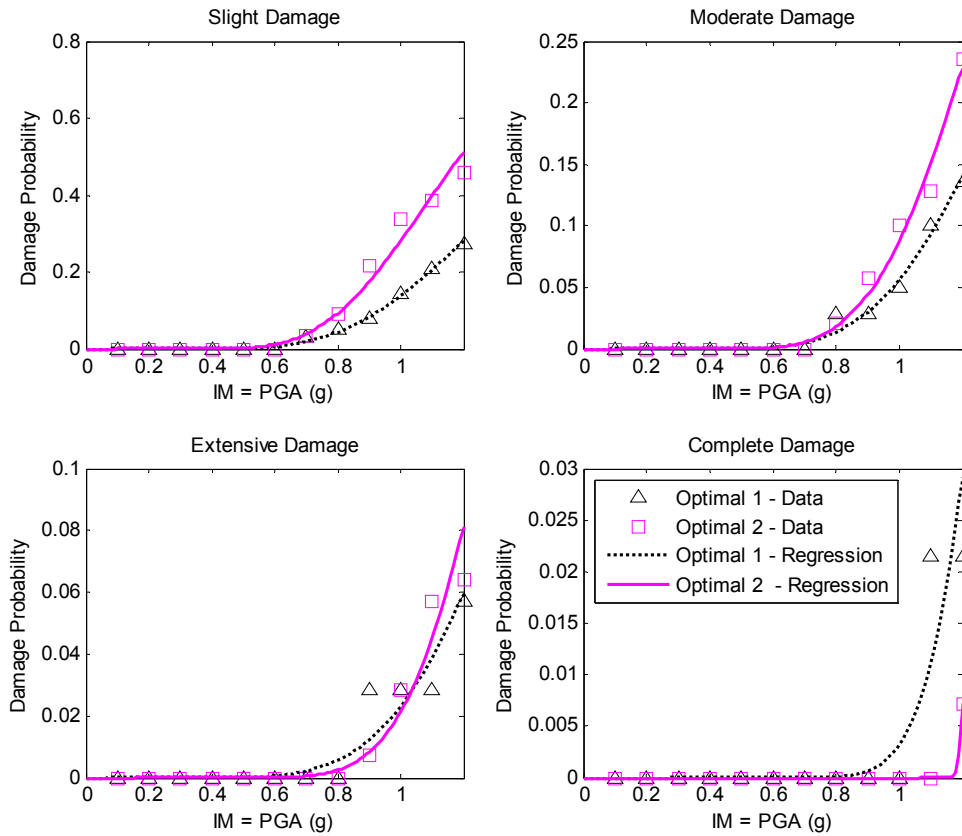
Figure 5.13.    Component-level fragility functions of pier columns for the two selected optimal designs

Figure 5.14 shows the seismic RCR values of the PSO that are installed with the two selected optimal designs under PGA levels up to 1.0g, which is the upper bound used for optimization in this study. For consistency purpose, replacement costs of pier column and isolation bearings are still assumed as $c_{stru}$:$c_{iso}$ = 0.75:0.25 respectively. The RCR values associated with the as-built bridge and the two initial isolation designs are provided in the same figure for comparison purpose, where 'Initial 1' refers to the case with weak isolation effect of $Q/Q_C$ = 0.9, $K_2/K_{2,C}$ = 0.09 and 'Initial 2' is the case that owns the strong isolation effect of $Q/Q_C$ = 0.1, $K_2/K_{2,C}$ = 0.01. As can be seen from the figure, the 'Initial 2' case

increases the RCR for the PSO when compared with the as-built bridge, which indicates that the repair cost of the PSO will be dominated by the bearings should their mechanical parameters are selected the same as the 'Initial 2' case. In other words, PBSD of protective devices is strongly suggested in practice since an improper isolation design may cause higher seismic loss of the bridge. On the other hand, both the 'Optimal 1' isolation case and the 'Optimal 2' case that utilizes isolation bearings and fluid dampers will reduce the repair costs of the PSO, which not only validates the effectiveness of the proposed performance-based design and optimization procedure, but also pinpoints the optimal design parameters of the PSO. Moreover, significant reductions are achieved for the 'Optimal 2' case, which promotes the design strategy of combining the optimally designed isolation bearings and fluid dampers. This phenomenon underlines that if designed properly, the inclusion of energy dissipation devices, like the fluid dampers in this study, can efficiently diminish bearing displacement without increasing the column drift too much. Therefore, superior seismic performance can be obtained when both isolation bearings and energy dissipation devices are installed.
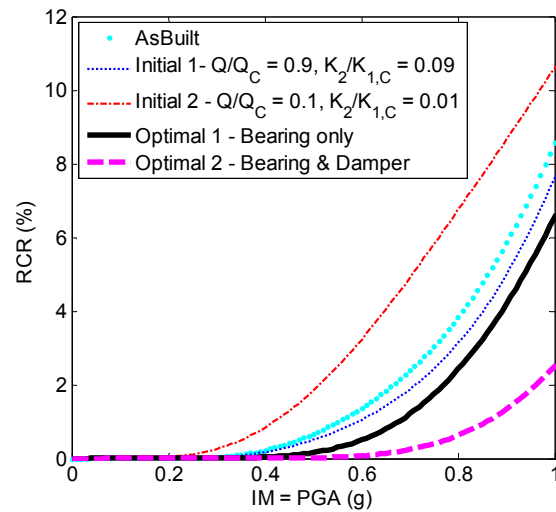


Figure 5.14.    RCR comparisons of various design cases for the PSO

## 5.3 CONCLUDING REMARKS

The performance-based framework is developed in this chapter to design and optimize seismic protective devices for highway bridges. First, the proposed framework takes account of ground motion uncertainty by setting up the multiple stripes analysis at important IM levels. Discrete component-level fragility functions are then derived and regressed as continuous ones by adopting the maximum likelihood concept. Because different protection designs will yield divergent fragility curves at the same IM level, a conventional PBSD of protective devices requires iteratively updating the fragility function at every time when a new design is considered. To avoid this tedious and inefficient process, the derived component-level fragility functions are conditioned on median EDPs instead, in which way a uniform curve can be obtained for various protection designs. Furthermore, bridge system-level RCR is calculated by considering the replacement costs, damage ratios and damage probabilities of critical components. The proposed framework directly links the system-level RCR to median EDPs of critical components for various isolated bridge systems, which significantly facilitates the design and optimization of protective devices in a probabilistic manner.

A case study is carried out on the PSO to examine the robustness of the proposed framework. Steps of deriving the uniform component-level fragility functions and calculating the system-level performance index of RCR are explained in detail. In addition, closed-form expressions of the RCR are regressed for two replacement ratios of pier columns and isolation bearings (i.e., the one with $c_{stru}$: $c_{iso}$ = 0.85:0.15 and the other with $c_{stru}$: $c_{iso}$ =

0.75:0.25). Using the derived performance index of RCR, genetic optimization is carried out to identify the optimal protection designs. The effectiveness of the proposed methodology is assessed through the PBSE that compares the optimal designs with the as-built case and two initial designs. The comparison entails the implementation of the performance-based seismic design and optimization of protective devices, because more repair costs would occur should inappropriate designs are selected. Moreover, the results indicate that by combining with optimally designed energy dissipation devices, significant reductions of system RCR can be achieved for the PSO.

Improvements can be made in two aspects in terms of the proposed design and optimization framework. First, an integral procedure to incorporate design parameters for both the bridge structure and protective devices may enable designers to further minimize the repair costs of highway bridges. Second, by taking account of all sources of uncertainty, the variance of the designed RCR surface can be determined. Nevertheless, compared with previous studies on the similar topic, the proposed framework is robust yet simple to be implemented in practices. It can serve as an efficient tool in evaluating, designing and optimizing the protective devices.

# 6. ROCKING COLUMNS WITH FOUNDATION FOR SEISMIC PROTECTIONS OF HIGHWAY BRIDGES

The rocking column-foundation systems with rigid supports are promising design concept for bridges because of their lower cost and good seismic performance. Nevertheless, the practical application of the rocking system is challenged due to the fact that an efficient tool to effectively analyze its seismic behavior is still lacking. To bridge this gap, this chapter develops simple yet reliable seismic demand models for rocking columns with foundation on rigid supports when subjected to horizontal near-fault motions. Analytical and numerical modeling, dimensional analysis methodology, and numerical validation for the proposed rocking system are presented in each section, respectively.

## 6.1 ANALYTICAL MODELING OF THE ROCKING COLUMNS WITH FOUNDATION

### 6.1.1 Equation of Motion

Figure 6.1 illustrates the scheme of the rocking column-foundation that is designed for bridges. The system features a detached rocking interface at the bottom of the foundation while supported on a rigid surface. Such design will allow the foundation to uplift and re-center when subject to horizontal ground excitations. Given that the self-weights of the column and the narrowed foundation are much less than the participating weight from the deck, the system can be idealized as a two degree-of-freedom system at the uplift phase; i.e. when foundation rotates along the pivot point of the base, the system variables are the uplift angle that defined as $\theta$ and

the column drift that defined as $u$. The deck mass inertia is represented by a concentrated mass $m$, and the column is considered to have a height of $H$, a base width of $2b$, an elastic stiffness of $E_cI_c$, and a damping coefficient of $C$.
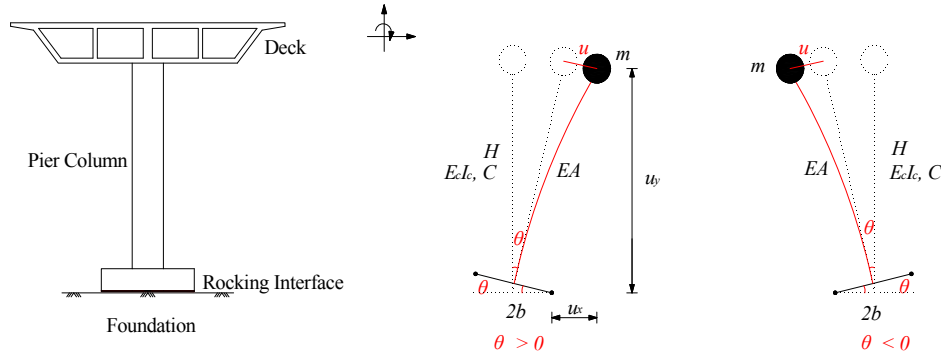


Figure 6.1.  Schematic of the rocking column-foundation for bridges

The kinematics of the mass point in Figure 6.1 when rotates clockwise along the right pivot (i.e. when $\theta > 0$) are:

$$\begin{cases} u_x = -b\cos\theta + H\sin\theta + u\cos\theta \\ u_y = b\sin\theta + H\cos\theta - u\sin\theta \end{cases} \quad (6.1)$$

where $u_x$ and $u_y$ are the relative displacements of the mass point to the right pivot in the horizontal and vertical directions, respectively. Therefore, the kinematic energy of the mass point can be calculated as:

$$T = \frac{1}{2}m(\dot{u}_x^2 + \dot{u}_y^2) = \frac{1}{2}m\left[(b^2 + H^2 + u^2 - 2bu)\dot{\theta}^2 + \dot{u}^2 + 2H\dot{\theta}\dot{u}\right] \quad (6.2)$$

161

The potential energy of the mass point that comes from gravity and the D'Alembert force, and the column strain energy can be calculated and summarized as:

$$V = mgu_y + m\ddot{u}_g u_x + \frac{3E_c I_c}{2H^3} u^2$$

$$= mg(b\sin\theta + H\cos\theta - u\sin\theta) + m\ddot{u}_g(-b\cos\theta + H\sin\theta + u\cos\theta) + \frac{3E_c I_c}{2H^3} u^2 \quad (6.3)$$

where $\ddot{u}_g$ is the acceleration magnitude of the input ground motion.

The Lagrange's equation shall be satisfied during the rocking motion:

$$\begin{cases} \dfrac{d}{dt}\dfrac{\partial(T-V)}{\partial\dot{\theta}} - \dfrac{\partial(T-V)}{\partial\theta} = 0 \\ \dfrac{d}{dt}\dfrac{\partial(T-V)}{\partial\dot{u}} - \dfrac{\partial(T-V)}{\partial u} = -C\dot{u} \end{cases} \quad (6.4)$$

The substitution of Eqs. (6.2) to (6.3) in Lagrange's Eqn (6.4) results in the EOMs of the rocking system for $\theta > 0$. Also, similar derivations for $\theta < 0$ lead to following equations that represent the system EOMs:

$$\ddot{\theta}[H^2 + b^2 - \text{sgn}(\theta)2bu + u^2] + H\ddot{u} - 2\dot{\theta}\dot{u}[\text{sgn}(\theta)b - u]$$
$$-g[H\sin\theta - \text{sgn}(\theta)b\cos\theta + u\cos\theta] = -\ddot{u}_g[H\cos\theta + \text{sgn}(\theta)b\sin\theta - u\sin\theta] \quad (6.5)$$

$$\ddot{\theta}H + \ddot{u} + 2\xi\omega_n\dot{u} + \dot{\theta}^2[\text{sgn}(\theta)b - u] - g\sin\theta + \omega_n^2 u = -\ddot{u}_g\cos\theta \quad (6.6)$$

where $\omega_n$ is the vibrational natural frequency of the column that equals to $\sqrt{3E_c I_c / (H^3 m)}$,

and $\xi$ is the associated damping ratio, which can be calculated as $\dfrac{C}{2}\sqrt{\dfrac{H^3}{3E_c I_c m}}$.

It is noted that when the ground motion is not strong enough to uplift the column (i.e. when $\ddot{\theta} = \dot{\theta} = \theta = 0$), Eq. (6.6) will lead to the force equilibrium for the full contact condition; and Eq. (6.5) turns out to be the moment equilibrium around the pivot point. At full contact, Eq. (6.6) can be simplified as:

$$\ddot{u} + 2\xi\omega_n\dot{u} + \omega_n^2 u = -\ddot{u}_g \tag{6.7}$$

## 6.1.2 Uplift Condition

The rocking system begins to uplift when the overturning moment due to external loads exceeds the resisting moment that provided by gravity and the initial tendon force. The overturning and resisting moments can be calculated by using Eqs. (6.8) and (6.9), respectively:

$$M_0 = \mp m(\ddot{u}_g + \ddot{u})H \tag{6.8}$$

$$M_r = mg(b \mp u) \tag{6.9}$$

where $M_0$ and $M_r$ are the overturning and the resisting moments, respectively. Therefore, the column uplifts when:

163

$$\mp m(\ddot{u}_g + \ddot{u})H > mg(b \mp u) \tag{6.10}$$

By substituting $\ddot{u}_g + \ddot{u}$ in Eq. (6.7) to Eq. (6.10), the uplift condition can be determined

as:

$$\pm(2\xi\omega_n\dot{u} + \omega_n^2 u)H > g(b \mp u) \tag{6.11}$$

For undamped systems and assume $u << b$, the above equation can be further simplified to

(Acikgoz and DeJong 2012; Vassiliou et al. 2015):

$$|u| > \frac{gb}{\omega_n^2 H} \tag{6.12}$$

### 6.1.3 Impact Mechanism

Energy loss during the rocking impact was originally addressed by Housner (1963) for the

rigid block. It was assumed that inelastic instantaneous impact happens when the base pivot

changes from one corner to the other, where the conservation of angular moment of momentum

about the new impact point yields (Figure 6.2(a)):

$$m(R\dot{\theta}_1)R_2 = m(R\dot{\theta}_2)R \tag{6.13}$$

where $R$ is defined as $\sqrt{H^2 + b^2}$, $\alpha$ is defined as $\tan^{-1}(b/H)$, $\dot{\theta}_1$ and $\dot{\theta}_2$ are the pre-impact

164

and post-impact angular velocities, respectively, $R_2$ is the distance from the new pivot point $o'$ to the pre-impact velocity tensor $R\dot{\theta}_1$. Eq. (6.13) further leads to the calculation of the coefficient of restitution for the rigid column case:

$$e = \frac{\dot{\theta}_2}{\dot{\theta}_1} = \cos 2\alpha \qquad (6.14)$$

Because of the additional vibrational mode that comes from column elasticity, the deformable rocking column and foundation shall experience a distinct impact mechanism when compared with the rigid case. Previous studies assumed that after each impact, the system will either stay full contact on the ground, or to immediately uplift about the new pivot and continue to rock, and the state with less total energy will govern (Oliveto et al. 2003; Acikgoz and DeJong 2012). Methods used in these studies to calculate column's post-impact angular and horizontal velocities include (1) the conservation of angular moment of momentum about the new impact point; (2) the preservation of the horizontal momentum. However, the experiment study conducted by Truniger et al. (2015) disclosed that the 'double impact' mode, i.e. the mode when the system immediately continues to rock after impact, does not exist during the impact. Instead, they calculated the post-impact velocity by assuming the column remains full contact after each impact and system's kinematic energy associated with vertical velocity components is lost during the impact.

The energy loss models considered by Acikgoz and DeJong (2012) and Vassiliou et al. (2015) has been investigated in the study of Truniger et al. (2015), where they compared the

impact-induced amplitude decay from theoretical results with those from experimental measurements. Table 6.1 lists the median and median absolute deviation (MAD) values of the rocking amplitude decay ratio, which is defined as the ratio of theoretical amplitude decay normalized by the corresponding experimental value (Truniger et al. 2015). It can been seen from the table that the median ratios for the study of Acikgoz and DeJong (2012) are all larger than 1, which means their method overestimated the impact energy dissipation. In contrast, the method used by Vassiliou et al. (2015) underestimated the impact energy loss, which can be reflected by the smaller-than-one median values.
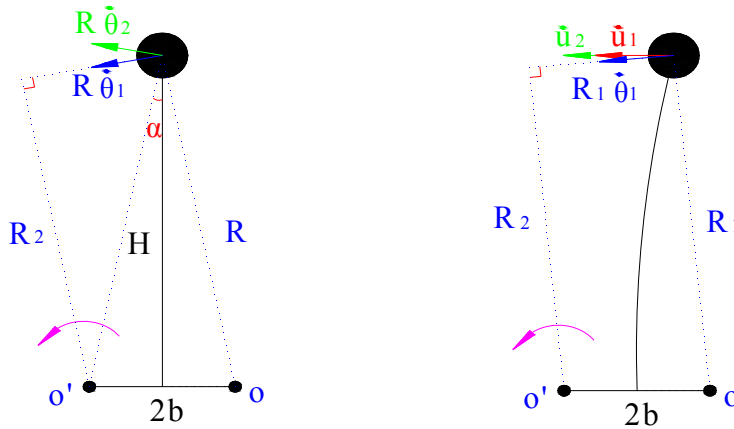


(a) Rigid column case          (b) Deformable column case

Figure 6.2. Rocking impact when the base pivot changes from right corner (point $o$) to left corner (point $o'$)

Table 6.1.   Median and MAD of the amplitude decay ratio (Truniger et al. (2015))

| Analytical model | All tests | | Long base tests only | | Short base tests only | |
|---|---|---|---|---|---|---|
| | Median | MAD | Median | MAD | Median | MAD |
| Acikgoz and DeJong [2012] | 1.487 | 0.890 | 2.040 | 1.706 | 1.380 | 0.465 |
| Vassiliou et al. [2015] | 0.630 | 0.435 | 1.059 | 0.562 | 0.507 | 0.194 |

In light of the experimental observation as well as the amplitude decay ratio comparisons from Truniger et al. (2015), this study considers that the full contact condition will follow each rocking impact, which means the post-impact horizontal velocity is the only variable that needs to be determined. As shown in Figure 6.2(b), the conservation of angular moment of momentum around point $o'$ leads to:

$$m\dot{u}_2 H = m(R_1\dot{\theta}_1)R_2 + m\dot{u}_1 H \tag{6.15}$$

where $R_1$ and $R_2$ are the distances from the pre-impact rotational velocity tensor to the pivot points of $o$ and $o'$ respectively, which can be calculated as: $R_1 = \sqrt{H^2 + (b-u)^2}$ and $R_2 = \dfrac{H^2 + u^2 - b^2}{\sqrt{H^2 + (b-u)^2}}$, and $\dot{u}_1$ and $\dot{u}_2$ are the pre-impact and post-impact horizontal velocities respectively. By substituting $R_1$ and $R_2$ into Eq. (6.15), it can be solved as:

$$\dot{u}_2 = \frac{H^2 + u^2 - b^2}{H}\dot{\theta}_1 + \dot{u}_1 \tag{6.16}$$

The associated pre-impact and post-impact kinematic energies can be calculated based on Figure 6.2(b) and Eq. (6.16). It is noted that by forcing the equilibrium of angular momentum for deformable rocking columns, it is possible that the post-impact kinematic energy is larger than the pre-impact one (Vassiliou et al. 2015), which is not physically meaningful. Under such conditions, this study abandoned the conservation of the angular momentum; instead the vertical pre-impact kinematic is considered to be lost (Chopra and Yim 1985), which gives:

$$\frac{1}{2}m(\dot{u}_1 + H\dot{\theta}_1)^2 = \frac{1}{2}m\dot{u}_2^2 \tag{6.17}$$

Therefore, the post-impact elastic velocity becomes:

$$\dot{u}_2 = \dot{u}_1 + H\dot{\theta}_1 \tag{6.18}$$

The effectiveness of the proposed energy dissipation model is examined by comparing the system responses with those from previous studies (Acikgoz and DeJong 2012; Vassiliou et al. 2015). The system EOMs (Eqs. (6.5) and (6.6)), the uplift condition (Eq. (6.11)), and the rocking impact energy loss (Eqs. (6.16) and (6.18)) are combined and solved by using the ODE solver in MATLAB. Figure 6.3 shows the response comparisons for the rocking system in Figure 6.1. In Figure 6.3, $u_{cr}$ equals to $gb/(\omega_n^2 H)$, which is the uplift displacement for the undamped system (Eqn (6.12)), $E$ is the total energy of the system, and $E_{ref}$ is a reference energy content that equals to $mgR(1-\cos\alpha)$. As can be seen in the figure, the model proposed in this study successfully captures the coupling of elasticity and rocking, which is reflected by the combination of both high and low frequency oscillations in the column drift responses (top right). In addition, as shown in the bottom left figure, the impact mechanism considered in this study will yield an intermediate total energy dissipation when compared with previous studies (Acikgoz and DeJong 2012; Vassiliou et al. 2015), which is more consistent with the experimental results that presented by Truniger et al. (2015).

168
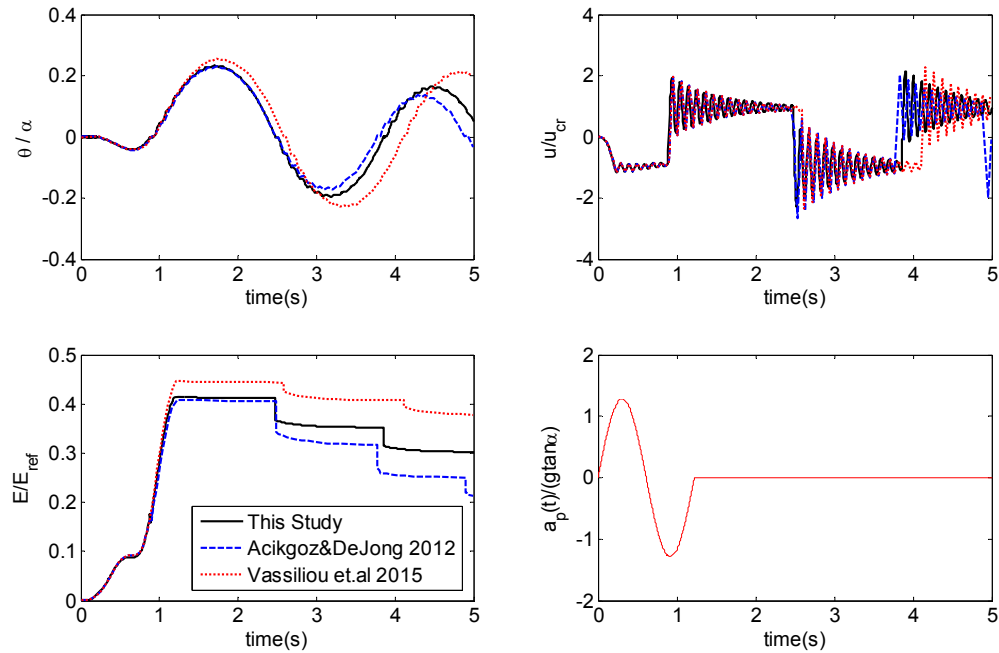
Figure 6.3. Comparisons of the rocking rotation (top left), column drift (top right), and energy loss (bottom left) subjected to one-cycle sinusoidal pulse excitation (bottom right) for $a_p/(gtan\alpha) = 1.30$, $\omega_n/p = 11.9$, $\omega/p = 5.1$, $\alpha = 0.2$ and $\zeta = 0.005$ ($a_p$ refers to the peak ground acceleration)

## 6.2 DIMENSIONAL ANALYSIS OF THE ROCKING SYSTEM

As previously discussed, the analytical modeling scheme turns out to be a robust way to capture both the rocking and elastic responses of the rocking column and foundation system. To facilitate its practical application, dimensional analysis is developed herein to further regress the closed-from expressions of the peak responses that calculated from the analytical model.

### 6.2.1 Characteristics of Near-fault Ground Motions

Although near-fault ground excitations are in general unpredictable, their dynamic features can be characterized by several intensity measures such as the prevailing frequency, the peak acceleration, the number of dominant cycles, etc. For the purpose of accurately

169

representing the dynamic features of near-fault ground motions, various mathematical models have been proposed during the last three decades, which include rectangular displacement pulses (Hall et al. 1995), piece-wise linear triangular velocity pulses (Alavi and Krawinkler 2001), sinusoidal acceleration pulses (Kalkan and Kunnath 2006), sinusoidal velocity pulses (Bray and Rodriguez 2004), general cycloidal pulses (Makris 1997; Makris and Chang 2000), and multi-parameter decaying velocity pulses (Mavroeidis and Papageorgiou 2003; He and Agrawal 2008). In addition, wavelet analysis (Baker 2007) and the Hilbert-Huang transform (Zhang et al. 2003) have been developed to extract velocity pulses from the recorded ground motions.

This study selects the velocity pulse model proposed by Mavroeidis and Papageorgiou (2003) (referred as M&P model herein) to represent near-fault ground motion inputs, because their model has been calibrated by using a large number of actual ground motion records. The M&P model can be expressed as the product of a harmonic oscillation and a bell-shaped function:

$$
\dot{u}_g(t) = 
\begin{cases}
A_p \dfrac{1}{2}\left[1 + \cos\left(\dfrac{2\pi f_p}{\gamma}(t - t_0)\right)\right]\cos\left[2\pi f_p(t - t_0) + \nu\right] & \text{when } t_0 - \dfrac{\gamma}{2f_p} \leq t \leq t_0 + \dfrac{\gamma}{2f_p} \\
0 & \text{otherwise}
\end{cases}
\tag{6.19}
$$

where $\dot{u}_g(t)$ is the velocity history of the pulse-type ground motion, and the five unknown parameters $A_p$, $f_p$, $\nu$, $\gamma$, and $t_0$ controls the motion amplitude, frequency, phase, oscillatory

170

character, and envelope, respectively. As shown in Eq. (6.19), the M&P model allows the user to resemble a variety of near-fault ground motions by changing five parameters, all of which have unambiguous physical interpretations and scales.

## 6.2.2 Dimensional Analysis

By taking the derivative of Eq. (6.19) and substituting acceleration history $\ddot{u}_g(t)$ into Eqs. (6.5) and (6.6), the peak responses of the system can be obtained as:

$$u_{max} = \max(|u(t)|) = F_1(m, \omega_n, \xi, \alpha, R, \omega_p, a_p, \gamma, v) \tag{6.20}$$

$$\theta_{max} = \max(|\theta(t)|) = F_2(m, \omega_n, \xi, \alpha, R, \omega_p, a_p, \gamma, v) \tag{6.21}$$

where $u_{max}$ and $\theta_{max}$ are the peak column drift and uplift angle, respectively, $\omega_p$ is the cyclic frequency of the M&P model that equals to $2\pi f_p$, $a_p$ is the peak ground acceleration of the M&P model, and all other parameters are the same as those defined before. The 10 terms appearing in Eq. (6.20) or (6.21) involve three reference dimensions that are force, length and time. According to Buckingham's $\Pi$-theorem (Barenblatt 1996), the number of independent dimensionless parameters is determined as: (10 variables)–(3 reference dimensions) = 7 $\Pi$-parameters for each equation. Hence, Eqs. (6.20) and (6.21) can be transferred into following dimensionless forms:

$$\Pi_u = \varphi_1(\Pi_{\omega_n}, \Pi_\xi, \Pi_\alpha, \Pi_{\omega_p}, \Pi_\gamma, \Pi_v) \tag{6.22}$$

$$\Pi_\theta = \varphi_2(\Pi_{\omega_n}, \Pi_\xi, \Pi_\alpha, \Pi_{\omega_p}, \Pi_\gamma, \Pi_v) \tag{6.23}$$

where the normalized natural frequency is $\Pi_{\omega_n}$ that equals to $\omega_n/p$, and $p$ is the rocking mode

frequency parameter, which can be calculated as $\sqrt{g/R}$, the normalized motion prevailing

frequency is $\Pi_{\omega_p}$, which can be calculated as $\omega_p/p$. The other four dimensionless parameters

are: column damping ratio ($\Pi_\xi = \xi$), column slenderness ratio ($\Pi_\alpha = \alpha$), the oscillatory character

of the M&P model ($\Pi_\gamma = \gamma$), and the phase angle of the M&P model ($\Pi_v = v$).

Previous studies have shown that if the column is designed with a fixed-base condition, its

inelastic deformation can be normalized by the characteristic length scale of the ground motion

(i.e. $a_p / \omega_p^2$) to yield a self-similar dimensional response quantity (Makris and Black 2004a, b;

Karavasilis et al. 2011). It is conjectured in this study that the $\Pi$-parameters of $\Pi_u$ in Eq. (6.22)

and $\Pi_\theta$ in Eq. (6.23) can be formed based on the characteristic length scale of the ground

motion; while additional physical quantities need to be incorporated to capture the specific

features associated with the deformable rocking system. The normalized $\Pi_u$ and $\Pi_\theta$ are

proposed as:

$$\Pi_u = \Pi_{u,o}\,\Pi_{u,r} = \frac{u_{\max}\omega_p^2}{a_p}\left[1+\left(\frac{\omega_p}{10p}\right)^\gamma \frac{a_p}{g\tan\alpha}\right] \tag{6.24}$$

$$\Pi_\theta = \Pi_{\theta,o}\,\Pi_{\theta,r} = \frac{\theta_{\max}R\omega_p^2}{2\pi a_p}\left[1+\left(\frac{\omega_p}{p}\right)^2\right] \tag{6.25}$$

As can be seen from Eqs. (6.24) and (6.25), the $\Pi$-parameters of $\Pi_u$ and $\Pi_\theta$ are proposed as

the products of the normalized responses that correspond to motion's characteristic length scale

(i.e. $\Pi_{u,o} = \dfrac{u_{max}\omega_p^2}{a_p}$ and $\Pi_{\theta,o} = \dfrac{\theta_{max}R\omega_p^2}{2\pi a_p}$), and the additional high-order 'rocking' terms of

$\Pi_{u,r} = 1 + \left(\dfrac{\omega_p}{10p}\right)^{\gamma} \dfrac{a_p}{g\tan\alpha}$ and $\Pi_{\theta,r} = 1 + \left(\dfrac{\omega_p}{p}\right)^2$, respectively. The soundness of including the

high-order terms in Eqs. (6.24) and (6.25) are illustrated in Figure 6.4. As can be seen from the

top row of the figure, if $\Pi_{u,o}$ is plotted against $1/\prod_{\omega_p}$ (top left), although a general trend can be

seen from the data in the middle figure, observable scattering still exists. While if the proposed

dimensionless parameter of $\Pi_u$ is considered (top right), a distinct curve can be formed.

Furthermore, later study shows that a simple power-law function can be chosen to correlate $\Pi_u$

with $1/\prod_{\omega_p}$. The effectiveness of using $\Pi_\theta$ to quantify the rotational responses of the system is

examined by comparing the bottom three figures of Figure 6.4. The bottom middle figure

shows the data when $\Pi_{\theta,o}$ is calculated, where significant scattering occurs and no clear trend

can be observed. However, by multiplying an addition dimensionless term, the data of $\Pi_\theta$ turn

out to be a distinguishable curve with clear trend, which significantly facilitates its closed-form

regression.

Sensitivity studies are conducted herein to investigate the influences of various parameters

to the dimensionless response quantities of $\Pi_u$ and $\Pi_\theta$. A large number of time history analyses

need to be performed to cover the general range for each parameter. As can be seen in Table 6.2,

the scope of rocking column's geometric, mass and dynamic parameters are determined by

considering typical highway bridges designed in U.S. Given that the rocking mode will

substantially alleviate the drift responses of the column, which will in turn reduce vibrational

damage and hysteretic damping, the vibrational damping parameter is considered to be smaller

than 5%. The ranges for M&P model parameters are considered based on the study by

Mavroeidis and Papageorgiou (2003). Table 6.2 also lists the ranges of the corresponding

dimensionless Π-parameters.
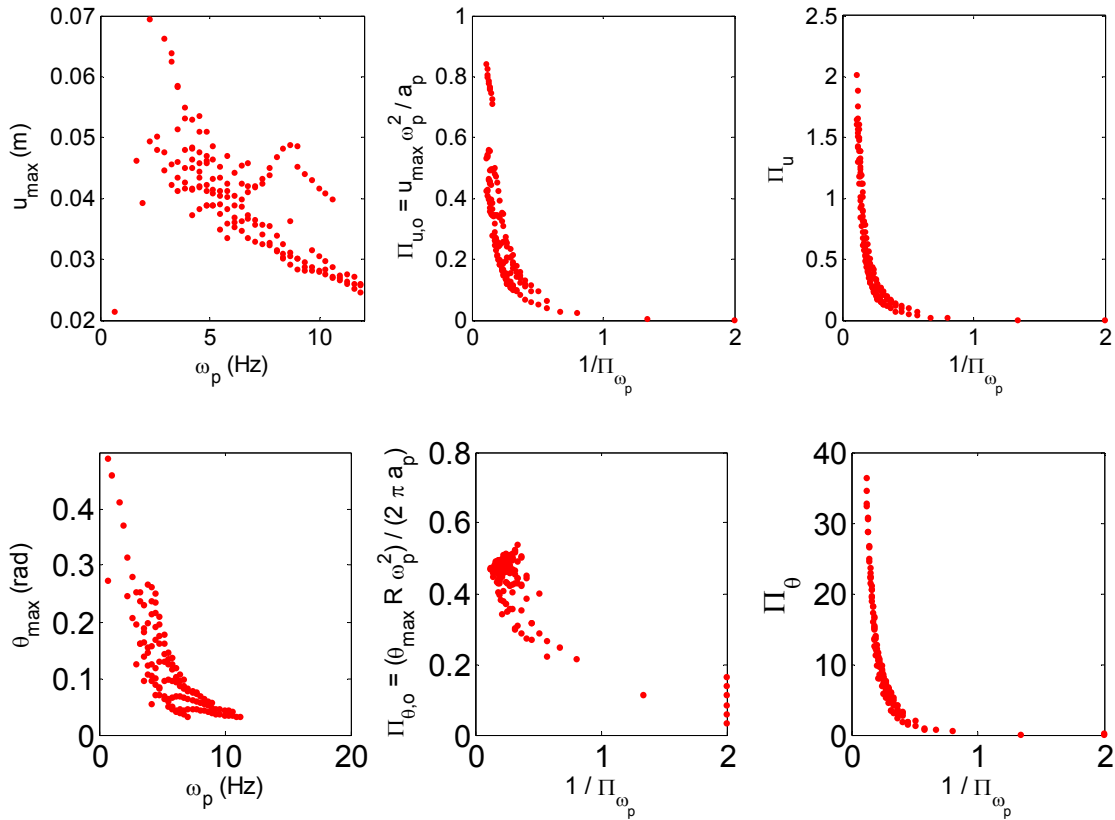


Figure 6.4. Illustration of the effectiveness of the proposed Π-parameters of $\Pi u$ and $\Pi\theta$ (for the case when $\Pi_{\omega_n} = 10$, $\Pi_\xi = 0.005$, $\Pi_\alpha = 15°$, $\Pi_\gamma = 2$, $\Pi_\nu = 0$)

Table 6.2.  General range considered for each parameter for time history analyses

| | $\omega_n$ | $R$ | $m$ | $\alpha$ | $\xi$ | $\omega_p$ | $a_p$ | $\gamma$ | $\nu$ |
|---|---|---|---|---|---|---|---|---|---|
| Physical parameters | (rad/s) | (m) | (kN/g) | (°) | (%) | (rad/s) | (g) | | (°) |
| | 2-30 | 3-9 | 100-2000 | 5-30 | 0.5-5 | 1-12 | 0.3-1 | 1-3 | 0-180 |
| Π parameters | $\Pi_{\omega_n}$ | $\Pi_{\omega_p}$ | $\Pi_\alpha$ | $\Pi_\xi$ | $\Pi_\gamma$ | $\Pi_\nu$ | -- | -- | -- |
| | 1-30 | 0.5-12 | $1/36\pi$-$1/6\pi$ | 0.005-0.05 | 1-3 | 0-0.5$\pi$ | -- | -- | -- |

### 6.2.3 Proposed Column Drift Demand Model

The sensitivity study is constructed based on the benchmark design with $R = 6$m, $\alpha = 15°$, $\omega_n = 10p$, $\xi = 0.5\%$, $\gamma = 2$, and $v = 0$. One of these parameters is varied once at each time to examine its influence to the dimensionless response parameter of $\Pi_u$. The two additional M&P model parameters (i.e., the peak ground acceleration $a_p$ and the cyclic frequency $\omega_p$) are varied within their ranges for each case to form a large group of ground motion inputs. The sensitivity of $\Pi_u$ is firstly examined for four parameters, namely the dimensionless parameters of $\Pi_\gamma$, $\Pi_v$, and $\Pi_\xi$, and the column size $R$. As shown in the left figure of Figure 6.5, the system response of $\Pi_u$ is not sensitive to the phase of the M&P motion; i.e., when $\Pi_v$ is changing from 0 to $0.5\pi$, no distinct difference can be observed for the response of $\Pi_u$. Similar trends can be found for the vibrational damping of the column ($\Pi_\xi$ in middle figure). On the other hand, as shown in Eq. (6.24), since the proposed dimensionless parameter of $\Pi_u$ already incorporates the M&P parameter of $\gamma$ and the column size $R$, which is embedded in the parameter of $p = \sqrt{g/R}$, the influences of $\gamma$ and $R$ to the response of $\Pi_u$ is very marginal (as shown in the left and right figures, respectively). Therefore, the proposed closed-form expression of $\Pi_u$ can exclude the above-mentioned four parameters.
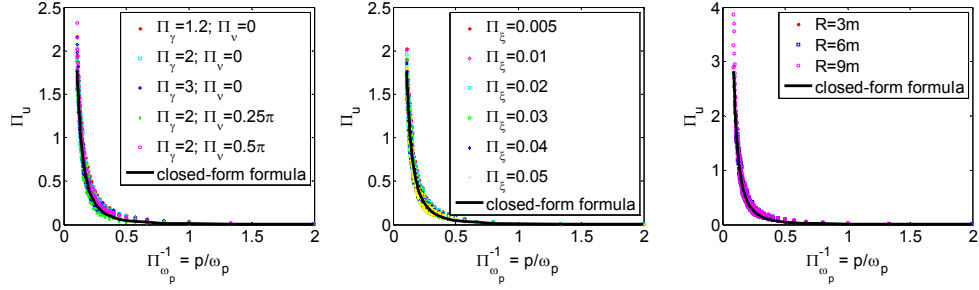
Figure 6.5. Sensitivity study of $\Pi_u$ with respect to $\Pi_\gamma$, $\Pi_\nu$, $\Pi_\xi$ and $R$

Further sensitivity study indicates that unlike above-mentioned four parameters, the variations of normalized parameters $\Pi_{\omega_n}$ and $\Pi_\alpha$ will affect the magnitudes of $\Pi_u$. In addition, as shown in Figure 6.5, a distinct functional curve can be observed between $\Pi_u$ and $\Pi_{\omega_p}$. Therefore, in this study $\Pi_u$ is considered as a function of $\Pi_{\omega_n}$, $\Pi_\alpha$, and $\Pi_{\omega_p}$. By assuming the influences of these three affecting $\Pi$-parameters uncoupled with each other, the closed-form expression of $\Pi_u$ is proposed as:

$$\Pi_{u,e} = f_1(\Pi_{\omega_p})f_2(\Pi_{\omega_n})f_3(\Pi_\alpha) \tag{6.26}$$

where $\Pi_{u,e}$ is the closed-form estimation of $\Pi_u$, and $f_1$, $f_2$, and $f_3$ are unknown functions that need to be determined for $\Pi_{\omega_p}$, $\Pi_{\omega_n}$, and $\Pi_\alpha$, respectively. To be simple, the unknown functions are selected from basic functions types such as the linear function, the power-law function, the exponential function, and the natural logarithm function. A two-step procedure is carried out to obtain the detailed expression of $\Pi_{u,e}$ by identifying both the function type and the unknown coefficients for each function. First, by assigning a specific function type to each

function, a group of possible cases for $\Pi_{u,e}$ is formed with each case composed by a different function combination. Second, a nonlinear optimization procedure is carried out for each case to determine the unknown coefficients for each function such that the following mean error quantity is minimized:

$$E_{\Pi_u} = \frac{1}{n}\sum_1^n \left| \frac{\Pi_{u,e} - \Pi_u}{\Pi_u} \right| \tag{6.27}$$

where $n$ is the total case number for the sensitivity study of $\Pi_u$ with respect to $\Pi_{\omega_p}$, $\Pi_{\omega_n}$, and $\Pi_\alpha$. By selecting the case with the smallest error among all scenarios, both the function types and their coefficients can be determined. The two-step procedure in this study yields the following closed-form expression for $\Pi_{u,e}$:

$$\Pi_{u,e} = 0.39 \; \Pi_{\omega_p}^{2.36} \; \Pi_{\omega_n}^{-1.36} \; \Pi_\alpha^{0.45} \tag{6.28}$$

As can be seen from Eq. (6.28), it turns out that the power-law function can be adopted to quantify the impacts of the normalized cyclic frequency of the M&P motion, the normalized natural frequency of the column, and the system slenderness. The soundness of using $\Pi_{u,e}$ to estimate $\Pi_u$ is examined in both Figures 6.5 and 6.6, where the solid lines are calculated from the closed-form formula. It can be seen from both figures that the solid lines are on top of the dotted data, which demonstrates that the proposed formula of $\Pi_{u,e}$ accurately captures both the trends and the values of $\Pi_u$ under a variety of conditions. By combining Eq. (6.28) and Eq.

177

(6.24), the maximum column drift can then be estimated as:

$$u_{\max,e} = \frac{0.39\,\Pi_{\omega_p}^{2.36}\,\Pi_{\omega_n}^{-1.36}\,\Pi_{\alpha}^{0.45}a_p}{\left[1+\left(\dfrac{\omega_p}{10p}\right)^{\gamma}\dfrac{a_p}{g\tan\alpha}\right]\omega_p^2}$$

(6.29)

The derived Eq. (6.29) for the drift response of the rocking system is physically convincing, which can be reflected by following observations: (1) when the column is considered to be fully rigid, i.e. when $\Pi_{\omega_n}$ approaches infinity, $u_{\max,e}$ is close to 0; (2) $u_{\max,e}$ increases when the slenderness of the system decreases, namely when $\Pi_{\alpha}$ becomes larger; it is because of the fact that when the rocking bridge with a given column height has a wider foundation base, its rocking-mode response will be diminished and its vibrational-mode response will be increased; (3) a simple parameter manipulation shows that $u_{\max,e}$ is positively correlated with the column height $R$, which reveals that the increased column size will stabilize the rocking-mode response and thereby increase the column drifts; (4) $u_{\max,e}$ is positively related to the peak ground acceleration of the M&P motion, $a_p$.
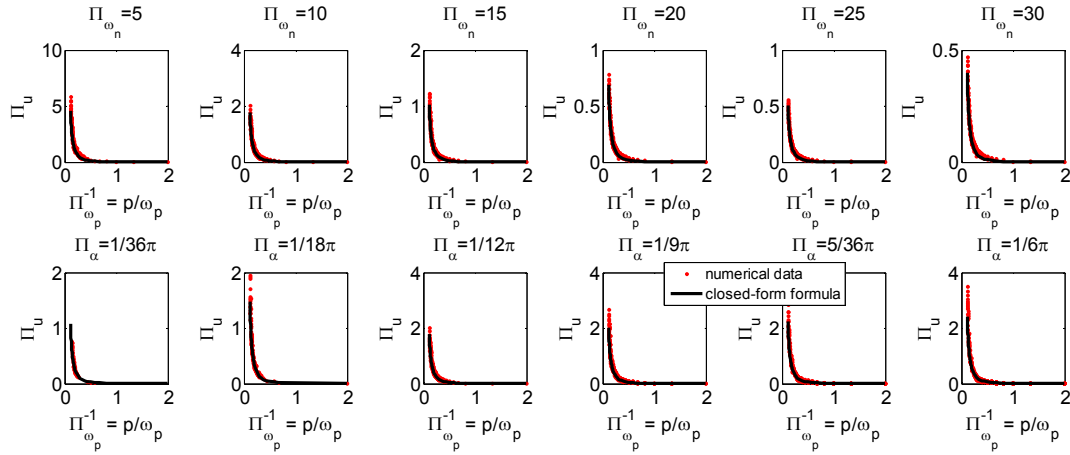
Figure 6.6. Sensitivity study of $\Pi_u$ with respect to $\Pi_{\omega_n}$ and $\Pi_\alpha$

### 6.2.4 Proposed Rocking Rotation Demand Model

The same sensitivity study is used to first identify the nonessential parameters to the normalized response of $\Pi_\theta$. As can be seen from Figure 6.7, it turns out that the normalized rotational response of $\Pi_\theta$ is insensitive to column's vibrational dynamic properties, namely the normalized natural frequency of $\Pi_{\omega_n}$ (the left figure), and the normalized damping ratio of $\Pi_\xi$ (the middle figure). Such insensitivity can be attributed to the fact that the vibrational mode of the rocking column has in general inconsiderable influences on its rocking mode; while as previously discussed, the same conclusion cannot be held for the reverse condition; that is, the rocking mode response indeed has substantial impacts on column drifts. On the other hand, as compared to $\Pi_u$, similar conclusions can be found for $\Pi_\theta$ in terms of the influences from column size $R$ (the right figure): because the proposed $\Pi_\theta$ formula of Eq. (6.25) already incorporates column height $R$, no further significant influence can be observed from this parameter.

179
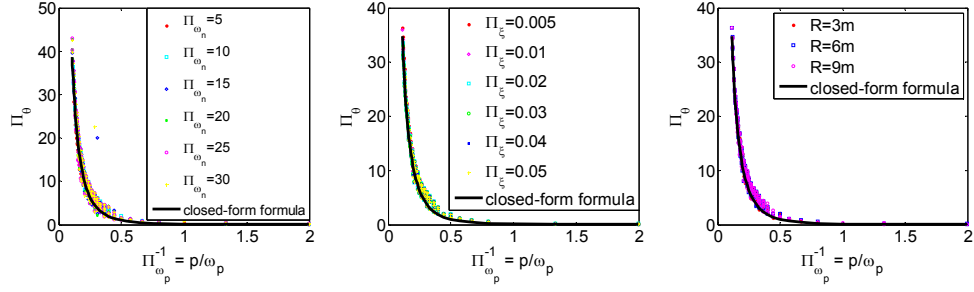
Figure 6.7. Sensitivity study of $\Pi_\theta$ with respect to $\Pi_{\omega_n}$, $\Pi_\xi$ and $R$

The remaining three influential Π-parameters, namely $\Pi_{\omega_p}$, $\Pi_\gamma$, and $\Pi_\alpha$, form the basis of

the derivation for the closed-form estimation of $\Pi_\theta$. The similar two-step procedure is utilized

to identify both the function type and the associated coefficients for each parameter. The

closed-form formula of $\Pi_\theta$ is proposed as:

$$\Pi_{\theta,e} = g_1(\Pi_{\omega_p})g_2(\Pi_\gamma)g_3(\Pi_\alpha) \tag{6.30}$$

where the unknown functions $g_1$, $g_2$, and $g_3$ are determined by a permutation and combination

of the above-mentioned simple function types and the coefficients for each case are obtained

through a general nonlinear optimization procedure that minimize the mean value of the error

between the formula-based results and the numerical data (i.e., using Eq. (6.27) with $\Pi_u$

substituted by $\Pi_\theta$ and $\Pi_{u,e}$ substituted by $\Pi_{\theta,e}$). The closed-form formula of $\Pi_{\theta,e}$ is obtained as:

$$\Pi_{\theta,e} = 0.06\ (\Pi_\gamma + 5.42)\ \ln(\Pi_{\omega_p} + 1)^{4.89}\ \Pi_\alpha^{-0.25} \tag{6.31}$$

180

As can be seen from Eq. (6.31), it turns out that a linear function can be used to quantify the influence of the number of zero crossings of the M&P motion, a natural logarithm function can be selected to determine the effects of the prevailing frequency of the motion, and a power-law function can quantify the system slenderness influence. The soundness of using $\Pi_{\theta,e}$ to estimate $\Pi_\theta$ is examined in both Figure 6.7 and Figure 6.8, where the solid lines are calculated from the closed-form formula. It can be seen from both figures that the solid lines agree well with the dotted data, which demonstrates that the proposed formula of $\Pi_{\theta,e}$ can be used in confidence to estimate $\Pi_\theta$ for various circumstances. By combining Eq. (6.30) and Eq. (6.25), the column rocking rotation angle can then be estimated as:

$$\theta_{\max,e} = \frac{0.12\pi a_p \ (\Pi_\gamma + 5.42) \ \ln(\Pi_{\omega_p} + 1)^{4.89} \ \Pi_\alpha^{-0.25}}{\left(1 + \Pi_{\omega_p}^2\right) R\omega_p^2} \tag{6.32}$$

The physical solidity of using Eq. (6.32) to estimate the rotation angle of the rocking column can be interpreted in following aspects: (1) $\theta_{\max,e}$ decreases when the system slenderness decreases, namely when the foundation base is wider and $\Pi_\alpha$ becomes larger; (2) a negative correlation exists between $\theta_{\max,e}$ and column size $R$, which reveals that the increased column size at given slenderness will reduce the peak uplift angle; (3) $\theta_{\max,e}$ is a positive linear function of M&P motion's peak ground acceleration $a_p$, and oscillatory character $\Pi_\gamma$, respectively, which denotes that a near-fault motion with bigger peak ground acceleration and more number of major pulses will surely increase the peak uplift angle of the rocking column.
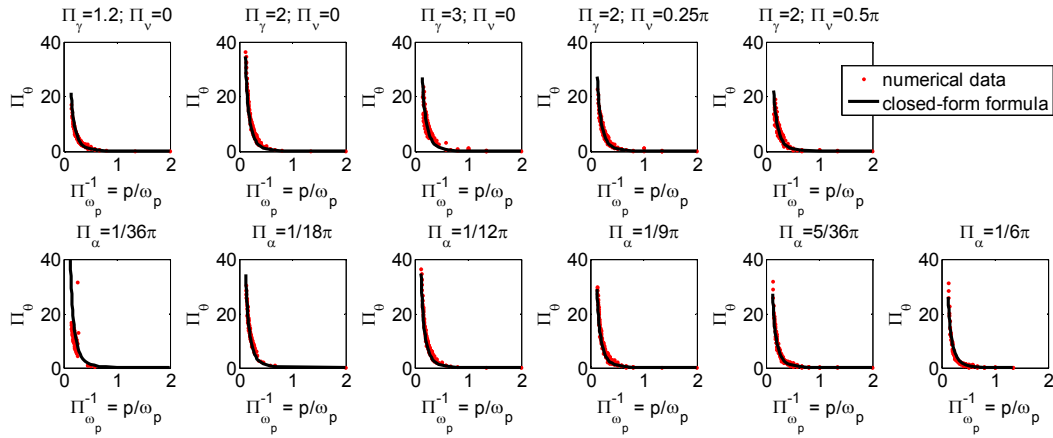
Figure 6.8. Sensitivity study of $\Pi_\theta$ with respect to $\Pi_\gamma$ and $\Pi_\alpha$

## 6.3 VALIDATION

In order to examine the accuracy of the proposed demand models for column drifts and uplift angles given in Eqs. (6.29) and (6.32), five as-built single-bent bridge cases in U.S. and twelve recorded near-fault motions are used to compute the seismic responses of the analytical model shown in Figure 6.1. The details of the selected five as-built bridges are shown in Table 6.3, where '$L_n$' refers to the selected span length, '$W$' refers to the participating weight of the column, '$K_n$' refers to the elastic stiffness of the column, '$T_n$' is the elastic natural period of the column, and all other terms are the same as those defined before. It is noted that the '$2b$' term in Table 6.3 refers to the base width of the rocking foundation that is redesigned for each bridge, such that the uplift condition can be met under the selected input motions. As can be seen from the table, the selected bridge designs exhibit large variances in terms of the column height, the slenderness ratio, and the vibrational natural frequency. Due to rocking, column's vibrational damage potential is reduced and the associated hysteretic damping ratio is assumed to be 0.5% for all bridge cases.

Table 6.3.  Five as-built bridge cases used in validation

| Cases | Bridges | $H$ (m) | $2b$ (m) | $L_n$ (m) | $W$ (kN) | $\alpha$ (°) | $R$ (m) | $K_n$ (kN/m) | $\omega_n$ (rad/s) | $T_n$ (s) |
|---|---|---|---|---|---|---|---|---|---|---|
| 1 | Meloland Road Overcrossing (MRO) | 5.2 | 1.6 | 31.7 | 3175.6 | 8.9 | 5.2 | 165153.9 | 22.6 | 0.28 |
| 2 | Manning Avenue Overcrossing (MAO)[1] | 7.2 | 3.2 | 25.8 | 1919.9 | 12.8 | 7.3 | 129690.8 | 25.7 | 0.24 |
| 3 | Manning Avenue Overcrossing (MAO)[2] | 7.5 | 3.2 | 39.6 | 2949.4 | 12.3 | 7.7 | 112229.6 | 19.3 | 0.33 |
| 4 | South Paso Robles Overhead (SPRO)[3] | 11.3 | 5.7 | 34.3 | 3025.0 | 14.2 | 11.6 | 47351.3 | 12.4 | 0.51 |
| 5 | Mondocino Avenue Bridge (MAB) | 6.5 | 3.2 | 27.1 | 3856.6 | 13.9 | 6.7 | 170801.5 | 20.8 | 0.30 |

Note: 1: the 1st bent; 2: the 2nd bent; 3: the 4th bent

The twelve pulse-like near-fault ground motions and their respective pulse representations are obtained based on the study of Tang and Zhang (2011), where they developed a mathematical tool to identify both velocity and acceleration pulses, and their M&P model parameters by using the geometric similarity and dislocations of the dimensionless response spectrum for a given M&P waveform with the dimensional response spectrum in the bi-logarithmic plotting. Table 6.4 lists the details of the selected twelve near-fault ground motions and their M&P pulse representations. As can be seen in the table, both velocity and acceleration pulse motions have been picked. The M&P parameters for each motion are also listed in the table, where the negative sign of $A_p$ denotes the shaking direction, and the peak ground acceleration $a_p$ ranges from 0.38g to 0.79g. Figure 6.9 shows the acceleration and velocity time histories, and the acceleration response spectra for 5% damping of these twelve selected motions and their M&P pulses. It can be observed from the figure that the selected M&P pulses agree well with the recorded motions in acceleration and velocity histories. In addition, the response spectra from the M&P pulses capture the dominant responses when compared to that from the recorded motions.

For each bridge, the seismic responses of the rocking system are analyzed under the twelve

recorded ground motions by using the derived system EOMs of Eqs. (6.5) and (6.6), the uplift condition of Eq. (6.11), and the impact mechanism of Eqs. (6.16) and (6.18). The peak responses of the column drift and the uplift angle are extracted and compared with the closed-form solutions from Eqs. (6.29) and (6.32), respectively, where pulse representations of the input ground motions are utilized. Therefore, for each bridge, 12 response data are available for comparisons. In this study, the effectiveness of the proposed closed-from demand models are evaluated by checking the mean and standard deviation for the distributions of $u_{max,e}/u_{max,g}$ and $\theta_{max,e}/\theta_{max,g}$, where $u_{max,e}$ and $\theta_{max,e}$ are calculated by using Eqs. (6.29) and (6.32), respectively, and $u_{max,g}$ and $\theta_{max,g}$ are the peak column drifts and uplift angles that analyzed under recorded motions. In addition, the mean error quantity is defined the same as Eq. (6.27) to quantify the errors of the demand models; namely in Eq. (6.27) $\Pi_u$ is substituted by $u_{max,g}$ and $\theta_{max,g}$ respectively, $\Pi_{u,e}$ is substituted by $u_{max,e}$ and $\theta_{max,e}$ respectively, and $n$ equals to 12 for each bridge. Table 6.5 provides the comparison results using the above-mentioned three measures. As can be found from the table, the mean of $u_{max,e}/u_{max,g}$ is about 0.9 for all cases, and the associated standard deviation stays within the bound of 0.10 to 0.18. On the other hand, the mean of $\theta_{max,e}/\theta_{max,g}$ varies between 0.97 and 1.24, and the corresponding standard deviation ranges from 0.21 to 0.35 for all cases. The overall mean error for column drifts is between 12% and 17%, and the error for uplift angles is about 15%-33% for all cases. Given the complex dynamics in association of the rocking system, both these three measures validates that the proposed formulae are able to offer reliable predictions for the seismic demands of the system.

Table 6.4.   Selected twelve near-fault ground motions and their pulse representations

| GM No. | Earthquake event | Year | Station | Pulse Type | $A_p$ (m/s) | $a_p$ (g) | $\gamma$ | $v$ | $f_p$ (Hz) | $t_0$ (sec) |
|---|---|---|---|---|---|---|---|---|---|---|
| 1 | Kobe, Japan | 1995 | KJMA | Both | 1.28 | 0.79 | 2.0 | 60 | 1.03 | 8.3 |
| 2 | Loma Prieta | 1989 | Los Gatos - Lexington Dam | Both | -1.19 | 0.54 | 1.5 | 120 | 0.74 | 4.3 |
| 3 | Cape Mendocino | 1992 | Petrolia | Both | 1.07 | 0.57 | 1.2 | 0 | 0.96 | 3.1 |
| 4 | Northridge | 1994 | Simi Valley—Katherine Rd | Velocity | 0.77 | 0.60 | 1.8 | 0 | 1.37 | 5.3 |
| 5 | Yountville | 2000 | Napa FireStation#3 | Velocity | -0.41 | 0.39 | 2.0 | 150 | 1.53 | 13.1 |
| 6 | San Salvador | 1986 | Geotech InvestigCenter | Velocity | -0.85 | 0.63 | 1.6 | 0 | 1.31 | 1.3 |
| 7 | Aigion, Greece | 1995 | AEG | Velocity | -0.40 | 0.42 | 2.6 | 0 | 1.75 | 3.4 |
| 8 | San Salvador | 1986 | National GeograficalInst | Velocity | 0.55 | 0.47 | 1.5 | 90 | 1.35 | 1.9 |
| 9 | Chi-Chi | 1999 | CHY080 | Acceleration | 0.69 | 0.38 | 3.0 | 60 | 0.90 | 11.5 |
| 10 | Sierra Madre | 1991 | Altadena—Eaton Canyon | Acceleration | 0.33 | 0.42 | 1.5 | 60 | 2.17 | 2.8 |
| 11 | Coalinga | 1984 | Coalinga-14th &Elm(OldCHP) | Acceleration | 0.48 | 0.76 | 1.5 | 150 | 2.55 | 3.0 |
| 12 | Northridge | 1994 | Pacoima Dam(downstr) | Acceleration | -0.49 | 0.51 | 1.6 | 0 | 1.83 | 3.4 |
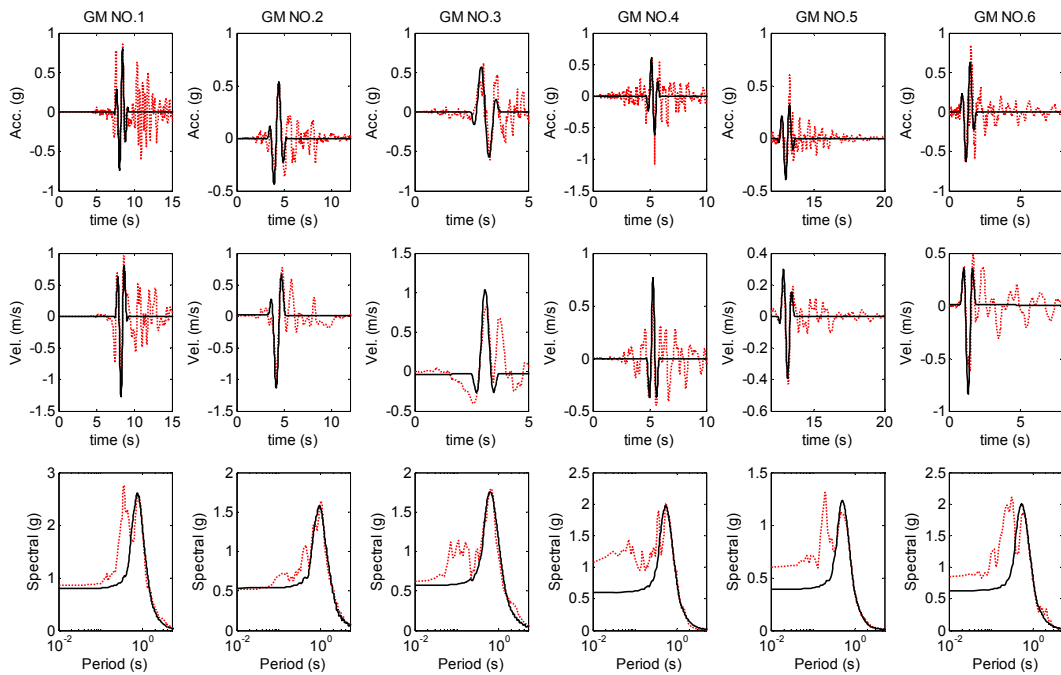


(a) Motion No.1 to No.6
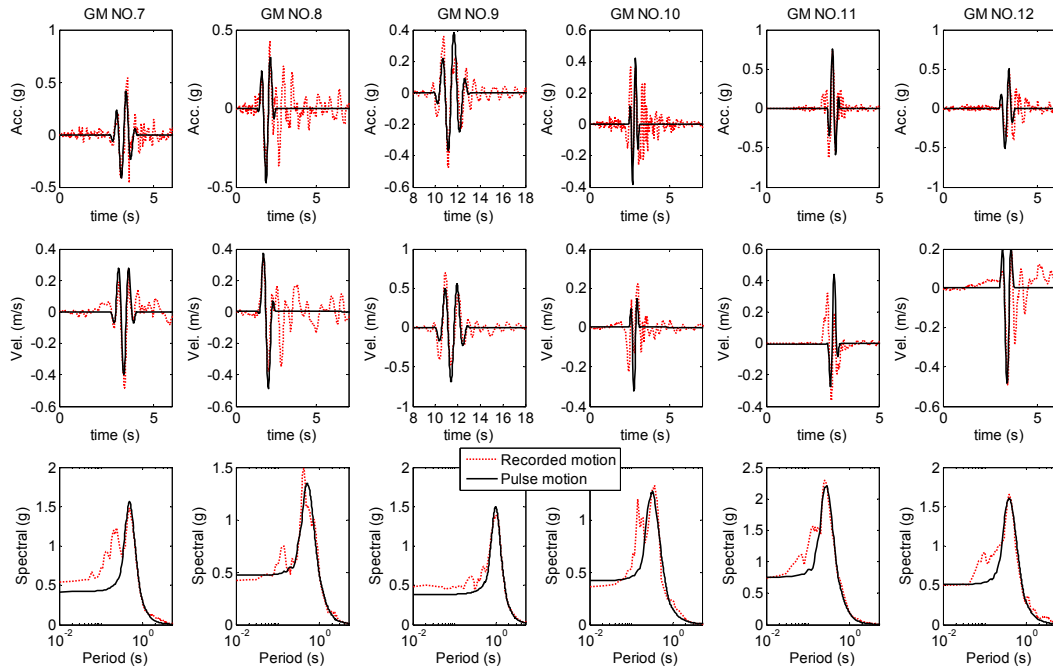
(b) Motion No.7 to No.12

Figure 6.9. Acceleration and velocity time histories, and acceleration response sepctra of the selected twelve near-fault ground motions and their pulse representations

Table 6.5. Validation of the proposed closed-form expressions of column drifts and uplift angles

| Cases | Bridges | $u_{\max,e}$ | | | $\theta_{\max,e}$ | | |
|---|---|---|---|---|---|---|---|
| | | Mean | Std | Error (%) | Mean | Std | Error (%) |
| 1 | Meloland Road Overcrossing (MRO) | 0.90 | 0.14 | 14% | 0.97 | 0.21 | 15% |
| 2 | Manning Avenue Overcrossing (MAO) | 0.86 | 0.10 | 16% | 1.24 | 0.33 | 32% |
| 3 | Manning Avenue Overcrossing (MAO) | 0.91 | 0.13 | 12% | 1.16 | 0.29 | 25% |
| 4 | South Paso Robles Overhead (SPRO) | 0.88 | 0.18 | 17% | 1.09 | 0.24 | 18% |
| 5 | Mondocino Avenue Bridge (MAB) | 0.88 | 0.15 | 15% | 1.20 | 0.35 | 33% |

In addition, Figure 6.10 compares the peak column drifts and uplift angles predicted by the proposed formulae with the numerical data, where $u_{\max,e}$ is plotted against $u_{\max,g}$ in the left two figures, and $\theta_{\max,e}$ is plotted against $\theta_{\max,g}$ in the right two figures. The top two figures show the comparisons that categorized by the bridge cases, while the data in the bottom two figures are

grouped by the pulse types of the input motions. It is evident from the top left figure that for the

column drift estimation, the worst scenario happens for the bridge case 4, resulting from the

fact that the column height in case 4 exceeds the range considered for formula derivation.

Meanwhile, the bottom right figure shows that the input ground motions with both velocity and

acceleration pulse characteristics will yield more deviated rotational demands than those

predicted by the formula.
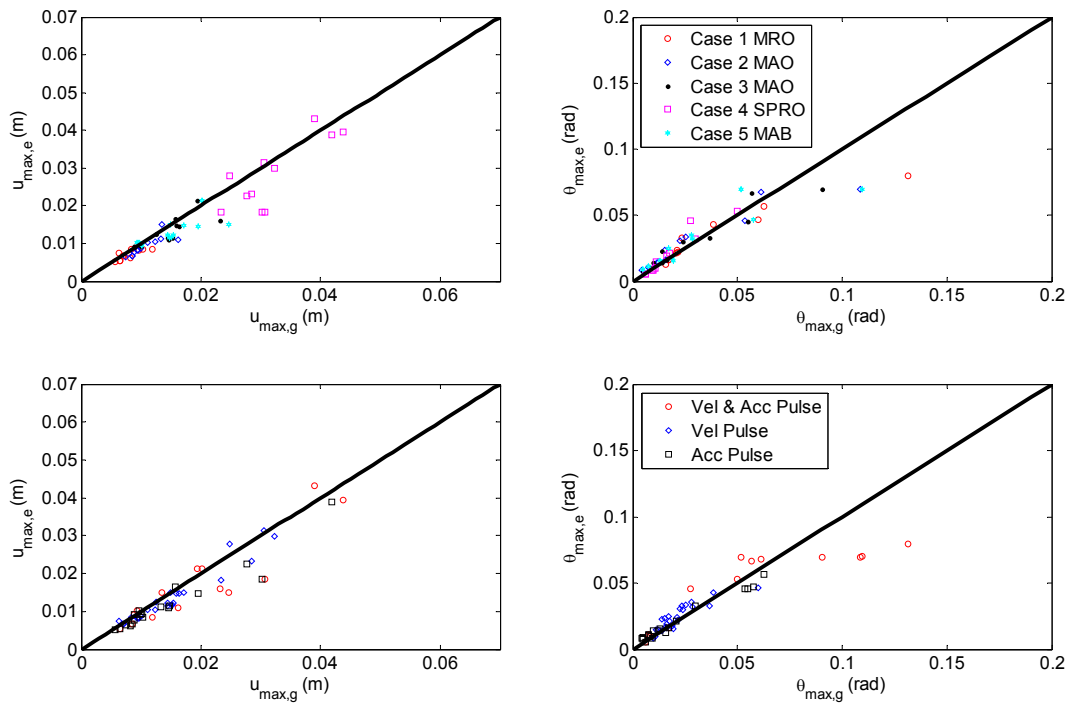


Figure 6.10.    Comparisons of peak column drifts and uplift angles with the predictions by
the proposed closed-form expressions and the numerical data

A time history comparison is provided in Figure 6.11 for bridge case 4 when subjected to

the motion No. 2. As can be seen from the figure, because the pulse representation only

captures the prevailing frequency of motion No. 2, a pace difference can be observed for the

drift and rotation time history responses when the recorded motion is substituted with the corresponding pulse. However, the M&P pulse used in this study is able to yield comparable responses when comparing with the seed motion results, which can be reflected by both the close peak responses and the matching trends in the time domain. Moreover, it can be found in the figure that the closed-form formulae are capable of providing almost identical peak response predictions for this case.
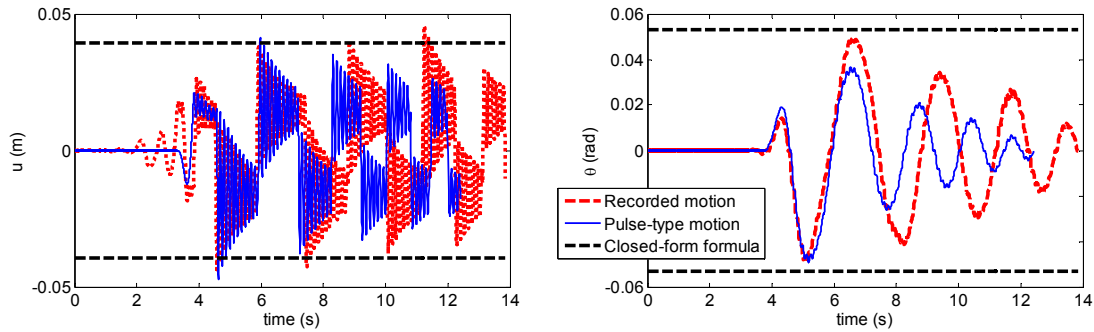


Figure 6.11.    Time history comparisons of bridge case 4 when subjected to motion No. 2

An equally important question for the proposed rocking system in this study lies in whether it indeed yields superior seismic performance when compared with the conventional design, namely the design with the fixed-base condition. To address this question, the bridge case 1 in Table 6.3 is selected and analyzed with the foundation base being fixed. The fiber-section element is built in OpenSees to incorporate the material nonlinearity and the column details, which include 18#18 longitudinal reinforcement bars and the 3 in. concrete cover. A 5% Rayleigh damping is considered for the fixed-base condition, given that considerable material nonlinearity is expected. Figure 6.12 illustrates the column drift history

188

comparisons for the rocking foundation case and the fixed-base case when subjected to motion No.3. As can be seen from the figure, a significant drift reduction can be achieved when the foundation is narrowed and designed for rocking. Moreover, by allowing the foundation to uplift, the permanent displacement of the column can be eliminated after earthquake excitation.
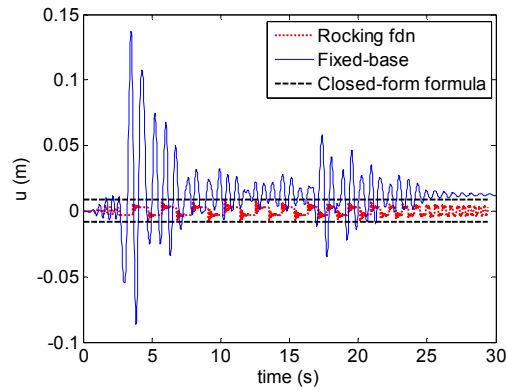


Figure 6.12.    Effectiveness of the rocking foundation for bridge case 1 when subjected to motion No. 3

## 6.4 CONCLUDING REMARKS

This chapter develops robust seismic demand models for the rocking columns with foundation on rigid supports subjected to horizontal near-fault motions. First, an analytical model is developed to establish the system EOMs that account for the superstructure mass inertia, the geometric nonlinearity, the column flexibility, the uplift condition, and the rocking impact. The transient drift and rocking responses of the system are solved through ordinary differential equations (ODE) method numerically. By representing the near-fault ground motions with M&P pulses, dimensional analyses are carried out to identify the corresponding functional dimensionless parameters for column drifts and uplift angles. Subsequently, a

sensitivity study and a two-step optimization procedure are carried out to regress the closed-form expressions for the drift and uplift demands as functions of ground motion characteristics, and column geometric and dynamic parameters. The derived demand models are physically convincing by reflecting the complex dynamics of the system. A rigorous validation process is carried out to examine the soundness of the derived models, where five as-built bridge cases are analyzed under twelve selected velocity and acceleration pulse-type motions. Compared to the simulation results under real earthquake scenarios, the proposed models are able to yield dependable predictions with the normalized errors less than 17% for column drift estimates and 33% for peak uplift angles. The error is larger for the top-pier case, and increases when the ground motions feature both velocity and acceleration pulse characteristics. In addition, a case study is provided to prove that both the peak and residual drifts of the column can be substantially reduced should the column is designed for rocking.

In summary, this study offers reliable models to estimate both the drift and uplift demands for the rocking column system. The proposed models are congruous with the underlying physics of the system and can be used with confidence in the assessment and design of the bridges with rocking columns.

# 7. CONCLUSIONS AND FUTURE WORK

## 7.1 CONCLUSIONS

This research addressed three main goals towards seismic resilient and sustainable highway bridges: (1) to derive robust modeling and analysis methodologies for bridge-foundation-soil systems under seismic shaking and liquefaction induced lateral spreading; (2) to develop performance-based evaluation, design and optimization frameworks for seismic protective devices for highway bridges; (3) to quantify the seismic responses of innovative devices, systems and technologies, such as the rocking column system, etc.

Recognizing that current simplified practical approaches, such as the substructure-based SSI provisions, fail to completely and accurately capture the various SSI effects associated with the highway bridge systems under strong shaking. This dissertation developed a step-by-step $p$-y spring based modeling approach to assess the seismic responses of highway bridges. Current procedures to compute the SSI effects for pile foundations, the depth varying ground motion inputs, and the embankment motion amplification effects were revisited and were implemented to the proposed method. Moreover, the nonlinear $p$-$y$ springs for embankments were originally derived based on nonlinear 2D and 3D continuum finite element analysis under passive loading condition along both longitudinal and transverse directions. The finite element analysis leaded to sound closed-form expressions for the two key input parameters of embankment $p$-$y$ models, namely the ultimate resistant force $p_{ult}$ and the displacement $y_{50}$, where $0.5p_{ult}$ is reached. The effectiveness of the proposed approach was examined by using it to simulate and validate the seismic responses of a well instrumented

highway overcrossing (the Painter Street Overcrossing) against the recorded responses under the 1992 Petrolia earthquake. It was shown through this case study that the flexibility and motion amplification at end abutments are the most crucial modeling aspects. The study also concluded that the proposed *p-y* modeling approach, including the closed-form *p-y* parameters, can realistically incorporate these two important aspects easily.

Subsequently, the seismic responses of the bridge-foundation-soil system under liquefaction induced lateral spreading were studied in this research. As a good candidate to balance between accuracy and efficiency, the dynamic *p-y* springs were still utilized. However, appropriate modeling modifications were considered to capture the distinct features associated with liquefaction induced lateral spreading, such as the use of the '*PyLiq*1' material that owns a stress-dependent ultimate capacity, the comparison of the individual mechanism and the block mechanism to determine the ultimate capacity of the crust clay layer, the pressure sensitive and insensitive soil materials used for the nonlinear site response analysis, as well as the pinning effect at end abutments due to liquefaction. Nonlinear time history responses were obtained for a benchmark bridge-foundation-soil system when it is subjected to a suite of input motions under lateral spreading (liquefaction) and seismic shaking (non-liquefaction) cases. To facilitate the practical application, a simplified response modification factor was derived to quantify the comparative influences of liquefaction induced lateral spreading on column drifts with respect to seismic shaking. Under seismic shaking, the column drift correlated well with the peak acceleration of the non-liquefied input motion at ground surface in addition to the dynamic characteristics of the bridge. Under lateral spreading and due to its near static loading

nature, the column drift related linear logarithmically to the crust layer energy imposed on the pile foundation at bridge piers, which was a function of the cumulative absolute velocity of non-liquefied ground motion at surface, the lateral resistances and geometric parameters of soil layers. By normalizing the column drift under the lateral spreading to that of under the seismic shaking, a closed-form expression was derived for the response modification factor. Additional multipliers were identified in the proposed formula to account for different bridge designs and soil conditions. The proposed method was validated against the simulation results for eight randomly selected bridge cases. This study concluded that the proposed model can effectively estimate the change of column drift due to lateral spreading with respect to seismic shaking.

The effectiveness of utilizing base isolators and energy dissipation devices to protect highway bridges against earthquake hazards was studied thoroughly in Chapter 4. The Painter Street Overcrossing that was considered in Chapter 2 was redesigned with seismic protective devices, where the three-dimensional stick model (i.e. the modeling scheme "Case 4" presented in Chapter 2) was adopted to model the bridge structure, and bilinear spring materials and dashpots were used to model the base isolators and fluid dampers, respectively. To effectively quantify the seismic vulnerability of the protected bridges in the system level, the bridge repair cost ratios under various levels of earthquake excitations were derived by using a performance-based methodology that accounts for the component failure probability, and the damage ratios and replacement costs of critical components. It was shown through an initial protection design that the proposed repair cost ratio can effectively quantify the seismic performance of highway bridges. Subsequently, a multi-objective genetic optimization method

with the Pareto optimal concept was employed to identify the optimal design parameters of protective designs for six design cases with various combinations of isolation bearings and fluid dampers. The optimal design parameters were identified as: (1) bearings' characteristic strength equals to 0.35 and 0.15 of columns' characteristic strength for the isolation only case and the case with both bearings and dampers, respectively; (2) bearings' post-yielding stiffness should be approximately 0.03 of columns' initial stiffness; (3) the additional damping ratio needs to be 33-44% when fluid dampers were used. This research also concluded that bearings' initial stiffness remains trivial in protecting highway bridges. In other words, as long as the above-mentioned two parameters, the characteristic strength and the post-yielding stiffness, were optimally designed, significant repair cost reductions could be achieved no matter which type of bearing is used. In addition, the combination of isolation bearings and fluid dampers would yield more excellent seismic protection when compared with the cases using only bearings.

Chapter 5 readdressed the evaluation and design of seismic protective devices for highway bridges in a probabilistic manner. To overcome the impediment that distinct protection designs would yield different fragility curves when conditioned on ground motion intensity measures, uniform fragility functions for various isolated bridge systems were developed by converting them as functions of the corresponding median-level engineering demand parameters (EDPs) instead. The multiple stripes analysis was carried out for various protected bridge systems to generate discrete fragility functions at distinct median EDP levels. The maximum likelihood concept was utilized to regress continuous curves for the discrete fragility functions.

Subsequently, the system-level repair cost ratio (RCR) that was derived in Chapter 4 was adopted in this chapter to generate the uniform RCR design surface as a function of multiple median EDPs. The derived RCR surface could be easily implemented to the performance-based seismic protection design and optimization framework without iteratively updating the design goal when a new group of design parameters were considered. A numerical example was conducted on the Painter Street Overcrossing, where performance-based genetic optimization was conducted to identify the optimal protection designs. The effectiveness of the identified optimal designs was further validated through the performance-based evaluation method that has been developed in Chapter 4.

Lastly, this study derived the seismic demand models for the rocking columns with foundation on rigid supports when subject to horizontal near-fault strong motions. The emphasis was placed to realistically predict the column drift and uplift responses for the rocking system. To achieve this goal, the system equations of motion were derived to account the superstructure mass inertia, the column flexibility, the uplift condition, and the rocking impact mechanism. The ordinary differential equations (ODE) method was utilized to solve the system's transient drift and rocking responses numerically. Given the complexity of the analytical derivation and the ODE method, this research developed transparent yet robust models to predict the peak responses of the rocking system. By representing the near-fault ground motions with corresponding pulses, dimensional analyses were carried out to regress the closed-form expressions of system's drift and uplift demands as functions of ground motion characteristics and column geometric and dynamic parameters. The derived sound demand

models not only quantified the influences of essential parameters, but also consistently reflected the complex dynamics of the rocking system. Thereafter, a validation process was carried out for five as-built bridge cases under twelve selected velocity and acceleration pulse-type motions. Compared to the simulation results under real earthquake scenarios, the proposed models was able to yield dependable predictions with small normalized errors. This study offered an innovative way to realistically predict the seismic demands of the rocking column-foundation system directly from structural and ground motion characteristics, which can significantly benefit the design of bridge columns incorporating the rocking column concept. In contrast with the conventional design, the rocking columns with foundation on rigid supports experienced superior seismic performance with less damage.

## 7.2 FUTURE WORK

Recommendations for future endeavors along the above-mentioned lines of research are summarized as follows:

(1) The dynamic $p$-$y$ springs that used to model the seismic performance of highway bridges under seismic shaking and liquefaction induced lateral spreading is one dimensional and is uncoupled in two orthogonal directions. The long-term goal that follows this research lies in the development of two-dimensional or three-dimensional coupled dynamic spring models to capture the soil structure interaction effects.

(2) The performance-based design and optimization method developed in Chapter 5 should be extended to a more general framework that incorporates both structural and protection design parameters, which will surely further improve the seismic performance of

highway bridges.

In addition, the general research scope addressed by this study enables the author to explore forward on relative subjects toward resilient and sustainable civil structures. Potential research interests include:

**(1)** *Analytical, numerical and experimental investigation of multi-hazard responses of structures*: This part of research focuses on the development of effective and efficient analysis tools for civil structure systems facing multiple threats, including aging and deterioration, and natural hazards such as earthquakes, tsunamis, hurricanes, floods, etc. Accurate modeling is necessary for individual structures and components, where supplemental analytical and experimental investigations must be carried out to reduce modeling uncertainties. Simulations based on advanced numerical models are entailed for understanding the key issues of the integrated systems under a multitude of hazards, such as the soil-foundation-structure systems in coastal regions under earthquakes, surge and wave hazards. Yet, simple and reliable analysis procedures under a unified framework have to be developed for practical applications. The laboratory and field tests, case histories, as well as the measurements from instrumented structures should be used to validate models and analysis procedures and provide key modeling parameters.

**(2)** *Resilience and sustainability based assessment and design frameworks for multiple hazards*: Current advancements in performance-based earthquake engineering and life cycle assessment should be extended to other types of natural hazards including hurricanes and floods. Transparent evaluation tools should be developed to link component-level engineering

measures to system-level socio-economic metrics, like life cycle costs (direct and indirect), environmental impacts and loss of functionality. Moreover, reliable quantitative methods are required to evaluate the resilience and sustainability for a portfolio of civil structures across communities. Integrated performance-based design frameworks are needed to account various hazards at the source and trade off multiple performance goals, where multi-objective optimization and decision-making frameworks are necessary for yielding optimal designs across different hazards. Frameworks like these would provide policy makers with information to plan more resilient and sustainable civil structure networks while engaging government, industry and private stakeholders.

**(3)** *Investigation of innovative materials, devices, systems and technologies for multi-hazard mitigation*: Many improvements and significant research work can be conducted for this part of research including investigating the reliability and effectiveness of smart materials, systems and technologies when facing a wide variety of conditions; identifying the optimal measures that can mitigate multiple hazards, and their roles as elements of large-scale distributed building and infrastructure systems.

# REFERENCES

Acikgoz S, DeJong MJ. Analytical modelling of multi-mass flexible rocking structures. *Earthquake Engineering and Structural Dynamics* 2016; DOI: 10.1002/eqe.2735.

Acikgoz S, DeJong MJ. The interaction of elasticity and rocking in flexible structures allowed to uplift. *Earthquake Engineering and Structural Dynamics* 2012; 41(15): 2177-2194.

Adeli H, Cheng NT. Concurrent genetic algorithms for optimization of large structures. *Journal of Aerospace Engineering* 1994; 7(3):276-96.

Agrawal AK, Nagarajaiah S. Benchmark structural control problem for a seismically excited highway bridge: Phase I and II. *Structural Control and Health Monitoring* 2009; 16: 503-508

Agrawal A, and Amjadian M. Chapter 20 - Seismic component devices, *Innovative Bridge Design Handbook*, Butterworth-Heinemann, Boston, 2016; 531-553, ISBN 9780128000588, http://dx.doi.org/10.1016/B978-0-12-800058-8.00020-7.

Agrawal A, Ghosn M, Alampalli S, Pan Y. Seismic Fragility of Retrofitted Multispan Continuous Steel Bridges in New York. *Journal of Bridge Engineering*, 2012; 10.1061/(ASCE)BE.1943-5592.0000290, 562-575.

Agrawal A, Tan P, Nagarajaiah S, Zhang J. Benchmark structural control problem for a seismically excited highway bridge-Part I: Phase I Problem definition. *Structural Control and Health Monitoring* 2009; 16:5, 509-529.

Alavi B, Krawinkler H. Effects of near-fault ground motions on frame structures. *John A. Blume Earthquake Engineering Center Report No. 138*, Stanford University, February 2001.

Al-Homoud AS, Whitman RV. Seismic analysis and design of rigid bridge abutments considering rotation and sliding incorporating non-linear soil behavior. *Soil Dynamics and Earthquake Engineering* 1999; 18(4): 247-277.

Alipour A, Shafei B, Shinozuka M. Performance evaluation of deteriorating highway bridges located in high seismic areas. *Journal of Bridge Engineering*. 2010 Nov 12; 16(5):597-611.

Allotey N, Naggar MHE. Generalized dynamic Winkler model for nonlinear soil–structure interaction analysis. *Canadian Geotechnical Journal* 2008; 45(4): 560-573.

American Association of State Highway and Transportation Officials (AASHTO) (2014). *Guide Specifications for Seismic Isolation Design (4th Edition)*, Washington, DC.

American Petroleum Institute (API). *Recommended practice for planning, designing and constructing fixed offshore platforms--Working stress design*, (20th edn), Washington, D.C., 1993.

Antonellis G, Gavras AG, Panagiotou M, Kutter BL, Guerrini G, Sander AC, Fox PJ. Shake table test of large-scale bridge columns supported on rocking shallow foundations. *Journal of Geotechnical and Geoenvironmental Engineering* 2015; 141(5):04015009.

Antonellis G, Panagiotou M. Seismic response of bridges with rocking foundations compared to fixed-base bridges at a near-fault site. *Journal of Bridge Engineering* 2013; 19(5).

Aygun B, Dueñas-Osorio L, Padgett JE, DesRoches R. Efficient longitudinal seismic fragility assessment of a multispan continuous steel bridge on liquefiable soils. *Journal of Bridge Engineering* 2011; 16(1):93-107.

Badoni D, Makris N. Nonlinear response of single piles under lateral inertial and seismic loads. *Soil Dynamics and Earthquake Engineering* 1996; 15(1): 29-43.

Baker JW, Cornell CA. Vector-valued ground motion intensity measures for probabilistic seismic demand analysis. *PEER report 2006/08*. Berkeley: Pacific Earthquake Engineering Research Center, University of California Berkeley; 2006

Baker JW, Lin T, Shahi SK, Jayaram N. New ground motion selection procedures and selected motions for the PEER transportation research program. *Report No. 2011/03*, Pacific Earthquake Engineering Research Center, University of California, Berkeley, CA, 2011.

Baker JW. Efficient analytical fragility function fitting using dynamic structural analysis. *Earthquake Spectra*. 2015 Feb;31(1):579-99.

Baker JW. Quantitative classification of near-fault ground motions using wavelet analysis. *Bulletin of the Seismological Society of America* 2007; 97(5):1486-1501.

Barenblatt GI. *Scaling, Self-Similarity, and Intermediate Asymptotics*. Cambridge University Press: Cambridge, U.K., 1996.

Barthes CB. *Design of earthquake resistant bridges using rocking columns*, PhD Thesis, 2012, UC Berkeley, USA.

Basoz NI, Kiremidjian AS, King SA, and Law KH. Statistical analysis of bridge damage date from the 1994 Northridge, CA, earthquake. *Earthquake Spectra*, 1999; 15(1), 25-54.

Billah AM, Alam MS, Bhuiyan MR. Fragility analysis of retrofitted multicolumn bridge bent subjected to near-fault and far-field ground motion. *Journal of Bridge Engineering*. 2012 Nov 8; 18(10):992-1004.

Boulanger RW, Chang D, Gulerce U, Brandenberg SJ, and Kutter BL. Evaluating pile pinning effects on abutments over liquefied ground. *Proc., Seismic Performance and Simulation of Pile Foundations in Liquefied and Laterally Spreading Ground*, Reston, VA, 2006; 306-318.

Boulanger RW, Curras C, Kutter B, Wilson D, and Abghari A. Seismic Soil-Pile-Structure Interaction Experiments and Analyses. *Journal of Geotechnical and Geoenvironmental Engineering* 1999; 125(9):750-759.

Boulanger RW, Ziotopoulou K. PM4Sand (Version 2): A sand plasticity model for earthquake engineering applications. *Report no. UCD/CGM-12/01*, center for Geotechnical Modeling, Department of Civil and Environmental Engineering, University of California, Davis, CA; 2012.

Bradley BA, Cubrinovski M, Dhakal RP, MacRae GA. Probabilistic seismic performance and loss assessment of a bridge–foundation–soil system. *Soil Dynamics and Earthquake Engineering*. 2010 May 31; 30(5):395-411.

Brandenberg SJ, Boulanger RW, Kutter BL, and Chang, D. Liquefaction-induced softening of load transfer between pile groups and laterally spreading crusts. *Journal of Geotechnical and Geoenvironmental Engineering* 2007; 133(1), 91-103.

Brandenberg SJ, Boulanger RW, Kutter BL, Chang D. Behavior of pile foundations in laterally spreading ground during centrifuge tests. *Journal of Geotechnical and Geoenvironmental Engineering* 2005; 131(11):1378-1391.

Brandenberg SJ, Zhao M, Boulanger R, Wilson DW. *p-y* plasticity model for nonlinear dynamic analysis of piles in liquefiable soil. *Journal of Geotechnical and Geoenvironmental Engineering* 2012; 139(8): 1262-1274.

Bray JD, Rodriguez-Marek A. Characterization of forward-directivity ground motions in the near-fault region. *Soil Dynamics and Earthquake Engineering* 2004; 24(11):815-828.

Buckle IG, Mayes RL. Seismic isolation: history, application, and performance-a world view. *Earthquake spectra*. 1990; 6(2):161-201.

Caltrans. The Continuing Challenge: the Northridge Earthquake of January 17, 1994, *Report to the Director*, 1994, California Department of Transportation, Sacramento, CA.

Caltrans. *Guidelines on Foundation Loading and Deformation due to Liquefaction Induced Lateral Spreading*, California Department of Transportation, Sacramento, CA. Originally published 2011; revised 2013.

Caquot, A. I., and Kerisel, J. Tables for the calculation of passive pressure, active pressure, and bearing capacity of foundations. *Libraire du Bureau des Longitudes, de L'ecole Polytechnique, Paris Gauthier- villars, Imprimeur-Editeur*, 120, 1948.

Carbonari S, Dezi F, Leoni G. Seismic soil-structure interaction in multi-span bridges: application to a railway bridge. *Earthquake Engineering and Structural Dynamics* 2011; 40(11):1219-1239.

Cha YJ, Agrawal AK, Kim Y, Raich AM. Multi-objective genetic algorithms for cost-effective distributions of actuators and sensors in large structures. *Expert Systems with Applications*. 2012 Jul 31; 39(9):7822-33.

Cha YJ, Raich A, Barroso L, Agrawal A. Optimal placement of active control devices and sensors in frame structures using multi-objective genetic algorithms. *Structural Control and Health Monitoring* 2013; 10.1002/stc.468, 20, 16-44.

Chang KC, Chang DW, Tsai MH, Sung YC. Seismic performance of highway bridges. *Earthquake Engineering and Engineering Seismology* 2000; 2(1):55-77.

Chaudhary MTA, Abe M, Fujino Y. Identification of soil-structure interaction effect in base-isolated bridges from earthquake records. *Soil Dynamics and Earthquake Engineering* 2001; 21:713-725.

Choi E, DesRoches R, Nielson B. Seismic fragility of typical bridges in moderate seismic zones. *Engineering Structures* 2004; 26:187-199.

Choi E, Park J, Yoon SJ, Choi DH, Park C. Comparison of seismic performance of three restrainers for multiple-span bridges using fragility analysis. *Nonlinear Dynamics* 2010; 61(1):83-99.

Choi J, Kim M, Brandenberg S. Cyclic p-y plasticity model applied to pile foundations in sand. *Journal of Geotechnical and Geoenvironmental Engineering* 2015; 141(5): 04015013.

Choi E, DesRoches R, Nielson BG. Seismic fragility of typical bridges in moderate seismic zones. *Engineering Structures* 2004; 26(2), 187-199.

Chopra A, Yim SC. Simplified earthquake analysis of structures with foundation uplift. *Journal of Structural Engineering* (ASCE) 1985; 111(4):906-930.

Chu DB, Brandenberg SJ, and Lin PS. Performance of bridges in liquefied ground during 1999 Chi-Chi earthquake. *14th World Conference on Earthquake Engineering*, Beijing, 2008.

Combescure D, Pegon P. α-operator splitting time integration technique for pseudodynamic testing-error propagation analysis. *Soil Dynamics and Earthquake Engineering* 1997; 16: 427-443.

Cornell CA, Jalayer F, Hamburger RO, Foutch DA. Probabilistic basis for 2000 SAC federal emergency management agency steel moment frame guidelines. *Journal of Structural Engineering* 2002; 128(4):526-33.

Crouse CB, Hushmand B, Martin GR. Dynamic soil–structure interaction of single-span bridge. *Earthquake Engineering and Structural Dynamics* 1987; 15:711-729.

Curras CJ, Boulanger RW, Kutter BL, Wilson DW. Dynamic experiments and analyses of a pile-group-supported structure. *Journal of Geotechnical and Geoenvironmental Engineering* 2001; 127(7): 585-596.

Deb K, Pratap A, Agrawal S, and Meyarivan T. A fast and elitist multi-objective genetic algorithm: NSGA-II. *IEEE Transactions on Evolutionary Computation*, Piscataway, N.J., 2002; 6(2), 182-197.

Deepu SP, Prajapat K, Ray-Chaudhuri S. Seismic vulnerability of skew bridges under bi-directional ground motions. *Engineering Structures*. 2014; 71:150-60.

Delis EA, Malla RB, Madani M, Thompson KJ. Energy dissipation devices in bridges using hydraulic dampers. *Proceedings of the Structures Congress XIV*, Chicago, IL, vol. 2, 1996; 1188 -1196.

Deng L, Kutter BL, Kunnath SK. Probabilistic seismic performance of rocking-foundation and hinging-column bridges. *Earthquake Spectra* 2012; 28(4):1423-1446.

Deng L, Kutter BL, Kunnath SK. Seismic design of rocking shallow foundations: displacement-based method-ology. *ASCE Journal of Bridge Engineering* 2014. DOI:10.1061/(ASCE)BE.1943-5592.0000616.

Dezi F, Carbonari S, Leoni G. A model for the 3D kinematic interaction analysis of pile groups in layered soils. *Earthquake Engineering and Structural Dynamics* 2009; 38(11):1281-1305.

Dimitrakopoulos EG, DeJong MJ. Overturning of retrofitted rocking structures under pulse-type excitations. *Journal of Engineering Mechanics* (ASCE) 2012; 138(8):963-972.

Dobry R, Gazetas G. Simple method for dynamic stiffness and damping of floating pile groups. *Geotechnique*. 1988; 38(4):557-74.

Dong Y, Frangopol DM, Saydam D. Time-variant sustainability assessment of seismically vulnerable bridges subjected to multiple hazards. *Earthquake Engineering & Structural Dynamics* 2013; 42(10):1451-67.

Elgamal A, Yan L, Yang Z, Conte J. Three-dimensional seismic response of Humboldt Bay bridge-foundation-ground system. *Journal of Structural Engineering* 2008; 134(7): 1165-1176.

Espinoza A, Mahin S. Seismic performance of reinforced concrete bridges allowed to uplift during multi-directional excitation. *PEER 2012-02*, Pacific Earthquake Engineering Research Center, Berkeley, CA, 2012.

Federal Highway Administration (FHWA). Seismic retrofitting manual for highway structures: Part 1-Bridges, *Publication No. FHWA-HRT-06-032*, Research, Development, and Technology Turner-Fairbank Highway Research Center, McLean, Va, 2006.

FEMA, F. E. M. A. Multi-hazard loss estimation methodology, Earthquake model. *HAZUS®MH MR4- Technical Manual*. FEMA Mitigation Division, Washington, D.C., 2003.

Gluck N, Reinhorn A, Gluck J, Levy R. Design of Supplemental Dampers for Control of Structures. *Journal of Structural Engineering* 1996; 10.1061/(ASCE)0733-9445(1996)122:12(1394), 1394-1399.

Goel RK, Chopra AK. Evaluation of bridge abutment capacity and stiffness during earthquakes. *Earthquake Spectra* 1997; 13(1): 1-23.

Gordon E. A Seismic Risk Model for A Designated Highway System: Comparing Predicted Actual Damage from the Loma Prieta Earthquake. *Mid-America Earthquake Center*, 2002.

Hakhamaneshi M, Kutter BL. Effect of Footing Shape and Embedment on the Settlement, Recentering, and Energy Dissipation of Shallow Footings Subjected to Rocking. *Journal of Geotechnical and Geoenvironmental Engineering* 2016; 142(12):04016070.

Hall JF, Heaton TH, Halling MW, Wald DJ. Near source ground motion and its effects on flexible buildings. *Earthquake Spectra* 1995; 11(4):569-605.

Hamada M, O'Rourke T. Case studies of liquefaction and lifeline performance during past earthquakes. *Japanese Case Studies Technical Rep NCEER-92-0001*, Hamada M, O'Rourke TD (eds.). National Center for Earthquake Engineering Research: Buffalo, N.Y., 1992.

Han Q, Du XL, Liu JB, Li ZX, Li LY, Zhao JF. Seismic Damage of Highway Bridges during the 2008 Wenchuan Earthquake, *Earthquake Engineering and Engineering Vibration* 2009; 8(2), 263-273.

He WL, Agrawal AK. Analytical model of ground motion pulses for the design and assessment of seismic protective systems. *Journal of Structural Engineering* 2008; 134(7):1177-1188.

Hogan SJ. The many steady state responses of a rigid block under harmonic forcing. *Earthquake Engineering and Structural Dynamics* 1990; 19(7): 1057-1071.

Housner GW. The behaviour of inverted pendulum structures during earthquakes. *Bulletin of the Seismological Society of America* 1963; 53(2):404-417.

Housner GW, Bergman LA, Caughey TK, Chassiakos AG, Claus RO, Masri SF, Skelton RE, Soong TT, Spencer BF, and Yao JTP. Structural Control: Past, Present, and Future. *Journal of Engineering Mechanics*, 1997; 123:9, 897-971.

Huo Y, Zhang J. Effects of pounding and skewness on seismic responses of typical multispan highway bridges using the fragility function method. *Journal of Bridge Engineering*. 2012 May 14;18(6):499-515.

Huo Y. *Seismic Response Assessment and Improvement of Highway Bridges Using Fragility Function Method*. University of California, Los Angeles, CA, 2011.

Hwang H, Liu JB, Chiu Y. *Seismic fragility analysis of highway bridges*. (http://hdl.handle.net/2142/9267) (March 12, 2010)

Idriss I, Sun JI. *User's manual for SHAKE91*. Davis, CA: Department of Civil and Environmental Engineering, University of California Davis 1992.

Iwasaki T, Tatsuoka F, Takagi Y. Shear moduli of sands under cyclic torsional shear loading. *Soils and Foundations* 1978; 18(1):39-56.

Jangid RS. Optimum friction pendulum system for near-fault motions. *Engineering Structures* 2005; 27, 349-359.

Jangid, RS. Optimal lead-rubber isolation bearings for near-fault motions. *Engineering Structures* 2007; 29, 2503-2513.

Jennings PC, Wood JH. Earthquake damage to freeway structures, Engineering Features of the San Fernando Earthquake, 9 February 1971. *Report EERL 71-02*, California Institute of Technology, Earthquake Engineering Research Laboratory, Pasadena, CA, 1971.

Jeremic   B, Jie   G, Preisig   M, Tafazzoli   N. Time   domain   simulation   of soil-foundation-structure interaction in non-uniform soils. *Earthquake Engineering and Structural Dynamics* 2009; 38(5):699-718.

Jiang X, Adeli H. Neuro-genetic algorithm for nonlinear active control of structures. *International Journal for Numerical Methods in Engineering* 2008; 75(7):770-86.

Kalkan E, Kunnath SK. Effects of fling step and forward directivity on seismic response of buildings. *Earthquake Spectra* 2006; 22(2):367-390.

Kampas G, Makris N. Modal identification of freeway overcrossings with soil-structure interaction: a case study. *Structural Control and Health Monitoring* 2013; 20(3): 304-319.

Kappos AJ, Manolis GD, and Moschonas IF. Seismic assessment and design of R/C bridges with irregular configuration, including SSI effects. *Engineering Structures* 2002; 24: 1337-1348.

Karavasilis TL, Seo CY, Makris N. Dimensional response analysis of bilinear systems subjected to non-pulse like earthquake ground motions. *Journal of Structural Engineering* 2011; 137(5):600-606.

Karim KR, and Yamazaki F. Effect of earthquake ground motions on fragility curves of highway bridge piers based on numerical simulation. *Earthquake Engineering and Structural Dynamics* 2001; 30(12), 1839-1856.

Karim KR, and Yamazaki F. Effect of isolation on fragility curves of highway bridges based on simplified approach. *Soil Dynamics and Earthquake Engineering* 2007; 27(5), 414-426.

Kaynia AM, Kausel E. Dynamic stiffness and seismic response of sleeved piles. *Report No. R80-12*. Cambridge, Mass.: Massachusetts Institute of Technology 1982.

Kelly JM, Quiroz E. Mechanical Characteristics Neoprene Isolations Bearings. *Report No. UBC/EERC-92/11*, University of California at Berkeley, 1992.

Kim HS, Roschke PN. Fuzzy Control of Base‐Isolation System Using Multi-Objective Genetic Algorithm. *Computer‐Aided Civil and Infrastructure Engineering*. 2006; 21(6):436-49.

Kiremidjian A, Moore J, Fan YY, Basoz N, Yazali O, and Williams M, Pacific earthquake engineering research center highway demonstration project, *Report No. 2006/02*, Pacific Earthquake Engineering Research Center, University of California, Berkeley, CA, 2006.

Kiremidjian A, Basoz N. Evalution of bridge damage data from recent earthquakes. *MCEER/NCEER Bulletin* 11(2): MCEER at Buffalo, NY, 1997.

Konak A, Coit DW, Smith AE. Multi-objective optimization using genetic algorithms: A tutorial. *Reliability Engineering & System Safety* 2006; 91(9), 992-1007.

Kramer SL, Arduino P, and Shin HS. Using OpenSees for performance-based evaluation of bridges on liquefiable soils, *Report No. 2008/07*, Pacific Earthquake Engineering Research Center, University of California, Berkeley, CA, 2008.

Kunde MC, Jangid RS. Seismic behavior of isolated bridges: A-state-of-the-art review. Electronic. *Journal of Structural Engineering* 2003; 3(2):140-69.

Kutter BL, Moore M, Hakhamaneshi M, Champion C. Rationale for shallow foundation rocking provisions in ASCE 41-13. *Earthquake Spectra* 2016; 32(2):1097-119.

Kwon OS, Elnashai AS. Seismic analysis of Meloland road overcrossing using multiplatform simulation software including SSI. *Journal of Structural Engineering* 2008; 134(4):651-660.

Kwon OS, Elnashai AS, and Spencer BF. A framework for distributed analytical and hybrid simulations. *Structural Engineering and Mechanics*, 2008; 30:3, 331-350.

Kwon OS, Nakata N, Park KS, Elnashai AS, and Spencer BF. *User manual and examples for UI-SIMCOR v2.6*. Department of Civil and Environmental Engineering, University of Illinois at Urbana-Champaign, Urbana, Illinois, 2007.

Lemnitzer A, Ahlberg ER, Nigbor RL, Shamsabadi A, Wallace JW, Stewart JP. Lateral performance of full-scale bridge abutment wall with granular backfill. *Journal of Geotechnical and Geoenvironmental Engineering* 2009; 135(4): 506-514.

Lesgidis N, Kwon O, Sextos A. A time-domain seismic SSI analysis method for inelastic bridge structures through the use of a frequency-dependent lumped parameter model. *Earthquake Engineering and Structural Dynamics* 2015; DOI: 10.1002/eqe.2573

Liu W, Hutchinson TC, Kutter BL, Hakhamaneshi M, Aschheim MA, Kunnath SK. Demonstration of compatible yielding between soil-foundation and superstructure components. *Journal of Structural Engineering* 2013; 139(8):1408-1420.

Lu J, Elgamal A, Yan L, Law KH, Conte JP. Large scale numerical modeling in geotechnical earthquake engineering. *International Journal of Geomechanics* 2011; 1943-56.

Mackie K, and Stojadinovic B. Fragility basis for California highway overpass bridge seismic decision making. *PEER Rep. 2005-02*, Pacific Earthquake Engineering Research Center, Berkeley, CA, 2005.

Makris N, Badoni D, Delis E, Gazetas G. Prediction of observed bridge response with soil-pile-structure interaction. *Journal of Structural Engineering* 1994; 120(10):2992-3011.

Makris N, Black CJ. Dimensional analysis of bilinear oscillators under pulse-type excitations. *Journal of Engineering Mechanics (ASCE)* 2004; 130(9):1019-1031.

Makris N, Black CJ. Dimensional analysis of rigid-plastic and elastoplastic structures under pulse type excitations. *Journal of Engineering Mechanics (ASCE)* 2004; 130(9):1006-1018.

Makris N, Chang SP. Effect of viscous, viscoplastic and friction damping on the response of seismic isolated structures. *Earthquake Engineering and Structural Dynamics* 2000; 29(1):85-107.

Makris N, Konstantinidis D. The rocking spectrum and the limitations of practical design methodologies. *Earthquake Engineering and Structural Dynamics* 2003; 32: 265-289.

Makris N, Vassiliou MF. Planar rocking response and stability analysis of an array of free standing columns capped with a freely supported rigid beam. *Earthquake Engineering and Structural Dynamics* 2013; 42(3): 431-449.

Makris N, Zhang J. Rocking response of anchored blocks under pulse-type motions. *Journal of Engineering Mechanics ASCE* 2001; 127(5):484-493.

Makris N. Rigidity-plasticity-viscosity: can electrorheological dampers protect base-isolated structures from near-source ground motions? *Earthquake Engineering and Structural Dynamics 1997*; 26(5):571-591.

Makris N, Zhang J. Seismic response analysis of a highway overcrossing equipped with elastomeric bearings and fluid dampers. *Journal of Structural Engineering (ASCE)* 2004; 130(6):830-845.

Maroney B, Romstad K, Chajes M. Interpretation of Rio Del freeway response during six recorded earthquake events. *Proc. 4th U.S. National Conference on Earthquake Engineering* 1990; (1): 1007-16.

Matlock H, Foo SHC, Bryant LM. Simulation of lateral pile behavior under earthquake motion. *Proceedings of the Specialty Conference on Earthquake Engineering and Soil Dynamics*, ASCE, Pasadena, Calif., 1978: 600-619.

Matlock H. Correlations for design of laterally loaded piles in soft clay. *Proceedings of the 2nd Annual Offshore Technology Conference*, vol. 1. Houston, TX, Paper ITC 1204, 1970; 577-594.

Mavroeidis GP, Papageorgiou AS. A mathematical representation of near-fault ground motions. *Bulletin of the Seismological Society of America* 2003; 93:1099-1131.

Mayes RL, Buckle IG, Kelly TE, Jones LR. AASHTO seismic isolation design requirements for highway bridges. *Journal of Structural Engineering*. 1992; 118(1):284-304.

Mazzoni S, McKenna F, Scott MH, Fenves GL, et al. *OpenSees Command Language Manual*. University of California Berkeley. 2006.

McCallen DB, Romstad KM. Dynamic analysis of a skewed short-span, box-girder overpass. *Earthquake Spectra* 1994; 10(4):729-755.

Mori A, Moss PJ, Cooke N, Carr AJ. Behavior of bearings used for seismic isolation under shear and axial load. *Earthquake Spectra* 1999; 15:199-224.

Muntasir Billah AH, Alam MS. Seismic fragility assessment of concrete bridge pier reinforced with superelastic shape memory alloy. *Earthquake Spectra*. 2015; 31(3):1515-41.

Mylonakis G, Kloukinas P, Papantonopoulos C. An alternative to the Mononobe-Okabe equations for seismic earth pressures. *Soil Dynamics and Earthquake Engineering* 2007; 27(10): 957-969.

Naeim F, Kelly JM. *Design of Seismic Isolated Structures: From Theory to Practice*, John Wiley & Sons, New York, USA, 1999.

Narasimhan S. Robust direct adaptive controller for the nonlinear highway bridge benchmark. *Structural Control and Health Monitoring*. 2009; 16(6):599-612.

Narasimhan S, Nagarajaiah S, Johnson EA, Gavin HP. Smart base isolated benchmark building. Part I: Problem definition. *Journal of Structural Control and Health Monitoring* 2006; 13(2-3):573-588.

Nielson BG, DesRoches R. Seismic fragility methodology for highway bridges using a component level approach. *Earthquake Engineering and Structural Dynamics* 2007; 36:823-839.

Nogami T, Otani J, Konagai K, Chen H. Nonlinear soil-pile interaction model for dynamic lateral motion. *Journal of Geotechnical Engineering* 1992; 118(1): 89-106.

Novak M, Sheta M. Approximate approach to contact effects of piles. Dynamic response of pile foundations: analytical aspects, *Proc. Specialty Session, ASCE National Convention* 1980: 53-79.

Oliveto G, Caliò I, Greco A. Large displacement behaviour of a structural model with foundation uplift under impulsive and earthquake excitations. *Earthquake Engineering and Structural Dynamics* 2003; 32: 369-393.

Ozbulut OE, Hurlebaus S. Optimal design of superelastic-friction base isolators for seismic protection of highway bridges against near-field earthquakes. *Earthquake Engineering and Structural Dynamics* 2011; 40:273-291.

Padgett JE, DesRoches R. Methodology for the development of analytical fragility curves for retrofitted bridges. *Earthquake Engineering and Structural Dynamics* 2008; 37(8): 1157-74.

Padgett JE, Nielson B, DesRoches R. Selection of optimal intensity measures in probabilistic seismic demand models of highway bridge portfolios. *Earthquake Engineering and Structural Dynamics* 2008; 37(5), 711-725. DOI: 10.1002/eqe.782.

Poulos HG. Analysis of the settlement of pile groups. *Geotechnique* 1968; 18(4): 449-71.

Price TE, Eberhard MO. Factors contributing to bridge-embankment interaction. *Journal of Structural Engineering* 2005; 131(9):1345-1354.

Priestley MJN, Seible F, Calvi GM. *Seismic design and retrofit of bridges*. Wiley, New York, 1996.

Psycharis IN, Jennings PC. Rocking of slender rigid bodies allowed to uplift. *Earthquake Engineering and Structural Dynamics* 1983; 11: 57-76.

Rahimi M, Yun G and Shang S. Inverse estimations of dynamic stiffness of highway bridge embankment from earthquake records. *Journal of Bridge Engineering* 2012; 19(8): A4014005.

Rahmani A, Taiebat M, Finn WDL. Nonlinear dynamic analysis of Meloland road overpass using three-dimensional continuum modeling approach. *Soil Dynamics and Earthquake Engineering* 2014; 57: 121-132.

Reinhorn AM, Lavan O, Cimellaro GP. Design of controlled elastic and inelastic structures. *Earthquake Engineering and Engineering Vibration* 2009; 8(4):469-79.

Richards RJ, Elms D. Seismic behavior of gravity retaining walls. *Journal of the Geotechnical Engineering Division*, 1979; 105(4): 449-464.

Roesset JM. Dynamic stiffness of pile groups. *In Pile Foundations*. New York: ASCE 1984.

Sanchez-Salinero I. Dynamic stiffness of pile groups: approximate solutions. *Geotechnical Engineering Report No. GR83-5*. Austin, Texas: University of Texas 1983.

Seed HB, Idriss IM. Soil moduli and damping factors for dynamic response analysis. *Report No. EERC 70 -10*, University of California, Berkeley, CA, 1970.

Seible F, Priestley MJ. Lessons learned from bridge performance during Northridge earthquake. *Special Publication*. 1999; 187:29-56.

Shamsabadi A, Khalili-Tehrani P, Stewart JP, Taciroglu E. Validated simulation models for lateral response of bridge abutments with typical backfills. *Journal of Bridge Engineering* 2010; 15 (3): 302-311.

Shinozuka M, Feng MQ, Lee J, Naganuma T. Statistical analysis of fragility curves. *Journal of engineering mechanics*. 2000; 126(12):1224-31.

Siqueira GH, Sanda AS, Paultre P, Padgett JE. Fragility curves for isolated bridges in eastern Canada using experimental results. *Engineering Structures* 2014; 74:311-24.

Skinner RI, Robinson WH, and McVerry GH. *An introduction to seismic isolation*. Wiley, New York, 1993.

Sokolovski VV. *Statics of granular media*. London: Pergamon Press. 1965.

Soneji BB, Jangid RS. Passive hybrid systems for earthquake protection of cable-stayed bridge. *Engineering Structures* 2007; 29(1):57-70.

Soong TT. *Active Structural Control: Theory and Practice.* Longman Scientific, London, 1990.

Soong T, Dargush GF. *Passive Energy Dissipation Systems in Structural Engineering*. Wiley, New York, USA, 1997.

Spencer Jr BF, Nagarajaiah S. State of the art of structural control. *Journal of structural engineering* 2003; 129(7):845-56.

Symans MD, Constantinou MC. Passive fluid viscous damping systems for seismic energy dissipation. *ISET Journal of Earthquake Technology* 1998; 35(4):185-206.

Tang Y, Zhang J. Response spectrum-oriented pulse identification and magnitude scaling of forward directivity pulses in near-fault ground motions. *Soil Dynamics and Earthquake Engineering* 2011; 31: 59-76.

Tarakji G. Lessons not Learned from 1989 Loma Prieta Earthquake. *Journal of Professional Issues in Engineering Education and Practice*. 1992; 118(2):132-8.

Tatsuoka F, Iwasaki T, Takagi Y. Hysteretic damping of sands under cyclic loading and its relation to shear modulus. *Soils and Foundations* 1978; 18(2):25-40.

Truniger R, Vassiliou MF, Stojadinovic B. An analytical model to study deformable cantilever structures rocking on a rigid surface: experimental Verification. *Earthquake Engineering and Structural Dynamics* 2015; 44(15):2795-2815.

Ugalde JA, Kutter BL, Jeremic B. Rocking response of bridges on shallow foundations. PEER 2010-101, *Pacific Earthquake Engineering Research Center*, University of California at Berkeley, Berkeley, CA, 2010.

Vamvatsikos D, Cornell CA. Incremental dynamic analysis. *Earthquake Engineering and Structural Dynamics* 2002; 31, 491-514.

Vassiliou MF, Mackie KR, Stojadinović B. Dynamic response analysis of solitary flexible rocking bodies: modeling and behavior under pulse-like ground excitation. *Earthquake Engineering and Structural Dynamics* 2014; 43(10):1463-1481.

Vassiliou MF, Mackie KR, Stojadinović B. A finite element model for seismic response analysis of deformable rocking frames. *Earthquake Engineering and Structural Dynamics* 2016; DOI: 10.1002/eqe.2799.

Vassiliou MF, Makris N. Analysis of the rocking response of rigid blocks standing free on a seismically isolated base. *Earthquake Engineering and Structural Dynamics* 2012; 41(2): 177-196.

Vassiliou MF, Makris N. The dynamics of the vertically restrained rocking column. *Journal of Engineering Mechanics* 2015; 141(12): 04015049.

Vassiliou MF, Truniger R, Stojadinovic B. An analytical model of a deformable cantilever structure rocking on a rigid surface: development and verification. *Earthquake Engineering and Structural Dynamics* 2015; 44(15):2795-2815.

Vucetic M, Dobry R. Effect of soil plasticity on cyclic response. *Journal of Geotechnical Engineering* 1991; 117(1):89-107.

Wang S, Kutter BL, Chacko MJ, Wilson DW, Boulanger RW, Abghari A. Nonlinear seismic soil-pile structure interaction. *Earthquake Spectra* 1998; 14(2): 377-396.

Wang Z, Dueñas-Osorio L, Padgett JE. Influence of soil-structure interaction and liquefaction on the isolation efficiency of a typical multispan continuous steel girder bridge. *Journal of Bridge Engineering 2014; 19, SPECIAL ISSUE: Recent Advances in Seismic Design, Analysis, and Protection of Highway Bridges*, A4014001.

Wang Z, Dueñas-Osorio L, Padgett JE. Seismic response of a bridge-soil-foundation system under the combined effect of vertical and horizontal ground motions. *Earthquake Engineering and Structural Dynamics* 2013; 42(4): 545-564.

Wang YP, Chung LL, Liao WH. Seismic response analysis of bridges isolated with friction pendulum *bearings. Earthquake Engineering and Structural Dynamics* 1998; 27: 1069-1093.

Werner SD, Beck JL, Levine MB. Seismic response evaluation of Meloland road overpass using 1979 Imperial Valley earthquake records. *Earthquake Engineering and Structural Dynamics* 1987; 15:249-274.

Xie Y, Zhang J. Optimal design of seismic protective devices for highway bridges using performance based methodology and multi-objective genetic optimization. *Journal of Bridge Engineering* 2016; 10.1061/(ASCE)BE.1943-5592.0001009, 04016129.

Yang Z, Elgamal A, Parra E. Computational model for cyclic mobility associated shear deformation. *Journal of Geotechnical and Geoenvironmental Engineering* 2003; 129(12):1119-1127.

Yang CS, Werner SD, DesRoches R. Seismic fragility analysis of skewed bridges in the central southeastern United States. *Engineering Structures* 2015; 83:116-28.

Yi JH, Kim SH, Kushiyama S. PDF interpolation technique for seismic fragility analysis of bridges. *Engineering Structures* 2007; 29(7):1312-22.

Zhang J, Huo Y, Brandenberg SJ, Kashighandi P. Effects of structural characterizations on fragility functions of bridges subject to seismic shaking and lateral spreading. *Earthquake Engineering and Engineering Vibration* 2008; 7(4):369-382.

Zhang J, Huo Y. Evaluating effectiveness and optimum design of isolation devices for highway bridges using the fragility function method. *Engineering Structures* 2009; 31(8):1648-60.

Zhang J, Makris N. Rocking response of free-standing blocks under cycloidal pulses. *Journal of Engineering Mechanics, ASCE* 2001; 127(5): 473-483.

Zhang J, Makris N. Seismic response analysis of highway overcrossings including soil–structure interaction, *PEER-2001/02*, Pacific Earthquake Engineering Research Center, University of California, Berkeley, 2001.

Zhang J, Makris N. Kinematic response functions and dynamic stiffnesses of bridge embankments. *Earthquake Engineering and Structural Dynamics* 2002a; 31:1933-1966.

Zhang J, Makris N. Seismic response analysis of highway overcrossings including soil–structure interaction. *Earthquake Engineering and Structural Dynamics* 2002b; 31:1967-1991.

Zhang RR, Ma S, Safak E, Hartzell S. Hilbert–Huang transformation analysis of dynamic and earthquake motion recordings. *Journal of Engineering Mechanics* 2003; 129(8):861-875.

Zhao M. *Response of Bridges to Lateral Spreading and Earthquake Shaking*. Ph.D. Thesis, University of California, Los Angeles, 2011.